The neuronal basis of auditory-induced and spontaneous behavior in the zebrafish larva

Martin Privat

Sorbonne Université

Ecole doctorale Cerveau-Cognition-Comportement

Institut de Biologie de l'École Normale Supérieure

The neuronal basis of auditory-induced and spontaneous behavior in the zebrafish larva

Par **Martin Privat**

Thèse de doctorat de Neurosciences

Dirigée par **Germán Sumbre**

Présentée et soutenue publiquement le 10 février 2021

Devant un jury composé de :

Brice BATHELLIER	Examinateur
Claire WYART	Examinatrice
Jennifer LI	Rapporteuse
Owen RANDLETT	Examinateur
Hernán LÓPEZ-SCHIER	Rapporteur
Germán SUMBRE	Directeur de thèse

Abstract

In the vertebrate brain, the mechanisms underlying the generation of flexible motor behavior in response to sensory stimuli, or as a result of a voluntary decision to move are not well understood. Zebrafish larvae swim by moving their tails in discrete episodes called tail bouts, which facilitates the study of neural activity associated with those discrete episodes. They are optically transparent and amenable to an all-optical approach for the recording and manipulation of their neural circuits, a crucial property that makes this genetically tractable vertebrate with a small brain (around 100,000 neurons at 7 days) very useful for neuroethology. They react to auditory stimuli by generating bouts of locomotor activity, but are also capable of generating locomotor behaviors with rich temporal and kinematic dynamics even in the absence of any salient stimulus. I characterized the neuronal activity involved in the generation of auditory induced behavior, as well as spontaneous activity preceding the onset of self-generated tail bouts, in order to refine our understanding of locomotor circuits in the zebrafish larva, and the flow of information allowing both spontaneous locomotor activity and sensorimotor integration.

I have described a new category of auditory behavior which I called long-latency tail movements (LLTM). To characterize the neuronal basis of the sensorimotor integration of sound stimuli in the zebrafish auditory system responsible for the generation of LLTMs, I used two-photon and light-sheet calcium imaging in intact, behaving zebrafish larvae. I monitored neural activity elicited by auditory stimuli while simultaneously recording tail movements. I mapped the representation of sound frequency (pure tones) in the brain and observed a spatial organization of neural activity according to four different response profiles, suggesting a low-dimensional representation of frequency information, maintained throughout the development of the larvae. Low frequencies (150–450 Hz) were locally processed in the hindbrain and elicited LLTMs. This behavior is elicited in response to low amplitude stimuli, and differs in the latency of the onset and the variability of tail kinematics form the auditory escape response mediated by the Mauthner cells. Higher frequencies (900–1,000 Hz) rarely induced motor behaviors and were represented in the hindbrain and in the midbrain. Finally, I found that the sensorimotor transformations in the zebrafish auditory system are a continuous and gradual process that involves the temporal integration of the sensory response in order to generate a motor behavior.

Using high speed recordings in the hindbrain with a light-sheet microscope, as well as a more exhaustive volumetric mapping of neuronal activity in zebrafish larvae head-embedded in agarose but free to move their tail, I characterized the neuronal activity preceding the onset of spontaneous tail bouts. Contrary to the gradual buildup of activity found in some animals before the onset of spontaneous movements, I found hinbrain circuits that were recruited before some, but not all spontaneous tail bouts, principally in the vagal lobe, and the octaval nuclei, as well as in the tegmentum. This probabilis-

tic activation of brain circuits probably reflects a hidden complexity in the generation of spontaneous movements, where several neural circuits could be involved in the generation of sponataneous behavior. Those preliminary results could indicate a widespread behavioral role for the octaval nuclei, which integrates lateral line, vestibular and auditory information, and are the recipients of cerebellar projections.

Further experiments to test the causal role of the octaval nuclei in the generation of behavior, coupled to future work on mesoscale and microscale connectomes should help us shed light on the mechanisms underlying the generation of locomotor behavior, and their conservation across vertebrates.

Contents

List of Figures

1

Introduction

Birds of paradise are a fascinating family of birds found mostly in eastern Australia and New Guinea rainforest. They are renowned for their beautiful plumage, with many species endowed with a remarkable sexual dimorphism (fig 1.1). If their wild and vivid feathers are a sight to behold, birds of paradise are truly remarkable in the way they behave during courtship behavior. To seduce females, the male western parotia engages in a well choreographed ballet. First he prepares his stage by removing any stray twig or leave. Should a female show up, he proceeds with the whole performance: starting with a courteous bow, he shakes his head in rhythm, and spreads is flank feathers into a tutu—only then does he begin with the fancy footwork. If the female shows interest, our male parotia carries on with some more head bobbing, flashes of his iridescent feather throat patch, colored eye rolling, and a whirling dervish-like series of side steps. She is mesmerized by the motion of the male's six head plumes with black oval-shaped tips, which protrude from his silhouette from above while he dances. If the show is faultless, and the female has stayed until the end, the male hops on the female's perch, and they finally mate.

The intricacy and apparent futility of this frivolous ritual may make one wonder: what causes such a behavior? The answer to this question is complex and has many layers. At the level of the individual (proximate cause), the most direct and less explanatory level of causation is that the western parotia muscles contract and relax in a very specific

Figure 1.1: **Lawes's parotia (*Parotia lawesii*)**, from Papua New Guinea. Bottom-left female individual, top-left males individual. *Parotia Lawesii* display a strong sexual dimorphism, and an elaborated courtship behavior shaped by sexual selection. From wikipedia, https://en.wikipedia.org/wiki/Parotia.

sequence that leads to the production of the behavior I just described. The next level of explanation involves the brain. Neuronal circuits have formed during the development of the young western parotia so that when it reaches adulthood, its brain would be able to determine when the behavior should be triggered and proceed to generate the right sequence of actions. At the level of the species (ultimate cause), this courtship behavior is performed in a stereotyped way by all the males and also shares striking similarities with the courtship behavior of other members of the Parotia genus [Scholes, 2008]. This is an example of sexual selection, which is a form of intraspecific reproductive competition, and more specifically of intersexual selection where the females chose which males they want to reproduce with. Sexual selection acts on both the morphology and behavior of animals, and often fosters extreme or surprising traits which may appear to decrease the fitness of the sex under selection: flashy dancing birds make easier preys for their natural predators. The proximate and ultimate levels of explanations were formalized by Nikolaas Tinbergen in what is famously referred to as Tinbergen's four questions [Tinbergen, 1963]: what are the mechanisms, ontogeny, function and phylogeny of animal behaviors? These questions offer a guideline for ethologists and neuroscientists who are interested in the study of animal behavior.

For behaviors to be selected by evolution, they need to improve the fitness of individuals, and to be heritable and mutable. Brains provide the physical implementation that supports behaviors through dedicated neuronal circuits. Neuronal circuits can serve a very specific purpose and underpin innate behaviors, or provide the basis for implementing learned behaviors. They offer the flexibility needed to produce relevant motor patterns with respect to the environmental context. Ultimately, the structure of these neuronal circuits are encoded in the genome, such that mutations in the genome can change the structure of neural circuits and generate the variability in behavior on which evolution thrives (see [Tosches, 2017] for more details, fig 1.2). Neuronal circuits are a

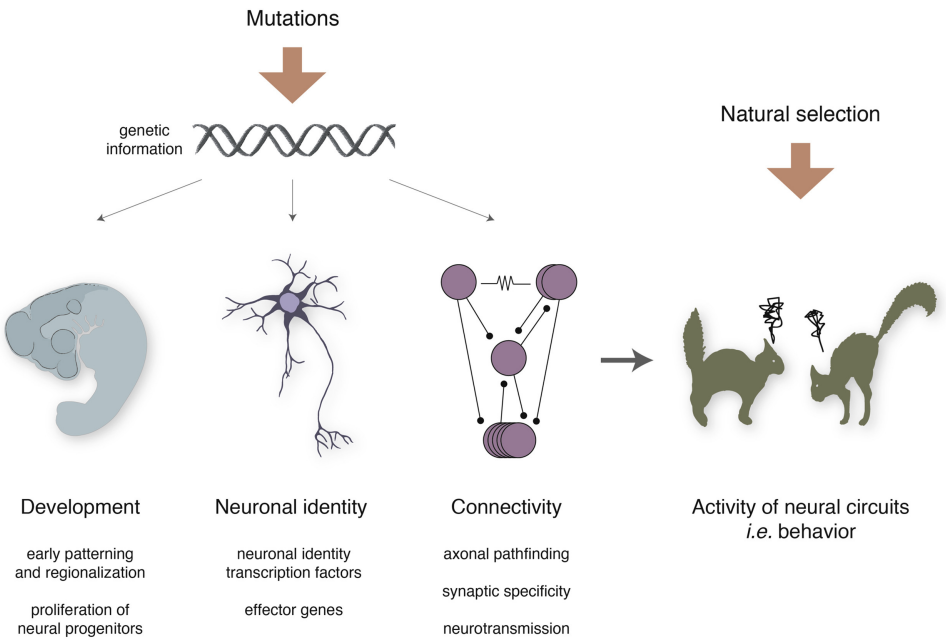

Figure 1.2: **Neural circuits are selected through evolution** Gene expression controls the establishment and function of neural circuits at multiple levels. During early development, transcription factors and morphogenes control the patterning of brain tissues, as well as the proliferation of neural progenitors. Genetic information also specifies the differentiation of neuronal cell types, as well as connectivity through axonal pathfinding, which depends on signaling molecules. Behavior emerges from the structure of neural networks, and animals that implement successful behavior will survive and pass on their genes. Mutations create variability which enables different behaviors to emerge and be selected. From [Tosches, 2017]

bridge between genetics and animal behavior, and provide an entry point for a deeper understanding of behavior.

During the second half of the twentieth century, the establishment of ethology combined with major technological developments for recording neural activity led to a renewed interest in the study of the neural basis of natural behavior, and the emergence of a new discipline called neuroethology (the study of the neural basis of behavior). Neuroethology combines cutting-edge neurophysiologic and behavioral experiments aiming at replicating the natural conditions in the lab. More recently, further innovations such as microelectrode arrays or calcium imaging have paved the way for recording populations of neurons in behaving animals. Today, it is possible to record tens of thousands of neurons—almost the whole brain—in a behaving zebrafish larva, which opens up unprecedented opportunities to further our understanding of brain function and behavior [Ahrens et al., 2013a]. With the rise of deep learning in the last decade, artificial neural networks are starting to pervade our lives and perform tasks, such as visual recognition, at a level of refinement close to human performance. Yet we still do not fully understand the mechanisms that make them so efficient. Despite all the recent advances in neuroscience and artificial

intelligence, we are still far away from "cracking the neural code". Now is a truly exciting time to do neuroscience, and try to understand how the collective activity of many neurons may contribute to a variety of fascinating behaviors.

During my PhD, I have used state-of-the-art techniques in calcium imaging to understand how zebrafish larva are able to gather information about their environment, and generate adequate motor patterns in response to external stimuli, a process called sensorimotor transformation. In addition, I also studied the neural basis of self-generated behaviors, in the absence of external stimuli (volition).

In this introduction, I will first talk about behavior, and its relationship with the nervous system. I will then attempt to outline the distributed and hierarchical architecture used by the brain to generate locomotor behavior. Finally, I will describe the neuronal processes underlying the generation of spontaneous and sensory-induced behavior, and argue that the zebrafish larva provides numerous advantages for the study of those systems. Although I have studied sensorimotor integration in the specific context of audition, I hope my results can be informative to a more general audience, along with the study of spontaneous behavior. To that end, I have decided not to include a specific paragraph about audition.

1.1 Brain, behavior, and the external world

Up to here, I have used the term behavior very lightly and without a precise definition, as if the meaning of this term was universally agreed upon and shared with the reader. While we all possess an intuitive understanding of what behavior is, and is not, there is a significant amount of debate on what constitutes behavior. In this section I will try to review what it means to talk about behavior, its relation with nervous systems, and the external world.

1.1.1 The elusive definition of behavior

Definitions in biology are seldom set in stone, however they help us understand the boundaries of the phenomena under scrutiny. In *The study of instinct (1951)*, Tinbergen defined behavior as: "The total movements made by the intact animal" [Tinbergen, 1951]. Behavioral biologists, however, do not agree on what constitutes behavior: in 2009, Levitis et al. surveyed 174 members of three behavior-focused scientific societies [Levitis et al., 2009]; they presented several statements that had to be qualified or disqualified as behavior by the respondents:

- Ants that are physiologically capable oflaying eggs do not do so because they are

not queens

- A sponge pumps water to gather food
- A spider builds a web
- A rabbit grows thicker fur in the winter
- A plant's stomata (respiration pores) close to conserve water
- A plant bends its leaves towards a light source
- A person's heart beats harder after a nightmare
- A person sweats in response to hot air
- A beetle is swept away by a strong current
- A rat has a dislike for salty food
- A person decides not to do anything tomorrow if it rains
- A horse becomes arthritic with age
- A mouse floats in zero gravity in outer space
- A group of unicellular algae swim towards water with a higher concentration of nutrients
- A frog orbits the Sun along with the rest of the Earth
- Flocks of geese fly in V formations
- A dog salivates in anticipation of feeding time
- Herds of zebras break up during the breeding season and reform afterwards
- A chameleon changes color in response to sunlight
- A cat produces insulin because of excess sugar in her blood

No consensus emerged as respondents had widespread disagreements on what characterizes behavior. These examples raise questions about different aspects of behavior, that can be loosely divided into issues about the nature of behavior and which systems can implement it. We will discuss these two issues in the following sections.

The nature of behavior

First, it must be noted that behavior can be seen as a specific instance (*e.g.* a drosophila is foraging for food) or a kind of generalizable category (*e.g.* courtship behavior is a kind of behavior displayed by many different animals). Behavior in itself is not a physical phenomenon, but rather a human ascription of physical events. We humans classify them in categories according to their evolutionary function or perceived purpose. This of course can be somewhat misleading, because:

- We don't know for sure that all behaviors are purposive or goal-directed or fulfill an evolutionary impetus, although there is a good reason to believe that behavior is costly in terms of energy expenditure, and therefore, random behaviors and evolutionary drift should be selected against.

- It is very hard to know the purpose of behavior just by observing it, and very easy to anthropomorphize what we see. Many animals perceive and interact with the environment in a way that we simply can't fathom at first sight (lateral line in fish, pit organs in snakes, echolocation in bats).

- Behaviors can be generated internally, not as a response to an external stimulus. This is generally related in animals to changes in internal states, and it is therefore hard to infer what causes behavior in such a case from the outside.

- Agency or volition is not necessary related to goal-directed, purposive or adaptive behavior, although there is likely some form of motivation to act in many animals. This is especially important to avoid the pitfalls of a "*natural teleology*": animals don't necessarily want to perform behavior A because it increases their chances of survival, but rather behavior A has been selected across generations by natural selection, thus individuals perform behavior A.

Some authors argue that behavior is a continuous process, and not a discrete one [Baum, 2013], and that animals are always behaving. However, it is still practical to chop up behavior into segments that may span different temporal scales in order to categorize them—for instance cichlid fish move rocks to create nests. This behavior can be studied alone, but on a larger time scale, it is part of a more complex courtship behavior.

Moreover, developmental changes are usually not considered as behaviors, since they occur on a large timescale. Whether other forms of phenotypic plasticity constitutes behavior is debated. For example, a wolf growing fur in winter senses and reacts to its environment, but the timescales over which it occurs is once again quite long and not very compatible with our intuitive understanding of behavior.

Finally, a last element in behavior is that it requires an action, inaction, or reaction to occur through a choice [Baum, 2013]. Once again this choice need not require any kind of agency or volition, only the opportunity to do different things, and a mechanism to select one option against others. This excludes passive motions where the cause is external: a fish carried away by the flow of water is not behaving.

The mechanisms underlying behavior

While behavior itself is not a physical process, it is the product of the activity of a material substrate. For a long time, behavioral studies focused on animals, with a strong emphasis on vertebrates, with brains as a substrate for their behaviors.

However, brains are not necessary for generating behavior. Porifera and Placozoans completely lack nerve cells, however they seem to do just fine in terms of behavior: *Trichoplax* can glide along a surface, which implies coordination of its beating cilia [Jorgensen, 2014]. Sponges are known to be able to contract in a timely fashion and to pump and filtrate water, and their larvae, which are motile, can perform phototaxis [Leys et al., 2019]. Non-bilaterian phyla possess specialized chemical signaling pathway that underlie these behaviors: sponges use slow acting G-protein coupled receptor pathways using glutamate as well as other commonly used small signaling molecules like nitric oxide [Elliott and Leys, 2010], and placozoans use complex peptidergic signaling [Varoqueaux et al., 2018].

Plants are also capable of generating behaviors. For example *mimosa pudica* can fold its leaves, and *Dionaea muscipula* can close its trap in response to external stimuli. Plants can open or close their stomata to avoid water loss, they are able to react to signals in their environment: gravity, light, humidity, temperature. The mechanisms underlying these behaviors depend on discrete chemical pathways or physical systems: for instance, gravitropism is made possible by the presence of statoliths, which are akin to sensory organs. Under the influence of gravity, statoliths modify the distribution of auxin in the root, which in turn produces a differential growth.

Even unicellular protists such as *Physarum polycephalum* may qualify for behavior (see fig 1.3): this slime mold is able to dynamically reshape its structure based on the location of food sources, and even shows some rudimentary form of memory [Saigusa et al., 2008]. This behavior could arise from oscillations in a chemical system, and can be modeled by a relatively simple system of differential equations. Along the same line, the social amoeba *Dictyostelium discoideum* is able to form aggregates of many cells, a collective behavior mediated by the periodic release of cAMP [Saigusa et al., 2008].

At this point, one might wonder: is life even a requirement for the production of

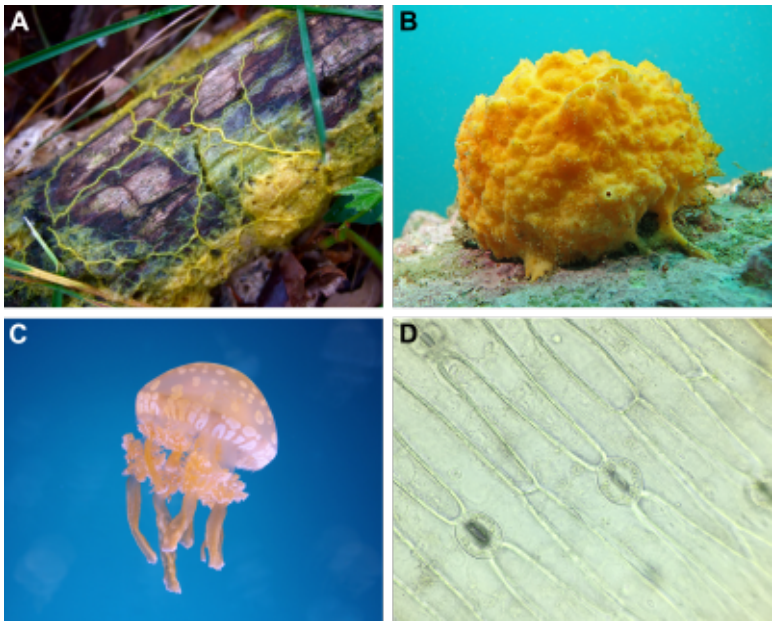

Figure 1.3: **Behavior across kingdoms**. Four eukariotes across different kingdoms displaying some form of behavior. **A**. *Physarum polycephalum*, an acellular slime mold endowed with remarkable maze-solving abilities. **B**. Sponge of the genus *Tethya*, among the most contractile poriferan species. **C**. A spotted jellyfish of the genus *Mastigias*. *Mastigias* host endosymbiotic dinoflagellates, which are photosynthetic. The jellyfish can migrate up to 1km a day to maximize light exposure, and moves down towards the depth at night. **D**. Plant cells can open and close their stomata to adapt to their environment. Images from wikipedia.

behavior? After all, a self-driving car may tick all the right boxes, it reacts to its surroundings, takes decisions, and is able to orient itself in space. Shouldn't this count as behavior, even more so than, for instance, a monosynaptic arc reflex such as the knee-jerk reflex? The consensus on this matter seems to be that although this kind of example may be convincing, the study of behavior in a biological framework excludes *de facto* that which is not alive.

As we have seen, there are different possible substrates for a given behavior, an idea sometimes referred to as multiple realizability. While plants or animals without nervous systems are able to produce behavior, we argue that the physical underpinning of this behavior is a collection of dedicated chemical cascade systems. These systems are generally rigid, capable of generating single behaviors, with limited adaptation capacities. Therefore, different behaviors will require additional chemical systems. Neural networks on the other hand are especially interesting because they offer a general solution implemented by a complex and non-linear system. They provide the flexibility and modularity necessary for complex behaviors to emerge. Ancestral neural circuits can be evolved to fit different functions in a way that is reminiscent of gene duplication or homeotic control [Tosches, 2017], which may allow relatively rapid innovations to occur in short evolutionary time.

1.1.2 The neural basis of behavior

The brain as a substrate for behavior: a brief history

The realization that brains are the physical substrate of behavior and thought has been a gradual process in the history of mankind, and has required two major shifts in our view of the world: the first one was to realize that both human and animal behavior relies on a physical substrate in the body, and the second one was to realize that human endeavor and animal behavior rely on the same fundamental processes.

In ancient Egypt, the dominant view was that the heart was a receptacle for the soul and the most important organ in the body. According to the mythology, the heart of the dead was weighed against a feather of the goddess Maat. If the heart was lighter than the feather, the deceased had led a virtuous life and would carry on to the Egyptian version of paradise, the fields of Aaru (fig 1.4). During the process of mummification, the embalmers started by removing and discarding the brain, but the heart was carefully preserved. The ancient Egyptians were however aware of some aspects of brain anatomy, and some side effects of brain injury including abnormal eye movements, paralysis and speech loss. Such wounds are described in the Edwin Smith surgical papyrus (17^{th} century BC), the oldest known medical treatise on trauma.

The Greek Alcmaeon of Croton ($^{5\text{th}}$ century BC), a pupil of Pythagoras and eminent

Figure 1.4: **The weighing of the heart, Book of the Dead**. The egyptian believed that the heart was the seat of the mind and an important part of the soul (the *ib*). The heart was the key to the afterlife, and special care was given to its preservation during the mummification process. The weighing of the heart against the feather of Maat, a goddess of truth and justice, was witnessed by Anubis (with the jackal head). If the deceased had led a virtuous life, the heart and feather would balance, and he would be admitted into the Fields of Reeds (*Aaru*) by Osiris. Image from wikipedia.

natural philosopher, is allegedly the first to propose that the brain is the location of the mind. Alcmaeon performed the dissection of the eye of an animal. In doing so, he discovered small tubes, the optic nerves, that projected to the brain. This led Alcmaeon to believe that the brain, being the place where the senses converge, should also be the seat of the mind. His views were not consensual at first, while Hippocrates (5th century BC) backed Alcmaeon, Aristotle (4^{th} century BC) was convinced that the brain's main function was to cool the passion of the heart.

Alcmaeon, who was once thought to have pioneered the use of dissection, may not actually have dissected the eye himself. However, the use of dissection as a systematic method to gain medical knowledge flourished after him. Eventually the deep taboo in Greek concerning human dissection was overcome by the strong push of the Ptolemaic government to make Alexandria an intellectual, scientific and cultural centre of the ancient Mediterranean world: Herophilus of Chalcedon and Erasistratus of Chios (3^{rd} century BC), considered as the founders of anatomy as a science, recognized the existence of sensory nerves entering the brain, and motor nerves leaving it to reach the muscles of the body. Their meticulous descriptions were completed by Galen of Pergamon (129–c.

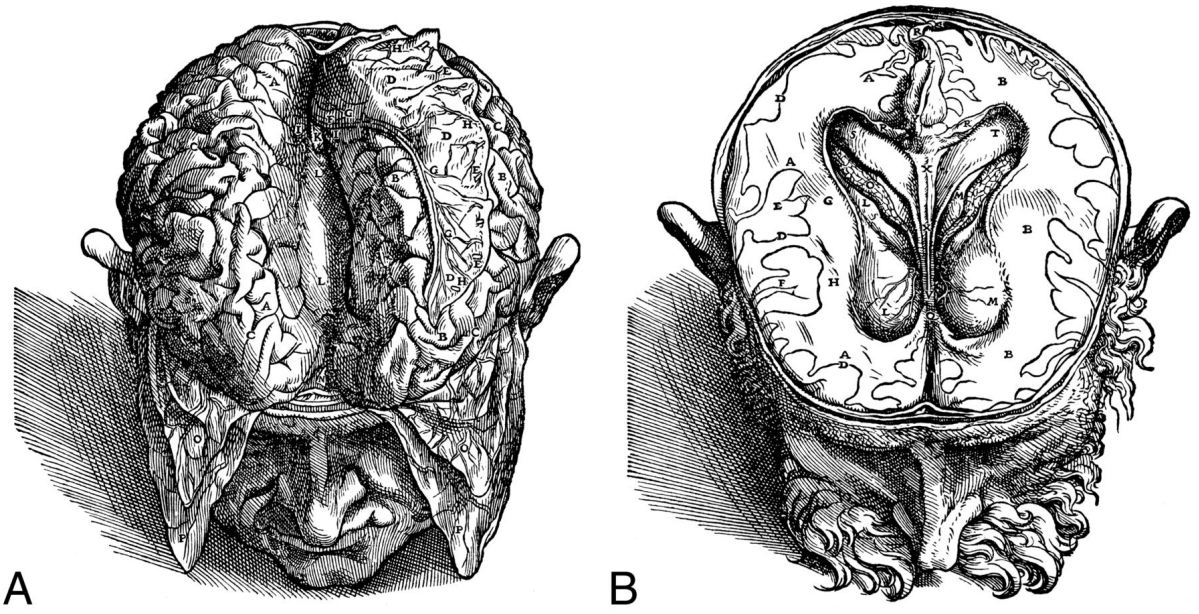

Figure 1.5: **Vesalius, De humani corporis fabrica**. *De humani corporis fabrica* was published in 1543, as a considerable overhaul of Galen's previous work. Vesalius relied heavily on human dissections, that he performed himself, and was a talented artist, well-versed in the technical advances brought by the Renaissance in drawing techniques as well as woodcut engraving for large scale printing. The *Fabrica* is a breathtaking piece of art, and has remained a reference textbook in anatomy, and notably in neuroscience, for centuries. Image from wikipedia.

210 AD), arguably the most influential medical researcher of antiquity, whose work remained mostly unrivaled until 1543, with the publication of *De humani corporis fabrica* by Andreas Vesalius (fig 1.5).

De humani corporis fabrica, along with Copernicus' *De Revolutionibus* are considered as the cornerstones of the scientific revolution, a new era of scientific inquiries permeated by the willingness to question previously held truths. Among those scientists and philosophers, René Descartes (1596-1650) brought to the fore two interesting concepts which have remained pregnant issues in philosophy ever since: the mind-body problem and the animal machine (fig 1.6). Descartes considered that animals were deprived of the ability to think, and that their behavior could be entirely understood in terms of mechanical processes, like cogs in a machine. This idea has laid the foundations for a reductionist program in the study of animal physiology and behavior. Humans however, according to Descartes, do possess a consciousness and the ability to think, which he couldn't reconcile with a mechanistic explanation. This lead to the formulation of the mind-body problem: how can humans, through the power of thought and consciousness, interact with the physical world?

Cartesian materialism was revolutionary, and inspired many scientists and thinkers to investigate further on the physical nature of brain function: while a growing amount

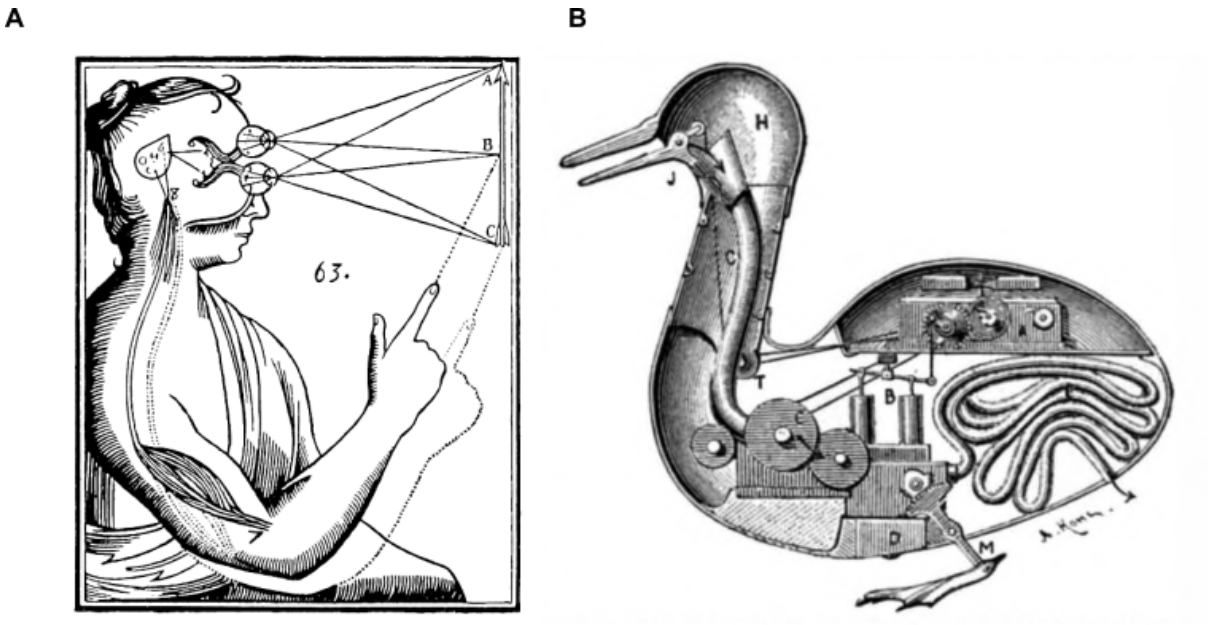

Figure 1.6: **The animal machine**. Descartes developed a pneumatic theory of brain function, whereby the brain acted on the muscles through the hydraulic motion of some fluid in the nerves to cause their contraction. Descartes proposed a purely mechanical view of the functions fulfilled by the body. He was however convinced of the existence of an immaterial soul, interacting with the body via the pinneal gland, a philosophical position called dualism. The possession of a soul was not extended to animals, which Decartes considered as living machines. **A**. Drawing from Descartes illustrating the mechanical nature of visual perception impinging on muscles. **B**. Vaucanson's digesting duck, an automaton created during the 18$^{\text{th}}$, mimicking the ability of animals to eat, and defecate. Vaucanson's duck illustrates, albeit trivially, the idea of the animal machine. Images from wikipedia.

of evidence hinted at the role of the brain as the center of thought, perception and motor command, there was no detailed theory of how the brain worked. Descartes, along with Galen or Herophilus, believed in a pneumatic, or balloonist theory of nerve action, whereby muscles would contract by inflating with fluid conducted by the nerves. This theory was finally disproved during the 18$^{\text{th}}$ century, notably by Galvani who showed that electricity made the muscles of dead frogs twitch.

During the 19$^{\text{th}}$ century, human exceptionalism—the idea that humans are very different from animals, and their behavior mostly controlled by culture and free will—started to gradually recede in scientific circles. Darwin's *On the Origin of Species* (1859) and *The Descent of Man* (1871) largely contributed to the downfall of the theory. The case of Phineas Gage, a railroad construction worker who recovered from a severe brain injury in 1848 and suffered from an alteration of his behavior as an aftermath of his accident, has become iconic as it may have been the first case suggesting the role of the brain in the determination of human personality. Broca, Charcot and others described many clinical cases linking the human brain, and lesions in specific regions, to behavioral deficits,

ushering in a new era for neurology and psychiatry.

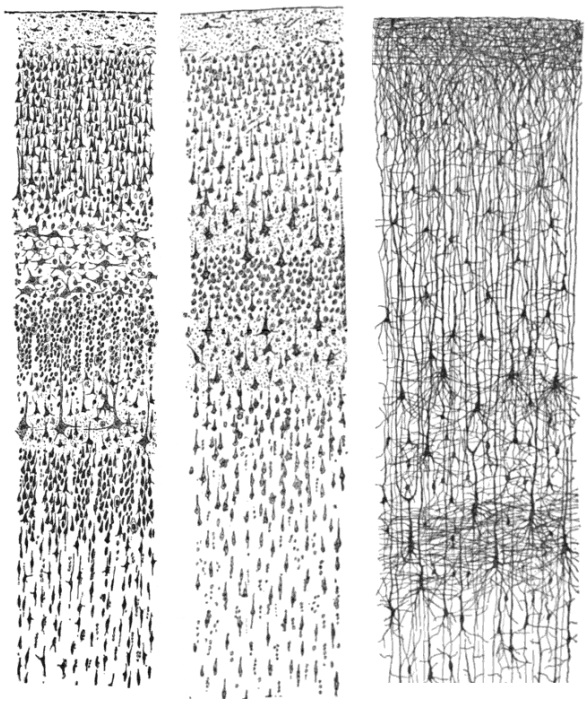

Figure 1.7: **The human cortex**, drawings of the human cortex by Santiago Ramón y Cajal, from *Comparative study of the sensory areas of the human cortex*. Cajal's drawings were influential in the adoption of the neuron doctrine, the idea that neurons are the discrete components of neural circuits. **Left**: Nissl-stained visual cortex of a human adult. **Middle**: Nissl-stained motor cortex of a human adult. **Right**: Golgi-stained cortex of a 1 1/2 month old infant. The structure of the different layers can be seen in these beautiful drawings. Image from wikipedia.

In laboratories around the world, fundamental discoveries laid the foundations of modern neuroscience, and allowed scientists to dream about a mechanistic understanding of animal behavior. Fritsch and Hitzig, in their 1870 seminal paper, where able to evoke movements of the paws in living dogs through the direct electrical stimulation of specific parts of their brain: they had proved the existence of the motor cortex, and provided a strong argument in favor of the hypothesis of the localization of function in the brain, which was still controversial at the time. Santiago Ramón y Cajal, building on the work of Camillo Golgi, brought an end to the debate between the reticular and neuron doctrine: the brain was made of distincts cells, called neurons (fig 1.7). Charles Sherrington, through his work on the physiology of simple and complex motor reflexes, supported the idea that the nervous system performs an integrative action, and hypothesized the existence of the synapse. Definite morphological proof of it's existence came in 1954, after the invention of the electronic microscope. The discovery of the mechanisms of the action potential, and chemical neurotransmission, completed the pictures of those foundational principles of brain function. New methods for recording neuronal activity in behaving animals together with a regain of interest in the study of behavior thus set the stage for

the emergence of brain and behavior research fields.

The 20th century witnessed the development of experimental sciences of behavior: psychology for human behavior and ethology for non-human animal behavior, along with their neuroscience-related disciplines, neuropsychology, cognitive science, and neuroethology.

The brain as a substrate for behavior: modern theories

Modern theories on the production of behavior can be broadly divided into three main categories, that correspond to three periods in the 20th century: behaviorism, cognitivism, and post-cognitivism. All three of them are still active and have shaped our current understanding of behavior.

Behaviorism Behaviorism was created in a laudable effort to make the study of behavior more empirical and objective. Building on the work of Ivan Pavlov on classical conditioning, John B. Watson proposed a new methodology: the study of behavior should not concern itself with mental states or events. Any reference to beliefs or desires should be eliminated from the vocabulary of the behaviorist. As Watson put it, the purpose of the study of behavior should be "To predict, given the stimulus, what reaction will take place; or, given the reaction, state what the situation or the stimulus is that has caused the reaction" (see fig 1.8.A). This position was refined by Burrhus F. Skinner. Skinner's radical behaviorism was focused on what Skinner called "contingencies of reinforcement", that described an antecedent-behavior-consequence relationship. For instance, if the consequences of a behavior are positive in a given context, the association between this context and the behavior will be reinforced. For Skinner the cause of behavior was in the history of these contingencies of reinforcement, not in the inner workings of the brain. Skinner was ready to talk about consciousness, feelings or states of mind, as long as they could be described as inner stimuli or identified with measurable behavior or environmental causes: he tried to replace mental terms by translating them into behavioral concepts. An example of this is given in Skinner's *About Behaviorism*, where he states that animals "feel pain in the sense of responding to painful stimuli" [Skinner, 1974].

Behaviorism, in it's dedication to get rid of the problem of dualism, ended up getting rid of the mind. For behaviorists, the brain was little more than a black box, and possessed no causal power: the brain was just an effector, the real cause of behavior lying in the previous co-occurence of stimuli and behavior, reinforced by the positive or negative consequences of that association on the organism. Starting in the late 1950's, the joint development of neuroscience, linguistics, artificial intelligence, and information theory have fueled the adoption of a theory of mind interested in behavior as well as

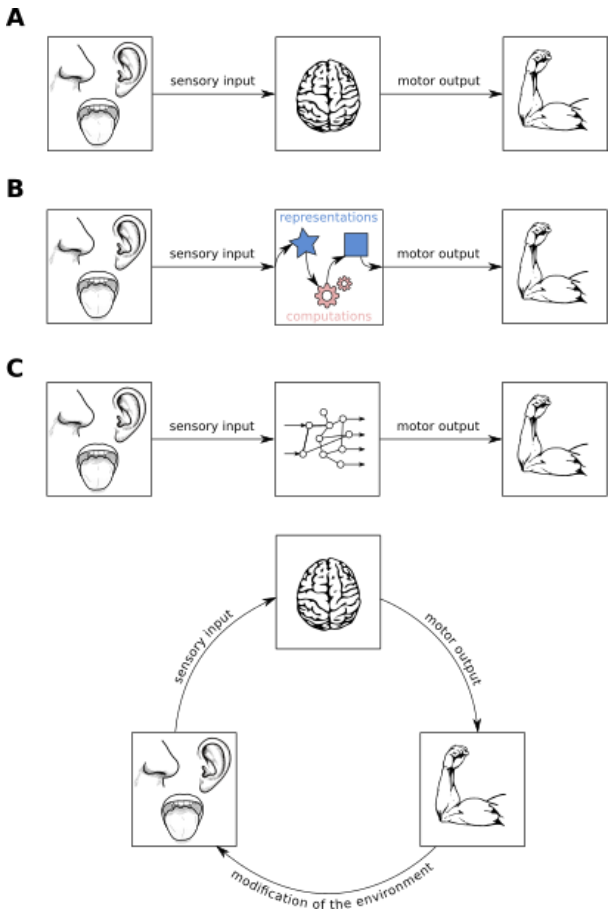

Figure 1.8: **Behaviorism, cognitivism, post-cognitivism A**. The central tenet of Behaviorism lies in the "contingencies of reinforcement", the association between stimuli, or context, and response via the consequences (positive or negative) of action. For behaviorist, the cause of behavior was in the history of associations between stimuli and responses. Behaviorist such as Skinner, considered the brain as little more than a black box, endowed with no causal role. Behaviorism was dominant, especially in the United States , most of the first half of the 20^{th} century. **B**. The central focus of Cognitivism is on the role of the brain in behavior. Cognitivism presuppose the existence of concepts such as mental representations, that can be acted upon by computations in the brain. **C**. Post-cognitivism either refutes the existence of mental representations or computations, or slightly adapt those concepts. Connectionists refute the computational theory of mind (or brain-computer metaphor), preferring the study of neural circuits dynamics to concepts like representations and algorithms. Enactivists argue for a closed loop account of action and perception, the brain-body-environment system should be considered in its entirety to describe cognitive functions.

mental states and information processing [Miller, 2003]. This process was called the cognitive revolution, and led to the creation of cognitive science.

Cognitivism Cognitivism relies on two core concepts: representations and computations (see fig 1.8.B). Representations are mental states, or structures, that store information. Computations are operations applied on those structures. A useful comparison

to understand representations and computations is the brain-computer metaphor: representations are the equivalent of data structures and computations are the algorithms. This metaphor is central to the classical stance of cognitive science, which posits that the brain really functions as a Turing-like computing device. Cognitivism has seen a widespread adoption, maybe due to a fruitful renewal in the study of attention, learning, memory, perception and other cognitive processes, but also to the development of brain imaging techniques such as positron emission tomography (PET), or more notably functional magnetic resonance imaging (fMRI), which allowed researchers to "see" the inner workings of the mind in action. One of the appeals of cognitivism could also stem from its compatibility, to a certain extent, with folk-psychology: concepts like "beliefs" or "desires", which appear very fruitful to describe and predict our behaviors, can be mapped to representations and computations and therefore can be studied under the paradigms of cognitive science.

Post-cognitivism Post-cognitivism comprehends several theories, among them, connectionism which contends that the computer metaphor shouldn't be taken too literally: the assumption that the brain functions like a Turing machine by serially manipulating symbols and representations is contested in favor of a more biologically plausible and parallel architecture, the neural network (see fig 1.8.C). Two strengths of connectionism are:

- The recent successes of deep learning, which relies on artificial neuronal networks, in the field of artificial intelligence (AI), enabling extraordinary improvements were symbolic AI was seeing diminishing returns.
- Its direct compatibility with dynamical systems which describe the activity of populations of neurons in time as trajectories in a state space. These trajectories can be classified into different categories such as attractors, limit cycles or chaotic system, which can be linked to specific kind of cognitive processes such as decision making, noise reduction, associative or short term memory and more.

Another flavor of post-cognitivism is enactivism. Enactivism challenges the traditional view of cognitive science by looking at what happens beyond the brain when an organism behaves. According to the enactivist theory, perception is an active process that arises through the interaction of an organism with its environment (see fig 1.8.C), via sensorimotor feedback loops [Varela et al., 1991]. In that respect, cognition is said to occur through these sensorimotor loops and it is not strictly restricted to the brain: the outside world can be considered as a form of external memory on which the organism draws through active sensing [O'Regan and Noë, 2001, Noë, 2004]. Enactivism often em-

braces the position of embodied cognition, which states that the body puts a constraint on, enables, or even takes part in certain types of cognitive processes:

- The physical structure of sensory organs, for instance the retina, already allows some form of processing since it samples the world as a kind of array, with nearby neurons on the retina being excited by nearby locations in the external world.
- The concepts of left and right would be meaningless to an organism with radial symmetry.
- Our bodies, joints, musculature, all put a constraint on the type of movements we can produce. Infants learn to control their bodies through a dynamic interaction with the world, and amputees learn new sensorimotor strategies to attain their goals.

1.1.3 Quantification of behavior

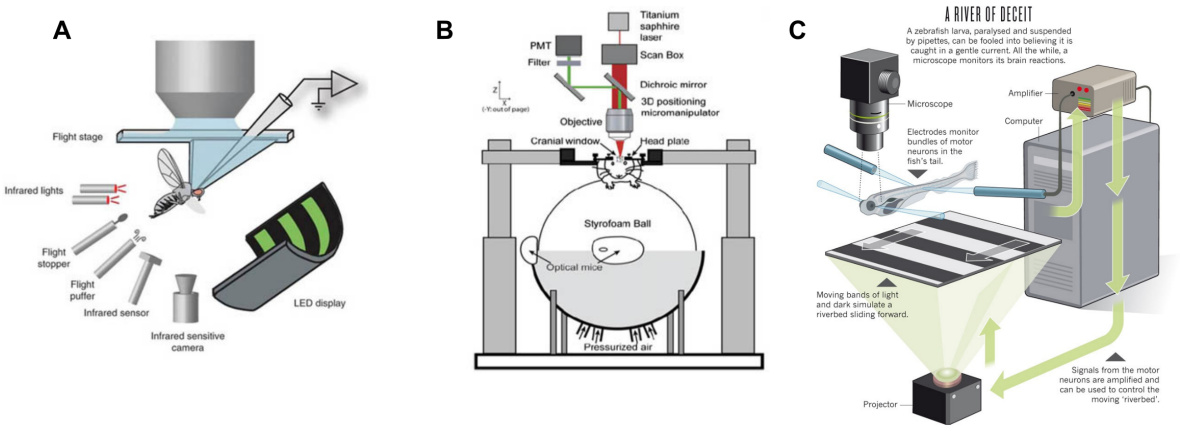

Figure 1.9: **Virtual reality**. Virtual reality systems are designed to close the loop between action and perception. The movements of tethered animals are recorded with an infrared camera (**A**) , sensors on a rolling styrofoam ball (**B**), EMG signals (**C**), or other techniques, and a computer program computes the displacement that would have resulted from those movements if the animals were free to move. The virtual environment is updated according to this prediction and fed back to the tethered animal. From [Hughes, 2013, Engert, 2013]

Neuroethologists and enactivists share a deep interest in the relationship between the brain and the surrounding environment: as a product of natural selection, behavior makes sense only in a natural context. As a response to these concerns, new paradigms in the study of behavior have emerged, such as closed loop and virtual reality experiments (see fig 1.9) which enable to record neural activity while monitoring behavior and modifying the environment. In such paradigm, the animal is usually tethered, but new approaches

enable to record neural activity in freely behaving animals [Kim et al., 2017, Marques et al., 2020].

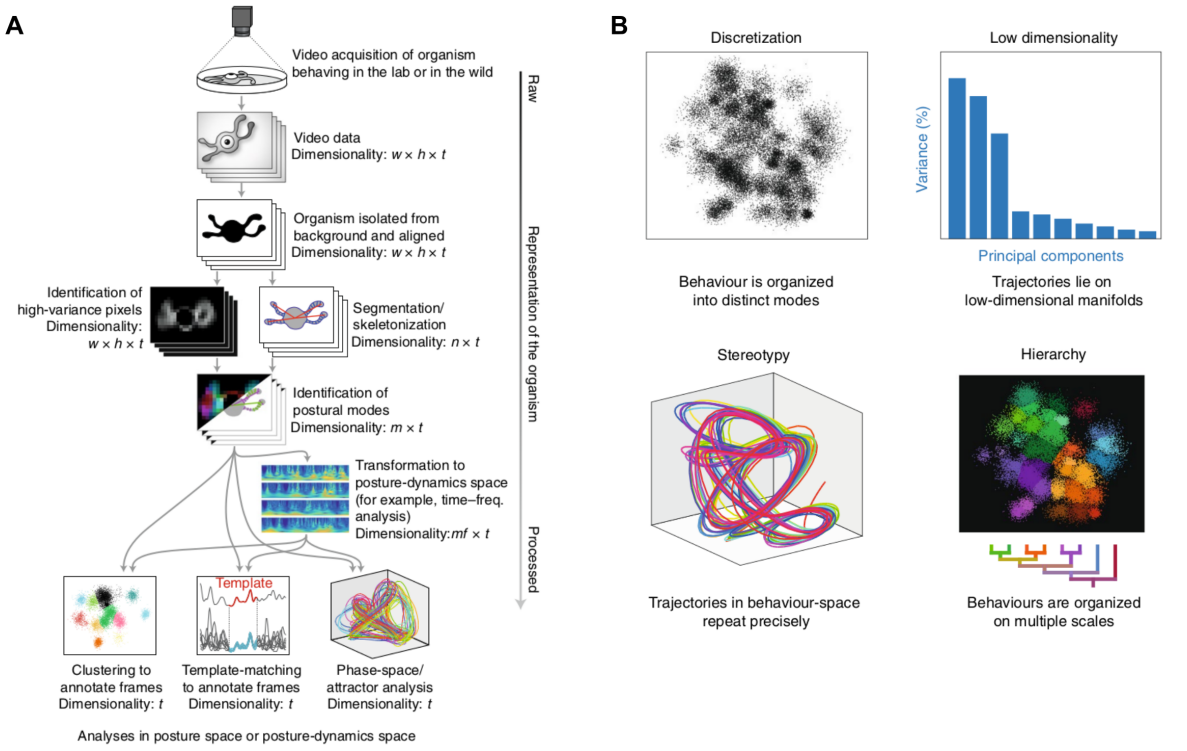

Figure 1.10: **Ethology as a physical science**. **A**. Raw video recordings of behaving organisms are analyzed using machine-learning techniques such as segmentation, or skeletonization. Kinematic features can be extracted from those representations, or they can be directly fed to other machine-learning algorithm to find recurring patterns of behavioral activity, and classify behavioral modules into distinct categories. **B**. Clustering techniques, dimensionality reduction techniques (linear such as PCA, or non-linear such as t-SNE) or representation of movements as trajectories in a abstract postural space point to four general organizing principles of behavior: discretization, low dimensionality, stereotypy and hierarchy. From [Brown and de Bivort, 2018].

During many decades, the study of behavior consisted in careful observation in the field, or manual inspection of video recordings to reconstruct ethograms. New quantitative methods based on the analysis of large behavioral recordings, aided by machine vision algorithm, big data approaches, and machine learning (see fig 1.10) are redefining how we are classifying behavior [Reiser, 2009, Brown and de Bivort, 2018, Berman et al., 2016]. The goal of these methods is to describe fine structures of behavior, using the same kind of approach that we use to describe neural activity.

1.2 Generating motor behavior

In the previous section I have talked about the definition of behavior, how behavior is implemented by physical substrates such as nervous systems, and how neuroscientists theorize the relationship between the brain and behavior. In this section I will dive further into the brain, from a brief overview of the mammalian motor system, to a more detailed description of the neural basis of motor behavior in the zebrafish larva.

1.2.1 The neural basis of motor behavior

The mammalian nervous system controls behavior via a distributed and hierarchical network in the brain and spinal cord (see fig 1.11.A,B). On top of the hierarchy, the motor cortices (motor, premotor and supplementary motor area in primates, M1 and M2 in rodents) are believed to control a variety of functions from specifying fine actions to integrating contextual cues. The motor cortex shows a somatotopic organization, where adjacent limbs in the body are represented in nearby regions in the motor cortex [Penfield and Boldrey, 1937]. The motor cortices project to different targets: directly to the spinal cord, to brainstem circuits such as the reticular formation, but also importantly to two different re-entrant loops formed by the basal ganglia and the cerebellum through the thalamus. The basal ganglia are involved in action selection and invigoration of movements [Park et al., 2020], while the cerebellum is believed to be necessary to fine tune movements, detect and correct errors [Grillner and El Manira, 2020]. The basal ganglia provide continuous inhibition of the different command centers in the mesencephalic locomotor region (MLR) and diencephalic locomotor region (DLR) preventing behavior to be generated in the resting state (fig 1.11.D). Locomotor behavior can be generated when this inhibitory influence from the basal ganglia is released through striatal inputs [Grillner and El Manira, 2020]. Some brainstem structures such as the superior colliculus are also able to generate behavior. Different descending pathways project to the spinal cord to drive locomotor behaviors: the corticospinal, rubrospinal, tectospinal, interstitiospinal, reticulospinal, and vestibulospinal tracts are the major descending pathways involved in motor control [Lemon, 2008] (fig 1.11.C). In the spinal cord, central pattern generators organize and sequence muscle activity to allow for rhythmic operations necessary for moving [Grillner, 2006].

The zebrafish motor system

The zebrafish motor system has been generating a lot of interest in the last decades. It opens a window on the inner processes of a vertebrate brain, with the potential to record the whole brain of a behaving animal with near single-cell resolution [Ahrens

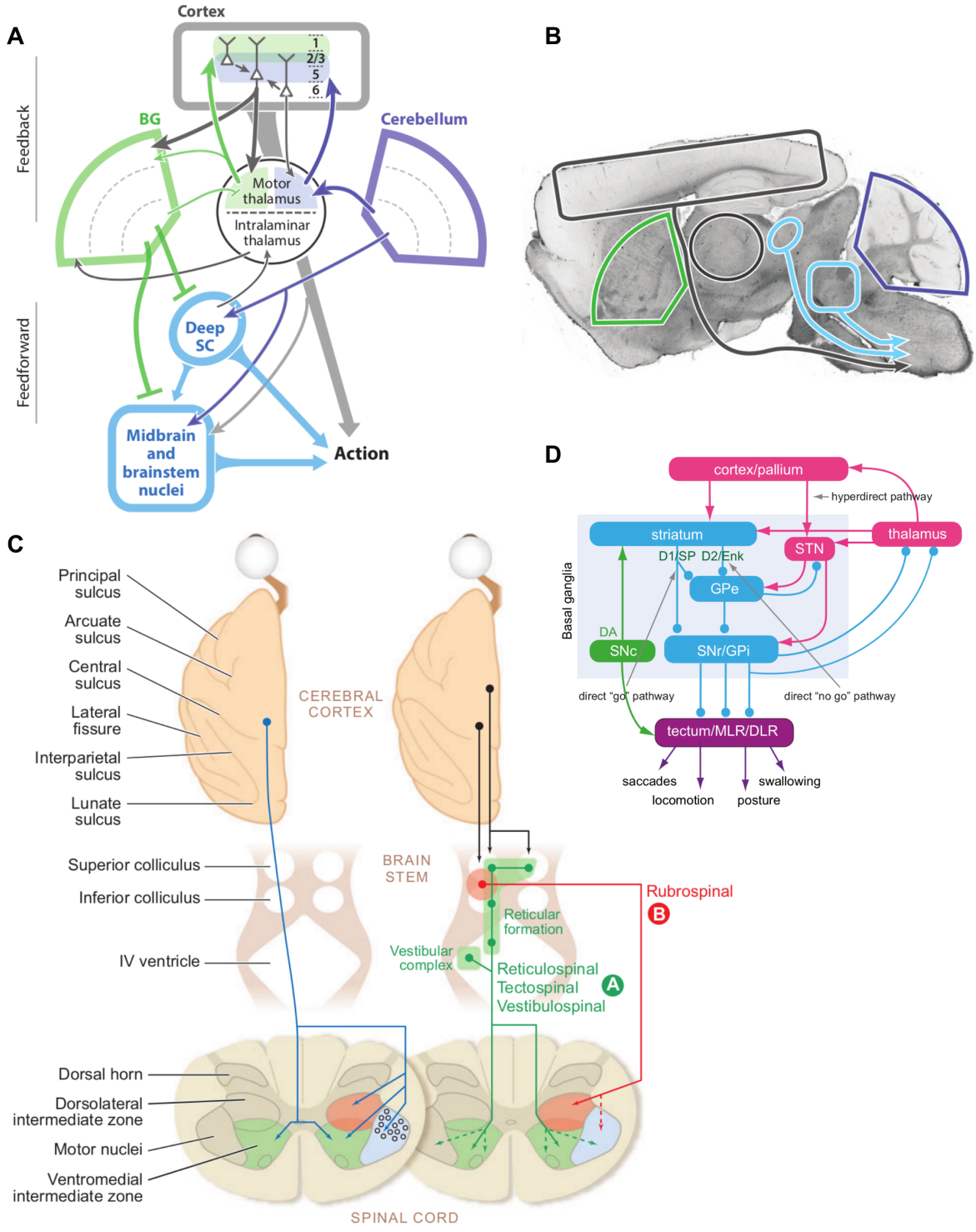

Figure 1.11: **The mammalian motor hierarchy**. **A**. Brain circuits involved in the generation of movements. The motor cortex projects directly to the spinal cord (see *C*), but also to the basal ganglia (striatum). The basal ganglia is involved in a control loop with the cortex via the motor thalamus. The basal ganglia also have an inhibitory influence on downstream targets in the midbrain and brainstem nuclei, as well as in the superior colliculus. (legend continued next page)

et al., 2013a]. It is also a valuable model to study the evolution of nervous systems in the vertebrate lineage: many parts of the mammalian motor system have a developmental and functional homologue in the teleost brain, while other parts are critically different. A general rule of thumb is that structures are well conserved up to the midbrain, while the forebrain has undergone significant changes between different vertebrate groups. One of the major hindrances in establishing homologies between ray-finned fishes such as zebrafish and mammals is that the telencephalon of the former undergoes a process called eversion during development, which is fundamentally different from the evagination seen in mammals [Mueller et al., 2011]. I will review the motor system of zebrafish in the light of the structures involved in the mammalian system.

The dorsal pallium Recent studies using the expression of genetic markers are starting to untangle the organization of the zebrafish telencephalon [Wullimann and Mueller, 2004, Mueller et al., 2011]. Zebrafish do not possess a six-layered isocortex in their telencephalon. Instead, the teleost telencephalon is organized into various nuclei. The central zone of the dorsal pallial division (Dc) corresponds to the mammalian dorsal pallium, which contains the isocortex. Yamamoto *et al.* have shown that the goldfish pallium receives sensory inputs from different modalities [Yamamoto and Ito, 2008], but

Figure 1.11 (continued): This inhibition can be released through the activation of the direct pathway of the basal ganglia (see *D*), to trigger the generation of movements. The cerebellum is also involved in a loop with the motor cortex, to refine movements, predict the consequences of motor commands, and correct errors. **B**. Anatomy of the network outlined in *A*, overlaid on a parasagittal section of a mouse brain. **C**. The descending motor pathways in the primate brain consist in a corticospinal tract (blue, on the left), a rubrospinal tract (red, on the right) as well as vestibulospinal, recticulospinal, and tectospinal tracts (green, on the right). Together they project to the spinal cord central pattern generators to control voluntary and autonomous motor activity. **D**. Basal ganglia circuits. The basal ganglia output nuclei (GPi/SNR) exert an inhibitory influence on downstream circuits, the Diencephalic and Mesencephalic Locomotor Regions (DLR/MLR), preventing the execution of movements. This inhibition can be released via cortical inputs in the striatum to the direct pathway, or strengthened via inputs to the indirect pathway. The direct pathway inhibits the output nuclei, which releases the inhibition on downstream premotor area, which can trigger movement execution. It also releases feedback inhibition to the thalamus, which sends inputs back to the cortex. The indirect pathway causes inhibition in the GPe, which is active at rest. GPe being inhibited, there is less inhibition in the STN and output nuclei. The output nuclei become active and inhibit DLR/MLR, the thalamus, and prevent the execution of movements. Finally, basal ganglia activity is modulated by dopaminergic activity via the D1 receptors in the direct pathway, and D2 receptors in the indirect pathway. Red: excitatory glutamatergic , blue: inhibitory GABAergic neurons, green: dopaminergic neurons. From [Park et al., 2020, Lemon, 2008, Grillner and El Manira, 2020].

so far, the function of the teleost dorsal pallium remains unclear.

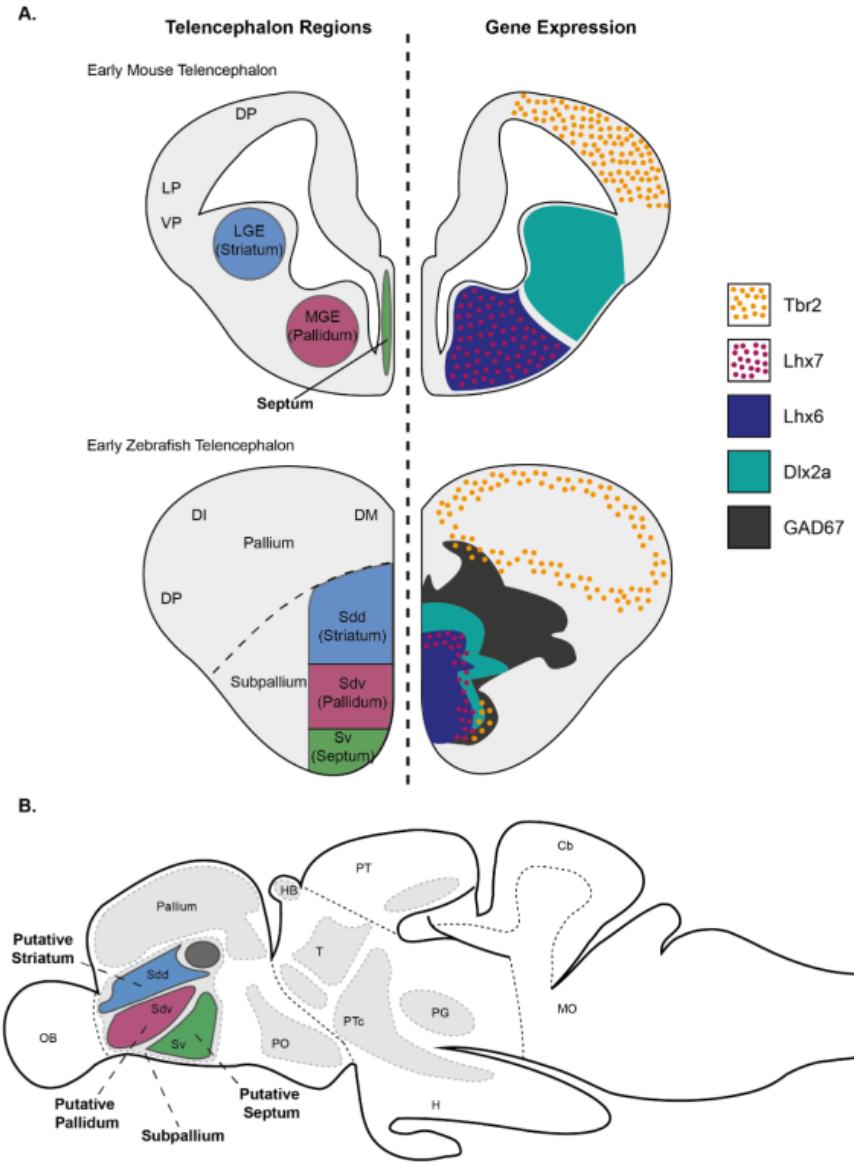

Figure 1.12: **The zebrafish striatum, comparative anatomy**. **A**. Molecular markers of the subpallium in the early telencephalon of mouse (upper panel) and zebrafish (lower panel). Zebrafish Tbr2 and Dlx2a demarcate pallial vs. subpallial territories, as in mouse. The lack of Lhx6 and Lhx7 in the dorsal subdivision (Sdd) of the dorsal subpallium, is interpreted as the homologue of the mammalian LGE (striatum). **B**. Sagittal view of the adult zebrafish brain specifying the subpallium and the regions of the putative striatum, pallidum and septum. From [Rimmer, 2019].

Thalamus The mammalian thalamus is involved in cortico-striatal and cortico-cerebellar loops, and thus plays an important role in the generation of motor behavior. The zebrafish thalamus however completely lacks this connectivity. It does not even act as a general sensory relay, with the exception of auditory information [Mueller, 2012]. The

preglomerular complex, a midbrain structure, seems to be functionally closer to the mammalian thalamus in that respect [Mueller, 2012, Bloch et al., 2020]. To date, the precise role of the thalamus and preglomerular complex in the generation of behavior is still unknown.

Basal ganglia Due to their phylogenetic position as an out-group, the lampreys are extraordinarily helpful to understand the evolution of vertebrates. They belong to the jawless fishes, a class of vertebrates that diverged from the jawed vertebrate more than 500 million years ago. A recent study by Stephenson-Jones *et al.*, using immunohistochemistry, tract tracing, and whole-cell recordings, showed that the major components of the mammalian basal ganglia (striatum, globus pallidus interna and externa, and subthalamic nucleus) are present in lampreys. This study supports the idea that at least a crude version of the basal ganglia might be common to all vertebrates. The use of molecular markers has refined our understanding of the localization and development of basal ganglia in zebrafish larva [Mueller et al., 2008], fig 1.12.

A dopaminergic nucleus, the posterior tuberculum, projects to the striatum (Sdd, fig 1.12) and the spinal cord, and could fulfill a role similar to the substantia nigra in zebrafish [Rink and Wullimann, 2001, Stephenson-Jones et al., 2011, Wullimann, 2011, Grillner and Robertson, 2016]. Laser ablation of posterior tuberculum neurons reduced spontaneous swimming movements in larval zebrafish [Jay et al., 2015], which is reminiscent of a Parkinsonian phenotype. The ascending dopaminergic system to the striatum comes from the midbrain in mammals (class A8-10 dopaminergic neurons), while the posterior tuberculum is a diecenphalic structure (class A11 dopaminergic neurons), suggesting that the dopaminergic striatal control may have different developmental origins among vertebrates, although they may share a common function [Matsui, 2017].

In a subsequent study, Filippi *et al.* have demonstrated that teleost also possess the forebrain structures and genetic markers of co-release of dopamine and GABA/Glutamate found in the mammalian basal ganglia [Filippi et al., 2014, Wullimann, 2014] (see fig 1.12). This evidence is compatible with the presence of a direct and indirect pathway, but no re-entrant pathway closing the loop. The functional role of the zebrafish basal ganglia in motor behavior remains, however, largely unknown.

Cerebellum The zebrafish cerebellum seems to be similar in structure and function to the mammalian cerebellum. The zebrafish cerebellum, as in all jawed vertebrates, can be divided in three major parts: the valvula cerebelli, the corpus cerebelli and the vestibulolateral lobe [Wullimann et al., 1996]. Contrary to the mammalian cerebellum, the zebrafish cerebellum lacks deep cerebellar nuclei. Instead, zebrafish possess eurydendroid cells, a specific cell type absent in mammals, which project to similar targets in the

brain stem and spinal cord as the deep cerebellar nuclei of other vertebrates [Bae et al., 2009]. The vestibulocerebellar tract is a second efferent pathway from the cerebellum , that emerges directly from gabaergic Purkinje cells [Bae et al., 2009]. The vertebrate cerebellum receives afferent input from two principal sources, the mossy and climbing fibers (fig 1.13).

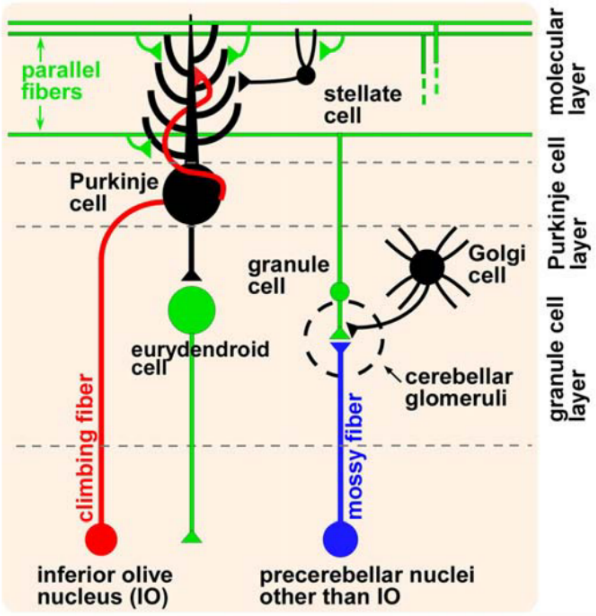

Figure 1.13: **Zebrafish cerebellum**. The two input channels to the cerebellum are the climbing fibers (red) from the inferior olive, which directly innervate the Purkinje cells, and the mossy fibers (blue) that originate in pre-cerebellar nuclei, excluding the inferior olive, and synapse onto the granule cells (green). Information from the mossy fibers is conveyed to the dendrites of Purkinje cells *via* the parallel fibers (axons of the granule cells), where it can be integrated with the information coming from the climbing fibers. The Purkinje cells in turn synapse with the eurydendroid cells, the which form the main output of the cerebellum, along with cerebellovestibular projections directly from the Purkinje cells. From [Bae et al., 2009].

From a functional point of view, sensory and motor representations are encoded by the Purkinje cells [Knogler et al., 2017, Knogler et al., 2019], which is compatible with a function in regulating sensorimotor behavior, and monitoring expected outcome of action. Moreover, olivocerebellar circuits could be involved in the computation of error signals during motor adaptation, which are necessary for driving motor learning mechanisms [Ahrens et al., 2012]. The zebrafish cerebellum's mossy fibers seem to get their inputs from the pretectum and medulla oblongata, but there does not seem to be a pallial-cerebellar-thalamic loop as in mammals [Dohaku et al., 2019].

Superior colliculus The superior colliculus, or optic tectum in non-mammalian species, is endowed with a retinotopic map, and the ability to control behavior: its role is potentially conserved across the whole vertebrate lineage [Suzuki et al., 2019]. The mammalian

superior colliculus (SC) is notably involved in the control of visuomotor and oculomotor behavior, such as saccadic eye movements [Oliveira and Yonehara, 2018, Basso and May, 2017, Sprague and Meikle, 1965]. In zebrafish, the optic tectum is homologous to the SC, and is instrumental in orchestrating many visuomotor behaviors: escape to looming stimuli [Temizer et al., 2015, Dunn et al., 2016a], prey capture [Gahtan et al., 2005, Bianco and Engert, 2015], or decision-making between approach or avoidance of a visual stimulus [Barker and Baier, 2015, Helmbrecht et al., 2018]. Finally, the zebrafish larva optic tectum displays rich neuronal dynamics, even in the absence of sensory stimuli, via the spontaneous activation of neuronal assemblies. These spontaneous assemblies strongly resemble stimulus-driven activity, and may have a role in triggering spontaneous behavior [Romano et al., 2015].

Mesencephalic and diencephalic locomotor regions The presence of a Mesencephalic and Diencephalic motor region (MLR,DLR respectively) has been attested in many vertebrates including lamprey [El Manira et al., 1997, Sirota et al., 2000, Dubuc et al., 2008]. They are both believed to generate behavior via the reticulospinal system. In the zebrafish larva, Chen *et al.* propose the existence of a MLR close to the nucleus of the medial longitudinal fascicle [Chen et al., 2018]. To the best of my knowledge, there is no reference to a DLR in the zebrafish larva yet in the literature.

Hindbrain motor and premotor centers Cells with different molecular identities in the hindbrain [Kinkhabwala et al., 2011, Koyama et al., 2011] have been linked with different roles in locomotor behavior. V2a neurons in the hindbrain show different pattern of rhythmicity, providing both tonic and phasic inputs to downstream spinal circuits [Kimura et al., 2013], while the activity of neurons in a medial stripe of glycinergic neurons in the domain of expression of the transcription factor engrailed1b is correlated with the onset of locomotion [Severi et al., 2018]. Finally, two bilaterally symmetric clusters of gabaergic and glutamatergic cells on each side of the midline called the hindbrain oscillator [Ahrens et al., 2013a], or anterior rhombencephalic turning region (ARTR), show a neural activity which is correlated to the direction of swim bouts [Dunn et al., 2016b]. Glutamatergic cells of the ARTR project to the reticulospinal system, and more specifically to cells which have been described to been involved in turning behavior such as RoV3 [Orger et al., 2008]. During locomotor behavior, a large number of cells in the hindbrain are active (see fig 1.14); there may be many more hindbrain populations involved in the control of locomotor behavior, which could constitute a “rhombencephalic locomotor region”, and will require further studies.

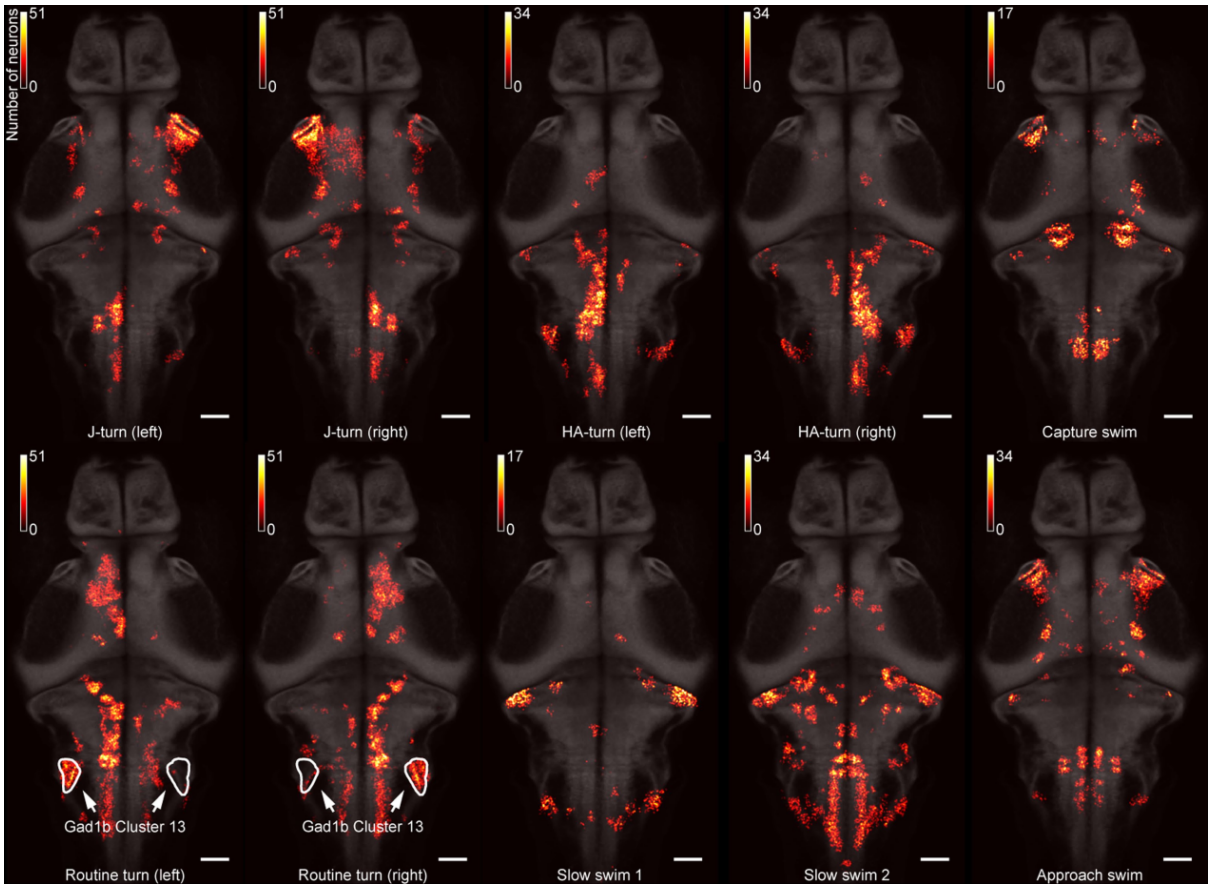

Figure 1.14: **Zebrafish visuomotor networks for the control of different categories of prey capture movements**. Visuomotor networks that drive distinct movement types associated with pursuit and capture of prey across animals. Motor networks were identified for all seven observed movement types. From [Marques et al., 2020].

Descending pathways The descending pathways in the zebrafish larva have been identified by backfilling projections in the spinal cord with horseradish peroxidase, or other markers [Kimmel et al., 1982, Metcalfe et al., 1986]. Some labelled neurons are large with a stereotypical morphology and can be individually identifiable between animals. One iconic example are the Mauthner cells, a pair of large neurons in the hindbrain which integrate information from different sensory modalities and mediate fast escape responses [Eaton et al., 1977]. Many descending tracts found in mammals are also present in fish, suggesting an ancient origin for the locomotor system of vertebrates.

The vestibulospinal tract runs from the lateral side of the hindbrain, (fig 1.15.A) to the spinal cord. While vestibulo-ocular responses have been described [Ehrlich and Schoppik, 2017], the vestibulospinal tract probably has a role in motor control depending on the sense of balance, but its precise function is not well known in larval zebrafish.

In zebrafish, the optic tectum sends descending fibers that do not reach the spinal cord, as in mammals, but instead end in the medulla, forming a tectobulbar rather than a tectospinal tract [Yamamoto et al., 2017]. This tectobulbar tract is thought to impinge

on behavior by recruiting reticulospinal neurons in the medulla.

The nucleus of the medial longitudinal fascicle (nMLF), due to its localization in the midbrain, at the beginning of the MLF, may be homologous to the interstitial nucleus of Cajal [Yamamoto et al., 2017, Smeets and Timerick, 1981]. In mammals, the interstitiospinal tract controls eye movements in coordination with the head and neck [Fukushima, 1987], while in zebrafish larva, specific neurons in the nMLF modulate locomotor kinematics of the tail, in particular the duration and oscillation frequency of tail movements, thus exerting a control on swimming speed [Severi et al., 2014]. Neurons on each side of the zebrafish nMLF are able to steer the direction of swimming [Thiele et al., 2014, dal Maschio et al., 2017]. In the recent zebrafish literature, it is most often described as part of the reticulospinal system.

In mammals, the rubrospinal tract, which emerges from the red nucleus or nucleus ruber, is involved in the motor control of limbs. Two teleost homologue of the red nucleus have been proposed by Goldstein and Nieuwenhuys & Pouwels, which correspond to two different regions in the midbrain [Yamamoto et al., 2017]. In both the adult and larval zebrafish, a midbrain structure corresponding to the red nucleus of Goldstein, that receives input from the contralateral cerebellum and projects to the spinal cord, has been identified by Matsui *et al.* [Matsui et al., 2014a, Matsui et al., 2014b], who hypothesize that it may be involved in the motor control of pectoral fins. Functional studies of the role of the red nucleus are however still lacking, maybe due to the lack of specific molecular markers.

One of the most extensively studied descending pathway involved in the control of behavior in the zebrafish larva is the reticulospinal pathway. Some giant neurons in the reticulospinal system can be robustly identified across different individuals (see fig 1.15.A). There are numerous reports of the implication of reticulospinal (RS) neurons in various motor behaviors in zebrafish, from reflex responses, such as the startle reflex, to more integrated sensorimotor behaviors [Dunn et al., 2016b, Migault et al., 2018, Naumann et al., 2016, Chen et al., 2018, Liu and Fetcho, 1999, Semmelhack et al., 2014, Thiele et al., 2014]. Some RS neurons could be selectively recruited for specific behaviors, such as MeLC and MeLr in visual prey capture [Gahtan et al., 2005], the Mauthner cells in the acousticovestibular fast escapes [Kimmel et al., 1974], MiD3cm in non-Mauthner-mediated escape response to tactile head stimuli [Kohashi and Oda, 2008]. Some authors argue that certain giant RS neurons (Mauthner, MiD2cm, MiD3cm) have undergone serial duplications in the successive segments of the hindbrain, which could provide the substrate for either a redundant and robust specification of locomotor commands, or functional diversification. The later hypothesis is supported by the discovery that patterns of activation of Mauthner, MiD2cm, MiD3cm during escape response depends on the location of the sensory stimulus used to elicit the escape [O'Malley et al., 1996, Liu and

Fetcho, 1999]. The reticulospinal system allows a fine level of control and behavioral flexibility. The perceived threats represented by slow versus fast approaching looming stimuli are encoded in a graded fashion in the reticulospinal system: slower looming stimuli are less likely to recruit the Mauthner cells and involve escapes that are more delayed and more variable in their kinematics than Mauthner-active escapes, which is reflected by the recruitment of different groups of RS neurons [Bhattacharyya et al., 2017]. Finally, when presented with moving gratings at different angles, the directionality of turns during the optomotor response is correlated with the activation of specific RS cells in the ventral hindbrain [Orger et al., 2008]. These cells are shown to be involved in turning in various behaviors, and specify early kinematic parameters during the first tail undulation [Huang et al., 2013].

Tract-tracing studies using spinal backfills have failed to reveal labeled neurons in the dorsal pallium of different teleost species including zebrafish [Kimmel et al., 1982]. The dorsal pallium may however still exert an influence on locomotor behavior, not via a direct palliospinal homologue to the corticospinal pathway, but through descending projections to more caudal brain regions.

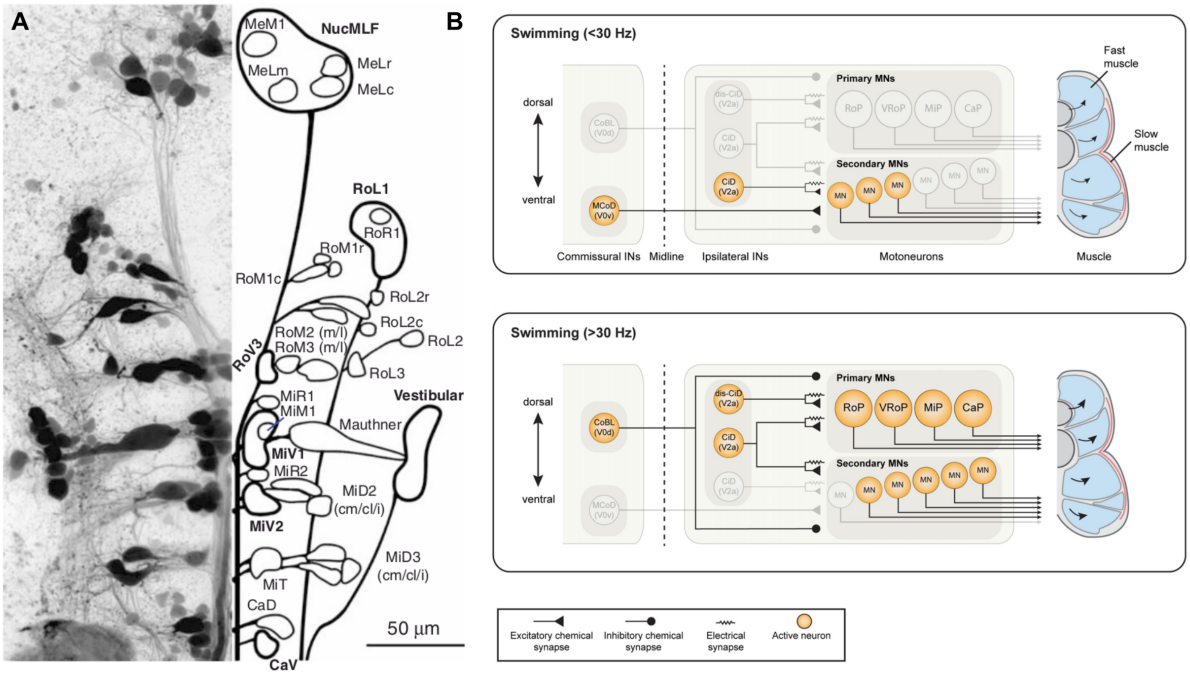

Figure 1.15: **Neural basis of locomotion in the zebrafish larva**. **A**. Spinal backfill and identified spinal projection neurons. Left: Z-projection of cells in the hindbrain retrogradely labelled from the spinal cord using Texas Red dextran. Right: identified cells (thin lines) or groups of spinal projection cells (bold lines). NucMLF neurons are involved mostly in controlling the speed of forward motion, while a group of ventral spinal projection neurons (RoV3,MiV1,MiV2) control the direction of turns. **B**. Ventro-dorsal pattern of recruitment of motor neurons in the spinal cord with increased swimming speed. From [Orger et al., 2008, Berg et al., 2018].

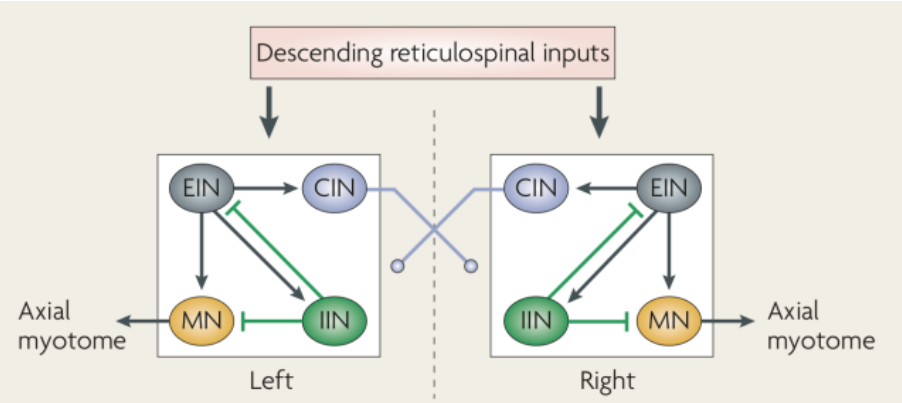

Jawless fish (lamprey)	Bony fish (zebrafish)	Amphibian (*Xenopus*)	Mammal (mouse)
Inhibitory CINs	CoBL neurons	CINs	dI6 neurons (Lbx1$^+$)
	CoSA neurons		$V0_D$ neurons (Dbx1$^+$, Evx1/2$^-$)
Excitatory CINs	MCoD neurons	Undetermined	$V0_V$ neurons (Evx1/2$^+$)
	UCoD neurons	Undetermined	$V3_v$ neurons (Sim1$^+$)
EINs	CiD neurons	dINs	V2a neurons (Chx10$^+$)
	VeMe neurons*		V3 neurons (Sim1$^+$)
			Hb9$^+$ neurons
L-interneurons	CiA neurons	aINs	V1 neurons (En1$^+$)
	eLD neurons		V2b neurons (Gata3$^+$)

* VeMe cells also have descending axons that may cross the ventral midline and are excitatory.

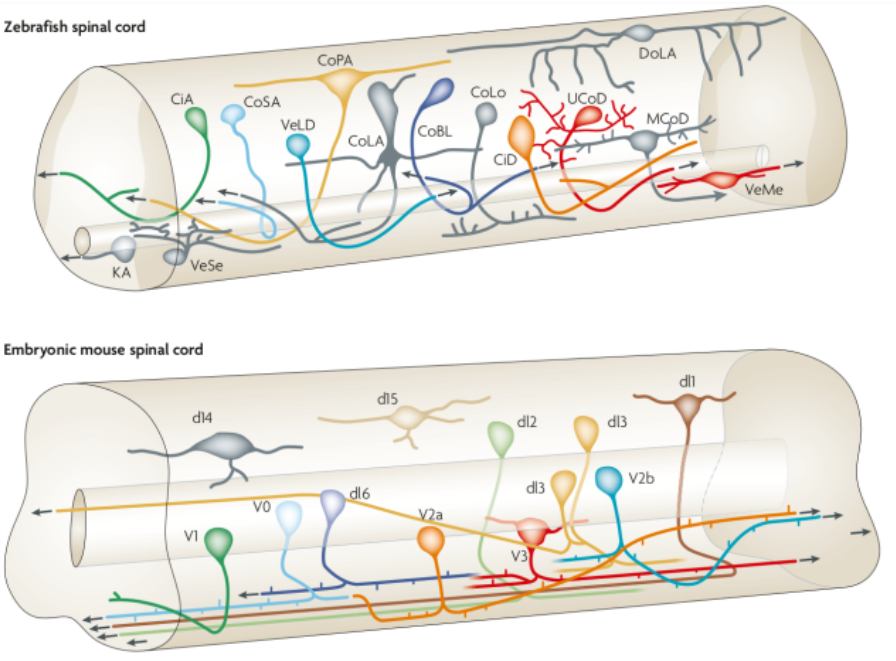

Figure 1.16: **Central pattern generators in the spinal cord**. **Top**. Central pattern generator (CPG) model in the zebrafish spinal cord. EIN: Excitatory interneuron. MN: Motor neuron. (legend continued next page)

Central pattern generators Central pattern generators (CPGs) are well conserved among vertebrates [Goulding, 2009, Grillner and El Manira, 2020], although the circuits involved are simpler, with less different cell types in lampreys and teleost with respect to mammals [Goulding, 2009]. In zebrafish, four groups of neurons organized in two mirrored modules on each side of the spinal cord constitute the CPG (fig 1.16):

- Large primary and small secondary motorneurons (MN) distributed in each segment which innervate the adjacent muscles.
- Excitatory interneurons (EIN) which project to all other cell types
- Inhibitory interneurons (IIN) that project ipsilaterally and provide inhibition to EINs and MNs.
- Commissural interneurons (CINs) which provide both inhibition and excitation to the other side of the spinal cord, and ensure left-right alternation.

Various spinal classes have been identified that pertain to those four groups of neurons, based first on an anatomical description of the position and morphological characteristics of the cells [Myers, 1985, Bernhardt et al., 1990, Hale et al., 2001], and later on their neurotransmitter [Higashijima et al., 2004a, Higashijima et al., 2004b, Higashijima et al., 2004c] and molecular identities [Kimura et al., 2006, Satou et al., 2012]. For a summary of the different types of spinal interneurons in the zebrafish CPGs, see fig 1.16.

The descending pathways project onto spinal circuits to trigger or stop activity in the CPG. We know for instance that nMLF projects at least to MNs [Wang et al., 2014], but we do not know precisely the overall patterns of connectivity in the different descending tracts, especially regarding the projections to interneurons (INs) [Berg et al., 2018]. Selective recruitment of populations of motorneurons could arise from different patterns of connectivity from the descending pathways to the spinal cord, or as a consequence of temporal integration of tonic drive in spinal neurons with different membrane properties [Wang et al., 2014].

Zebrafish larvae can swim in a beat-and-glide pattern across a range of frequencies: 20–80 Hz with a mean frequency of approximately 35 Hz [Budick and O'Malley, 2000, Buss and Drapeau, 2001]; and produces discrete bouts of activity that can be classified into different categories [Marques et al., 2018]. Spinal CPGs must accommodate those

Figure 1.16 (continued): IIN: Inhibitory interneuron, or L-interneuron. CIN: Commissural interneuron. **Middle**. Class of interneurons in zebrafish, and their *Xenopus* and mouse homologue. **Bottom**. Interneurons in the zebrafish spinal cord, compared with the embryonic mouse spinal cord. From [Goulding, 2009].

changes of bout categories and speeds and allow for smooth transitions. How the different categories of movements relate to different patterns of activity in the spinal cord, and how transitions occur between them remains unknown. However, there is an emerging understanding on the control of swimming speed in the spinal cord.

In the zebrafish larva spinal cord, the control of swimming speed is organized topographically along a dorso-ventral axis [McLean et al., 2007]. Ventral secondary MNs are recruited first at slow frequencies, while early born primary MNs in more dorsal position are included in the active pool as swim frequency increases [McLean et al., 2007]. Excitatory IN (MCoD,CiD) follow the same pattern of ventro-dorsal recruitment, whereas the opposite happens for inhibitory IN (CiA,CoBL): more dorsal inhibitory IN are active during low swimming frequencies, whereas more ventral inhibitory IN are recruited as the speed of swimming increase [McLean et al., 2007]. However, the pattern of recruitment of interneurons and motorneurons differ. Motorneurons are added to the motor pool according to the "size principle": the small secondary MN are recruited first while the large primary MN are recruited last, and the size of the motor pool grows as new MN are added [McLean et al., 2008]. As more dorsal excitatory IN (MCoD,CiD) are recruited, the more ventral ones are silenced, resulting in a dorsal shift in the population of active cells [McLean et al., 2008] (fig 1.15.B).

The source of excitation to the CPG can also be local to the spinal cord. In the spinal cord, CiD interneurons provide an intrinsic source of excitation necessary for the production of movements: selective ablation of CiD interneurons increases the threshold for the induction of swimming, decreases burst frequency, and impairs the rostro-caudal propagation of activity, while optogenetic activation of CiD interneurons induces swimming activity [Eklöf-Ljunggren et al., 2012, Eklöf Ljunggren et al., 2014].

Moreover, spinal sensory neurons such as the glutamatergic Rohon-Beard (RB) and GABAergic CSF-contacting neurons (CSF-cNs), or Kolmer-Agduhr cells, also influence locally the CPG circuits in the spinal cord to modulate swim frequency as well as postural control by synapsing directly to excitatory or inhibitory interneurons [Knafo and Wyart, 2018]. This cells provide proprioceptive feedback as well as sensory information

Finally, spinal circuits are also the target of neuromodulatory influence. McLean *et al.* traced the innervation pattern of aminergic systems in the larval zebrafish [McLean and Fetcho, 2004a]. They show that the posterior tuberculum (dopamine), and the raphe region (5-HT) project to the spinal cord [McLean and Fetcho, 2004b]. The locus coeruleus (noradrenaline) also seems to project in the spinal cord in the zebrafish larva [Tay et al., 2011]. Dopaminergic diencephalospinal neurons (DDN) in the posterior tuberculum could regulate spinal network excitability [Jay et al., 2015], and be involved in the integration of sensory information [Reinig et al., 2017]. Serotonin can be delivered to the spinal

cord either from the raphespinal tract [McLean and Fetcho, 2004b], or from intraspinal serotonergic neurons [Montgomery et al., 2018]. Application of exogenous serotonin increases motor output in larval zebrafish by reducing intervals of inactivity, leaving swim frequency unchanged [Brustein et al., 2003]. The precise role of endogenous serotonine, or noradrenaline, on spinal networks remains however not very well known in the zebrafish larva.

1.2.2 Internally generated vs externally triggered actions

Behaviors can be classified into different categories, which correspond to different neural circuits generating them. A first level of classification is to separate voluntary from involuntary actions. This separation is not always clear, but voluntary actions usually require some amount of integration and decision-making from the agent that performs them, while involuntary actions are thought to arise without intentionality.

Voluntary behaviors can be externally triggered by a stimulus, to which the organism responds to or interacts with, or triggered by internal causes, when no obvious external cause can be found [Passingham et al., 2010b]. Again, this separation is not always strict, and behaviors that seem to be internally generated could be the result of some form of interaction with the environment [Nachev and Husain, 2010, Passingham et al., 2010a]. An animal that tracks a prey, or engages in exploratory behavior, is performing voluntary actions, the former being externally triggered and the latter internally motivated.

Involuntary actions can range from very straightforward responses to a stimulus, such as the monosynaptic stretch reflex, to internally generated unintentional actions such as breathing.

As a final note, internally generated voluntary action can occur in two situations: a delayed task in which an animal is given a cue and has to process it to act, or a "free choice" paradigm where the animal can move whenever he chooses to. Here, I have studied the voluntary response to externally triggered auditory stimuli, and the spontaneous generation of voluntary actions in the zebrafish larva.

1.3 Self-generated behavior

Motor behaviors are a complex phenomenon which requires many different cognitive processes to be fulfilled correctly. They are traditionally not studied as a whole, but separated into different components [Gallivan et al., 2018]. Whether these components are strictly partitioned, interact together, act in parallel or in series, and correspond to a direct physical implementation in the brain is subject to debate [Cisek, 2007], but this

categorization can prove useful to try to untangle this unwieldy topic. Here we will focus on preparatory activity, which occurs before the onset of behavior and determines what the animal will do and when it will occur. In this section, I will talk about preparatory activity representing motivational drives, the initiation of actions, and action selection.

1.3.1 Why: Context integration and motivation for action

To implement flexible behaviors, animals must be able to integrate contextual cues to produce relevant motor patterns. Such contextual cues can be external to the animal, through sensory stimulation [Portugues and Engert, 2011], or internally generated by motivational drives or mental states (fear, hunger, thirst, *etc.*) [Allen et al., 2019, Marques et al., 2020].

Behaviors can be reactive if they are mostly driven by external stimuli, intrinsically motivated if they are driven by internal causes, or may lie somewhere in between (hunting behavior may be motivated by hunger but requires the integration of sensory stimuli). The study of motivation is delicate in non-human animals, as it can be subject to overinterpretation or anthropomorphism. It does however sound reasonable to say that food-seeking in a food-deprived animal is motivated by hunger [Horstick et al., 2016]. There is a growing body of evidence that such states as hunger, thirst or fear correspond to well defined states that can be linked to specific patterns of neural activity, neuromodulation, and changes in behavior [Allen et al., 2019, Marques et al., 2020, Gründemann et al., 2019]. Patterns of activation corresponding to internal states may be specific to species or individuals, which is why ascribing labels such as hunger or thirst may prove useful to compare neuronal mechanisms inside and across species. Finally, motivation is strongly linked with reward, learning and value estimation. The repetitive association of a given context with positive outcomes for the animal can create a motivational drive, and bias the balance between exploration and exploitation: this is the basis for reinforcement learning [Dayan, 2012]. When all homeostatic drives are satiated, it is postulated that organisms could modify their behaviors to obtain information about their surroundings [Gottlieb et al., 2013], or rehearse sensorimotor skills such as vocal practice in songbirds [Garst-Orozco et al., 2014], which may increase their fitness in the long-term by reducing uncertainty. Therefore curiosity [Gottlieb and Oudeyer, 2018] and learning could themselves constitute intrinsic motivational drives.

The neural basis of motivation are increasingly investigated. In mammals, cortical and subcortical regions seem to be involved in the generation of internal drives. The mammalian cortex—more specifically the insular, anterior cingulate (ACC), orbitofrontal (OFC), and medial prefrontal cortices (mPFC)—seems to be involved in the regulation of motivation, reward signals, value estimation, and their integration with cognitive control

[Kouneiher et al., 2009, Cardinal et al., 2002]. These cortical area form a loop with subcortical structures (see fig 1.17). Many of those subcortical structures (ventral tegmental area, basal ganglia, basal cholinergic septum) are involved in neuromodulation, which acts on a timescale compatible with the duration of motivational states. Other systems, such as the amygdala, which act as a controller of brainstem arousal and encodes behavioral states [Cardinal et al., 2002, Gründemann et al., 2019], and the hypothalamus involved in the control of homeostasis via its role as a neuropeptidergic relay, seem to also play an important role in motivation. Interestingly, the basal ganglia, a structure which plays a central role in the control of movements, seems to also be involved in different aspects of the initiation of movements, including motivation for action [Ikemoto et al., 2015, Aoki et al., 2019].

In zebrafish, the central zone of the dorsal pallium (Dc) seems to correspond topologically and developmentally to the mammalian isocortex [Mueller et al., 2011]. Its function is however still obscure, and we don't know if it plays a role in the regulation of motivated behavior. The medial zone of the dorsal pallium (Dm) is thought to be homologous to the amygdala, and is involved in amphetamine-conditioned motivational behavior [von Trotha et al., 2014]. The hypothalamus seems to play a role in the integration of visual inputs with hunger state to promote feeding behavior [Muto et al., 2017]. Concerning neuromodulation, the locus coeruleus, which produces norepinephrine, has been found to be involved in alertness [Lovett-Barron et al., 2017], and the serotonergic dorsal raphe has been associated with an increased motivation to hunt for prey [Marques et al., 2020]. Multiple studies have linked dopaminergic signaling to motor behavior in zebrafish larvae [Souza et al., 2011, Irons et al., 2013, McPherson et al., 2016], but the specific neuronal populations concerned and their relationship with the mammalian dopaminergic system, in particular the basal ganglia, are still unclear.

Arousal is often defined as a heightened responsiveness to external stimuli and increased spontaneous locomotor activity. That second aspect makes it akin to a form of motivation for action. Interestingly, it is possible for those two aspects of arousal to be dissociated. Woods *et al.* systematically dissected the neuropeptidergic modulation of arousal in the zebrafish larva. They showed that hypocretin and calcitonin gene-related peptide stimulate spontaneous locomotor activity, whereas galanin and nociceptin attenuate these behaviors. In contrast, cocaine-related and amphetamine-related transcript and adenylate cyclase activating polypeptide 1b enhance sensory responsiveness yet have minimal impacts on spontaneous activity, and cholecystokinin expression induces the opposite effects [Woods et al., 2014].

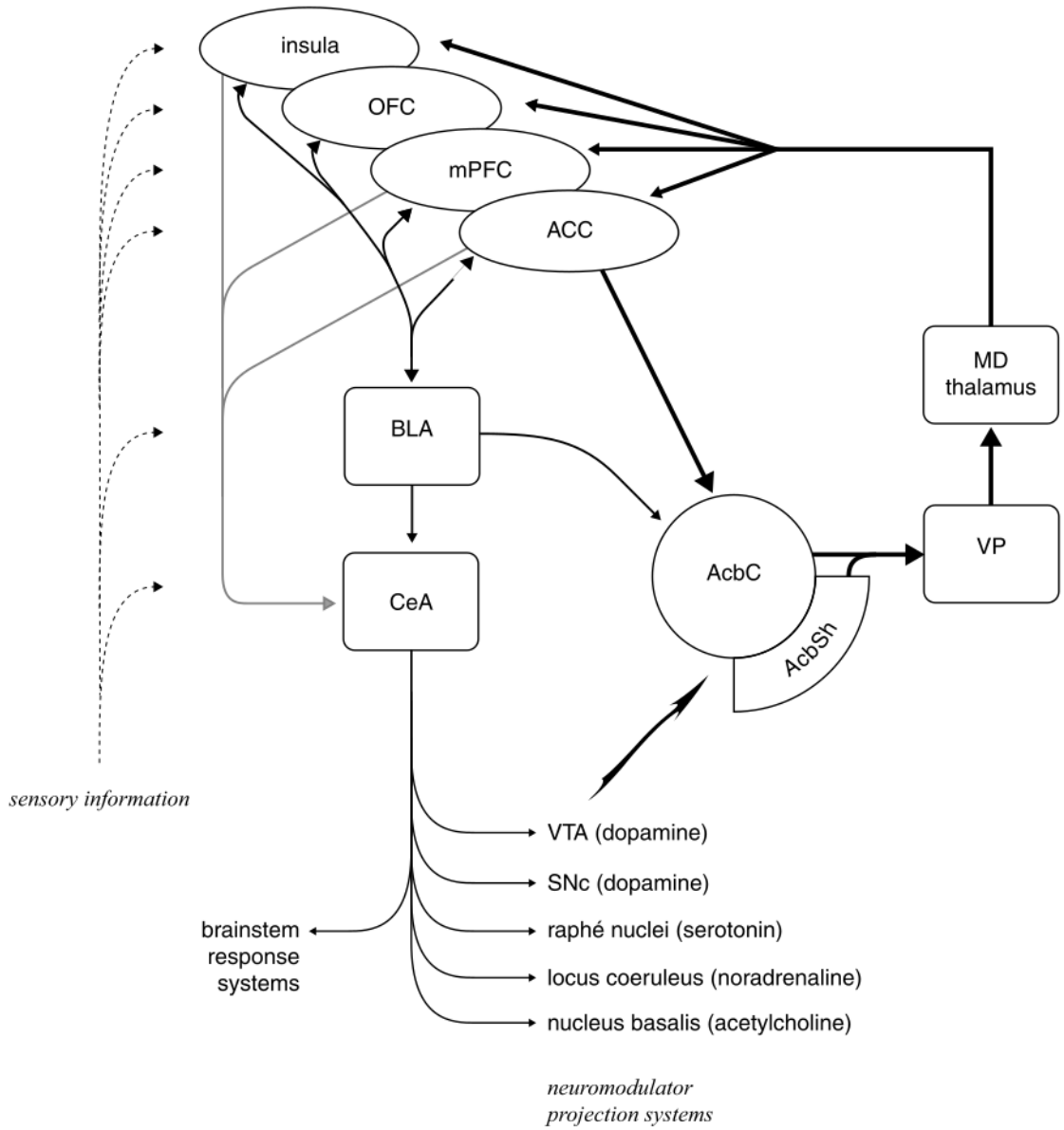

Figure 1.17: **Neural basis of the mammalian motivation system**. Heavy lines delineate the limbic corticostriatal loop between the prefrontal cortex, amygdala, ventral striatum and thalamus. The amygdala also projects to major neuromodulatory systems in the brain, that may be involved in motivational states. Abbreviations: OFC, orbitofrontal cortex; mPFC, medial prefrontal cortex; ACC, anterior cingulate cortex; BLA, basolateral amygdala; CeA, central nucleus of the amygdala; VTA, ventral tegmental area; SNc, substantia nigra pars compacta; AcbC, nucleus accumbens core; AcbSh, nucleus accumbens shell; VP, ventral pallidum; MD, mediodorsal. From [Cardinal et al., 2002].

1.3.2 When to act: timing of the action

Voluntary movements require some amount of preparation to be properly released at the right moment. A lioness hunting its prey must carefully examine its surroundings, plan a trajectory and decide when to strike. In the absence of any external cues however, how does the brain decide when to take an action?

In the early 1960's, the study of event related potentials (ERPs), the averaged brain response around the onset of some specific motor, sensory, or cognitive event, started to develop. In a seminal study, Kornhuber and Deecke discovered the Bereitschaftspotential, or readiness potential (RP) in English, a slow rise in EEG potential building up for several hundreds of milliseconds before the onset of voluntary, self-paced movements (see fig 1.18.A,B) [Kornhuber and Deecke, 1964, Kornhuber and Deecke, 2016]. This buildup in activity, hypothesized to be linked to preparatory motor activity, was later associated with the supplementary motor area (SMA) [Deecke and Kornhuber, 1978, Brinkman and Porter, 1979, Eccles, 1982].

The RP was popularized by a famous experiment led by Benjamin Libet. Libet recorded an EEG of his participants while they were performing a voluntary, self-initiated finger or wrist movement. They were asked to report when they felt the urge to move. Libet demonstrated that the buildup in the RP starts well before the participants thought they consciously decided to move [Libet et al., 1983].

Neurons firing before the onset of spontaneous movements were recorded in the monkey SMA and premotor cortex [Brinkman and Porter, 1979, Romo and Schultz, 1987] (see fig 1.18.C,D), but also in the basal ganglia [Schultz and Romo, 1992], suggesting the involvement of a cortico-basal circuit in the initiation of movement (see fig 1.18.E,F). It was also observed in humans using fMRI and electrophysiology [Cunnington, 2002, Hoffstaedter et al., 2013, Khalighinejad et al., 2020, Klaus et al., 2019, Fried et al., 2011] in SMA, pre-SMA, cingulate cortex and basal ganglia. In mouse, dopaminergic neurons of the nigrostriatal pathway show a ramping in activity linked with the timing of the decision to move [Hamilos et al., 2020]. Interestingly, there seems to be a deficit in the initiation of voluntary movement in Parkinson's disease, which could be linked to the cooperation of the SMA with the basal ganglia to initiate actions [Jahanshahi, 1995, Da Silva et al., 2018]. Finally, a recent study suggest the involvement of both basal ganglia at a supra-second time scale, and cerebellum at a sub-second time scale, in the preparatory activity of a self-timed saccade task [Kunimatsu et al., 2018]. This buildup in neuronal activity could provide a mechanistic basis for a "when" pathway, whereby actions are released when the RP reaches a certain threshold.

Ramping activity during motor preparation is not restricted to primates, but found across taxa. In rodents, a role similar to that if the primate SMA has been attributed to M2 [Murakami et al., 2014, Barthas and Kwan, 2017], and a readiness discharge has been described in crayfish [Kagaya and Takahata, 2011]. In the zebrafish larva, pre-movement activity was found in a group of neurons in the hindbrain that display an oscillatory behavior with a period of several seconds (anterior rhombencephalic turning region, ARTR). These oscillations are correlated with the generation of lateralized spontaneous behavior during exploratory locomotion [Dunn et al., 2016b], see fig 1.21.A,D. Ramping neurons

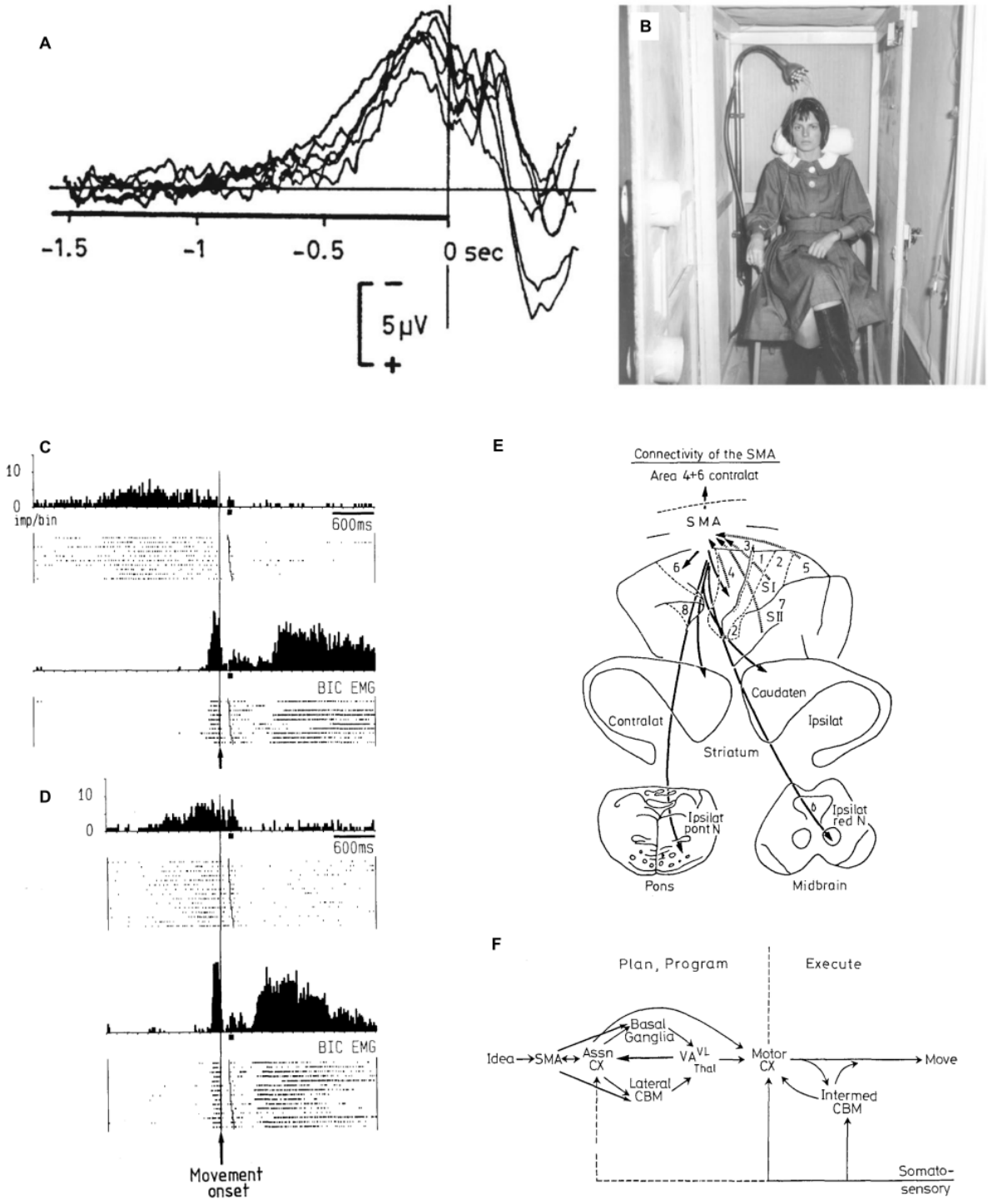

Figure 1.18: **When to act: readiness potential in the macaque SMA A**. Reverse-computation of EEG signal before self-initiated voluntary finger flexion. Superposition of 6 experiments of the same participant at 6 different days with 250 trials each, i.e. 1500 self-initiated finger movements. **B**. Original experimental setup used by Kornhuber and Deecke to measure the readiness potential. **C**. Top: Activity of a monkey cortical neuron in the supplementary motor area (SMA), around the onset of self-initiated movements (arrow and vertical bar). Bottom, biceps electromyogram. (legend continued next page)

have been found very recently in the context of sensory decision-making and evidence accumulation displaying a ramp-to-threshold dynamic [Lin et al., 2020, Bahl and Engert, 2020], and for the generation of spontaneous eye saccades [Ramirez and Aksay, 2020]. They all point to neuronal activity in the anterior rhombencephalon, a likely site for visuomotor integration [Chen et al., 2018]. Whether the same mechanism could be involved in the timing of sensory-evoked and spontaneous behavior in the zebrafish larva is currently unknown.

There are different interpretations over what ramping activity may represent. For some authors, it reflects to preparation of voluntary actions, for others it reflects the complexity of the task, uncertainty about what to do, or it could even be the result of averaging stochastic fluctuations [Travers et al., 2020, Schurger et al., 2012, Maoz et al., 2019, Nachev et al., 2008]. The RP could also result from slow cortical potentials (SCP) [Sanes and Donoghue, 1993, Armstrong et al., 2018, Schmidt et al., 2016], defined as electrical potentials recorded from the brain with a frequency below 1 Hz. Some authors argue that movements are more likely to be initiated during negative periods of the SCP, thus averaging at the onset of movement could produce the curve of the RP [Armstrong et al., 2018]. This could be compatible with the oscillatory behavior of the ARTR in the zebrafish hindbrain [Dunn et al., 2016b].

The RP is usually understood as a ramp-to-threshold mechanism for the timing of action, and many neurons seem to show this kind of profile [Schurger et al., 2012]. Another hypothesis is that the timing of action could be encoded in the population dynamics of many neurons (see fig 1.19) [Murakami and Mainen, 2015]. This could include neurons that do not show a ramp-to-threshold activity but are still instrumental in deciding when to move. Finally, the mechanisms that produce ramping activity in single cells are not well known. They could result from cell-autonomous properties, such as long membrane time constant which would allow temporal summation, or circuit properties such as recurrent connectivity [Laje and Buonomano, 2013], or discrete attractor dynamics [Inagaki et al., 2019].

Figure 1.18 (continued): Spike timings in different trials are shown as dot, from which the peristimulus time histogram is derived. **D**. Same as *A* for a neuron in the premotor cortex. **E**. Afferent and efferent connections of the SMA. **F**. Pathways involved in the execution and control of voluntary movement. Abbreviations: ASSN CX, association cortex; lateral CBM, cerebellar hemisphere; intermed. CBM, pars intermedia of cerebellum. From [Romo and Schultz, 1987, Nann et al., 2019, Eccles, 1982].

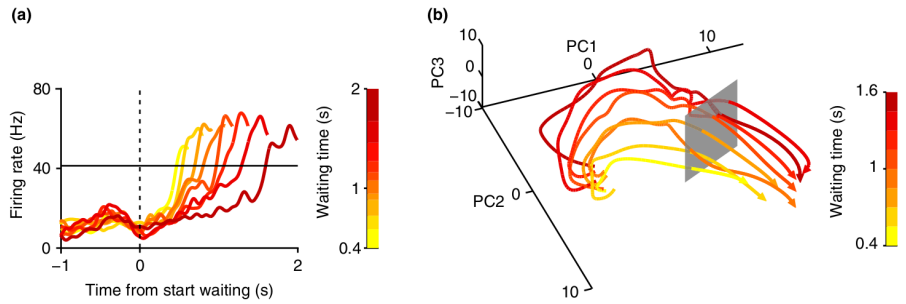

Figure 1.19: **When to act: ramp-to-threshold or population dynamics**. **A**. A single-neuron from the rat secondary motor cortex was recorded in a task where the rat could spontaneously give up waiting. The firing rates were grouped by decision time bins. At a firing rate of approximately 40 Hz, the rat gave up waiting, which is compatible with a ramp-to-threshold mechanism. **B**. Population dynamics of 188 neurons recorded from the rat secondary motor cortex in the same task. Note that population activity crosses a hypothetical threshold plane just before giving up waiting. From [Murakami and Mainen, 2015].

1.3.3 What do to: action selection

During a game of chess, a player will be presented with several possible moves for a given turn. He needs to ponderate the context to decide which action to take in order to win. Choosing between many possible actions is called action selection. Action selection is observed in virtually all animals and is considered a vital ability.

While a wide range of studies have focused on the readiness potential, less have studied the neuronal basis of action selection, or the "*what*" pathway, for voluntary, endogenous actions. One of the reasons may be the large number of potential confounding factors related to the design of the study. In a "free choice" paradigm, what are the actions that the subject may perform? Is it possible for him to be influenced by past actions when generating of new ones? When subjects are asked to chose between two actions (for instance tapping with the left or right finger), is this relevant *vis-à-vis* the complexity of action selection outside the lab?

As a general principle, many authors point to the basal ganglia for their role in action selection [Redgrave et al., 1999, Prescott, 2007, Klaus et al., 2019, Park et al., 2020]. This role is not restricted to self-initiated actions, but also actions in response to external cues. The basal ganglia receive input via the striatum from several cortical areas, and feed back information to the cortex via the thalamus, while their output is gated by the dopaminergic system. This is a perfect design to integrate, select, and invigorate motor patterns [Park et al., 2020]. Another potential mechanism for action selection is the affordance competition hypothesis [Cisek, 2007]. It postulates that the brain processes different aspects of action selection and specification in a distributed and parallel manner. In this way, different actions can be prepared at the same time until one

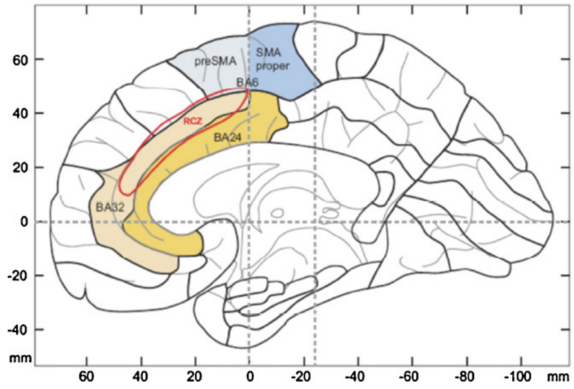

Figure 1.20: **What to do: preSMA and RCZ**. Location of preSMA, SMA proper and RCZ in the human cortex. From [Krieghoff et al., 2011].

action is finally selected. This would occur through the concerted activity of different cortical areas (depending on whether the action is internally or externally triggered, and by which sensory modality in the second case) and basal ganglia.

For the specific task of action selection during self-generated behaviors, several cortical structures have been found to be significantly more active during the selection of self-generated behaviors in contrast to externally triggered actions, such as the rostral cingulate zone (RCZ) in humans as well as the pre-SMA (see fig 1.20) [Lau et al., 2004, Walton et al., 2004, Mueller et al., 2007, Brass and Haggard, 2008, Krieghoff, 2009, Krieghoff et al., 2011, Hoffstaedter et al., 2013]. The specific cognitive function supported by each region during motor preparation is however still controversial.

In the zebrafish larva, Dunn et al. studied the generation of spontaneous swim bouts in a homogeneous environment without any salient sensory cues [Dunn et al., 2016b]. They found that spontaneous behavior is structured in both space and time: zebrafish larvae tend to generate series of bouts in the same direction, then alternate to another direction. The authors identified a brain structure that is correlated to the direction of swim bouts, which they named the anterior rhombencephalic turning region (ARTR, see fig 1.21.A,B,C). Optogenetic stimulation caused an increase in the number of turns in the direction ipsilateral to the stimulated ARTR region, thus showing a causal implication of ARTR in biasing swim direction. Interestingly, while this was not the focus of the study, the increase in ARTR activity ipsilateral to the turn direction before the onset of movement (fig 1.21.D) suggests that the ARTR could potentially implement a neural mechanism for action selection during the preparatory, pre-movement period. This was not however directly investigated by Dunn and colleagues, and they do not show that pre-motor activity can predict the direction of subsequent swim bouts.

Most of the literature on motor preparation has focused on single-cell recordings or the averaged activity of regions of the brain using fMRI or EEG. Another possibility is

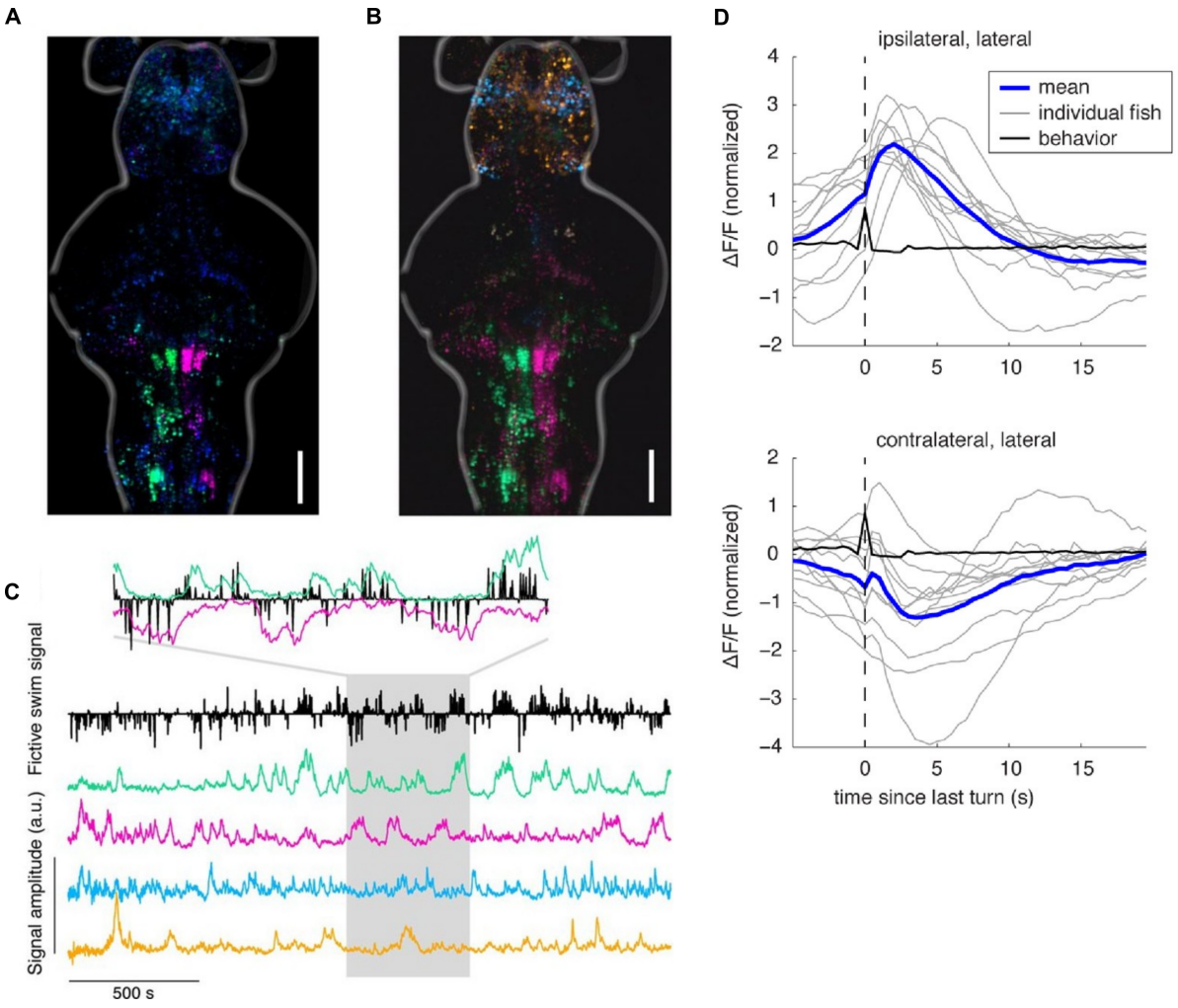

Figure 1.21: **What to do: left turn vs. right turn in the zebrafish larva**. **A**. Regression analysis of neural activity related to fictive swim signals (direction and amplitude) in a single larva. The anterior rhombencephalic turning region (ARTR), appears as four cluster on neurons in the anterior hindbrain, whose activity is lateralized according to the direction of swimming. Green: left, magenta: right, blue: forward swimming. **B**. The ARTR is also revealed by an unsupervised technique (ICA), which is commonly used for blind source separation of a signal into independent components. **C**. Fictive swim signal aligned with the neuronal activity of the 4 idependent components identified in *B*. **D**. Turn-triggered average of ARTR (lateral cluster) activity. Individual fish are shown in gray, average in blue, and behavior in black. There is a relative increase in activity in the ARTR ipsilateral to the turn direction, which rises before the onset of the turn, peaks approximately 2 s after the onset, and decays. From [Dunn et al., 2016b].

that much of the complexity underlying action selection lies in the concerted activity of populations of neurons. This has been studied mostly using externally triggered actions as in a delayed-task paradigm [Shenoy et al., 2013, Kaufman et al., 2014, Elsayed et al., 2016, Vyas et al., 2020, Lin et al., 2020]. These studies suggest that preparatory activity in motor and premotor cortices is not a subthreshold version of the neural activity during movement, but is actually independent from the activity during movement [Elsayed et al.,

2016]. Preparatory activity is however predictive of movement activity [Elsayed et al., 2016] and linked to the motor activity via a rotation in the state space [Churchland et al., 2012, Shenoy et al., 2013]. Preparatory activity therefore represents an initial population state that makes movement execution smoother, decreases reaction times [Vyas et al., 2020], and lies in a subspace that does not output motor commands to the spinal cord [Kaufman et al., 2014]. How this can apply to internally generated behavior is not known yet. It is possible that the preparatory activity described above in response to a stimulus results from sensorimotor learning, as proposed by Lin *et al.* in the zebrafish larva [Lin et al., 2020]. Thus, preparatory activity before sensory-induced behavior may differ from that involving internally generated behavior.

The zebrafish larva naturally generates discrete motor behaviors and whole brain activity can be recorded optically while monitoring behavior. These advantages could prove very useful for the study of population dynamics underlying the preparation of spontaneous, internally-generated actions.

1.4 Sensory induced behavior

Animals can dynamically gather information about their external or internal environment through their sensory systems and generate adequate motor patterns, adapted to an ever-changing world. This process is called sensorimotor integration, or sensorimotor transformation, and is a core function of nervous systems throughout the animal kingdom. Sensorimotor integration is not a unitary framework, as it consists of many different interacting components, sometimes with blurry boundaries and precarious definitions, and it occurs in systems of vastly different complexity, from relatively simple reflex responses to highly integrated behaviors. In the following paragraphs I will briefly outline different aspects of sensorimotor integration such as sensory coding, active sensing, perceptual decision-making, motor control, efference copy and corollary discharge, and sensorimotor learning. I will provide examples from the zebrafish literature when possible. In a second part, provide some examples of sensorimotor integration at the cellular level in *C. elegans*, and at the circuit level in the zebrafish larva.

1.4.1 Sensorimotor integration: general principles

Representation of stimulus features: sensory coding

To perform sensorimotor integration, an organism needs to measure and manipulate relevant physical features of its surrounding environment. At the sensory periphery, sensory transduction transforms physical features of a stimulus into trains of action potentials.

Some of the computations necessary to extract relevant features happen at the sensory periphery. In mammals for instance, the cochlea implements a Fourier transform of acoustic signals, and sends frequency information through parallel channels to the central nervous system. Along the same lines, two points which are close together in the visual field will be detected by adjacent rods and cones in the retina, and drive activity in nearby retinal ganglion cells. In both cases, this decomposition of the stimulus is preserved up to cortical areas to form topographic maps of physical features. In the primary auditory cortex nearby neurons are sensitive to nearby frequencies, a property called tonotopy, while two neurons close together in the visual cortex V1 will be stimulated by adjacent sources of light in the visual space: this is called retinotopy [Patel et al., 2014], (fig 1.22). This organization however, may arise more from developmental rather than computational constraints [Avitan et al., 2016].

Topographic maps are a widespread feature of animal nervous system, but not all sensory variables are encoded topographically in the brain. In mammals, sensory-related activity is found in sensory cortices, and across the sensory hierarchy, but also in other regions of the brain, such as motor cortices [Barthas and Kwan, 2017, Ebbesen et al., 2018], cerebellum [Proville et al., 2014] and other subcortical structures. Receptive fields (the portion of stimulus space able to drive activity in a neuron) and tuning curves (the evolution of the firing rate of a neuron along one dimension of the stimulus) are widely used to describe the neural representation of stimuli. Characterizing those features can pay off if the underlying sensory code is sparse, that is if only a restricted number of cells represent a stimulus feature [Olshausen and Field, 2004].

However, receptive fields and tuning curves can change depending on the context, and the timing of spike may also carry important sensory information [Mauk and Buonomano, 2004, Buonomano and Maass, 2009], for instance birdsong recognition depends crucially on temporal pattern. Additionally, some features may be encoded in the activity of whole populations of neurons, and not at the single neuron level, rendering simple descriptions like receptive fields and tuning curves insufficient to account for the whole coding scheme [Fairhall, 2014, Sompolinsky, 2014]. Recent technological developments for the recording of population of neurons allowed the analysis of circuit dynamics to study the temporal evolution of high-dimensional population activity in a dynamical systems framework [McKenna et al., 1994, Izhikevich, 2007]. Finally, the brain can be seen as a circular close-loop system where movements are caused by sensations but sensations are also caused by movements while the context changes, making the environment a constitutive part of the "coding" scheme. This prompts some authors to abandon the coding metaphor [Brette, 2019], and embrace an enactive view of the world made of sensorimotor contingencies [O'Regan and Noë, 2001, Ahissar and Assa, 2016].

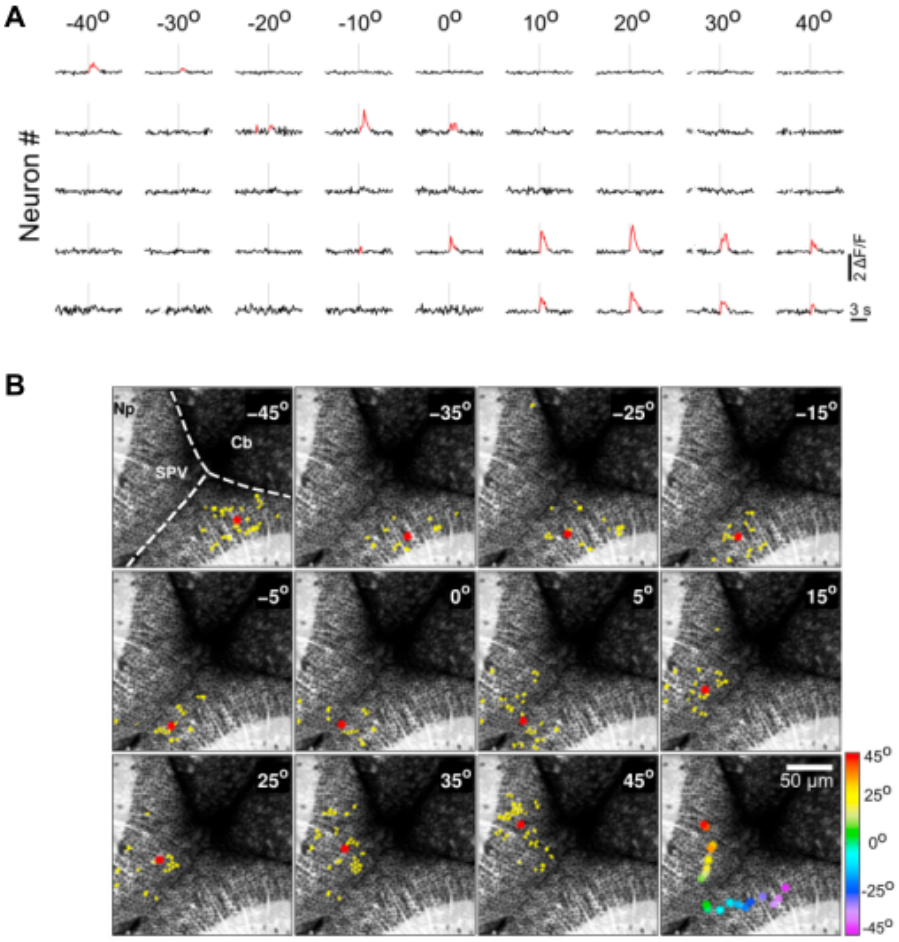

Figure 1.22: **Sensory coding in the zebrafish optic tectum**. **A**. Single-trial neuronal activity induced by 1 s visual stimulation (light dot) at different azimuthal location in the field of view. Vertical gray line: stimulus onset. Red: significant calcium event. **B**. Topography of neurons robustly activated at different azimuthal angles. Yellow: activated neuron, red: centroid of the group. Bottom right, position of all centroid, color-coded by azimuthal angle, showing a retinotopic map in the zebrafish optic tectum. From [Romano et al., 2015].

Perceptual decision-making

Decision-making is a vast topic in neuroscience, as many cognitive processes can be described within a decision-making framework. Categorizing sensory inputs, integrating value or reward to choose a policy, choosing an action to perform, choosing how to perform an action are different manifestations of decision-making [Gold and Shadlen, 2007]. In this paragraph, I will talk mostly about perceptual decision-making, but it should be noted that sometimes, different forms of decision-making are intricately intertwined.

Perceptual decision-making is the process which allows to discriminate sensory inputs into relevant categories. This can be very straightforward, as in the reflex response to loud auditory stimuli mediated by the Mauthner cells in teleost fish, which is implement

by a hardwired circuits. In many instances however, sensory information is noisy and incomplete, or contains spatial and temporal information that needs to be integrated: for instance recognizing the voice of a person you haven't seen in a while over the telephone may take some time. Sensory evidence can be accumulated to inform perceptual decisions in order to generate relevant behavior. The dominant theory is that perceptual decision-making about noisy or uncertain inputs is implemented in the brain via a repeated sequential sampling of sensory information and linear integration of a decision variable to a fixed threshold [Gold and Shadlen, 2007].

This ability to accumulate sensory evidence has been witnessed in many different animal species. Canonical models of evidence accumulation for decision-making have been developed from recordings in the lateral intraparietal (LIP) area in monkeys performing a visual decision task. Monkeys trained to perform saccades in a random dot motion coherence test (where a fraction of dots move in a given direction) show an increase in single LIP cell activity during the presentation of the stimulus, predictive of the direction subsequent eye saccades [Shadlen and Newsome, 2001]. Similarly, a slow rise in the membrane potential of a subset of Kenyon cells in the fly mushroom body appears related with the olfactory decision to avoid a repulsive odorant [Groschner et al., 2018]. Along the same lines, a graded value of the accumulating evidence can be found in the posterior parietal cortex of rats which had to discriminate the number of auditory clicks coming from two speakers, to left and to the right of the animal [Hanks et al., 2015]. In all those studies, evidence accumulation is manifested through the ramping activity of neurons or groups of neurons up to some threshold. This ramping dynamic is usually modeled using drift-diffusion models (also called integration-to-bound), or leaky integrator models [Ratcliff et al., 2016].

Recent challenges to this canonical view have emerged. The decision threshold to which evidence accumulates can be dynamic instead of fixed, this adaptive threshold could be used to control the urgency to commit to a decision [Murphy et al., 2016, Bahl and Engert, 2020]. Ramping activity averaged over trials could emerge from different single-trial dynamics: neurons could display ramping at the single-trial level, or step-like dynamics at different time points, that could result in a ramping average [Churchland et al., 2006, Latimer et al., 2015, Churchland and Kiani, 2016, Shadlen et al., 2016]. Decision-making could also arise from the concerted dynamics of populations of neurons. In the leech, population activity reliably informs about the decision to crawl or swim ahead of time of the onset of movement [Briggman et al., 2005]. Importantly, prediction based on populations of neurons were able to predict the upcoming movement before any single-cell could. Mante *et al.* suggest that population dynamics in the prefrontal cortex during a random dot coherence task are compatible with a line attractor were end points represent converged decisions [Mante et al., 2013].

In the zebrafish larva, perceptual decision-making can be implemented as relatively simple circuits, hardwired to perform rapid decision-making, such as the Mauthner cell escape system [Korn and Faber, 2005]. The escape/avoidance choice made by the larvae when presented with small or large stimuli [Barker and Baier, 2015] could obey similar principles by using labelled-lines from the tectum to hindbrain motor centers [Helmbrecht et al., 2018]. However, recent work has shown that zebrafish can implement decision-making strategies on longer time-scales, through the temporal integration of sensory evidence. Bahl and Engert took advantage of the optomotor response (OMR) to show that the activity in clusters of cells in the anterior hindbrain can be modeled by a leaky integrator model during a random dot OMR task [Bahl and Engert, 2020]. Interestingly, these cells show ramping activity at the individual trial level, and the threshold observed to trigger tail bout was dynamic. Similarly, based on a slightly different random dot OMR task design aimed at triggering turns, Dragomir *et al.* also report ramping activity in the anterior hindbrain [Dragomir et al., 2020]. Finally, Lin *et al.* describe ramping dynamics in the cerebellum and anterior hindbrain (fig 1.23) during a trained task were larvae need to move in a given direction to avoid a mildly aversive heat stimulus [Lin et al., 2020].

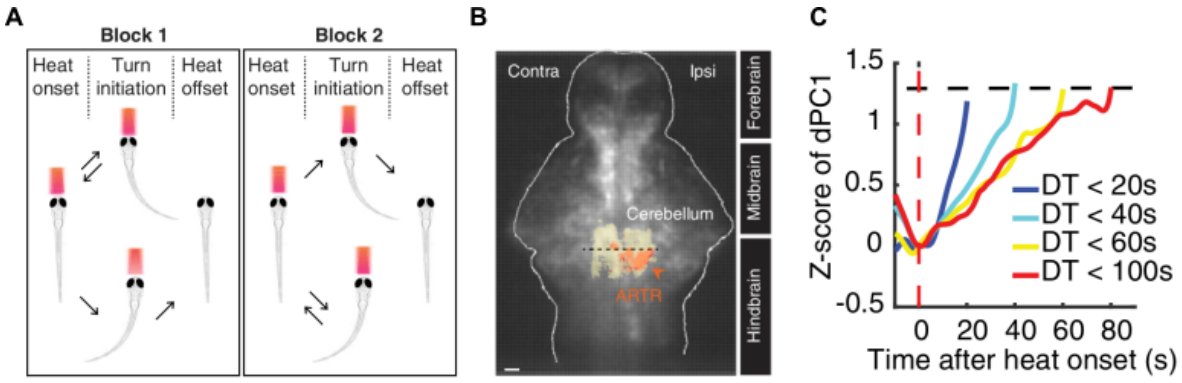

Figure 1.23: **Decision-making: ramping activity to bound in the zebrafish hindbrain**. **A**. Training paradigm: head-fixed zebrafish larvae receive a mildly aversive heat stimulus delivered by an infrared laser at the beginning of a trial. A reward direction is chosen for block 1. The laser is turned off if the fish makes a tail movement in the reward direction, it remains on otherwise. The reward direction is switched for the second block. **B**. Location of ramping neurons. These neurons mainly overlap with the ipsilateral ARTR, colored red. Other active neurons from the rest of the cerebellum and ARTR are indicated in yellow, they do not show ramping at the individual level but contribute to ramping activity through their addition to the pool of active neurons. **C**. Monotonic ramping of bilateral cerebellar population activity grouped by desision time. Turns appear to be initiated when ramping activity reaches a common decision-time-independent threshold. This ramping may mainly reflect the addition of yellow neurons (see *B*) to the active pool, and to some extent from truly ramping neurons in the ipsilateral ARTR. From [Lin et al., 2020].

Motor planning and motor control

Motor planning corresponds to pre-motor activity involved in the selection (what to do), specification (how to act) and initiation of movements (when to act). In a sensorimotor context, motor planning in informed by the integration of sensory information, potentially from different modalities, as well as the current state of the organism (current position of the body in the environment, head direction, ...) and motivational drives. Interestingly, some aspects of motor planning, such as action specification, may not be restricted to preparatory motor activity but extend after the onset of movements. Movement kinematics for instance are refined while they are produced . Since I have already covered action selection, and action initiation in Section 1.3, I will briefly review the neuronal basis of action specification hereafter.

How does the brain specify the right combination of muscle contraction and relaxation, that will produce the desired movement? There are often multiple ways for animals to perform movements to achieve the same goal, this redundancy is due to a large number of degrees of freedom in the control of limbs [Bernstein, 1967]. Several frameworks have been proposed to solve the degree of freedom problem. Here, I will talk briefly about muscle synergies and optimal feedback control. Those theories, although concerned with different aspects of motor control, are not necessarily incompatible.

Muscle synergies, which are coordinated activations of groups of muscle can provide a reduction in the dimensionality of control space [D'Avella et al., 2003]. The motor periphery may be largely engaged in the generation of motor primitives, doing the heavy-lifting for the generation of the kinematic parameters [Sumbre et al., 2001, Flash and Hochner, 2005, Hart and Giszter, 2010], leaving to the central nervous system the task to coordinate different limbs.

Optimal feedback control (OFC) proposes that the degree of freedom problem can be solved by optimizing movement trajectories with respect to a cost function: energy expenditure, smoothness of movements or other possible variables. OFC requires two kinds of models which link motor commands with the external world. Inverse model: the brain transforms the representation of a goal into the sequence of action needed to reach it, and provide the neural command necessary to control movement kinematics [Wolpert et al., 1998]. Forward model: the brain predicts the consequences of its action using a copy of the motor command (see the section on efference copy below) and integrates this prediction with sensory feedback to adjust the motor command optimally [Wolpert and Ghahramani, 2000, Scott, 2012] (fig 1.24). The exact details of the neuronal implementation of OFC are not known, but it likely involves the motor cortices, cerebellum and basal ganglia [Scott, 2012], see fig 1.24).

If there is a motor code in the motor cortex, similar to a sensory code in sensory

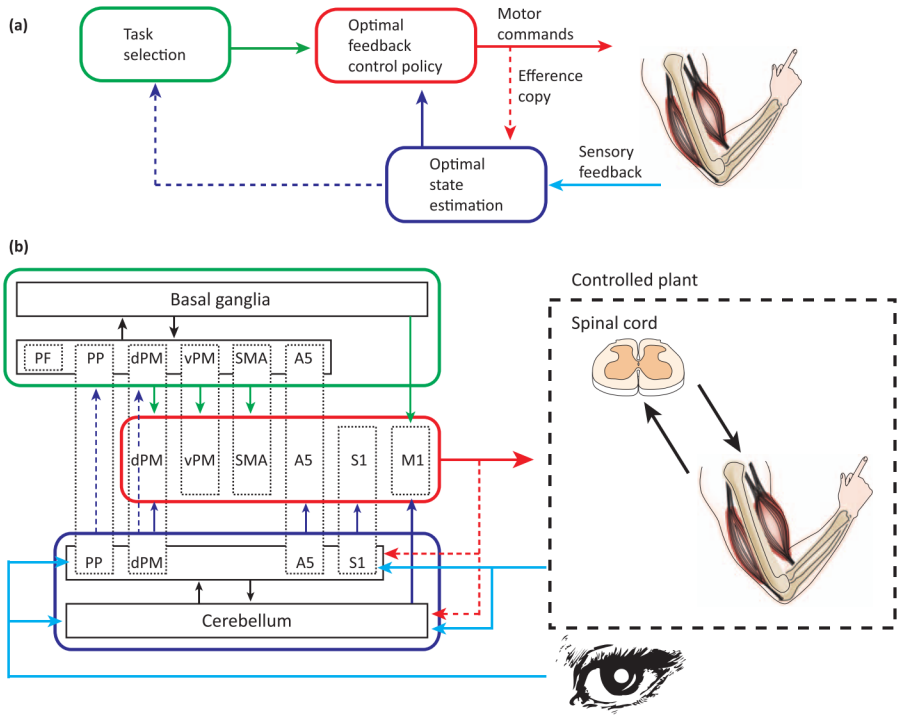

Figure 1.24: **The neural basis of optimal feedback control**. **A**. Optimal Feedback Control Policy converts state variables to motor commands. Optimal State Estimation uses efference copy of motor commands and sensory feedback to estimate state variables. Task Selection specifies the goal of the behaviour which then defines the corresponding control policy. **B**. Neural implementation of OFC-like voluntary control. The controlled plant is assumed to include the limb and spinal cord. The three basic processes, task selection, control policy, and state estimation, are each generated by highly distributed circuits. Dashed boxes denote individual cortical regions and some cortical regions are assumed to participate in two or even all three processes. Cortical connections are assumed amongst cortical regions involved in a given process. PF, PP and S1 include multiple subdivisions not displayed for simplicity. Cortical abbreviations: PF, prefrontal; PP, posterior parietal; dPM, dorsal premotor; vPM, ventral premotor; SMA, supplementary motor area; A5, area 5; S1, primary somatosensory; M1, primary motor. From [Scott, 2012].

cortices, it still remains to this day rather elusive. Many attempts have tried to link particular kinematic parameters, or directly correlate specific muscle contractions to neural activity in the motor cortices with limited success and generalization power. While the seminal experiments of Fritsch & Hitzig (1870) on the dog motor cortex and Ferrier (1873) on monkeys revealed a crude topographical organization of the motor cortex regarding the recruitment of the limbs upon stimulation, modern findings seem to suggest that this somatotopic map may be organized to promote coordination rather than reflect a muscle to muscle, within-limb topographic arrangement [Sanes and Schieber, 2001]. Activity in M1 may encode complex parameters, or even sequences of movements [Hatsopoulos et al., 2003, Lu and Ashe, 2005, Graziano et al., 2005]. In line with those observations, Graziano and colleagues proposed that M1 may encode ethologically relevant behaviors,

such as grasping and bringing an arm towards the mouth [Graziano, 2006]. This may be achieved through the concerted activity of populations of cells in the motor cortices [Shenoy et al., 2013], impinging directly on spinal circuits or through subcortical structures (basal ganglia, cerebellum) and other descending pathways.

In zebrafish, while some understanding in starting to emerge on motor representations in the hindbrain and spinal cord circuits (see Section 1.2, in particular how swimming speed can be controlled at the level of the spinal cord), there is no consensus on the existence of high-level representation of ethologically relevant behavioral sequences, or which regions could subserve this function.

Efference copy and corollary discharge

Motor control relies on predicting the outcome of actions on the external world as well as on future sensory experiences, and on the reaction to proprioceptive and sensory feedback to dynamically readjust movement kinematics in real time. This is necessary for interacting with the environment for at least three reasons:

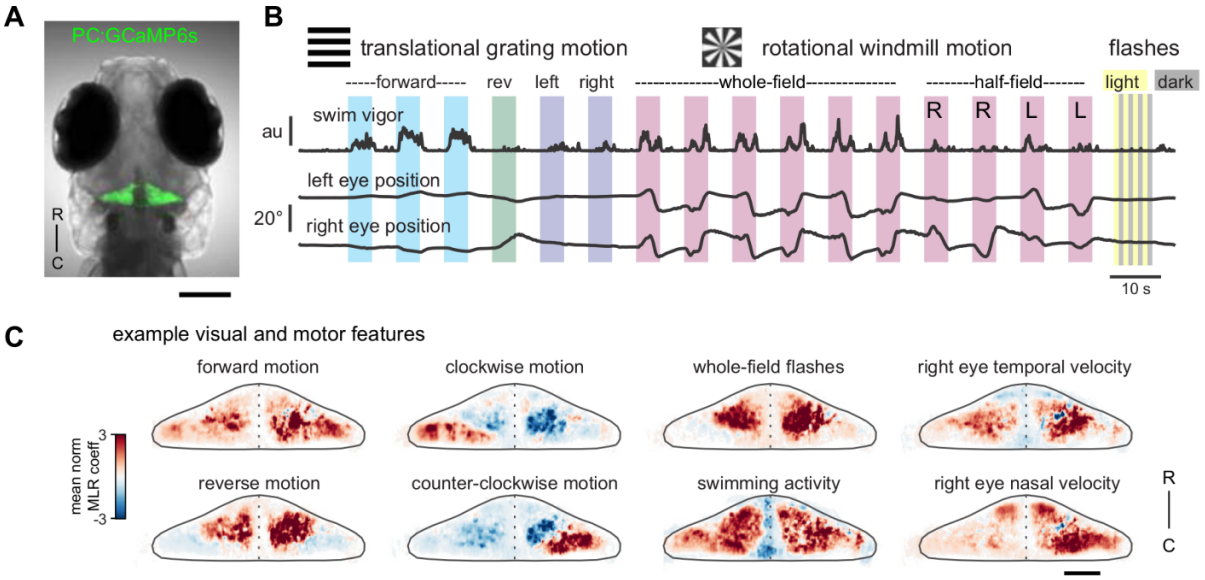

Figure 1.25: **Efference copy in the zebrafish larva cerebellum**. **A**. GCaMP6 expression in the Purkinje cells of a 7 days old larva. **B**. Battery of visual stimuli submitted to the larva while recording neuronal activity in Purkinje cells, and simultaneously monitoring tail and eye movements. **C**. Visual stimuli, as well as motor variables, are represented in the cerebellum, were motor related activity may represent an efference copy used for sensorimotor integration. From [Knogler et al., 2019].

- being able to select between motor actions based on their expected consequences
- being able to react quickly to discrepancies between the real world and the prediction to readjust a movement

- disambiguate between sensory experience that results from the generation of movements (*e.g.* hitting a ball) and sensory experience emanating from the outside world (being hit by a ball)

Efference copy and corollary discharge are two types of forward models which allow to predict the expected outcome and sensory consequences of an action. While the efference copy generally refers to an exact copy of the motor commands used for predicting motor output, corollary discharge is more loosely defined as an input from motor centers to different parts of the sensory hierarchy and can be used to inhibit reflexes or filter sensory inputs [Crapse and Sommer, 2008]. The cerebellum may provide the substrate for efference copies and error prediction in both mammals and zebrafish [Wolpert et al., 1998, Ahrens et al., 2012]. Recent studies shows that both sensory and motor representations arise in the zebrafish larva cerebellum (fig 1.25) [Knogler et al., 2017, Knogler et al., 2019]. The authors suggest that zebrafish Purkinje cells encode sensory features in complex spikes, whereas swimming activity emerging form efference copies are encoded by simple spikes [Knogler et al., 2019]. Complex and simple spikes may interact in the cerebellum depending on the motor context [Knogler et al., 2019].

1.4.2 Examples of sensorimotor transformations

Chemotaxis in *Caenorhabditis Elegans*: sensorimotor transformation at the cellular level

Chemotactic behavior in *C. elegans* An innate behavior of *Caenorhabditis* nematodes is to search for food. Although little is known about their ecology outside the lab, it seems that they mainly eat soil bacteria. *C. elegans* can adapt their locomotor gait to swim in liquid media, or crawl on their side on solid soil, and can use an array of sensory neurons to guide their navigation. The locomotor repertoire of the worm on agarose is relatively simple, it consists in forward runs and turns: reversals and omega turns [Croll, 1975], as well as shallow turns [Kim et al., 2011]. Those basic movements can be combined into episodes of locomotor sequences to navigate through their environment.

Chemotaxis in *C. elegans* relies on the alternation of smooth swimming (run) periods with pirouettes (short series of turns) when the concentration of odorant changes. This strategy forms the basis for a biased random walk, which enables the worm to navigate towards or away from the source of odorant [Pierce-Shimomura et al., 1999]. Another strategy called weathervaning implies more shallow turns [Iino and Yoshida, 2009], and acts in parallel of pirouettes for a more efficient navigation (fig 1.26). Additionally, *C. Elegans* are able to switch between two patterns of locomotor activity, one where they mostly run forward and cover long distances, and another where they produce more

turns and stay in a restricted area. This switch can be triggered by the encounter of chemical gradients [Hums et al., 2016, Gray et al., 2005]. Those alternating patterns are reminiscent of the switch between exploration and exploitation that occur in many animal species.

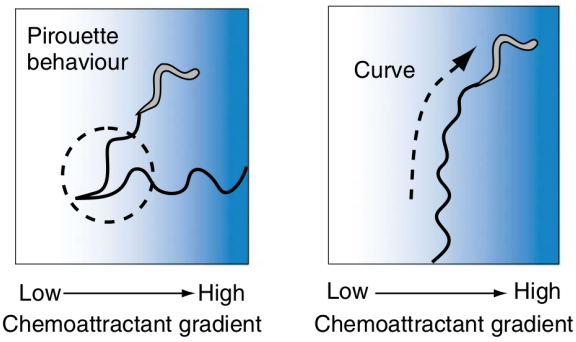

Figure 1.26: **Chemotaxis behavior in *C. elegans*.** *C. elegans* are able to navigate gradients of odorants to localize food sources. They employ two behavioral strategies in parallel. Pirouette behavior (left), which consist of high angle turns and reversals, are employed when the odor fades to make the worm go back towards the source of odor. The navigation strategy implement by pirouettes is a biased random walk. Weathervaning (right) is a more subtle strategy that enables efficient navigation towards food source using information about the magnitude of the gradient. From [Yoshida et al., 2012].

The neural basis of *C. elegans* chemotaxis The nervous system of *C. elegans* presents numerous advantages for the study of the neural basis of behavior. Its 302 neurons can be identified from individual to individual, and all be recorded simultaneously with optical techniques, while the worm behaves freely. *C. elegans* is to date the only animal whose entire connectome has been traced with electron microscopy, down to the synaptic level [White et al., 1986]. Contrary to vertebrates, *C. elegans* possesses a ventral nervous system, with a head and tail ganglia. The nerve ring, a horseshoe shaped bundle of axons in the head ganglia that loops around the pharynx, contains processes from a large fraction of the 302 neurons, receives input from sensory neurons in the head, and forms a large amount of synapses with neurons controlling behavior [White et al., 1986]. Finally, most of *C. elegans* neurons come by pairs, with three letter names. They do not produce action potentials, except for a few pairs of neurons (RMD, AVA and AWA) [Mellem et al., 2008, Liu et al., 2018b], instead, they just show graded potentials which propagate passively.

C. elegans can use chemotactic behavior to localize water-soluble (gustatory) or volatile (olfactory) substances with different valence (attractants/repellents), as well as navigate in oxygen gradients [Bargmann, 2006]. Different neurons are recruited according to the modality (gustatory, olfactory, oxygen-sensing), and valence of the stimulus. In this section, I will describe the circuits mechanisms of olfactory chemotaxis to attractants

mediated by the sensory neurons AWA and AWC [Bargmann et al., 1993, Troemel et al., 1997].

AWC neurons are activated by odor removal, and inhibited by odor presentation [Chalasani et al., 2007]. AWA in contrast are activated by an increase in odor concentration [Larsch et al., 2015], in response to which they produce action potentials [Liu et al., 2018b]. Behaviorally, AWA activity has been shown to suppress large turning events (omega turns and reversals) [Larsch et al., 2015], while AWC activity is correlated with reversals [Larsch et al., 2013]. Itskovits *et al.* suggest that AWC encodes robustly the sign of the gradient, promoting reversals when the gradient vanishes, while AWA may adapt to small changes in the magnitude of the gradient derivative in a more stochastic way, promoting forward movements when the gradient increases [Itskovits et al., 2018].

These sensory neurons project to a first layer of interneurons: AIA, AIB, AIY and AIZ [White et al., 1986, Wakabayashi et al., 2004]. Selective optogenetic activation and inhibition of these neurons have shown that AIY neurons play a primordial role in promoting reversal and gradual turn: symmetric AIY drive during head undulations suppresses reversals while asymmetric drive elicits turning [Kocabas et al., 2012], (see fig 1.27).

AIY neurons in turn projects to RIA, a pair of second layer interneurons which occupy a central circuit position, receiving inputs from different sensory networks, and reciprocally connected with head motor neurons SMDD and SMDV [White et al., 1986]. Remarkably, RIA neurons single-handedly implement the sensorimotor integration necessary for chemotaxis. Motor information from SMDD and SMDV are represented in subcellular compartments of RIA axons in the nerve ring, called nrD (nerve ring Dorsal) and nrV (nerve ring Ventral) respectively. Robust and independent calcium dynamics, correlated with head movements, can be observed in those two compartments (fig 1.27) [Hendricks, 2012]. This motor-related activity depends on acetylcholine release from SMDD and SMDV, and is integrated with sensory-evoked activity from AIY: if an odorant is detected during an undulation of the head, there is an in phase, domain specific suppression of the motor-encoding activity by the sensory-evoked activity. Consequently, the nrV domain displays a weaker activity than nrD when a worm steers toward a ventrally located odorant, while nrD domain displays a weaker activity than nrV when a worm steers toward a dorsally located odorant [Liu et al., 2018a] (fig 1.27).

To summarize, RIA centralizes motor and sensory inputs in different axonal compartments, where sensory activity suppresses motor inputs to bias the crawling direction of the worm. The circuit involves feedforward sensory inhibition, and reciprocal excitation of RIA and premotor neurons, effectively implementing a single-cell corollary discharge. *C. elegans* employs an active sensing strategy: they need to move their body across chem-

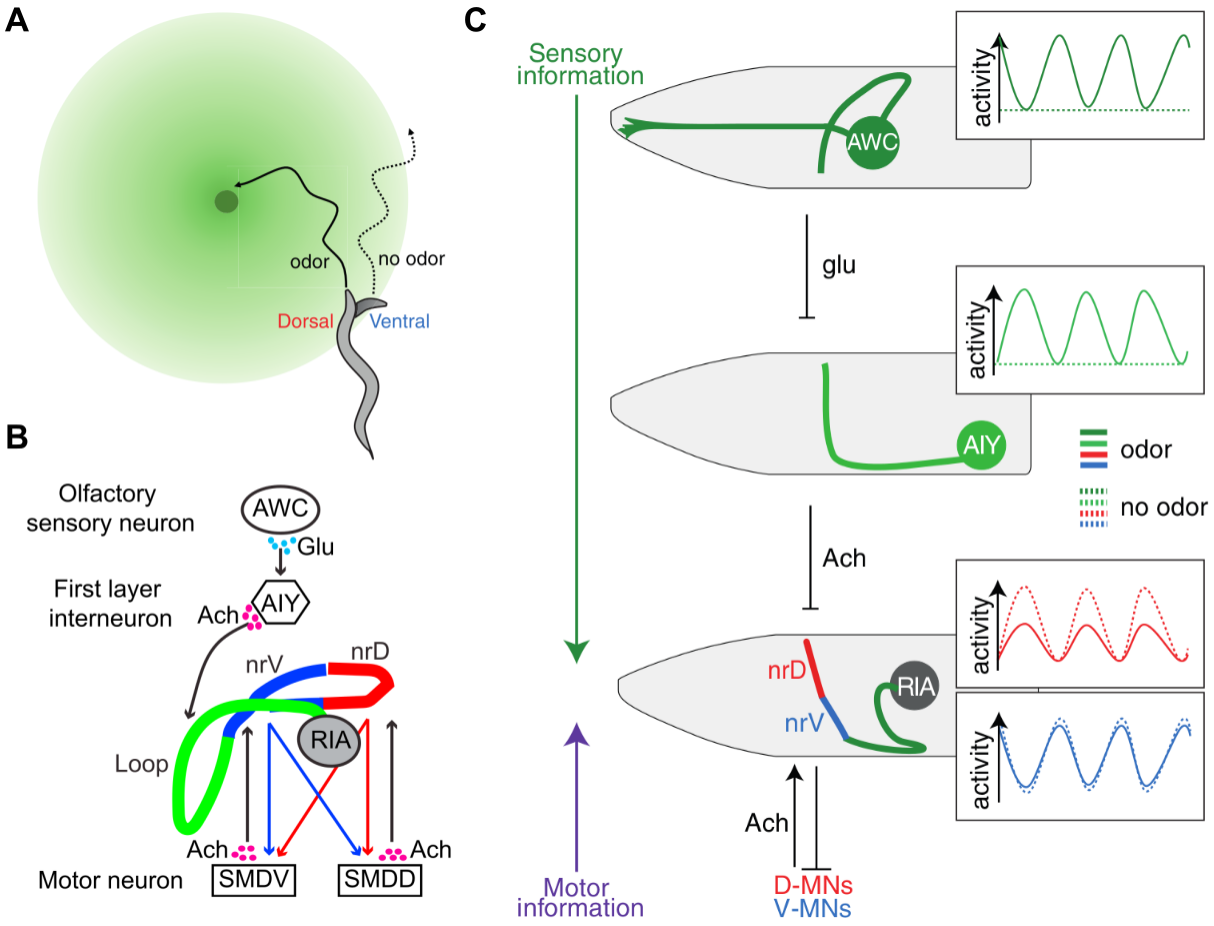

Figure 1.27: **Sensorimotor integration during olfactory steering**. **A**. Gradient navigation during chemotaxis. **B,C**. Neural circuit for olfactory chemotaxis. The interneuron RIA posses different and independent compartments in their axons inside the nerve ring called nrV (for nerve ring ventral), and nrD (nerve ring dorsal). During chemotaxis, *C. elegans* are actively moving while sensing odors: they bend their heads to the dorsal or ventral side rythmically. The ventral head motor neuron SMDV sends feedback to nrV, while the dorsal motor neuron SMDD sends feedback to nrD, both via a muscarinic acetylcholine receptor. The activity of olfactory sensory neuron AWC is inversely correlated with odorant concentration. If the odorant concentration increases when the worm is flexing his head dorsally, AWC is inactivated, thus AIY which receives glutamatergic input from AWC is also inactivated. AIY, releases its inhibition on nrD, which causes an imbalance and steers the worm dorsally. If the odorant concentration decreases when the worm is flexing his head ventrally, AWC is active and recruits AIY, which inhibits activity in nrV, thus causing an imbalance and steering the worm dorsally. RIA acts as a converging center for sensory and motor information, and performs their integration through the compartimentalization of its axon. From [Kaplan and Zimmer, 2018, Liu et al., 2018a].

ical gradients to properly sample their spatial properties for the sensorimotor integration process to occur. RIA neurons are recruited downstream of different sensory systems [Mori and Ohshima, 1995, Guillermin et al., 2017], and may also provide a solution for multimodal integration.

1.4.3 Convergent visuomotor transformations in the zebrafish larva: sensorimotor transformations at the circuit level

Sensory convergence of different modalities to premotor circuits may be an important feature of nervous systems to perform multimodal integration. Zebrafish larvae are able to perform a large array of visuomotor behaviors, such as phototaxis [Burgess et al., 2010, Chen and Engert, 2014, Wolf et al., 2017, Karpenko et al., 2020], the optomotor response (OMR) [Orger et al., 2000, Orger et al., 2008, Naumann et al., 2016], escapes to loomings [Temizer et al., 2015, Barker and Baier, 2015, Dunn et al., 2016a], and dark-flash responses [Burgess and Granato, 2007a, Chen and Engert, 2014].

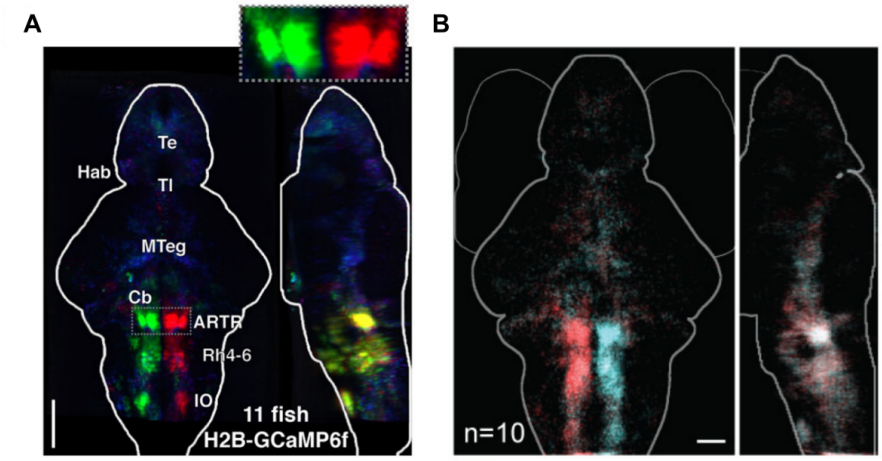

Figure 1.28: **Motor circuits during spontaneous behavior**. **A**. Motor circuits for spontaneous behavior found by Dunn *et al.*. Green: left turns, Red: right turns. **B**. Same circuit described by Chen *et al.*. Red: left turns, blue: right turns. ARTR: anterior rhombencephalic turning region. Rh4-6: rhombomeres 4 to 6. IO: inferior olive. MTeg: midbrain tegmentum, contains the nMLF. From [Dunn et al., 2016b, Chen et al., 2018].

Chen *et al.* tested whether those different sensorimotor responses can recruit the same motor circuits, and if and where different sensorimotor representations converge [Chen et al., 2018]. To do so they recorded the brain-wide neuronal activity of zebrafish larvae expressing GCaMP6f in the nucleus of neurons using a light-sheet microscope, while simultaneously presenting an array of visual stimuli, and recording fictive swimming signals. They used a regression-based approach to identify sensory and motor-related activity, taking advantage of the periodicity of the stimulation design to disentangle purely motor from sensory-evoked motor activity.

Groups of neurons active during spontaneous behavior were identified (fig 1.28), yielding a motor map compatible with a previous study [Dunn et al., 2016b], featuring the anterior rhombencephalic turning region (ARTR), inferior olive (IO), and neurons in rhombomeres 4-6. Activity in the hindbrain is largely lateralized with respect to tail direction

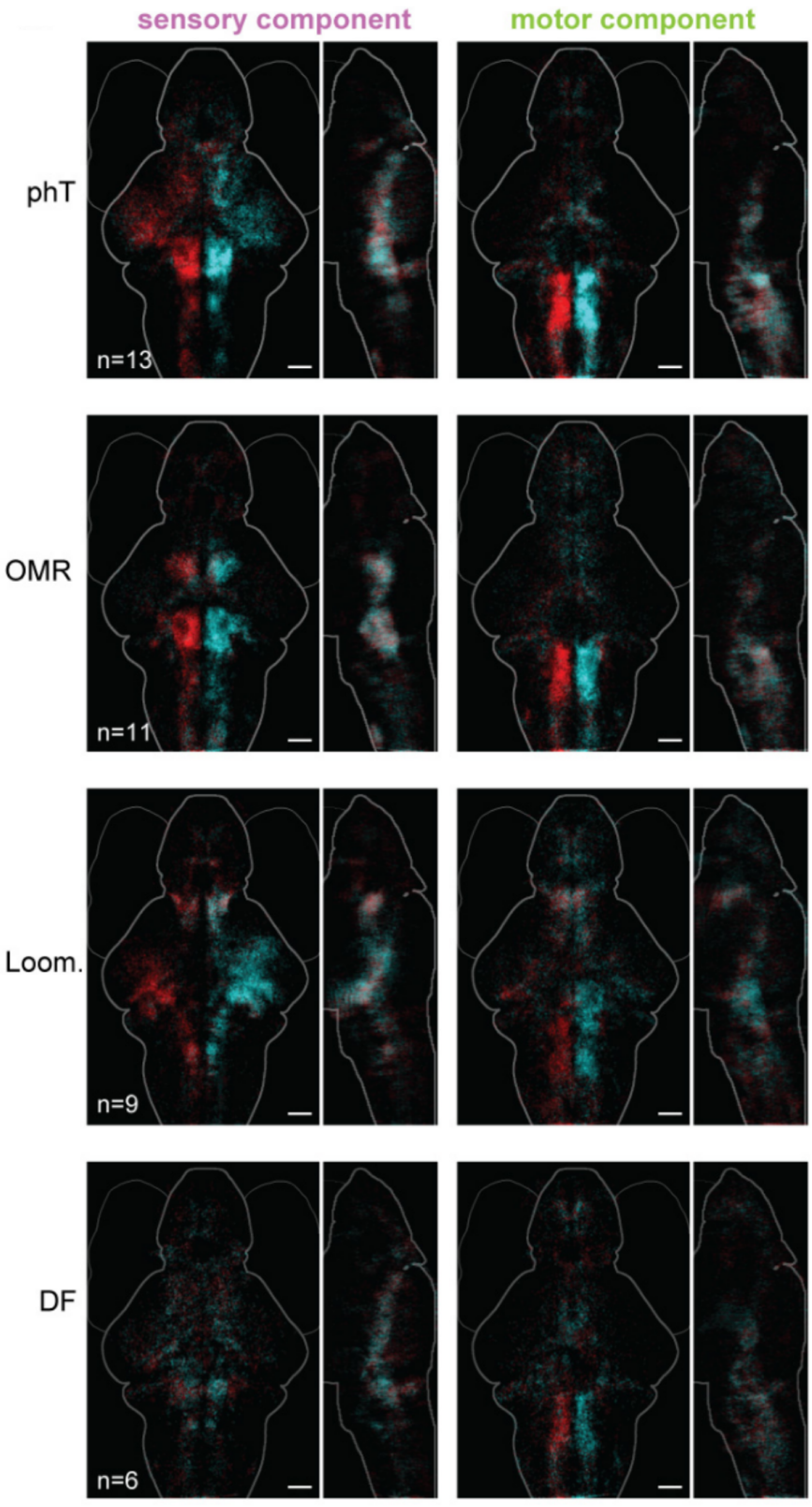

Figure 1.29: **Sensory and motor responses to different visual stimuli**. Regression based maps of sensory (left) and motor (right) neurons active during phototaxis (phT), optomotor response (OMR), presentation of looming stimuli (Loom.) and dark flashes (DF). Red: left turn, Blue: right turn. From [Chen et al., 2018].

and symmetrical. The ARTR biases swim directions [Dunn et al., 2016b], and its activity may be modulated during navigation [Johnson et al., 2020, Wolf et al., 2017, Naumann et al., 2016] to generate different locomotor modes, or implement navigational strategies. The inferior olive is involved in gain adaptation, a form of sensorimotor learning [Ahrens et al., 2012]. It receives both motor information from descending pathways and afferent circuits from the spinal cord, as well as sensory information [Knogler et al., 2019]. The IO projects to the cerebellum, with which it could interact to represent motor context, integrate sensory information or adapt behavior [Knogler et al., 2019, Lin et al., 2020]. In line with these hypotheses, the inferior olive is present in both spontaneous and sensory induced motor activity (fig 1.28,1.29), but also in sensory maps, at least for OMR and phototaxis (fig 1.29).

Interestingly, very similar groups of neurons are recruited as the motor components of different visuomotor behaviors (fig 1.29, right), while the sensory parts of the network appear very different across modalities. This suggests a modular and hierarchical organization of motor control, where different sensory modalities converge to a unique motor control system.

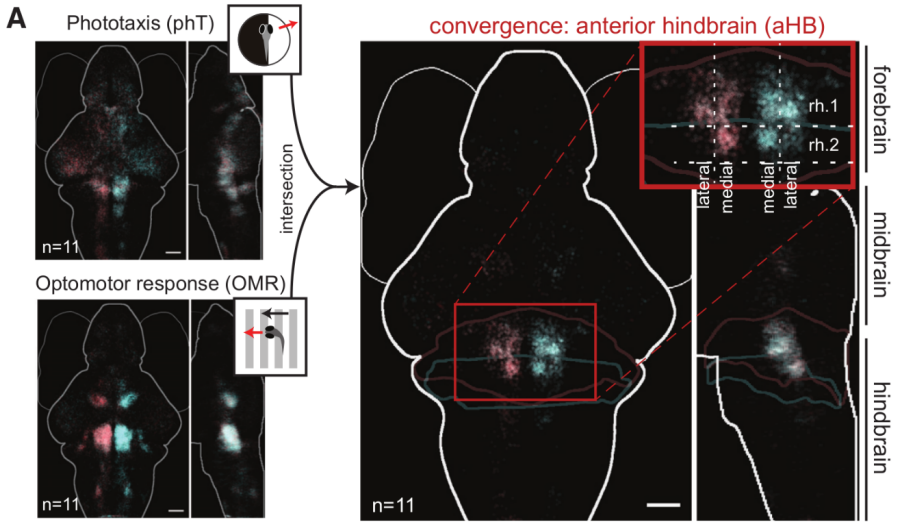

Figure 1.30: **Sensorimotor convergence in aH1-2**. Convergent sensory inputs to aHB1-2 during OMR and phototaxis. From [Chen et al., 2018].

After mapping both sensory and motor parts of the networks, Chen *et al.* asked whether sensory information converges to a common pre-motor region across different types of stimuli. To answer this question, they mapped the intersection of different sensory representation for each pair of stimulus delivered (fig 1.30, only OMR and phototaxis is shown). Across all modalities, they found a substantial amount of overlap in a region of the anterior hindbrain in rhombomeres 1 and 2, which they named aHB[1-2]. This region was only weakly correlated to motor activity, suggesting it informs, but does not directly generate behavioral choices. As an additional piece of evidence towards this hypothesis,

lateralized optogenetics activation of aHB[1-2] did not increase swimming frequency but biased turning to the ipsilateral direction.

1.5 Zebrafish: a model for behavioral and circuits neuroscience

The zebrafish *Danio Rerio* is a freshwater fish of the minnow family (Cyprinidae) which owes its name to the horizontal blue stripes on the side of its body (see fig 1.31). Their natural habitat is in India, Pakistan, Bengladesh, Nepal and possibly Myanmar, and they thrive in various environments: small streams, but also shallow waters with low currents or small ponds [Parichy, 2015]. They usually live in clear waters, but can also cope with turbid waters when it rains, and are found across a large array of environmental conditions. They typically form loose social aggregates, or shoals, of tens of individuals. Zebrafish are omnivorous fish, which can grow up to 4 cm and become sexually mature at 3 months. Dragonfly larvae, as well as other invertebrates are thought to prey on zebrafish larvae and juveniles [Engeszer et al., 2007].

Zebrafish has become a model organism in developmental biology under the impulse of George Streisinger in the 1980s, not for specific ecological or behavioral reasons but for very practical ones: its potential for genetic analysis and cellular observation, as well as the relative ease of care and short generation time. Remarkably little is known about the life of this small fish in the wild, which could hinder research on behavior and sensory system since we don't really know which features of their environment are important for their survival.

In the last two decades, the zebrafish larva has risen as a major player in the field of systems neuroscience.

1.5.1 Calcium imaging: optical recording of neural activity in neuronal circuits

Calcium signals in neurons can be used as a proxy for electrical activity

The first innovation that allowed the zebrafish larva to become a model organism in neuroscience is the development of calcium imaging. Calcium is a fundamental intracellular messenger in neurons; calcium imaging exploits the relationship between the concentration of calcium in neurons and neuronal activity: neurons have an intracellular calcium concentration of about 50–100 nM at rest, that can rise temporarily with electrical activity to levels that are tens to a hundred times higher [Grienberger and Konnerth, 2012].

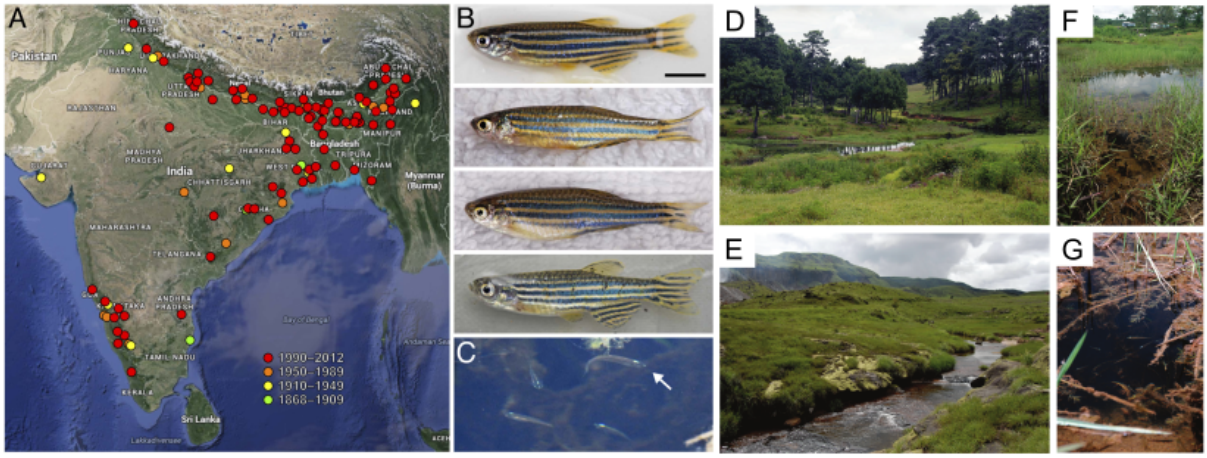

Figure 1.31: **Zebrafish in their natural habitat**. **A**. Zebrafish and their geographic range. Historic and more recent sites where zebrafish have been reported in India, Nepal, Bangladesh and possibly Myanmar. **B**. Zebrafish from northeastern India. The upper two fish are males and the lower two fish are females. **C-G** Zebrafish can live in various habitat, form small stream-side pools (C,G) to calm (D) or more tumultuous streams (E), or even rice paddies (F). From [Engeszer et al., 2007, Parichy, 2015].

Calcium sensors are fluorescent proteins or synthetic molecules. When excited, they emit a level of fluorescence that depends on the cytoplasmic concentration of calcium. Importantly, in neurons the relationship between membrane potential or firing rate and fluorescence changes of calcium sensors are not exactly linear, nor are they strictly homogeneous across the different compartments of the cell. Computational approaches such as deconvolution can be used to infer the firing rates and even the timing and number of spikes from fluorescence traces [Yaksi and Friedrich, 2006, Moreaux, 2007, Pnevmatikakis et al., 2016]. Relative changes in the fluorescence of calcium sensors provide a good proxy for neuronal activity across vast population of neurons.

Calcium sensors

The first calcium sensor that was used for imaging calcium in cells was aequorin, d bioluminescent sensor discovered by Shimomura *et al.* [Shimomura et al., 1962]. It was later used in neurons to detect calcium changes in relation to neuronal activity in the squid [Baker et al., 1971, Hallett and Carbone, 1972, Llinás et al., 1972], and in aplysia neurons [Stinnakre and Tauc, 1973]. More sensitive and versatile fluorescent calcium indicators, such as fura-2, were developped in the laboratory of Roger Tsien [Tsien, 1980, Grynkiewicz et al., 1985], and brought a large improvement over previous dyes, ushering in the possibility to record many neurons in live animals.

One of the main difficulties to be resolved at that time was the proper delivery of the calcium indicator to a well-defined population of cells. The development of a family of genetically encoded calcium indicators (GECI) called cameleons [Miyawaki et al., 1997],

later followed by GCaMPs [Nakai et al., 2001] opened up a vast array of possibilities due to the versatility offered by the use of various promoters to obtain tissue specific expression of calcium indicators [Higashijima et al., 2003, Scott et al., 2007].

Microscopy techniques for calcium imaging

New development in microscopy enabled monitoring the changes in fluorescence at high speed in thick brain tissues with cellular resolution. Wide field microscopy combined with CCD or CMOS sensor allows very fast recordings but the source of the signal, cannot be determined precisely since it is contaminated by out-of-focus fluorescence.

Confocal imaging allowed for optical sectioning. The light collected from the sample goes through a pinhole placed in the conjugate plane of the sample plane, which results in the rejection of all the fluorescence that is out-of-focus. Only the fluorescence at, or very close to, the focal plane of the objective, which means that a single plane (with a thickness of a few microns) of the sample is imaged. Fluorophore excitation is obtained by scanning a laser across the sample point by point with galvo mirrors, and recording the emitted light with a photomultiplier tube (PMT). The fluorescence measured at each point of the sample is used to reconstruct an image of the sample. Scanning each point of the image is however a slow process. The confocal microscope therefore possesses a better spatial resolution than wide field fluorescence and allows optical sectioning, at the expense of temporal resolution. Confocal imaging has been adopted early in neuroscience and calcium imaging [Fine et al., 1988] and has been instrumental in many studies to resolve the population activity of whole circuits [Fetcho and O'Malley, 1995], however it is not very well suited for imaging in thick, scattering tissue, for instance to record neurons lying inside the deepest layers of the murine neocortex.

Two-photon imaging was adopted in the field of neuroscience to palliate this specific problem [Denk et al., 1990, Yuste and Denk, 1995, Svoboda et al., 1997]. Two photon microscopy relies on the two-photon absorption effect: a fluorophore that can be excited by one photon of wavelength λ can often be excited by two photons of twice the wavelength (2λ), if they are delivered simultaneously (within a time window of femtoseconds). This phenomenon makes it possible to use infrared (IR) photons to stimulate fluorophores. IR photons suffer much less from scattering than higher wavelength, which allows them to penetrate deeper in the tissue—up to approximately one millimeter. In addition to this, the two-photon effect is non-linear, the probability of the simultaneous absorption of two photon is much higher in the focal plane than anywhere else, which result in an excitation of fluorophores restricted to the focal plane: this is essentially another way to perform optical sectioning. Two-photon microscopy is usually implemented as a point-scanning microscopy technique and therefore suffers from the same drawbacks

as confocal microscopy in terms of temporal resolution, although both can benefit from resonant scanners [Rochefort et al., 2009] and acousto-optics deflectors to increase the scanning speed [Grewe et al., 2010].

Some organisms, such as the zebrafish larva, are optically transparent during some stage of their development and can be optically accessed through a direction that is orthogonal to the detection objective. This crucial property can be leveraged to alleviate the hurdles of classical fluorescence microscopy techniques. Light-sheet fluorescence microscopy (LSFM), sometimes also called selective or single plane imaging microscopy (SPIM), takes advantage of this transparency to provide optical sectioning by exciting all the fluorophores in one plane at the same time, and recording images at high speed using a CMOS or CCD camera. Contrary to point scanning microscopes, which scan all the pixels of an image in series, with a light-sheet microscope, all the pixels are recorded in parallel, which enables much faster frame rates, only limited by the amount of light one can supply and the maximum frame rate of the camera. The formation of the light-sheet, which is microns thin to provide optical sectioning, is obtained by using a cylindrical lens, or by scanning a laser with galvo mirrors through a low numerical aperture objective. Light-sheet microscope is an old invention that was only recently rediscovered and applied to the study of biological samples [Huisken et al., 2004] and calcium imaging (see fig 1.32) [Holekamp et al., 2008, Panier et al., 2013, Ahrens et al., 2013b]. Light-sheet microscopy can therefore be used to monitor very large number of neurons, up to virtually the entire brain of a zebrafish larva (which contains approximately 100,000 neurons) at low frame rates, or a single plane containing hundreds to thousands of neurons at high frame rates.

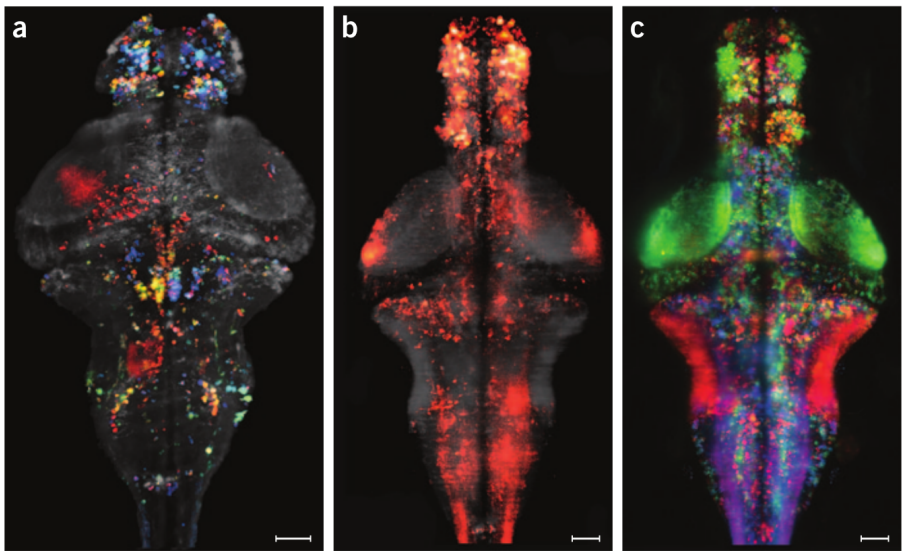

Figure 1.32: **Whole-brain activity recorded with a light-sheet microscope**. **A**. Neural activity color coded at a different time point. **B**. Activity at a single time point. **C**. Computational map of correlated activity across the same brain as in *B*. Shared colors indicate common dynamic patterns of activity From [Keller et al., 2014].

Other microscopy techniques are in development, and are very promising for the study of the activity of large swathes of neurons in behaving animals. Such techniques include swept confocally-aligned planar excitation (SCAPE) [Bouchard et al., 2015, Voleti et al., 2019] which could allow high frame rate volumetric imaging. A modified version of light-field microscopy, which uses arrays of lens positioned before the camera sensor to reconstruct 3D information computationally, allows recording neural activity in freely moving zebrafish larva with near cellular resolution [Cong et al., 2017]. This impressive feat was also achieved with an adapted version of HiLo microscopy called DIFF, which uses a combination of structured illumination and spectral filtering to obtain a reconstructed optical sectioning [Kim et al., 2017, Marques et al., 2020].

Calcium imaging in the zebrafish larva

Larval zebrafish is particularly well suited for the study of its nervous system using calcium imaging. Genetically encoded calcium indicators can be expressed in the whole brain, or restricted to very specific tissues, leveraging a versatile genetic toolkit available in this model organism [Howe et al., 2013]: many promoters can be used to drive circuit specific expression of calcium sensors and optogenetic actuators, and binary systems such as UAS/Gal4 and Cre/lox provide a large array of possible combinations of drivers and effectors. Thousands of transgenic zebrafish lines already exist, created from enhancer/promoter sequences from known genes or through enhancer trap screening [Scott et al., 2007, Scott, 2009]. Larval zebrafish can be embedded in a drop of agarose, and their tail and eyes, once released from the gel, can be recorded with a high-speed camera to study their kinematics. The seminal paper of Fetcho and O'Malley in 1995 [Fetcho and O'Malley, 1995] imaging calcium dynamics in spinal motorneurons during escape behaviors with a confocal microscope paved the way for recording populations of neurons in the brain and spinal cord of zebrafish larva. The zebrafish optic tectum in particular has been extensively studied using two photon microscopy, as it is thought to be a high level integration center for visuomotor behavior. Light-sheet recording of calcium signals in the zebrafish larva has been a significant breakthrough for systems neuroscience: for the first time it was possible to record the entire brain of a living, behaving vertebrate with cellular resolution [Ahrens et al., 2013b, Panier et al., 2013]. Functionally defined population of cells can now be registered to brain atlases shared by the community [Randlett et al., 2015], which fosters collaboration between groups and makes comparison of data with between different lines easier. Reconstruction of the zebrafish larva connectome using tracing techniques and EM microscopy are under way [Hildebrand et al., 2017, Kunst et al., 2019], promising to bridge functional and structural connectivity. Finally, new techniques allow the recording of whole-brain activity in freely swimming larvae, opening the way for implementing more naturalistic experiments in the lab [Kim et al., 2017, Cong

et al., 2017, Marques et al., 2020].

1.5.2 Locomotor behavior of the zebrafish larva

Zebrafish larvae swim in discrete episodes of locomotor activity involving their tail in coordination with their pectoral fins. They launch themselves and glide through the water, pause, and start again, in a pattern called "beat and glide" [Buss and Drapeau, 2001]. These discrete segments of activity are called tail bouts.

The discrete nature of the larva's locomotion facilitates the quantification of behavior. The larva can perform different categories of tail bouts to turn left, right, or move forward with a fine control over the amplitude and direction of movements. Early on, this categorization was made carefully by the experimenter based on video recordings [Budick and O'Malley, 2000]. As time went by, it relied more heavily on quantifying different kinematic parameters. Today, we apply machine learning algorithms to a large array of kinematic parameters in order to classify movements (fig 1.33), if possible using unsupervised algorithms [Marques et al., 2018].

In order to properly sample from the behavioral repertoire of the zebrafish larva, it is important to record behavior is the most naturalistic setting possible, with the largest array of stimuli to which the larva is susceptible to respond. Using this approach, Marques *et al.* have found that the zebrafish larva's behavioral repertoire is based on the combination of 13 different basic behavioral units [Marques et al., 2018].

Zebrafish larvae are able to perform various kinds of taxis (movements that are directed towards, or away from a source) such as rheotaxis [Olive et al., 2016] or phototaxis [Wolf et al., 2017], and kinesis (non-directional response to a stimulus, *e.g.* the optokinetic response [Rinner et al., 2005]). Moreover, they show complex spatiotemporal dynamics in the chaining of actions they can perform during spontaneous or induced behaviors [Dunn et al., 2016b, Mearns et al., 2020, Johnson et al., 2020], thus displaying a rich behavioral repertoire.

1.6 Objectives of the thesis

In the introduction, I have brushed a large portrait of the mechanisms underlying the generation of locomotor behavior, with a special focus on vertebrates. Along the main lines of this introduction, I have argued that the generation of behavior by nervous systems is a hierarchical process. As we move up the motor hierarchy, form circuits in the spinal cord, to descending spinal pathways, to brainstem circuits, to higher order motor centers, motor-related neuronal activity is more and more complex and integrated

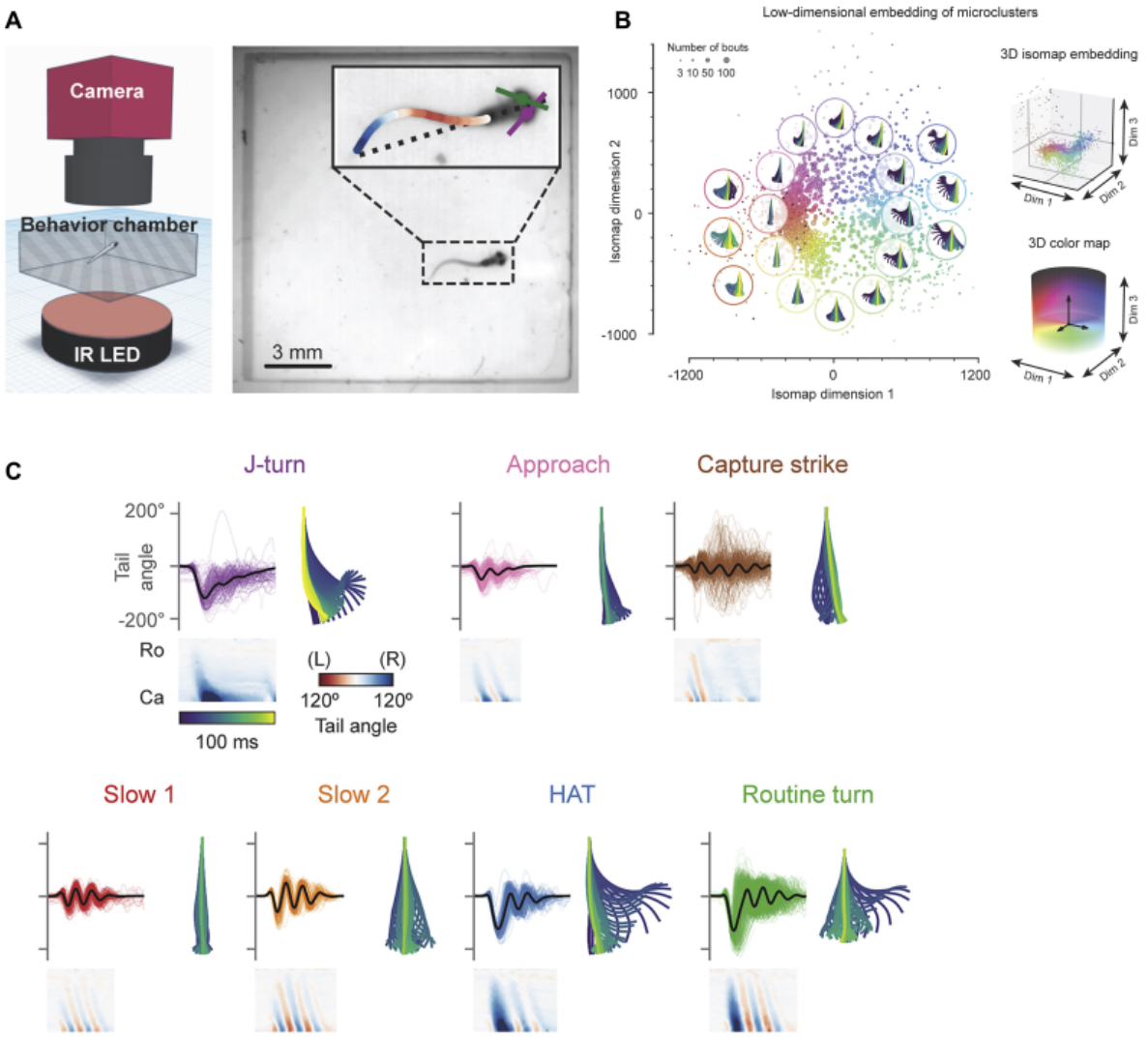

Figure 1.33: **Classification of discrete swim bouts**. **A** Schematic of the setup used to record behavioral data. The angle of the eyes, and small segments all along the tail are measured to extract kinematic parameters. **B** Non-linear embedding of kinematic parameters in a low dimensional space. **C** Discrete categories of tail bouts. From [Mearns et al., 2020].

with other cognitive functions. The zebrafish larva presents major advantages to study how higher order brain centers integrate information, such as internal drives, or external sensory stimuli, to generate adaptive behavior.

The full understanding of sensorimotor integration requires a description of the whole system, from sensory percepetion to the generation of behavior and back, at the level of the whole brain. Today this kind of mechanistic, end-to-end understanding, is only possible in optically accessible small animals, with a "simple" nervous system, such as *C. elegans*, *Drosophila* larvae, or the zebrafish larva. In the first part of this dissertation, we leverage the advantages offered by the zebrafish larva to study the sensorimotor integration of pure tones in the auditory system. More specifically, we will study the sensory

representation of frequency in the brain, motor-related neural activity, and how these two circuits converge to enable the larva to react to auditory stimuli.

In the second part, I will investigate the neuronal mechanisms of preparatory motor activity for self-generated movements. The main goal of this part is to identify groups of neurons active before the onset of movements, and investigate whether their activity is predictive of the timing and laterality of movements to come.

Finally I will discuss my findings concerning the generation of sensory-induced and self-generated behavior in the light of the recent zebrafish literature, to identify potential common grounds between the two systems, a raise new questions for future investigations.

2

Sensorimotor transformation

2.1 Introduction

The zebrafish larva is a relatively recent model in neuroscience, whose potential has been unleashed by the development of calcium imaging techniques like two-photon imaging in the late 1990s and the use of light-sheet microscopy in the last decade. One of the early endeavors in zebrafish neuroscience, which is still in progress, has been to map sensory representations in the brain. A lot of work has focused on vision, and the neuronal representation of visual features. This made sense since many visuomotor behaviors, such as the optomotor or optokinetic response, have been identified in the zebrafish larva. Other sensory modalities however, some of which are completely alien to us like the lateral line, carry crucial information about the external world.

When I started studying the neuronal basis of audition in 2015, the only body of knowledge for auditory processing in the zebrafish larva came from the escape response to loud stimuli mediated by the Mauthner cells. What we knew about frequency representation in different brain nuclei in teleosts came from studies in adults of other species, notably the goldfish. In December 2015, the PhD dissertation of Raphael Olive [Olive, 2015] demonstrated the existence of clusters of cells responding to different amplitude profiles of auditory stimuli in larvae stimulated with a piezoelectric actuator, revealing for the first time the regions of the brain active in response to auditory stimuli in the

zebrafish larva.

Preliminary studies in the lab demonstrated that larvae could display variable behavioral responses to different stimulus frequencies, suggesting that the auditory system in the zebrafish larva is more subtle than just triggering escapes in response to very loud stimuli.

We therefore set out to study the neuronal representation of sound frequency in the zebrafish larva's brain, and how this information can be used to generate behavior. To do so, we combined behavioral experiments with recordings of neuronal activity using calcium imaging with a two-photon and a light-sheet microscope.

We confirmed that the zebrafish larvae can produce tail movements in reaction to sounds that didn't evoke a Mauthner cell-mediated, fast escape response, mainly at low frequencies (150-400 Hz). This behavioral response, which we called long-latency tail movements (LLTM), suggests a more integrated, and more variable response than the Mauthner reflex. We found a low-dimensional representation of frequency information in the 150-1000 Hz range, separating high frequencies from low frequencies in the hindbrain (octaval nuclei) and midbrain (torus semicircularis). Finally, we identified neurons that may be responsible for a temporal integration of the sensory activity to generate long-latency tail movements.

2.2 Article

Article

Current Biology

Sensorimotor Transformations in the Zebrafish Auditory System

Graphical Abstract

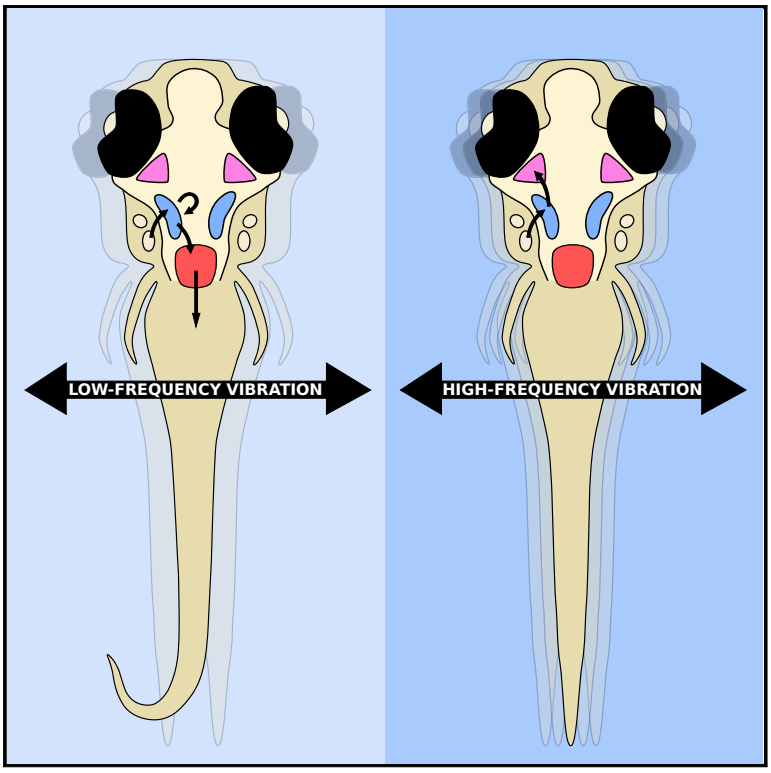

Highlights

- Representation of sound frequencies in the zebrafish brain is low dimensional
- Low frequencies are processed in the hindbrain and induce tail movements
- High frequencies are represented in the hindbrain and midbrain
- Auditory stimuli are temporally integrated to generate tail movements

Authors

Martin Privat, Sebastián A. Romano, Thomas Pietri, ..., Auriane Duchemin, Daphne Soares, Germán Sumbre

Correspondence

sumbre@biologie.ens.fr

In Brief

How do zebrafish larvae use auditory information to generate behavior? Privat et al. show that sensorimotor transformations are represented in a topographically continuous manner. The auditory response is temporally integrated to improve the extraction of sensory information and adapt the motor response to the auditory changes in the environment.

Privat et al., 2019, Current Biology *29*, 1–14
December 2, 2019
https://doi.org/10.1016/j.cub.2019.10.020

CellPress

Please cite this article in press as: Privat et al., Sensorimotor Transformations in the Zebrafish Auditory System, Current Biology (2019), https://doi.org/10.1016/j.cub.2019.10.020

Current Biology
Article

Sensorimotor Transformations in the Zebrafish Auditory System

Martin Privat,[1] Sebastián A. Romano,[1,2,7] Thomas Pietri,[1,6,7] Adrien Jouary,[1,3] Jonathan Boulanger-Weill,[1,4] Nicolas Elbaz,[1] Auriane Duchemin,[1] Daphne Soares,[5] and Germán Sumbre[1,8,*]
[1]Institut de Biologie de l'ENS (IBENS), Département de Biologie, École Normale Supérieure, CNRS, INSERM, Université PSL, 75005 Paris, France
[2]Instituto de Investigación en Biomedicina de Buenos Aires (IBioBA) – CONICET - Partner Institute of the Max Planck Society, Godoy Cruz 2390, C1425FQD Buenos Aires, Argentina
[3]Champalimaud Research, Champalimaud Centre for the Unknown, Lisbon 1400-038, Portugal
[4]Department of Molecular and Cellular Biology, Center for Brain Science, Harvard University, Cambridge, MA, USA
[5]Department of Biological Sciences, New Jersey Institute of Technology, Newark, NJ 07102, USA
[6]Present address: *Cell Reports*, Cell Press, 1043NX Amsterdam, the Netherlands
[7]These authors contributed equally
[8]Lead Contact
*Correspondence: sumbre@biologie.ens.fr
https://doi.org/10.1016/j.cub.2019.10.020

SUMMARY

Organisms use their sensory systems to acquire information from their environment and integrate this information to produce relevant behaviors. Nevertheless, how sensory information is converted into adequate motor patterns in the brain remains an open question. Here, we addressed this question using two-photon and light-sheet calcium imaging in intact, behaving zebrafish larvae. We monitored neural activity elicited by auditory stimuli while simultaneously recording tail movements. We observed a spatial organization of neural activity according to four different response profiles (frequency tuning curves), suggesting a low-dimensional representation of frequency information, maintained throughout the development of the larvae. Low frequencies (150–450 Hz) were locally processed in the hindbrain and elicited motor behaviors. In contrast, higher frequencies (900–1,000 Hz) rarely induced motor behaviors and were also represented in the midbrain. Finally, we found that the sensorimotor transformations in the zebrafish auditory system are a continuous and gradual process that involves the temporal integration of the sensory response in order to generate a motor behavior.

INTRODUCTION

One of the main goals in neuroscience is to understand how sensory information is represented in the brain and later integrated to produce relevant behaviors.

For several sensory modalities, information about the external world is represented in topographic maps. For instance, two visual stimuli that are close together in space will elicit responses in neighboring neurons (retinotopy). In mammals, birds, and lizards, acoustic frequency discrimination occurs in the cochlea due to the properties of the basilar membrane (for review, see [1]). This spatial map of the frequency spectrum on the cochlea is called tonotopy and is propagated to the CNS through parallel channels and along the auditory hierarchy up to the primary auditory areas [2–5]. Teleosts fish do not have a cochlea, but their inner ear consists of otoliths and a series of hair cells used for both the auditory and the vestibular system capable of detecting the acceleration component of sound [6]. In juveniles and adult fish, the emergence of the Weberian ossicles enables the transmission of sound pressure detected by the swim bladder to the inner earþ. In some species, this structure decreases the detection threshold and increases the sensitivity for high frequencies [7]. However, they are capable of using auditory information to detect prey, avoid predators, or to eavesdrop on animals from the same or different species [8–10]. Therefore, teleost fish should be capable of performing basic frequency discrimination at the level of the sensory hair cells or the nervous system. Indeed, frequency segregation was observed in the goldfish, where rostral saccular afferents respond to high frequencies and caudal afferents are tuned to lower frequencies [11], probably due to mechanical properties of the hair cells.

In teleost fish, the octaval column receives inputs from the primary afferents of the inner ear and projects in turn to the torus semicircularis [12]. These two regions are thought to be homologous to the mammalian cochlear nucleus and the inferior colliculus. In goldfish, crude tonotopy was reported in the torus semicircularis [13]. In zebrafish larva, a coarse spatial frequency organization was hypothesized [14, 15], but it still remains to be demonstrated.

Sensory representations are used to decode and interpret the external sensory world and generate motor patterns to respond to an ever-changing environment. For this purpose, the brain needs to compute sensorimotor transformations to convert the sensory responses into relevant motor behaviors.

Sensorimotor transformations have been studied in the context of chemotaxis and olfaction in the fruit fly [16–19] and in *C. elegans* [20, 21], active sensing and exploration [22–24], and sensorimotor learning in mice [25]. However, these studies

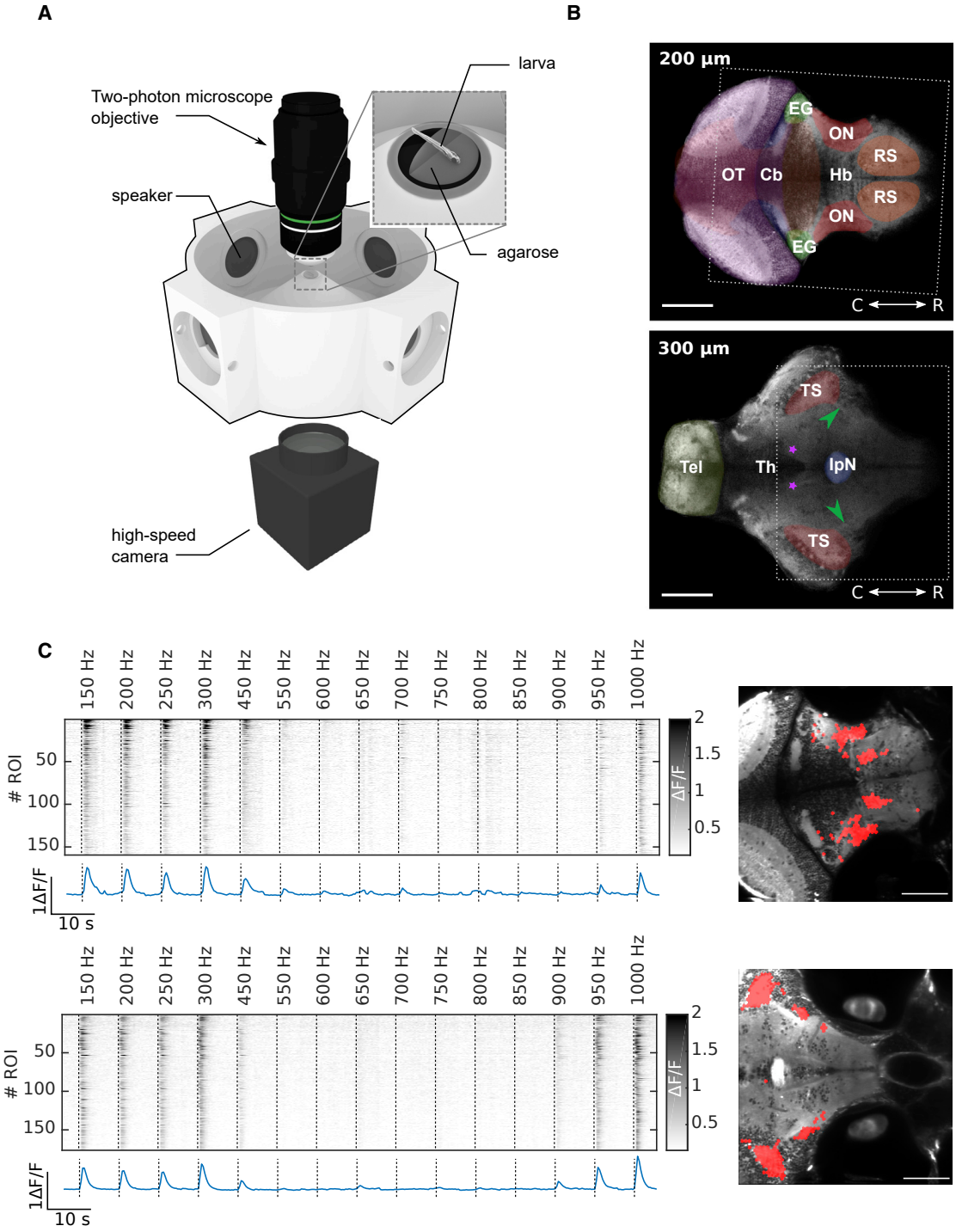

Figure 1. Experimental Setup for Acoustic Stimulation and Simultaneous Recording of Neural Activity and Behavior

(A) Zebrafish larvae were head restrained in a drop of low-melting-point agarose inside a 3D-printed recording chamber. Acoustic stimulations (pure tones at different frequencies) were delivered using waterproof speakers. Spontaneous and evoked neuronal activity was monitored by two-photon calcium imaging while movements of the tail were simultaneously recorded with a high-speed camera.

(B) Two optical sections of a larva's brain pan-neuronally expressing GCaMP5 (Huc:GCaMP5). Cb, cerebellum; EG, eminentia granularis; Hb, hindbrain; IpN, interpeduncular nucleus; ON, octaval nuclei; OT, optic tectum; RS, reticulospinal neurons; Th, thalamus; Tel, telencephalon; TS, torus semicircularis. Green

(legend continued on next page)

involve transformations at the cellular level or by monitoring a relatively small group of neurons. Using the zebrafish larva, which allows simultaneously monitoring sensory and motor circuits and motor behaviors, it is possible to study sensorimotor transformations at the circuit level [26–29]. For example, visuomotor transformations are thought to occur at a brain region in the anterior hindbrain, where several visual responses converge [28].

Despite these advances, the neuronal circuit principles and mechanisms underlying sensorimotor transformations remain elusive.

Here, we took advantage of the auditory system of the zebrafish to study sound representations in the brain and the principles underlying their transformation into motor patterns. For this purpose, we used light-sheet and two-photon calcium imaging in intact, behaving zebrafish larvae expressing the genetically encoded calcium indicator GCaMP5. We monitored neural activity elicited by pure tones (150–1,000 Hz) and broadband noise across large portions of the brain with near single-cell resolution while simultaneously recording motor activity.

We found that auditory-induced neuronal responses were spatially organized according to four main different response profiles. Low frequencies (150–450 Hz) were locally processed in the hindbrain although higher ones (900–1,000 Hz) were transferred to the midbrain, suggesting the existence of two channels for processing auditory information. We propose that the local low-frequency channel is mainly used for the generation of an adequate motor behavior, although the second channel (low and high sound frequencies) may be involved in the modulation of other sensory modalities [30].

To study how sounds are processed and transformed into motor patterns, we classified the neuronal responses according to their correlation with the auditory stimuli and the larva's tail movements. We found that auditory-induced activity propagated in the brain from sensory to motor areas via an intermediate sensorimotor circuit that was active upon the presentation of a stimulus but also during motor behaviors. Sensory networks faithfully encoded auditory information, regardless of the behavioral output, and motor networks did not show sensory-related activity. However, sensorimotor circuits were more active when a stimulus was followed by a motor behavior than in response to stimuli alone. Finally, we observed that the duration of the neuronal response was longer across the whole network when an auditory stimulus was followed by a motor behavior, suggesting that, in the auditory system of the zebrafish larva, sensorimotor transformations involve a temporal integrative process of the neuronal sensory response.

RESULTS

Auditory Responses in the Brain

To study how auditory stimuli are represented, integrated, and transformed into motor patterns in the auditory system of the zebrafish larva, we built a 3D-printed recording chamber with waterproof speakers (Visaton K28 WP) that enables delivering auditory stimuli, monitoring motor behaviors (tail movements), and recording neuronal activity using two-photon microscopy (Figure 1A). Eight days post-fertilization (dpf), transgenic zebrafish larvae expressing pan-neuronally GCaMP5 (*Huc:GCaMP5*) were restrained in low-melting agarose and placed in the center of the recording chamber. Calcium dynamics were monitored using a two-photon microscope from above the chamber. The agarose around the tail was removed, allowing monitoring the deflections of the tail using a high-speed camera (Figure 1A). Under these conditions, we presented to the larvae pure tones with frequencies ranging from 150 Hz to 1,000 Hz (STAR Methods). This range was selected based on previous studies [14, 31–33]. Due to the acoustic properties of the recording chamber and the non-linearities of the speakers, the presented auditory stimuli may have deviated from those generated by the computer. Therefore, we measured for each frequency stimulus the sound pressure and the particle acceleration within the chamber. Both pressure and acceleration were then equalized to obtain almost equal values across the frequency range used in our experiments (Figures S1B and S3B). In addition, to minimize the generation of harmonics, we used an auditory pulse with a ramping onset and a decaying offset (Figure S1A).

Neuronal activity was recorded from different optical planes containing the octaval nuclei (ON) in the hindbrain, which is the first known relay for auditory information in teleost fish; the reticulo-spinal circuit; the cerebellum; the nucleus of the medial longitudinal fascicle (nucMLF); and the torus semicircularis in the midbrain region, homologous to the inferior colliculus in mammals (Figures 1B, 6D, and 6E).

To extract regions of interest (ROIs) responsive to the auditory stimuli, we used a regression approach (STAR Methods) based on stimulus-related regressors, one for each presented frequency. We then used this series of regressors to fit a linear model to the fluorescence time series of each ROI (Figure S2). The goodness of fit was assessed by computing the percentage of variance in the time series explained by the model (R^2_{stim}). Only ROIs with high R^2 were kept for further analysis (STAR Methods). Using this approach, we found auditory-responsive ROIs in the octaval nuclei, in the eminentia granularis, in the torus semicircularis, and in a small nucleus on the lateral side of the lateral longitudinal fascicle (a total of 1,917 ROIs from 13 larvae; STAR Methods; Figure 1C).

Auditory signals convey information through their intensity, their frequency content, and their variations over time. Here, we focused on the sound frequency content, which may carry crucial information about the nature of the sound source and trigger relevant motor behaviors. For example, the largemouth bass (*Micropterus salmoides*) produces ~170 dB at ~200 Hz when feeding on guppies [34], and cyprinid fish are attracted

arrowheads, lateral longitudinal fascicle; purple asterisks, nucleus of the medial longitudinal fascicle. Scale bars, 100 μm. Dotted rectangles correspond to area displayed in (C).

(C) Two examples of sensory activity in the octaval nuclei (top) and torus semicircularis (bottom). Top: raster example for one larva averaged across trials for each stimulus frequency is shown. Bottom: activity averaged across ROIs is shown. Right: topography of ROIs selected as responsive using linear regression corresponding to the rasters on the left is shown. Scale bar, 100 μm. See also Figures S1 and S2.

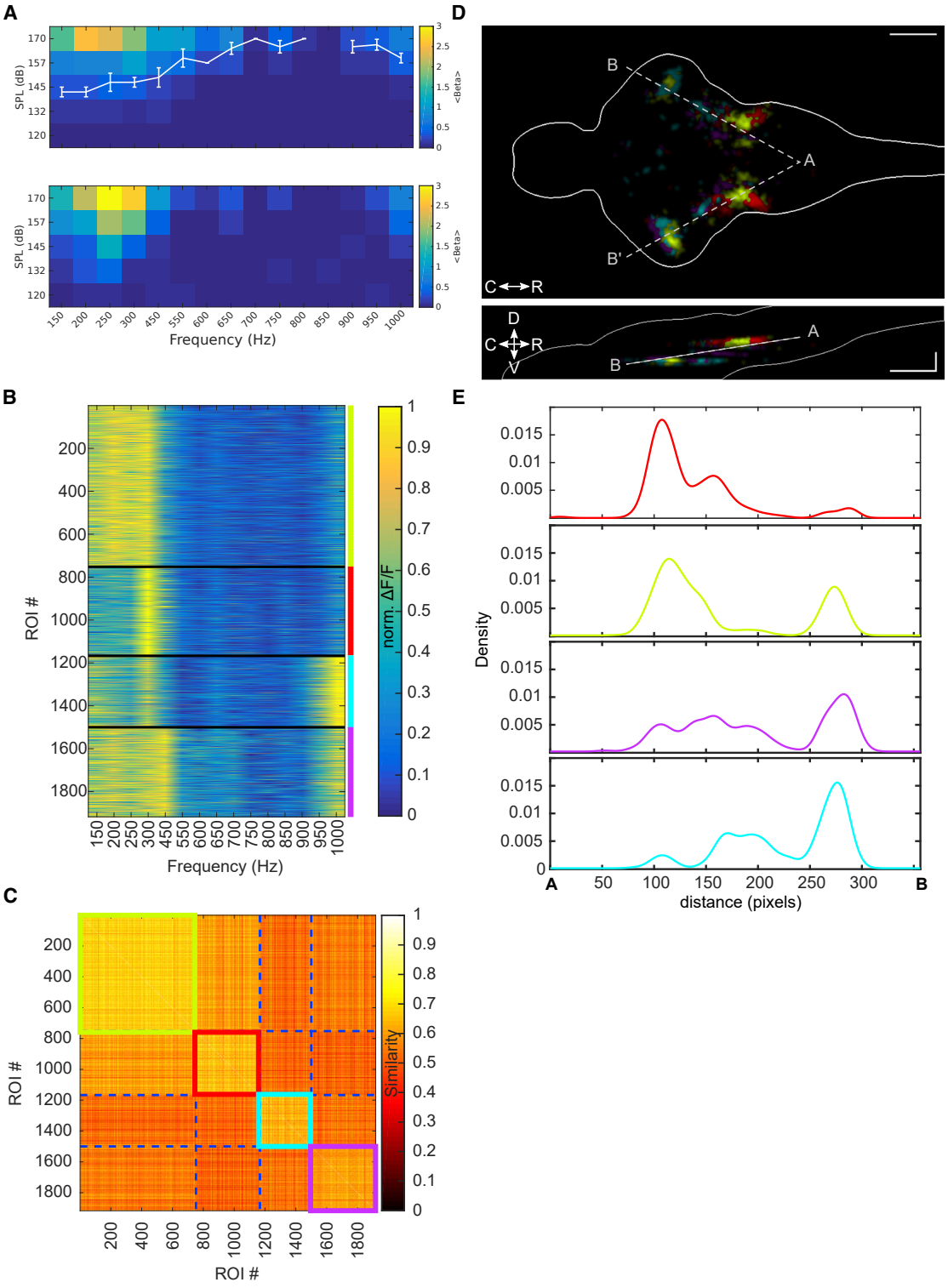

Figure 2. Spatially Distinct Clusters Represent Low- and High-Frequency Information

(A) Top: average audiogram (5 larvae at 8 dpf), measured as the amplitude of the neuronal response fit by a linear regression model, averaged over all ROIs in the brain. White curve: average threshold and SEM are shown. Bottom: single larva example is shown.

(B) Frequency tuning curves for 13 larvae at 8 dpf, grouped in 4 clusters using k-means clustering algorithm with Euclidean distance on normalized ΔF/F values. Different larvae were imaged at different optical sections. Clusters 1–4 are represented in red, green, cyan, and magenta.

(legend continued on next page)

by the emitted sound of shuffling rocks, as they probably learned to associate it with new food sources previously hidden under the rocks [35].

Frequency Representation in the Brain

To study how auditory stimuli of different frequencies are represented in the brain of the larva, we first calculated the larvae audiograms (STAR Methods). The audiograms displayed two main frequency bands: a low-frequency band from 150 to 450 Hz and a high-frequency band from 950 to 1,000 Hz. The average amplitude threshold was 138 ± 3.05 dB for the low-band frequency (Figure 2A). We then computed the frequency tuning curves of each responsive ROI across the auditory circuits of the larva. To study the tuning curves, we used auditory stimuli with an amplitude of 155 dB (an amplitude above the detectable threshold, capable of triggering motor behaviors and inducing strong, but not saturated, neuronal circuit responses; Figure 2A). Using k-means, we found that, among all ROIs, the frequency tuning curves could be classified in four main clusters that best represented the diversity of the obtained tuning curves (Figures 2B and 2C; STAR Methods). Among these clusters, two contained a frequency band ranging from 150 to 450 Hz and two others had an additional high-frequency band at 950 and 1,000 Hz. The use of 4 clusters was supported by two clustering validation methods (Silhouette and Calinski-Harabasz index; Figure S5A) and two alternative and independent clustering approaches (principal-component analysis and hierarchical clustering; Figures S5B and S5C). The stimulus-induced neuronal responses were principally auditory because ablation of the lateral line was relatively similar to those observed under normal conditions (especially in the low-frequency band; Figure S4).

To study the spatial organization of these four clusters across the different brain regions, we registered the brains' anatomy of each recorded larvae (8 dpf; n = 13) to a common reference space using an affine transformation (STAR Methods). We subsequently computed a normalized 3D density map for each cluster and projected the maximum density along the dorsoventral and mediolateral axis (Figure 2D; STAR Methods). We observed that the different clusters were organized along a rostrocaudal axis (dashed line in Figure 2E), encompassing both the octaval nucleus and the torus semicircularis. The density histogram along this axis for each cluster (STAR Methods) showed that clusters with only the low-frequency band (150 and 450 Hz) were more represented in the caudal part of the axis (the octaval nuclei), although the clusters containing the high-frequency band (950 and 1,000 Hz) were more represented in the rostral part of the axis (the torus semicircularis; Figure 2E).

This finding suggests that 8-dpf zebrafish larvae may process two relevant frequency bands via two different pathways. Low frequencies are locally processed in the hindbrain although low and high bands are transferred to the midbrain.

Development of the Auditory Responses

To find out whether the low dimensionality in the response profiles was the consequence of an immature nervous system and to study whether it changes as the larva develops, we reproduced these analyses at different developmental stages (from 7 to 21 dpf). We first observed that there were no major changes in terms of the audiograms (Figures 3A and S3A), and their detection thresholds were not significantly different across the different developmental stages (average 7 dpf, 141.8 ± 3.11; average 8 dpf, 137.5 ± 3.0; average 9 dpf, 144.9 ± 2.7; average 14 dpf, 136.6 ± 4.1; average 21 dpf, 142.5 ± 4.7; $p = 0.44$; ANOVA; Figures 3A, S3A, and S3B). Moreover, the 4 types of tuning curves across the different developmental stages were also very similar (Figure 4; average correlation: 0.85 ± 0.14; Figure 4C). The only exceptions were two clusters at 9 dpf, with tuning curves showing the emergence of a new mid-range frequency band at ~650 Hz (Figures 4A and 4B). This mid-range band was still observed at 14 dpf but fully disappeared at 21 dpf.

Auditory-Induced Motor Behaviors

To further understand the biological relevance of these two auditory processing channels, we presented to the zebrafish larvae auditory stimuli of different frequencies while monitoring their motor behavior (tail deflections) using a high-speed camera (STAR Methods).

Previous studies showed that strong acoustic or vibrational stimuli can trigger startle responses of two different types: short-latency C-start (SLC) (~5 ms) and long-latency C-start (LLC) (~28 ms) [36, 37]. SLC responses are triggered by strong auditory stimuli and are Mauthner cell dependent. In contrast, LLCs are elicited by weaker auditory stimuli and are otolith dependent [37].

To study the type of tail movements elicited by the auditory stimuli, we computed the latency from the stimulus to the onset of the induced motor behavior. For this purpose, we used two types of broad-band noise auditory stimuli: high amplitude (170 dB) and low amplitude (155 dB; the amplitude used in this study). We observed that high-amplitude stimuli generated movements with a probability of 0.92 and latencies displaying a bimodal distribution. The short latency population had an average latency of 11.82 ± 2.51 ms, most probably corresponding to SLCs. The longer latency population had an average latency of 60.62 ± 13.33 ms, resembling LLCs. In contrast, lower amplitude stimuli (155 dB) induced tail motor behaviors with a probability of 0.4 and more sparsely distributed latencies with an average of 150.75 ± 65.73 ms. The latter were significantly longer than those of LLCs ($p = 5 \times 10^{-14}$; rank-sum; Figure 5A). We named this type of behavior as long-latency tail movements (LLTMs), because they resembled symmetrical or asymmetrical scoots rather than C-start-like tail movements (Figure 5A) [38]. These results suggest that the amplitude of the auditory stimuli used throughout the experiments induces tail motor behaviors mediated by a neuronal circuit integration process rather than a rapid reflex response.

(C) Similarity matrix based on the Euclidean distance for the clusters in (B).

(D) Spatial distribution of the 4 clusters presented in (B). All 13 larvae were aligned on a reference stack using affine transformation. Top: maximum density projection across the Z axis is shown. Bottom: maximum density projection across the y axis is shown. Scale bar, 100 μm.

(E) Spatial density of ROIs for each cluster along the gray dashed AB axis in (D), averaged across both hemispheres. See also Figures S4 and S5.

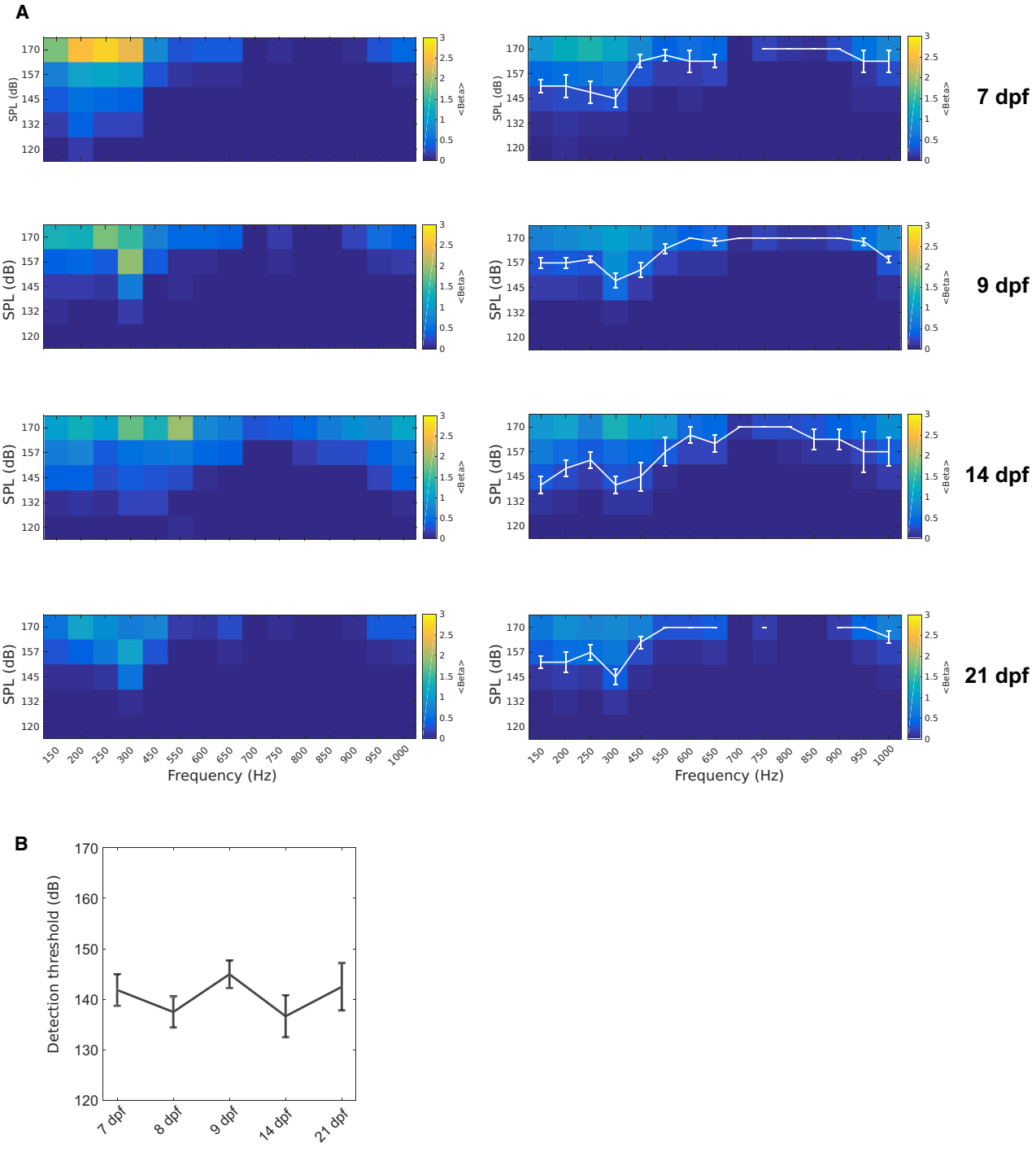

Figure 3. Audiograms at Different Development Stages

(A) Right: average audiogram at 7 dpf (4 larvae), 9 dpf (7 larvae), 14 dpf (3 larvae), and 21 dpf (5 larvae) measured as the amplitude of the neuronal response fit by a linear regression model, averaged over all ROIs in the brain. White curve: average threshold and SEM are shown. Left: single larva example is shown.

(B) Detection threshold, the lowest amplitude at which a neuronal response was detected, averaged across larvae during the different developmental stages (mean ± SEM). Means at different ages were not significantly different ($p = 0.4381$; one-way ANOVA). See also Figure S3.

To infer the significance of the correlation between auditory stimulation and LLTMs, we compared the datasets against a set of shuffled motor events. In this null model, the inter-event distribution of tail bouts was preserved but the onset of tail bouts was randomized (STAR Methods). Using this null model, we defined a threshold corresponding to the 95th percentile of its

Please cite this article in press as: Privat et al., Sensorimotor Transformations in the Zebrafish Auditory System, Current Biology (2019), https://doi.org/10.1016/j.cub.2019.10.020

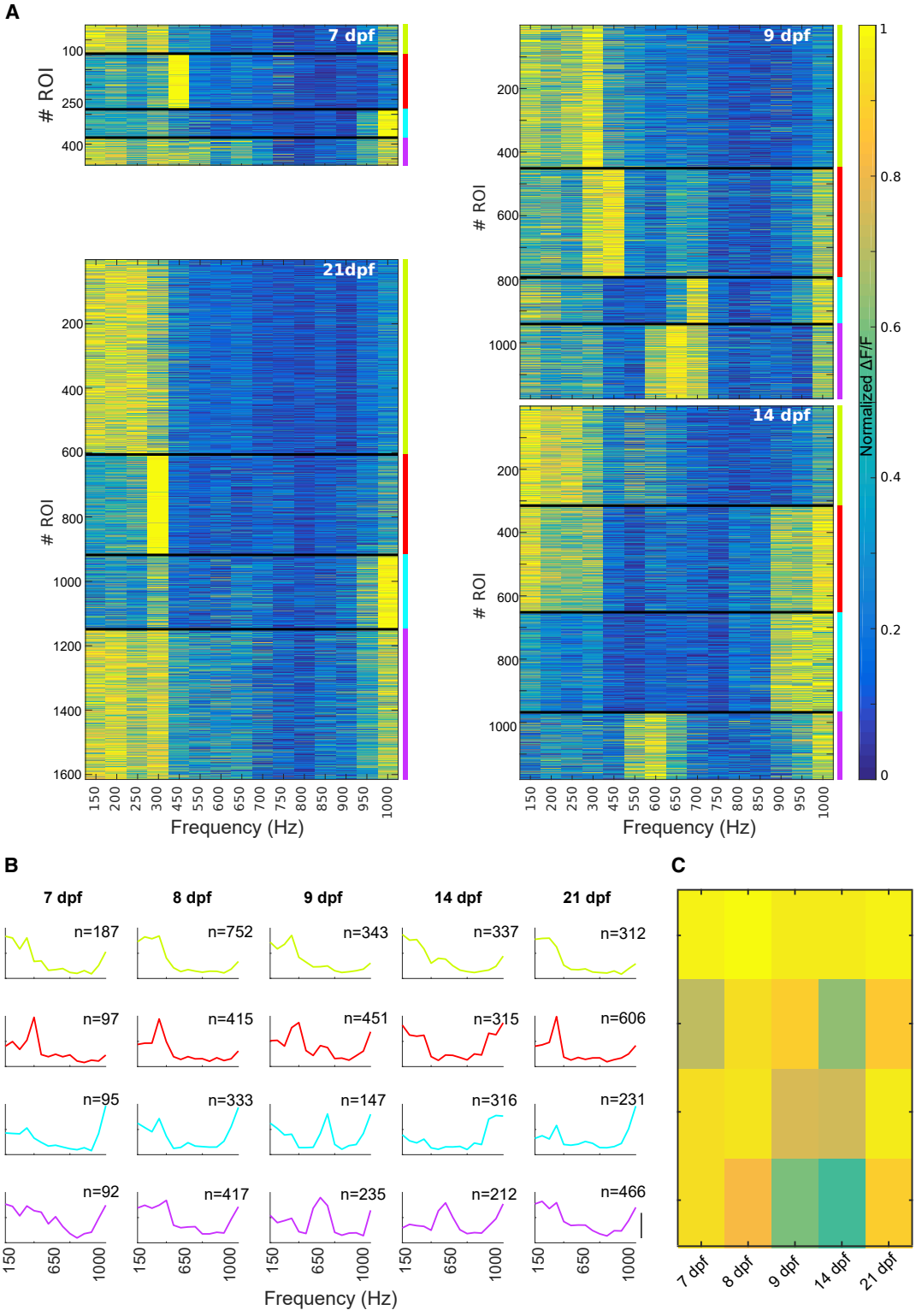

(legend on next page)

distribution that enabled us to determine whether the auditory stimuli significantly induced motor behaviors. We observed that auditory stimuli of frequencies ranging from 150 Hz to 450 Hz were able to significantly elicit tail movements ($p < 10^{-4}$ for 150–400 Hz; $p = 0.014$ for 450 Hz after Bonferroni correction). Frequencies of 150 and 300 Hz were capable of inducing a motor behavior with a probability above 0.25. Auditory stimuli of 950 Hz and 1,000 Hz also significantly induced motor behaviors ($p = 0.014$ for 950 Hz; $p = 0.041$ for 1,000 Hz after Bonferroni correction) but with a much lower probability (0.1). Furthermore, the amplitude of the auditory-induced tail movements displayed a bimodal distribution, probably reflecting two different types of movements. When we compared the distributions of tail movement amplitudes elicited by low- or high-frequency band stimuli, we observed that both distributions were not significantly different ($p = 0.73$; rank-sum; Figure 5C).

Sensorimotor Transformation

To characterize the neuronal processes mediating the auditory sensorimotor transformations, we described each ROI according to a sensorimotor ratio. For this purpose, we first computed (1) the level of correlation of the Ca^{2+} transients of each ROI with the presentation of the auditory stimulus, which we defined as the percentage of variance of the stimulus responses explained by the linear model (R^2_{stim}; Figure S2A; STAR Methods) and (2) the level of correlation of the Ca^{2+} transients of each ROI with the generation of a tail movement. For the latter, we also used a regression-based approach. Because ROIs correlated with behavior could be active before or after the onset of a movement, we used a series of regressors (one for each time frame) that spanned 3.5 s around the onset of each tail movement. The goodness of fit (R^2_{mvt}) was computed for the whole series of regressors (Figure S2D; STAR Methods).

We then defined the sensorimotor ratio (SMR) as the difference between the percentage of variance explained by the stimulus and the behavior regressors divided by the total fraction of the explained variance: $SMR = (R^2_{mvt} - R^2_{stim})/(R^2_{mvt} + R^2_{stim})$. This ratio ranges from −1 (purely sensory) to +1 (purely behavior related; Figure S6).

Using this approach, we identified (1) ROIs whose variance was mostly explained by the sensory inputs, (2) a group of ROIs whose variance was mostly explained by the occurrence of a motor behavior, and (3) a group of ROIs whose variance was explained by both stimuli and behavior (2,915 ROIs from 10 larvae; Figures 5D and 6A, left; STAR Methods). The latter may represent candidate ROIs involved in the sensorimotor transformations (Figures 6A and 6B; Video S1). This approach revealed that ROIs with a large positive sensorimotor ratio (motor ROIs) were also active during self-generated (spontaneous) behaviors (Figure 5D). This suggests that the same motor circuit rather than an auditory dedicated one is active during self-generated and auditory-evoked motor behaviors (Figure 5D). This was further confirmed at the whole population level (n = 27 larvae), where we found similar levels of activity during self-generated and auditory-induced tail movements for ROIs with large positive sensorimotor ratios (motor ROIs; Figures S7A–S7C).

To visualize the topography of the ROIs according to their sensorimotor ratio, we aligned the positions of each ROI to a reference brain (Figure 6A, right panel; STAR Methods), which was then aligned to the z-brain atlas [39]. The latter enabled the identification of anatomical regions (Figures 6D and 6E) and the neuron types (glutamatergic, GABAergic, and glycinergic; Video S2). The average sensorimotor map showed auditory sensory areas in (1) the octaval nuclei (ON), which contained anatomically segregated glutamatergic, GABAergic, and glycinergic neurons; (2) parts of the cerebellum containing two segregated groups of glutamatergic and GABAergic neurons; and (3) the torus semicircularis (mostly GABAergic). The motor ROIs were mainly observed in (4) the reticulo-spinal circuit (overlapping glutamatergic, GABAergic, and glycinergic neuronal populations), (5) the cerebellum (anatomically segregated glutamatergic and GABAergic neurons), and (6) the rostral part of the nucleus of the medial longitudinal fascicle (nucMLF), which was mainly glutamatergic. Sensorimotor regions were localized at the boundaries of the sensory areas at the intersection with the motor regions. In addition, sensorimotor circuits were also observed toward the caudal part of the nucMLF (Figures 6A, 6D, and 6E; Video S2).

To learn about the mechanisms underlying the sensorimotor transformations, we grouped our ROIs from 10 larvae into bins based on the value of their sensorimotor ratio. We pooled together results from stimulus frequencies that robustly elicited behavioral responses (150–450 Hz). We took advantage of the variability in the behavioral outcome of the auditory stimulations and averaged the activity of ROIs in each sensorimotor bin across trials for which the auditory stimuli failed to induce a behavioral response (black curve, top row, Figures 6B and 6C) and across trials where auditory stimuli elicited a tail bout (orange curve, top and bottom row, Figures 6B and 6C). We also averaged the neural activity around the onset of spontaneous movements (purple curve, bottom row, Figures 6B and 6C). The average over trials was once time locked to the onset of the stimuli (Figures 6B and 6C, top row) and once to the onset of the tail movements (Figures 6B and 6C, bottom row). We observed that ROIs with a low sensorimotor ratio (sensory ROIs) faithfully represented sensory information independently of the behavioral outcome (Figures 6B and 6C, top left). Reciprocally, ROIs with a high sensorimotor ratio (motor ROIs) represented motor-related information with similar levels of activity

Figure 4. Frequency Tuning Curves at Different Developmental Stages

(A) Frequency tuning curves grouped in 4 clusters using k-means clustering algorithm at 7 dpf (6 larvae), 9 dpf (11 larvae), 14 dpf (3 larvae), and 21 dpf (5 larvae).

(B) Average normalized tuning curves across ROIs grouped in 4 clusters throughout the larva's development, from 7 to 21 dpf. Similar tuning curves were assigned to the same cluster across developmental stages by maximizing the correlation between the tuning curves and the average tuning across ages. Scale bar, 0.5 ΔF/F. The colors represent the clusters indicated in (A). Top right corner: the number of ROIs per cluster is shown.

(C) Correlation matrix used to order the clusters in (B). We correlated the tuning curve for each cluster at each developmental stage with the average tuning curve across ages. All possible permutations of cluster assignments were tested. The matrix shows the solution that maximized the average correlation. Average correlation: 0.85 ± 0.14 (SD).

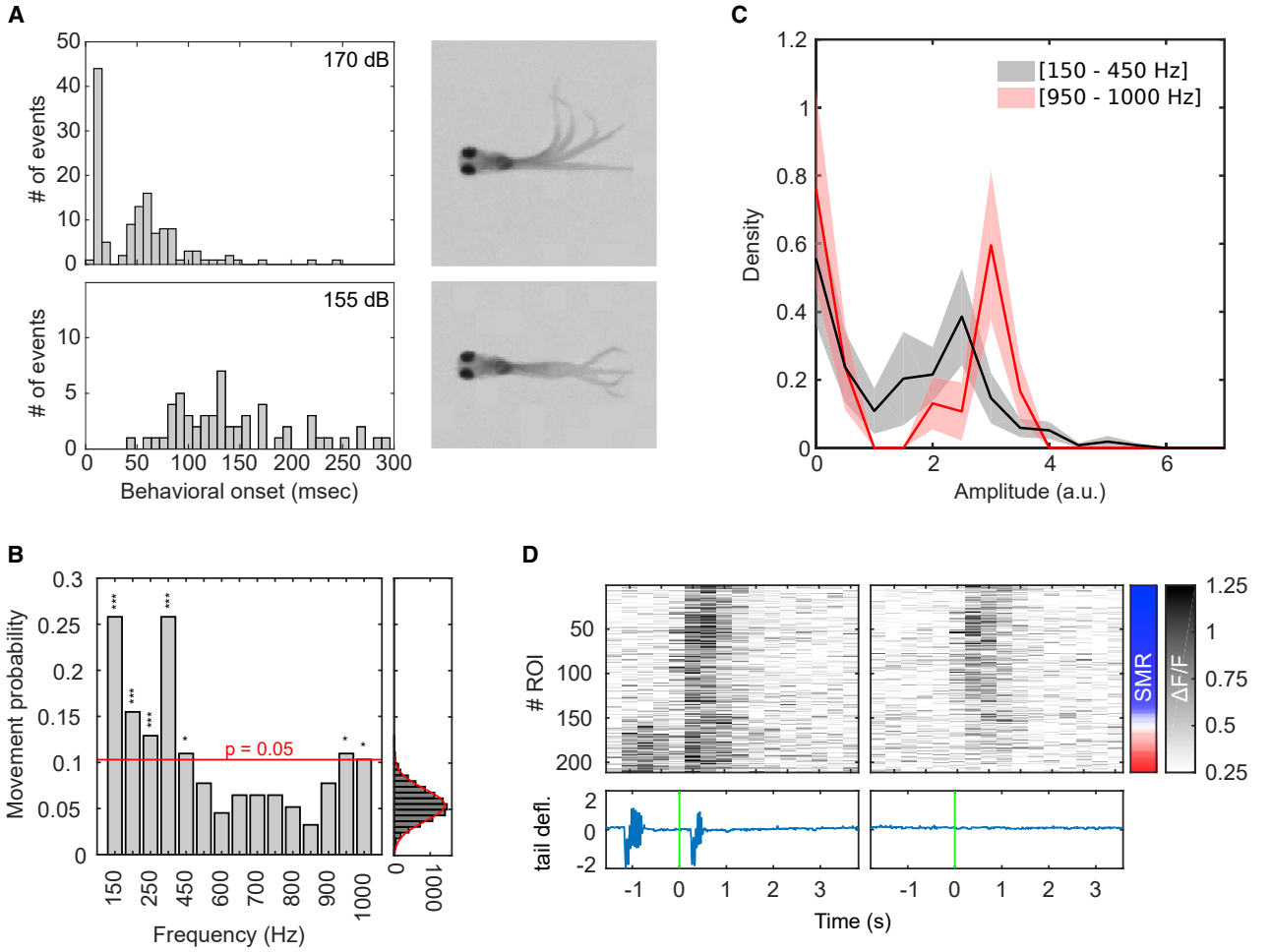

Figure 5. Auditory-Induced Tail Motor Behaviors

(A) Delay histogram between the onset of auditory stimulation and the onset of tail movements (7 larvae) Top: auditory stimulation using 170 dB re 1 μPa stimuli resulted in a bimodal distribution probably representing short latency C-starts and long-latency C-starts. Bottom: auditory stimulation using 155 dB re 1 μPa stimuli resulted in a distribution of longer and more variable latencies.

(B) Probability of having at least one tail bout in a 500-ms time window after stimulus onset for each frequency. A null model was created by generating data following the same inter-bouts interval distribution as the experimental data (left). p values were computed using the null model distribution and subsequently adjusted using Bonferroni correction. Red dashed line, significance threshold for $\alpha = 0.05$ after Bonferroni correction. n = 10 larvae.

(C) Average density distribution (mean ± SEM) of bout amplitudes (10 larvae), elicited by low-frequency stimuli (150 Hz and 450 Hz; 134 bouts) in black and high-frequency stimuli (950 Hz and 1,000 Hz; 30 bouts) in red. The amplitude of a tail bout was defined as the maximum curvature during the bout. The medians of the two distributions were not significantly different (p = 0.73; two-sided rank-sum test).

(D) Top: single trial raster on a single larva. ROIs are ordered by their sensorimotor ratio, computed as $(R^2_{mvt} - R^2_{stim})/(R^2_{mvt} + R^2_{stim})$. The sensorimotor ratio ranges from −1 (sensory ROIs, in blue) to +1 (behavior-related ROIs, in red). Bottom: tail deflection is shown, green bar, auditory stimulus onset.

independently of the sensory stimuli (Figures 6B and 6C, bottom right). In contrast, ROIs with a sensorimotor ratio close to zero (sensorimotor ROIs) showed levels of activity that were significantly different when a stimulus induced a motor behavior than when the stimulus failed to induce one (Figures 6B and 6C).

To further study of the temporal dynamics of the auditory sensorimotor transformations, we used light-sheet microscopy using high-acquisition rates (20 Hz). We recorded the neural activity and the motor behavior of 27 larvae in response to a broadband auditory stimulus (250–1,000 Hz; Figure 7A; Video S2; STAR Methods). Using this approach, we calculated the onset of the calcium transients with respect to the onset of the auditory stimuli (STAR Methods; Figure 7A). We observed that neuronal responses to auditory stimuli that failed to trigger a motor behavior were limited to the sensory ROIs (Figure 7B). In contrast, sensory stimuli that successfully triggered a motor behavior induced neuronal responses among ROIs with a full spectrum of sensorimotor ratios (Figure 7B). This analysis and the spatial distribution of the onsets of the different ROIs (Figure 7D) suggest that information flows from sensory to motor-related areas via the sensorimotor ROIs. The latter is also supported by the positive correlation between the averaged onset of the ROIs against the sensorimotor ratio (Figure 7C).

To investigate the mechanisms mediating the sensorimotor transformations in the zebrafish auditory system, we calculated (1) the number of activated ROIs (ROIs whose activity was above

Please cite this article in press as: Privat et al., Sensorimotor Transformations in the Zebrafish Auditory System, Current Biology (2019), https://doi.org/10.1016/j.cub.2019.10.020

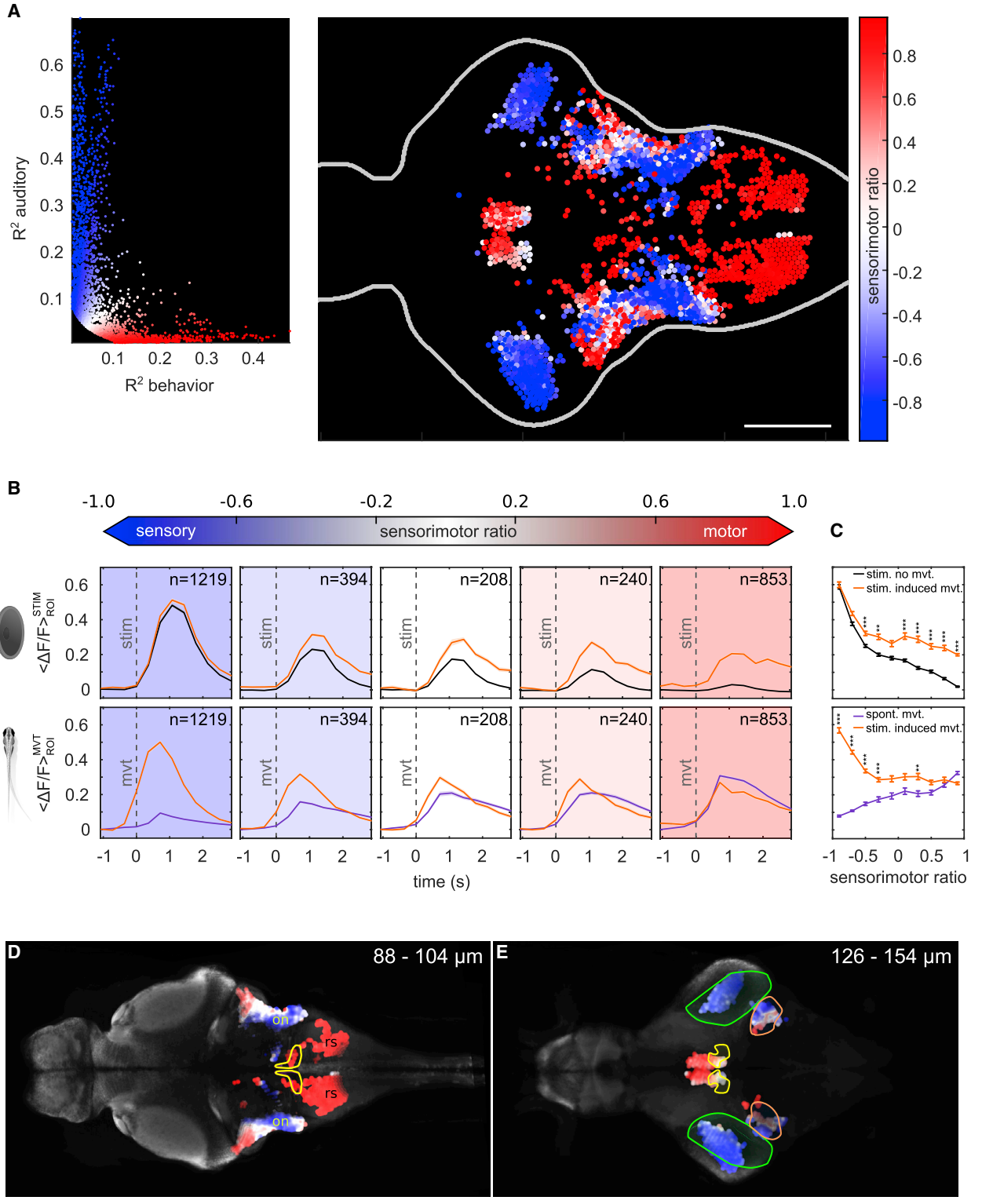

Figure 6. Sensorimotor Properties of the Auditory Neural Circuit

(A) Left: distribution of ROIs R^2 values for movement and behavior with the corresponding sensorimotor ratio value. Right: topography of ROI's sensorimotor ratio for 10 larvae at 8 dpf is shown. Scale bar, 100 µm.

(B) Top: average ΔF/F over ROIs after an auditory stimulation around auditory stimulus onset (t = 0 s) for ROIs grouped in 5 bins according to their sensorimotor ratio. Stimulus frequencies from 150 to 450 Hz were pooled together. Orange curve, stimulus followed by a tail movement within a 500-ms time window after

(legend continued on next page)

a threshold of 2 SDs from the average activity, 500 ms before stimulation), (2) the ΔF/F, and (3) the duration of the auditory-induced Ca^{2+} transients for the ROIs of different sensorimotor ratios, when the stimulus induced a motor behavior or when it failed to do so (Figure 7E). We observed that the number of recruited ROIs with low sensorimotor ratios (sensory ROIs) when stimuli induced a motor behavior was not significantly different from the number of recruited ROIs than for trials in which the stimuli failed to do so (Figure 7E, top; p = 0.1936, 0.0323, 0.0059, 0.0024, and 0.0003; one-tailed paired Wilcoxon signed-rank test after Bonferroni correction). Along the same lines, the ΔF/F of the induced Ca^{2+} transients in sensory ROIs when the stimuli succeeded in inducing a motor behavior was not significantly different from the ΔF/F than for trials in which stimuli failed to do so (Figure 7E, middle). However, for the sensorimotor ROIs, the amplitude of the induced Ca^{2+} events was significantly higher when a stimulus induced a tail movement than when it did not (Figure 7E, middle; p = 1, 0.0096, 0.0011, 0.0015, and 0.0391; one-tailed paired Wilcoxon signed-rank test after Bonferroni correction). In contrast, the duration of the induced Ca^{2+} transients was significantly larger for the sensory and sensorimotor ROIs when a tail movement followed the auditory stimulation (Figure 7E, bottom; p = 0.0162, 0.0131, 0.0052, 0.0037, and 0.7812; one-tailed paired Wilcoxon signed-rank test after Bonferroni correction). These results show that the duration of the auditory-induced response is determinant for the sensorimotor transformations. In addition, we observed that ongoing spontaneous activity before the onset of the auditory stimulation failed to predict the outcome of the sensory response (Figure S7D). Thus, we suggest that the increase in duration of the auditory responses does not result from its integration with the current state of the network, but it rather represents the integration of the sensory response in order to activate the sensorimotor and motor circuits.

DISCUSSION

The neuronal representation of sensory information has been exhaustively studied. However, how this information is then integrated and transformed into motor patterns still remains elusive. In this study, we simultaneously recorded auditory-induced neuronal responses of both sensory and motor circuits while monitoring tail motor movements. We found auditory-induced responses to frequencies ranging from 150 to 1,000 Hz in the octaval nuclei, the torus semicircularis, the eminentia granularis, and the nucleus of the lateral longitudinal fascicle [40].

The audiograms of zebrafish larva displayed sensitivities for two main frequency bands (150–450 Hz and 950–1,000 Hz), as observed in [11].

In contrast to other studies that suggest a tonotopic organization in fish [13, 14, 41], here, we only found four different frequency response profiles represented in the brain. These four different types of tuning curves involved low- and high-frequency bands. These two bands may directly emerge from the mechanical properties of the two different populations of the saccular hair cells (rostral saccular afferents respond to high frequencies although caudal afferents are tuned to lower frequencies) [11], probably due to mechanical properties of the hair cells [42].This low-dimensional auditory representation of sound frequency in the zebrafish larvae is different from the high-dimensional processing in cochlear animals where neurons with sharp and broader tuning curves are observed for a large range of frequencies across several auditory brain regions [11], along with many other neurons with more complex response profiles: sound onsets and offsets of particular amplitude; amplitude modulation; frequency modulation; or harmonicity [43], for which more complex methods are necessary for their response description (e.g., spectro-temporal receptive fields) [44].

Two of these profiles were sensitive to low-frequency bands, which were processed locally in the hindbrain. The two others were bimodal, containing a low-frequency band and an additional high-frequency one. They were both represented in the hindbrain and the midbrain of the larva. This finding suggests that young larvae may process low and high frequencies differently via two different channels with different biological or functional relevance. Low frequencies are locally processed in the hindbrain to generate motor behaviors (e.g., the largemouth predator generates ~200 Hz when attacking prey) [34], although low and high bands are transferred to the midbrain. It is possible that the latter channel serves for modulation of the tectal visual response because previous studies showed that simultaneous presentation of visual and auditory stimuli to zebrafish larva reduced the visual response in the optic tectum [30]. This hypothesis is supported by the fact that tail movements were induced mainly by low-frequency sounds and that the auditory responses in the torus semicircularis were colocalized with mainly GABAergic neurons.

Both audiograms and tuning curves did not differ much between 7 and 21 dpf. The audiograms and the auditory thresholds at the different developmental stages were relatively similar. The 4 types of frequency tuning curves were also observed at all developmental larval stages. Therefore, we suggest that the low-dimensional encoding in zebrafish larvae emerges early in development and remains stable thereafter. However, a mid-range-frequency band transiently emerged at 9 dpf, disappearing around 21 dpf. Whether this transient frequency band

stimulus onset. Black curve, stimulus not followed by a tail movement. Bottom: average ΔF/F across ROIs when the fish moved is shown (t = 0 s: movement onset). Orange curve, tail movement preceded by an auditory stimulation. Purple curve, self-generated movement. In the bottom panels, the delay between the orange curve (stimulus-induced movement) and the purple curve (self-generated movement) corresponds to sensory processing, because the stimulus occurs before the movements.

(C) Average peak ΔF/F value (mean ± SEM) across ROIs around auditory stimulus onset (top panel) or tail movement onset (bottom panel). ROIs were binned into 10 groups based on their sensorimotor ratio value. Bins were compared using the two-tailed Wilcoxon rank sum test, and p values were subsequently adjusted using Bonferroni correction.

(D) The topography of the sensorimotor ratio (blue, sensory; white, sensorimotor; red, motor), superimposed to the Elavl3-GCaMP5 line in the z-brain atlas. Yellow, facial motor and octavolateralis efferent; on, octaval nuclei; rs, reticulospinal circuits. Top right corner: depth of the imaged plane is shown.

(E) The topography of the sensorimotor ratio over the Elavl3-GCaMP5 line in the z-brain atlas. Green, torus semicircularis; yellow, nucleus of the medial longitudinal fascicle; orange, cerebellar vglut2-enriched area. Top right corner: depth of the imaged plane is shown. See also Figure S6 and Videos S1 and S2.

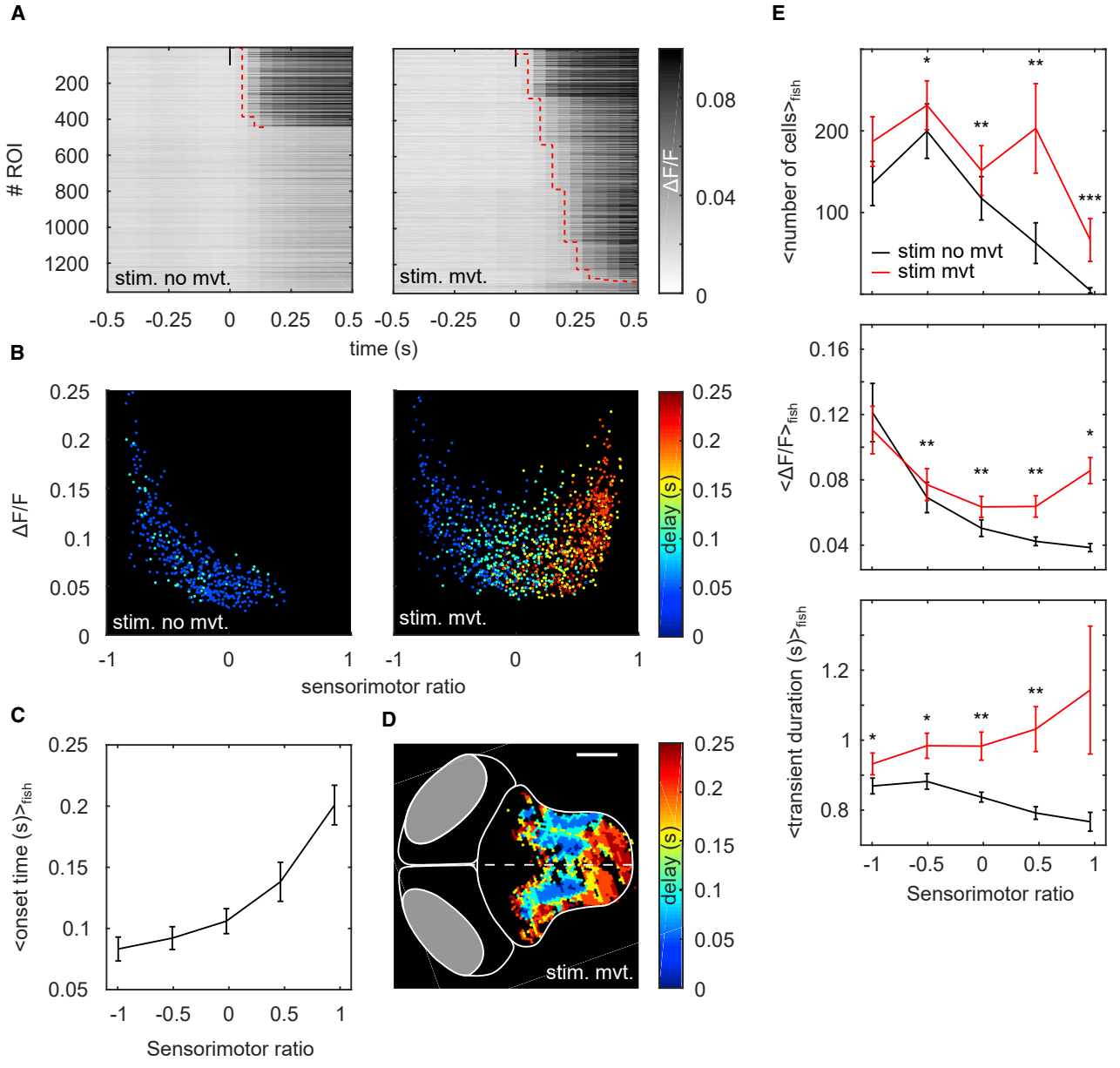

Figure 7. Increased Network Activity and Duration of Calcium Transients Mediates Sensorimotor Transformation

(A) Example rasters of a single larva averaged over trials for which auditory stimuli induced (stim. mvt.) or did not induce a tail movement (stim. no mvt.). ROIs are sorted by the onset time of their calcium transients. Red dotted line, transient onset. Transient onset was estimated only for ROIs whose activity after stimulation was 2 SDs above their mean activity before stimulation (activity baseline).

(B) Example of ΔF/F as a function of sensorimotor ratio; colormap, onset time of the calcium transients.

(C) Onset time (mean ± SEM) as a function of sensorimotor ratio for 27 larvae. ROIs were binned into 5 groups based on their sensorimotor ratio.

(D) Topography of the onset time for the same larva as in (A) and (B). Scale bar, 100 μm.

(E) Top: number of ROIs above the 3 SD threshold for each sensorimotor ratio bin (mean ± SEM). Middle: peak ΔF/F for each bin is shown (mean ± SEM). Bottom: transient duration computed as the full width at half maximum of the calcium transients for each bin is shown (mean ± SEM). Red line, auditory stimulation followed by a tail movement in a 500-ms time window after stimulation onset. Black line, auditory stimulation not followed by a tail movement. Results were pooled across 27 larvae. Bins were compared using the one-tailed Wilcoxon paired signed rank test, and p values were subsequently adjusted using Bonferroni correction. See also Figure S7.

represents a relevant developmental process remains to be determined.

The ability to simultaneously monitor neuronal activity and tail motor behavior allowed us to study the processes underlying sensorimotor transformations in the hindbrain of the larva. Using a linear regression approach to classify ROIs according to a sensorimotor ratio, we found a topographic and functional continuum of the sensorimotor representation, suggesting a gradual

transformation of sensory information into motor patterns. This continuous gradual transformation of the sensory information into motor patterns and the increase in the duration of the auditory-induced calcium transients when a stimulus induced a motor behavior suggest that the sensorimotor transformations do not reflect a gating mechanism (e.g., controlling the passage of neuronal activity from the sensory to the motor circuits by an independent modulatory circuit) [45] but rather the capacity of the circuit to integrate the auditory-induced neuronal response. This hypothesis is also supported by the long and variable latency of the induced tail movements. This increase in the duration of the calcium transients could be driven through recurrent connectivity to sufficiently amplify neural activity and reach the threshold required to activate the motor circuits.

This mechanism may help integrate auditory information to obtain reliable information about the detected stimulus to generate a relevant behavioral response.

STAR★METHODS

Detailed methods are provided in the online version of this paper and include the following:

- KEY RESOURCES TABLE
- LEAD CONTACT AND MATERIALS AVAILABILITY
- EXPERIMENTAL MODEL AND SUBJECT DETAILS
- METHOD DETAILS
  - Auditory stimulation
  - Calcium imaging
  - Data analysis
- QUANTIFICATION AND STATISTICAL ANALYSIS
- DATA AND CODE AVAILABILITY

SUPPLEMENTAL INFORMATION

Supplemental Information can be found online at https://doi.org/10.1016/j.cub.2019.10.020.

ACKNOWLEDGMENTS

We thank V. Candat and F. Bouallague for help with zebrafish, A. Kulkarni for discussions on data analysis, and O. Lahrach and Anahid Jeant-Maloumian for preliminary experiments. M.P. was supported by the Fondation pour la Recherche Medicale (FRM: FDT201904008327) and the ENS Lyon. A.J. was supported by the Fondation pour la Recherche Medicale (FRM: FDT20140930915) and the ENS Cachan. A.D. was supported by the ENS Cachan, and G.S. was supported by ERC StG 243106, ERC CoG 726280, ANR-10-LABX-54 MEMO LIFE, and ANR-11-IDEX-0001-02 PSL Research University. D.S. was supported by the Ecole Normale Supérieure invited professor program and NIH R15EY027112.

AUTHOR CONTRIBUTIONS

G.S. and M.P. designed and conducted the experiments. S.A.R., T.P., A.D., N.E., and D.S. performed preliminary experiments. M.P. analyzed the data. M.P., D.S., and G.S. wrote the manuscript. S.A.R., J.B.-W., A.J., and T.P. provided help for the data analysis and experimental design.

DECLARATION OF INTERESTS

The authors declare no competing interests.

Received: June 19, 2019
Revised: September 27, 2019
Accepted: October 15, 2019
Published: November 7, 2019

REFERENCES

1. Mann, Z.F., and Kelley, M.W. (2011). Development of tonotopy in the auditory periphery. Hear. Res. *276*, 2–15.
2. Zaretsky, M.D., and Konishi, M. (1976). Tonotopic organization in the avian telencephalon. Brain Res. *111*, 167–171.
3. Romani, G.L., Williamson, S.J., and Kaufman, L. (1982). Tonotopic organization of the human auditory cortex. Science *216*, 1339–1340.
4. Merzenich, M.M., and Schreiner, C.E. (1992). Mammalian auditory cortex—some comparative observations. In The Evolutionary Biology of Hearing, D.B. Webster, A.N. Popper, and R.R. Fay, eds. (Springer New York), pp. 673–688.
5. Carr, C.E. (1992). Evolution of the central auditory system in reptiles and birds. In The Evolutionary Biology of Hearing, D.B. Webster, A.N. Popper, and R.R. Fay, eds. (Springer New York), pp. 511–543.
6. Inoue, M., Tanimoto, M., and Oda, Y. (2013). The role of ear stone size in hair cell acoustic sensory transduction. Sci. Rep. *3*, 2114.
7. Lechner, W., Heiss, E., Schwaha, T., Glösmann, M., and Ladich, F. (2011). Ontogenetic development of weberian ossicles and hearing abilities in the African bullhead catfish. PLoS ONE *6*, e18511.
8. Higgs, D.M., Souza, M.J., Wilkins, H.R., Presson, J.C., and Popper, A.N. (2002). Age- and size-related changes in the inner ear and hearing ability of the adult zebrafish (Danio rerio). J. Assoc. Res. Otolaryngol. *3*, 174–184.
9. Popper, A.N., and Fay, R.R. (2011). Rethinking sound detection by fishes. Hear. Res. *273*, 25–36.
10. Mohr, R.A., Chang, Y., Bhandiwad, A.A., Forlano, P.M., and Sisneros, J.A. (2018). Brain activation patterns in response to conspecific and heterospecific social acoustic signals in female plainfin midshipman fish, Porichthys notatus. Brain Behav. Evol. *91*, 31–44.
11. Furukawa, T., and Ishii, Y. (1967). Neurophysiological studies on hearing in goldfish. J. Neurophysiol. *30*, 1377–1403.
12. McCormick, C.A. (1999). Anatomy of the central auditory pathways of fish and amphibians. In Comparative Hearing: Fish and Amphibians, R.R. Fay, and A.N. Popper, eds. (Springer), pp. 155–217.
13. Echteler, S.M. (1985). Tonotopic organization in the midbrain of a teleost fish. Brain Res. *338*, 387–391.
14. Vanwalleghem, G., Heap, L.A., and Scott, E.K. (2017). A profile of auditory-responsive neurons in the larval zebrafish brain. J. Comp. Neurol. *525*, 3031–3043.
15. Olive, R. (2015). Perception des écoulements et des vibrations chez la larve de poisson-zèbre: étude comportementale et imagerie. PhD thesis (Université Pierre et Marie Curie).
16. Schulze, A., Gomez-Marin, A., Rajendran, V.G., Lott, G., Musy, M., Ahammad, P., Deogade, A., Sharpe, J., Riedl, J., Jarriault, D., et al. (2015). Dynamical feature extraction at the sensory periphery guides chemotaxis. eLife *4*, e06694.
17. Tastekin, I., Khandelwal, A., Tadres, D., Fessner, N.D., Truman, J.W., Zlatic, M., Cardona, A., and Louis, M. (2018). Sensorimotor pathway controlling stopping behavior during chemotaxis in the *Drosophila melanogaster* larva. eLife *7*, e38740.
18. Álvarez-Salvado, E., Licata, A.M., Connor, E.G., McHugh, M.K., King, B.M., Stavropoulos, N., Victor, J.D., Crimaldi, J.P., and Nagel, K.I. (2018). Elementary sensory-motor transformations underlying olfactory navigation in walking fruit-flies. eLife *7*, e37815.
19. Min, S., Ai, M., Shin, S.A., and Suh, G.S.B. (2013). Dedicated olfactory neurons mediating attraction behavior to ammonia and amines in Drosophila. Proc. Natl. Acad. Sci. USA *110*, E1321–E1329.

20. Liu, H., Yang, W., Wu, T., Duan, F., Soucy, E., Jin, X., and Zhang, Y. (2018). Cholinergic sensorimotor integration regulates olfactory steering. Neuron *97*, 390–405.e3.

21. Samuel, A.D.T., and Sengupta, P. (2005). Sensorimotor integration: locating locomotion in neural circuits. Curr. Biol. *15*, R341–R343.

22. Ferezou, I., Haiss, F., Gentet, L.J., Aronoff, R., Weber, B., and Petersen, C.C.H. (2007). Spatiotemporal dynamics of cortical sensorimotor integration in behaving mice. Neuron *56*, 907–923.

23. Proville, R.D., Spolidoro, M., Guyon, N., Dugué, G.P., Selimi, F., Isope, P., Popa, D., and Léna, C. (2014). Cerebellum involvement in cortical sensorimotor circuits for the control of voluntary movements. Nat. Neurosci. *17*, 1233–1239.

24. Campagner, D., Evans, M.H., Bale, M.R., Erskine, A., and Petersen, R.S. (2016). Prediction of primary somatosensory neuron activity during active tactile exploration. eLife *5*, e10696.

25. Crochet, S., Lee, S.-H., and Petersen, C.C.H. (2019). Neural circuits for goal-directed sensorimotor transformations. Trends Neurosci. *42*, 66–77.

26. Naumann, E.A., Fitzgerald, J.E., Dunn, T.W., Rihel, J., Sompolinsky, H., and Engert, F. (2016). From whole-brain data to functional circuit models: the zebrafish optomotor response. Cell *167*, 947–960.e20.

27. Wolf, S., Dubreuil, A.M., Bertoni, T., Böhm, U.L., Bormuth, V., Candelier, R., Karpenko, S., Hildebrand, D.G.C., Bianco, I.H., Monasson, R., and Debrégeas, G. (2017). Sensorimotor computation underlying phototaxis in zebrafish. Nat. Commun. *8*, 651.

28. Chen, X., Mu, Y., Hu, Y., Kuan, A.T., Nikitchenko, M., Randlett, O., Chen, A.B., Gavornik, J.P., Sompolinsky, H., Engert, F., and Ahrens, M.B. (2018). Brain-wide organization of neuronal activity and convergent sensorimotor transformations in larval zebrafish. Neuron *100*, 876–890.e5.

29. Haesemeyer, M., Robson, D.N., Li, J.M., Schier, A.F., and Engert, F. (2018). A brain-wide circuit model of heat-evoked swimming behavior in larval zebrafish. Neuron *98*, 817–831.e6.

30. Thompson, A.W., Vanwalleghem, G.C., Heap, L.A., and Scott, E.K. (2016). Functional Profiles of Visual-, Auditory-, and Water Flow-Responsive Neurons in the Zebrafish Tectum. Curr. Biol. *26*, 743–754.

31. Bhandiwad, A.A., Zeddies, D.G., Raible, D.W., Rubel, E.W., and Sisneros, J.A. (2013). Auditory sensitivity of larval zebrafish (*Danio rerio*) measured using a behavioral prepulse inhibition assay. J. Exp. Biol. *216*, 3504–3513.

32. Zeddies, D.G., and Fay, R.R. (2005). Development of the acoustically evoked behavioral response in zebrafish to pure tones. J. Exp. Biol. *208*, 1363–1372.

33. Yao, Q., DeSmidt, A.A., Tekin, M., Liu, X., and Lu, Z. (2016). Hearing assessment in zebrafish during the first week postfertilization. Zebrafish *13*, 79–86.

34. Canfield, J.G., and Rose, G.J. (1996). Hierarchical sensory guidance of mauthner-mediated escape responses in goldfish (*Carassius auratus*) and cichlids (*Haplochromis burtoni*). Brain Behav. Evol. *48*, 137–156.

35. Holt, D.E., and Johnston, C.E. (2011). Can you hear the dinner bell? Response of cyprinid fishes to environmental acoustic cues. Anim. Behav. *82*, 529–534.

36. Burgess, H.A., and Granato, M. (2007). Sensorimotor gating in larval zebrafish. J. Neurosci. *27*, 4984–4994.

37. Jain, R.A., Wolman, M.A., Marsden, K.C., Nelson, J.C., Shoenhard, H., Echeverry, F.A., Szi, C., Bell, H., Skinner, J., Cobbs, E.N., et al. (2018). A forward genetic screen in zebrafish identifies the G-protein-coupled receptor CaSR as a modulator of sensorimotor decision making. Curr. Biol. *28*, 1357–1369.e5.

38. Jouary, A., and Sumbre, G. (2016). Automatic classification of behavior in zebrafish larvae. bioRxiv. https://doi.org/10.1101/052324.

39. Randlett, O., Wee, C.L., Naumann, E.A., Nnaemeka, O., Schoppik, D., Fitzgerald, J.E., Portugues, R., Lacoste, A.M.B., Riegler, C., Engert, F., and Schier, A.F. (2015). Whole-brain activity mapping onto a zebrafish brain atlas. Nat. Methods *12*, 1039–1046.

40. Fay, R.R., and Edds-Walton, P.L. (2008). Structures and functions of the auditory nervous system of fishes. In Fish Bioacoustics, J.F. Webb, R.R. Fay, and A.N. Popper, eds. (Springer New York), pp. 49–97.

41. Smith, M.E., Schuck, J.B., Gilley, R.R., and Rogers, B.D. (2011). Structural and functional effects of acoustic exposure in goldfish: evidence for tonotopy in the teleost saccule. BMC Neurosci. *12*, 19.

42. Lanford, P.J., Platt, C., and Popper, A.N. (2000). Structure and function in the saccule of the goldfish (Carassius auratus): a model of diversity in the non-amniote ear. Hear. Res. *143*, 1–13.

43. Kuchibhotla, K., and Bathellier, B. (2018). Neural encoding of sensory and behavioral complexity in the auditory cortex. Curr. Opin. Neurobiol. *52*, 65–71.

44. Klein, D.J., Depireux, D.A., Simon, J.Z., and Shamma, S.A. (2000). Robust spectrotemporal reverse correlation for the auditory system: optimizing stimulus design. J. Comput. Neurosci. *9*, 85–111.

45. Mu, Y., Li, X.Q., Zhang, B., and Du, J.L. (2012). Visual input modulates audiomotor function via hypothalamic dopaminergic neurons through a cooperative mechanism. Neuron *75*, 688–699.

46. Boulanger-Weill, J., Candat, V., Jouary, A., Romano, S.A., Pérez-Schuster, V., and Sumbre, G. (2017). Functional interactions between newborn and mature neurons leading to integration into established neuronal circuits. Curr. Biol. *27*, 1707–1720.e5.

47. Pologruto, T.A., Sabatini, B.L., and Svoboda, K. (2003). ScanImage: flexible software for operating laser scanning microscopes. Biomed. Eng. Online *2*, 13.

48. Harris, J.A., Cheng, A.G., Cunningham, L.L., MacDonald, G., Raible, D.W., and Rubel, E.W. (2003). Neomycin-induced hair cell death and rapid regeneration in the lateral line of zebrafish (Danio rerio). J. Assoc. Res. Otolaryngol. *4*, 219–234.

49. Rohlfing, T., and Maurer, C.R., Jr. (2003). Nonrigid image registration in shared-memory multiprocessor environments with application to brains, breasts, and bees. IEEE Trans. Inf. Technol. Biomed. *7*, 16–25.

STAR★METHODS

KEY RESOURCES TABLE

REAGENT or RESOURCE	SOURCE	IDENTIFIER
Chemicals, Peptides, and Recombinant Proteins		
Neomycin sulfate	Sigma-Aldrich	CAS: 1405-10-3
Experimental Models: Organisms/Strains		
Zebrafish: Tg(huC:GCaMP5G)^{ens102Tg}	[46]	RRID: ZDB-ALT-161209-7
Software and Algorithms		
MATLAB 2016a	Mathworks	https://www.mathworks.com/
ScanImage 3.8 (Calcium recordings acquisition)	[47]	http://scanimage.vidriotechnologies.com
HCImageLive 4.3 (Image acquisition)	Hamamatsu	https://hcimage.com/hcimage-overview/hcimage-live/

LEAD CONTACT AND MATERIALS AVAILABILITY

This study did not generate new unique reagents. Further information and requests for resources and reagents should be directed to Lead Contact, Germán Sumbre (sumbre@biologie.ens.fr).

EXPERIMENTAL MODEL AND SUBJECT DETAILS

Experiments were performed on transgenic zebrafish larvae from 7 to 21 dpf, expressing pan-neuronally the genetically encoded calcium indicator GCaMP5 (*Huc:GcaMP5* nacre line). The embryos were collected and raised at 28 °C in 0.5x E3 embryo medium. Larvae were kept under 14/10 hours on/off light cycles and fed after 5 dpf with Paramecia. All experiments were approved by the Comité d'éthique pour l'expérimentation animale Charles Darwin (03839.03).

METHOD DETAILS

Auditory stimulation

Stimulation protocol

We designed and 3D printed two recording chambers (one for the two-photon microscope and one for the light-sheet microscope) to deliver auditory stimuli via waterproof speakers (*Visaton K28 WP*) while simultaneously recording neural activity and motor behavior (Figure 1A). We designed two stimulation protocols:

(1) To study stimulus frequency representation: we delivered pure tones of 15 different frequencies (150, 200, 250, 300, 450, 550, 600, 650, 700, 750, 800, 850, 900, 950 and 1000 Hz). These frequencies were randomly presented for 1 s with inter-stimulus intervals of 10 s. Each frequency was presented 5 times for each experiment. To minimize the generation of unwanted harmonics, the stimuli were cosine-squared gated with a raise and decay time of 150 ms. To overcome the non-linearities of the speakers and the complex acoustic properties of the chamber, we used a miniature hydrophone (*Bruel and Kjaer 8103*) and a triaxial accelerometer (*PCB Piezotronics W356A12*) to equalize the amplitude and the acceleration of the emitted stimuli. Both probes were placed inside the chamber, 2 cm away from the speaker (Figure S1).

(2) To study sensorimotor transformations: we monitor Ca^{2+} dynamics using a light-sheet microscope with a high acquisition rate (20 Hz). Due to the constraints of the light-sheet microscope, the recording chamber was relatively small (45 × 36 × 33 mm), making impossible to record sound pressure levels. Therefore, we presented only one broadband auditory stimulus (between 250 and 1000 Hz). This stimulus was presented for 500 ms and were separated by an inter-stimulus interval of 30 s. The stimulus was repeated 55 times.

Audiograms

In order to assess the hearing thresholds of larvae, we delivered acoustic stimuli at 5 different intensity levels while recording neural activity. We delivered pure tones of 15 different frequencies (150, 200, 250, 300, 450, 550, 600, 650, 700, 750, 800, 850, 900, 950 and 1000 Hz). We calibrated the recording chamber using a miniature hydrophone (*Bruel and Kjaer 8103*) and a triaxial accelerometer (*PCB Piezotronics W356A12*) to equalize the amplitude and the acceleration of the emitted stimuli. The 5 sound pressure levels and corresponding particle acceleration levels were set to 120, 132, 145, 157 and 170 dB re. 1 μPa and −54 (below the detection level with our setup), −54,-43,-33, and −22 dB re. 1g respectively (Figures S3B and S3C). Each stimulus was presented 5 times with a 9 s inter-stimulus interval.

Some of the highest sound intensity produced vibration artifacts in the imaging, the corresponding frames were therefore removed from the recordings. We were still able to record neural activity due to the slow dynamics of GCaMP5. A multiple regression model was fit to estimate the amplitude of the neural response. ROIs responsive to the stimulus were identified as previously stated, and only those ROIs activity was kept for further analysis. To evaluate the threshold at which neural activity was deemed significant, we estimated the null distribution of the regression coefficients by fitting neural activity in between stimulations. Regression coefficients with a value above the 95th percentile of the null distribution were considered significant.

Finally, the regression coefficients from all detected ROIs were averaged together to obtain a single number, representative of the overall brain activity at each frequency and intensity level.

Calcium imaging

Two-photon calcium imaging

Zebrafish larvae (*Huc:GcaMP5)* from 7 to 21 dpf were head-embedded in 2% low-melting agarose inside a recording chamber filled with E3 embryo medium (Figure 1A). The tail of the larva was freed from agarose and tail bouts were recorded (150 Hz) from below with a high-speed camera (*Baumer HXG20NIR*) and infra-red illumination. Neural activity was monitored using a two-photon microscope (MOM, *Sutter Instruments) controlled by Scanimage 3.8.* We used a 25x, NA 1.05 objective (*Olympus*) and a Ti:Sapphire laser (*Spectra-Physics Mai Tai DeepSee*) tuned at 920 nm. The whole hindbrain was recorded at different depths with a frame rate of 2.79 Hz. Auditory stimuli, behavior recordings and two-photon imaging were synchronized using TTL signals (*Arduino Uno*).

Selective-plane illumination microscopy

We used selective-plane illumination microscopy (SPIM) to record the neuronal activity from different optical sections of the zebrafish hindbrain, with near cellular resolution. Optical sectioning was achieved by the generation of a micrometer-thick light sheet to excite GCaMP5 from the side of the larva. The GCaMP emission was collected by a camera whose optical axis was orthogonal to the excitation plane (a 488 nm laser, Phoxx 480-200, Omicron). The laser beam was first filtered by a 488 cleanup filter (XX.F488 Omicron) and coupled to a single-mode fiber optic. The beam was expanded using a telescope (f = 50 mm, LA1131-A, and f = 150 mm, LA1433-A, Thorlabs) and projected onto two orthogonal galvanometric mirrors (HP 6215H Cambridge technology) to scan the laser beam, whose angular displacement were converted into position displacement by a scan lens (f = 75 mm AC508-075-A-ML, Thorlabs). The laser beam was then refocused by a tube lens (f = 180 mm, U-TLUIR, Olympus) and focused on the pupil of a low-NA (0.16) objective lens (UPlan SAPO 4x, NA = 0.16, Olympus) facing the specimen chamber. This arrangement yielded a 1mm-wide illumination sheet and a beam waist of 3.2 μm (1/e2). The emitted fluorescence light was collected by a high-NA water-dipping objective (N16XLWD-PF, 16x, NA = 0.8, Nikon) mounted vertically on a piezo translation stage (PI PZ222E). A tube lens (f = 180mm U-TR30IR, Olympus), a notch filter (NF03-488, to filter the laser's excitation light), a band-pass filter (FF01 525/50 Semrock) and a low-pass filter (FF01 680 SP25 Semrock, to filter the IR light) were used to create an image of the GCaMP5 emitted fluorescence on a sCMOS sensor (Orca Flash 4.0, Hamamatsu). The acquisition rate was 20 Hz.

Data analysis

Pre-processing of neural data

The acquired series of images were registered to correct for potential drifts in the XY plane using a custom script written in MATLAB which computes the cross correlations in the Fourier domain and the offset value for each frame in the dataset. We then smoothed the curve describing the offset values against time using a running average with a sliding window of 100 frames, and subtracted each offset value from this smoothed curve. This difference was then used to estimate the deviation of the position of each frame the baseline. Then, we computed the Z-scores across a sliding window of 100 frames and tagged displacements that had a Z-score over a threshold of 3. These displacement events above the threshold were then manually curated to remove movement artifacts. This procedure removed on average 2.27 ± 0.74% of the frame per larva. Since the expression of Huc:GCaMP5 is cytosolic, most of the recorded signals originate at the neuropil. We therefore decided to segment images using small hexagons that matched the size of neurons. The time series of pixel belonging to the same hexagon were averaged together. We computed the baseline fluorescence as the 8^{th} percentile in a running window of 30 s [14] to obtain the relative change of fluorescence (ΔF/F).

The same procedure was applied to pre-process the light-sheet datasets. However, since the larvae were more constrained within a capillary tube, and we recorded at a higher frame rate (20 Hz), movements of the larvae did not affect the analysis of the datasets, and therefore no frames were removed from the registered datasets.

Selection of regions of interest and sensorimotor ratio

We selected ROIs responsive to auditory stimuli of different frequencies and ROIs according to their correlation with motor behavior using a multivariate linear regression approach. We built one regressor for each frequency of the presented auditory stimuli as the convolution between the indicator function of the stimulus presentation (0 in the absence of stimulus and 1 when a stimulus was presented) and the GCaMP5 kernel (Figure S2A).

To find ROIs correlated with behavior we built one regressor for each frame around the onset of the tail movements (from 10 frames before to 10 frames after the onset of the movement for the two-photon experiments, making a total of 21 regressors, Figure S2D, and from 10 frames before to 40 frames after the onset of the movement for the light-sheet experiments, making a total of 51 regressors). The two linear models for auditory stimuli and motor behavior were fit separately on the datasets. Generally, the neural responses that

correlated with motor behavior displayed larger amounts of trial-to-trial variability compared to sensory responses. This, and the design of the linear model for motor behavior resulted in lower values for R^2 values describing motor behavior when compared to R^2 values for auditory stimuli.

In order to select ROIs responsive to the auditory stimuli or correlated with the motor behaviors, we built a null model were the stimulus timings were shifted to fall into regions of spontaneous activity, while the inter-stimulus intervals were preserved. We applied the regression analysis to the shifted regressors and obtained a null distribution for the R^2 values in 2 dimensions. Only regions of interest with a mahalanobis distance of 7 from the center of a 2D Gaussian fit to the null distribution were considered as responsive ROIs and were kept for further analysis (Figure S5). For experiments in which behavior was not recorded, we kept ROIs with a R^2 value above a threshold of 0.10 for the regression with auditory stimuli.

To determine whether a ROI was more responsive to auditory stimuli or correlated with behavior, we computed a sensorimotor ratio (SMR) based on the percentage of variance explained by the linear regression analysis: $SMR = (R^2_{mvt} - R^2_{stim}) / (R^2_{mvt} + R^2_{stim})$.

Spatial normalization

As a reference stack, we imaged the whole brain of a 7 dpf *Huc:GCaMP5* larva (132 planes) using a confocal microscope (Leica SP5) with a lateral resolution of 1.21 μm per pixel and an axial resolution of 2.98 μm per pixel. Individual optical sections of different larvae were manually registered to the confocal stack using an affine transformation. This allowed us to project the position of ROIs from different larvae into a common 3D reference space.

Density maps

To obtain the cell-density map for each frequency-tuning cluster (Figure 2D), we computed the density of ROIs in each cluster in the 3D reference space by convolving with a Gaussian kernel (sigma = 3.63 μm in the XY axis, 8.94 μm in the Z axis). We then projected the normalized maximum density along the Z and y axis, color-coded according to the cluster whose density is maximal. To compute the density along a relevant axis, we projected on this axis the number of ROIs of each cluster, and then computed the density along that axis using kernel density estimation.

Detection of the onset and the duration of Ca^{2+} transients

To compute the onset and the duration of calcium transients in the datasets acquired using the light-sheet microscope at 20 Hz, we averaged across trials the ΔF/F traces. These were then smoothed temporally using a Gaussian filter (σ = 150 ms) to remove noise in the signal. The onset was computed as the time point where the second derivative of the smoothed traces was maximal. The duration was defined as the full width at half-maximum of the smoothed traces. For this purpose we used a linear interpolation.

Pre-processing of behavioral data

Videos of the tail of the larva were analyzed as previously described in Olive et al. [42]. Briefly, the tail was segmented and two ellipses fit to the head and tail of the larva. The tail deflection was defined as the inverse of the average distance between all the pixels in the larva and the intersection of the minor axis of the two ellipses. To obtain a dimensionless value, the result was multiplied by the length of the larva at rest.

Analysis of motor behavior

Movements that occurred in a 500 ms time window after the onset of an auditory stimulation were considered as elicited by the stimulation. To validate this approach, we used a permutation-based approach. We counted the number of stimuli followed by at least one tail bout in a 500 ms time window and compared this number to a null model where the onset of movements was shuffled but the inter-bout interval distribution was kept intact.

Clustering of tuning curves and clustering validation

To calculate the frequency tuning curves of each ROI, we computed for each presented frequency the average ΔF/F within a 2 s time window starting at the onset of the stimulus. This was further averaged across the different trials. To cluster the frequency tuning curves, we pooled the tuning curves from all ROIs responding to the auditory stimuli from all animals. The tuning curves were normalized so that the minimum value was set to zero and the maximum to one, which allows clustering together tuning curves of similar shape but different amplitudes. We used the k-means algorithm with euclidean distance to cluster the tuning curves.

To validate the clustering solution, we used a set of convergent approaches. We computed two clustering indices, the Calinski-Harbasz index which is based on the ratio of between and within-cluster variance, and the Silhouette index, which describes how similar each observation is to observations in its own cluster, when compared to observation in other clusters.

The Calinski-Harabasz criterion is defined as:

$$CH(k) = \frac{SS_B}{SS_W} \times \frac{N-k}{k-1}$$

where k is the number of clusters, and N is the number of observations. The between-cluster variance is defined as:

$$SS_B = \sum_{i=1}^{k} n_i \times \|m_i - m\|^2$$

where n_i is the number of observations in cluster i, m_i is the centroid of cluster i, m is the overall mean of the data. The within-cluster variance is defined as:

$$SS_W = \sum_{i=1}^{k} \sum_{x \in c_i} \| x - m_i \|^2$$

where x is a data point, c_i is the ith cluster, and m_i is the centroid of cluster i.

The silhouette index for one observation i is defined as:

$$S_i = \frac{b_i - a_i}{max(a_i, b_i)}$$

where a_i is the average distance from the ith point to the other points in the same cluster as i, and b_i is the minimum average distance from the ith point to points in a different cluster, minimized over clusters. The silhouette value ranges from –1 to 1. A high silhouette value indicates that i is well-matched to its own cluster, and poorly matched to other clusters.

We also used a hierarchical clustering approach, using Ward's method, which iteratively merges clusters together to minimize the overall within-cluster variance. Hierarchical clustering also yields a dendrogram, which describes the structure of the clustering solution in terms of distance between clusters. The distance between two clusters A and B is computed as:

$$\Delta(A,B) = \frac{n_A n_B}{n_A + n_B} \| m_A - m_B \|^2$$

where n_A is the number of points in cluster A, n_B is the number of points in cluster B, m_A is the centroid of cluster A and m_B is the centroid of cluster B. A large distance between clusters indicates a high cost for merging the clusters in terms of overall within-cluster variance.

Finally, we also used principal component analysis. We inspected the distribution of scores in PC space, to find signs of multimodality. Gaussian-mixture models with 2 components were fit to the distribution of scores for PC1 and PC2 to find the value that best separated between components. We used these thresholds as a linear separation to classify the data in 4 groups and compare it with our k-means clustering results.

Presenting auditory stimuli with higher frequency resolution (150 – 300 Hz using frequency steps of 10 Hz) showed similar clustering results suggesting that the low dimensionality of frequency representation in the larva's nervous system is not due to the type of auditory stimuli used.

High speed recording of behavior

To characterize the delay between the onset of the acoustic stimulation and the onset of behavior, we recorded the behavior of the larvae using a high-speed camera at 1000 Hz (Baumer HXG20NIR) with infrared illumination. To synchronize the video recordings with the auditory stimuli (500 ms broadband noise between 250 Hz and 1000 Hz), we triggered the camera with a National Instruments NI PCI-6711 card. The resulting videos were then analyzed manually to determine the onset of behavior. We used 3 types of stimulation: 0dB (no sound), 155dB and 170dB re. 1 μPa, with an inter-stimulus interval of 30 s. For the strong stimulus, the histogram of delay was multimodal, we estimated the statistics of each component separately using a Gaussian mixture model.

Lateral line ablation

To evaluate the contribution of the lateral line system to the auditory neural responses, we chemically ablated the lateral line using neomycin. Larvae were incubated during one hour in a 200 μM neomycin solution (Sigma) in E3 medium, rinsed for one hour in E3 medium and placed under the microscope for recording [14, 48]

Registration to the z-brain atlas

Our reference brain (7 dpf Huc:GCaMP5 larva, 132 planes) was registered against the Elavl3:GCaMP5 brain in the z-brain atlas [39] using the Computational Morphometry Toolkit (CMTK) [49]. We used the command:

cmtk registration –initial initial.xform -v –dofs 6,9,12 -o affine.xform reference.nrrd sample.nrrd to produce the initial affine transformation and cmtk warp -v –registration-metric nmi –jacobian-weight 1e-5 –fast -e 16 –grid-spacing 100 –energy-weight 1e-1 –refine 2 –coarsest 4 –ic-weight 0 –accuracy 0.5 –output-intermediate -o warp.xform –initial affine.xform reference.nrrd sample.nrrd, to perform the final elastic registration.

QUANTIFICATION AND STATISTICAL ANALYSIS

Whenever we could not assume a normal distribution of the data, the statistical inference was made using a non-parametric framework: permutation-based tests, Wilcoxon rank sum test for independent samples, or Wilcoxon signed rank test for paired samples.

In the cases where multiple testing were performed, we used Bonferonni correction (p values are adjusted by multiplying by the number of tests performed) to control for the number of false positives.

DATA AND CODE AVAILABILITY

Raw data and codes from the current study were not deposited into a public repository due to the large size, but are available from the Lead Contact upon request.

Current Biology, Volume *29*

Supplemental Information

Sensorimotor Transformations in the Zebrafish Auditory System

Martin Privat, Sebastián A. Romano, Thomas Pietri, Adrien Jouary, Jonathan Boulanger-Weill, Nicolas Elbaz, Auriane Duchemin, Daphne Soares, and Germán Sumbre

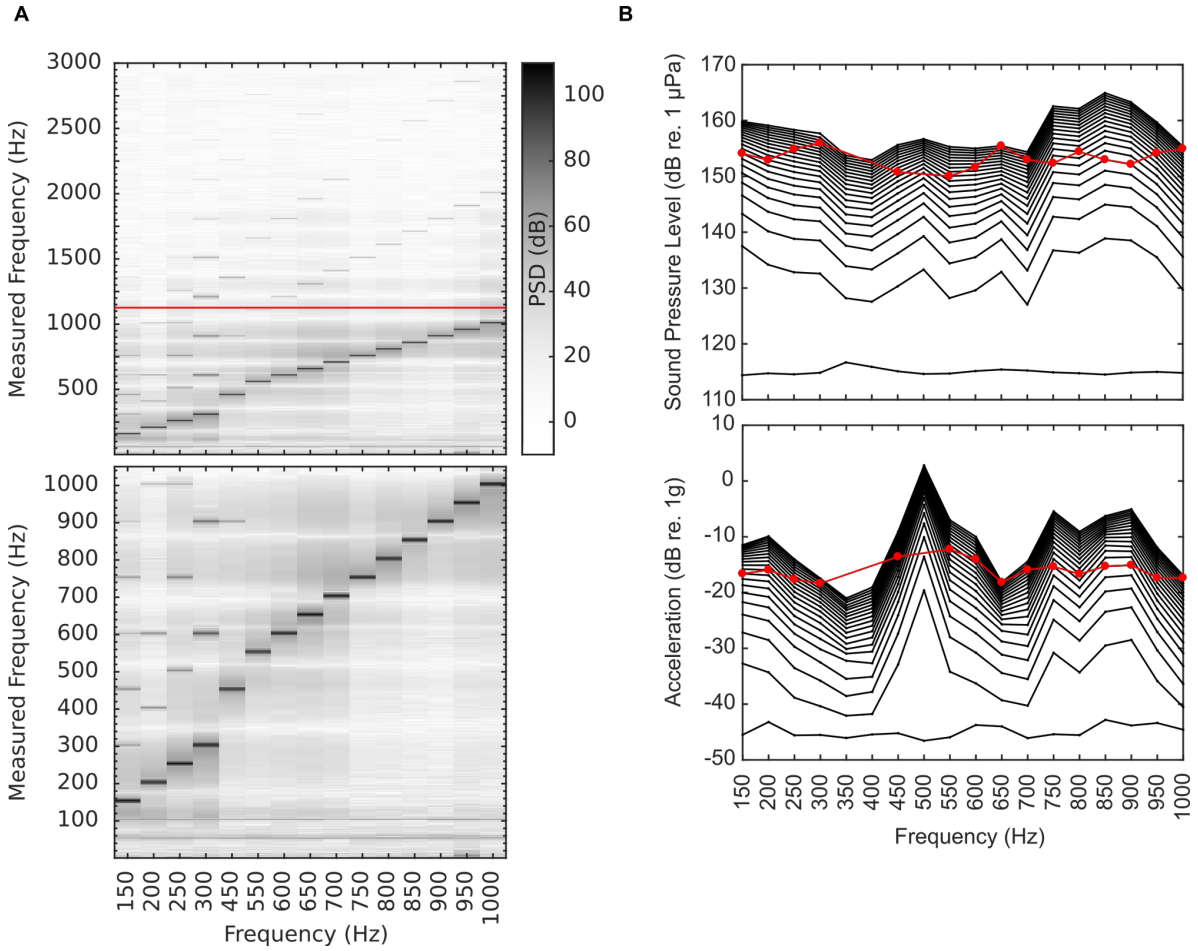

Figure S1. Acoustic calibration of the recording chamber. Related to Figure 1.
(A) The spectral content of acoustic stimulation was controlled to ensure that most of the power lies in the fundamental frequency. Top: power spectrum between 1 and 3000 Hz; bottom: close-up between 1 and 1000 Hz.
(B) Pure tones with frequency ranging from 150 to 1000 Hz were used to stimulate the larvae. The recording chamber was calibrated using a hydrophone and a suspended accelerometer to control sound pressure levels and particle acceleration across frequencies. The larvae were stimulated with a sound pressure level of 155 dB re. 1µPa (measured at 2 cm from the speaker due to the shape of the chamber), and a particle acceleration close to -15 dB re. 1g (red lines).

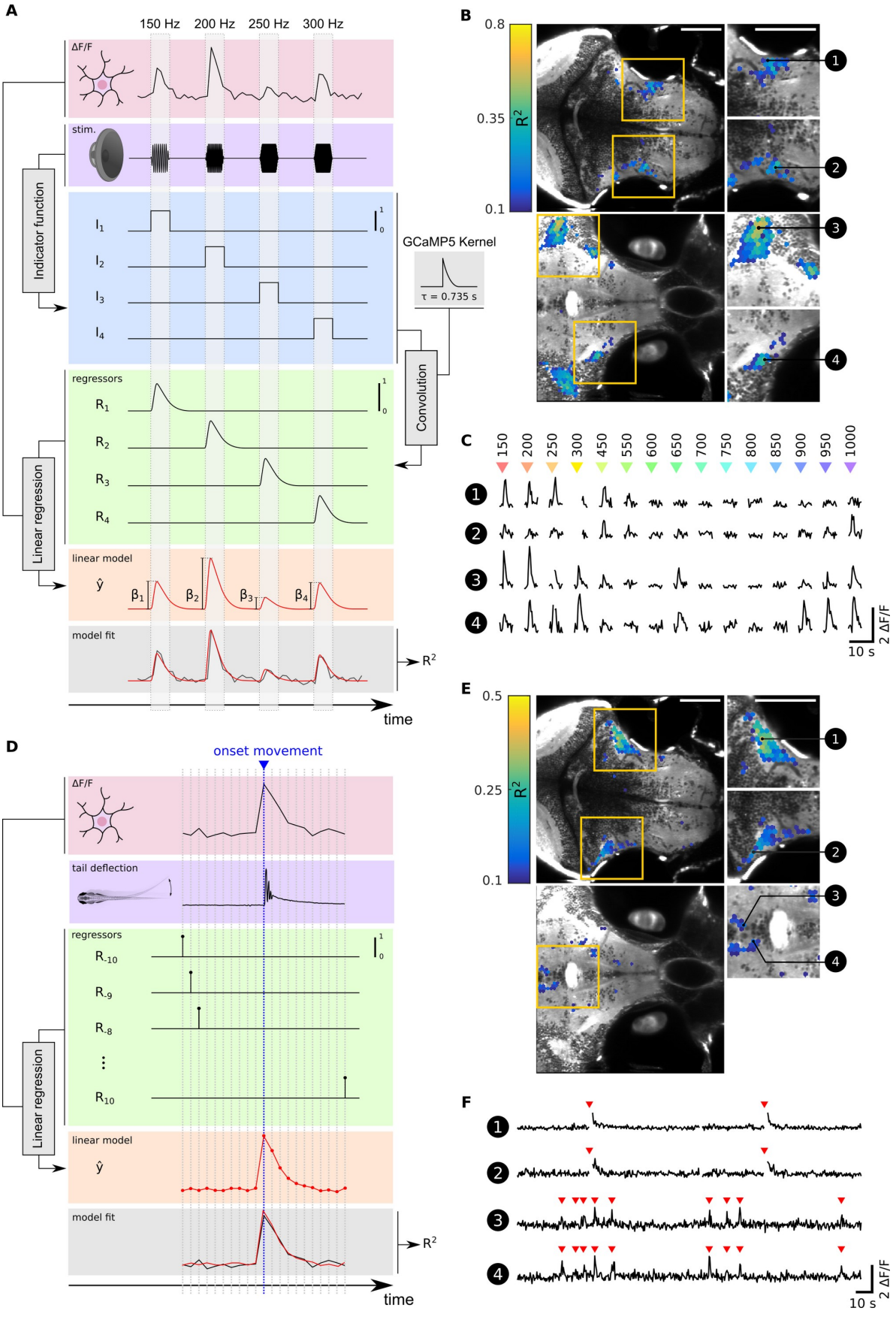
A
150 Hz
200 Hz
250 Hz
300 Hz
ΔF/F
stim.
Indicator function
I1
I2
I3
I4
GCaMP5 Kernel
τ = 0.735 s
Convolution
regressors
R1
R2
R3
R4
Linear regression
linear model
ŷ
β1
β2
β3
β4
model fit
R2
time
B
0.8
0.35
0.1
R2
1
2
3
4
C
150
200
250
300
450
550
600
650
700
750
800
850
900
950
1000
2 ΔF/F
10 s
D
onset movement
ΔF/F
tail deflection
regressors
R-10
R-9
R-8
R10
Linear regression
linear model
ŷ
model fit
R2
time
E
0.5
0.25
0.1
R2
F
2 ΔF/F
10 s

Figure S2. Detection of regions of interest correlated with acoustic stimuli and behavior. Related to Figure 1.

(A) Linear regression model used to detect regions of interest whose activity is correlated with acoustic stimuli. For each frequency presented, a regressor was build as the convolution between an indicator function (which takes the value 1 when the stimulus is presented and 0 everywhere else), and the calcium impulse response function for GCaMP5 (GCaMP5 kernel). The goodness of fit was measured by the percentage of variance explained by the model (R^2).

(B) Example topography of the neural responses to acoustic stimuli for two optical sections, in the octaval nuclei (top), and in the torus semicircularis (bottom). The color code reflects how well the variance in the neural activity is explained by the regression model. Right panels, close-up on the regions outline by the yellow squares. Scale bar, 100 µm. Activity traces for regions of interest 1 to 4 are represented in c).

(C) Single-trial traces of neural activity for regions of interest 1 to 4 defined in b) induced by 1s acoustic stimulation. Arrowheads: stimulus onset and corresponding frequency in Hz. Breaks in the traces are discarded frames due to movement artifacts.

(D) Linear regression model used to detect regions of interest whose activity is correlated with behavior. One regressor was used for each frame in a 10 frames window around movement onset.

(E) Example topography of the neural activity associated with movements of the tail. Activity traces for regions of interest 1 to 4 are represented in (F).

(F) Traces of neural activity for regions of interest 1 to 4 defined in (E). Red arrowheads: onset of tail movements.

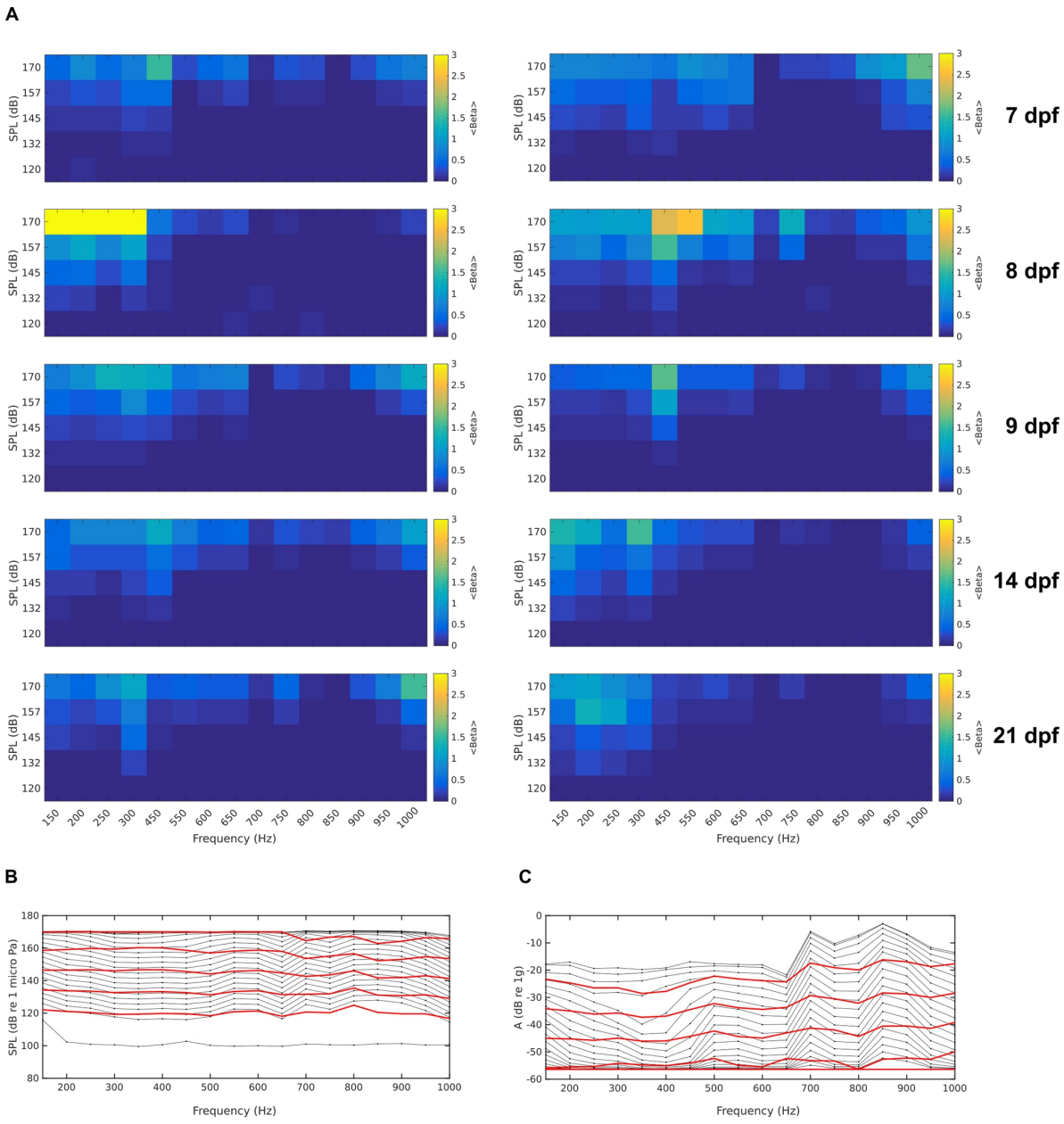

Figure S3. Audiograms at different developmental stages and calibration of the recording chamber. Related to Figure 3.

(A) Two examples of audiograms of individual larvae at different developmental stages from 7 to 21 dpf.

(B-C) The recording chamber was calibrated to deliver acoustic stimuli with 5 intensity levels equally spaced and equalized over frequencies for sound pressure level (B), and particle acceleration (C). Black curves: the recorded sound pressure and acceleration for each frequency and for a given voltage stimulus. Red curves: the calibrated voltages for the different frequencies to obtain homogeneous sound pressure levels and accelerations across the whole range of tested frequencies.

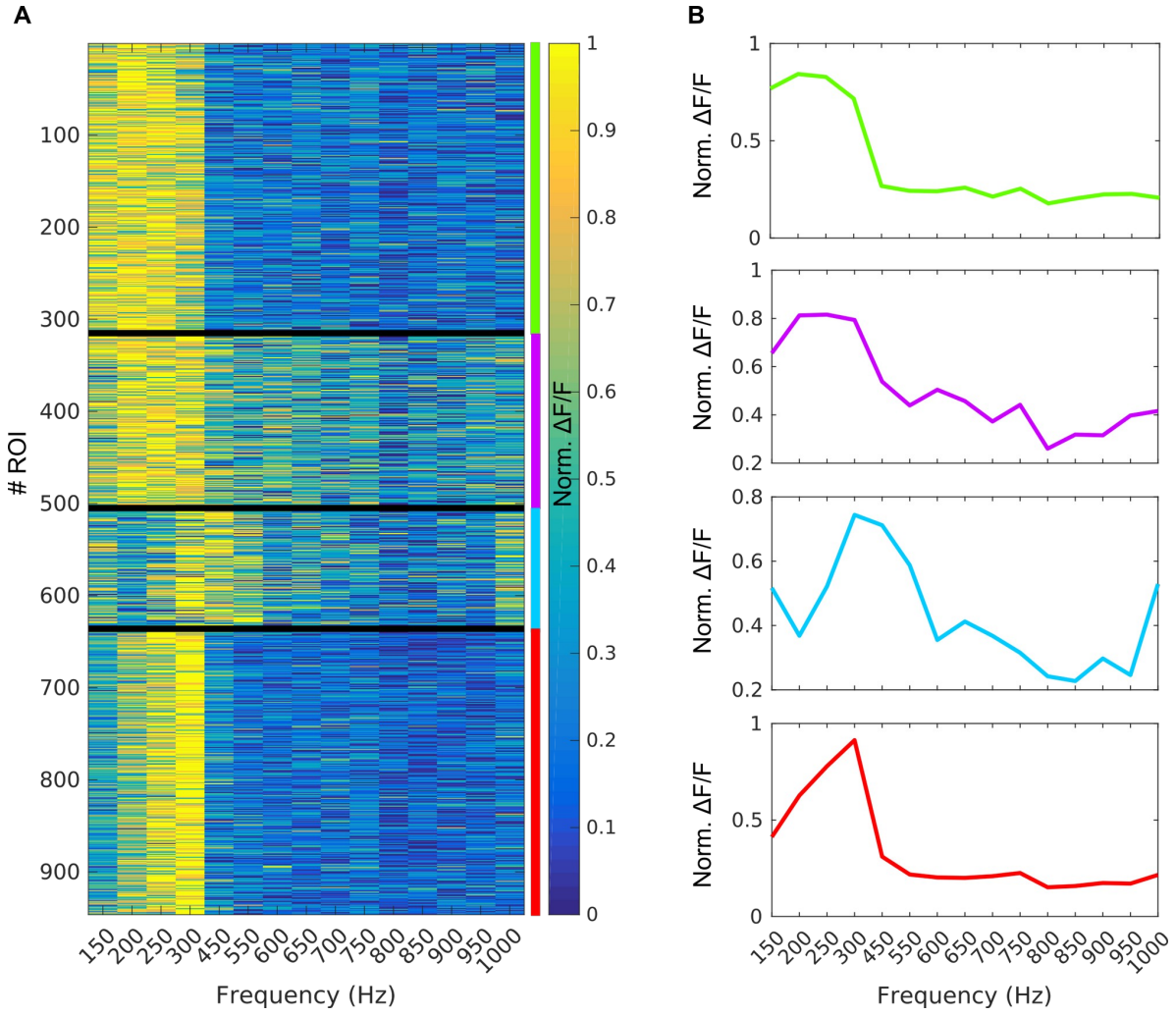

Figure S4. Auditory induced neuronal responses are unaffected by lateral line ablation with neomycin. Related to Figure 2.
(A) Frequency tuning curves of 8 dpf larvae (N=7) exposed for 1 hour to neomycin to ablate the lateral line, grouped in 4 clusters using k-means clustering algorithm.
(B) Average tuning curve for each cluster.

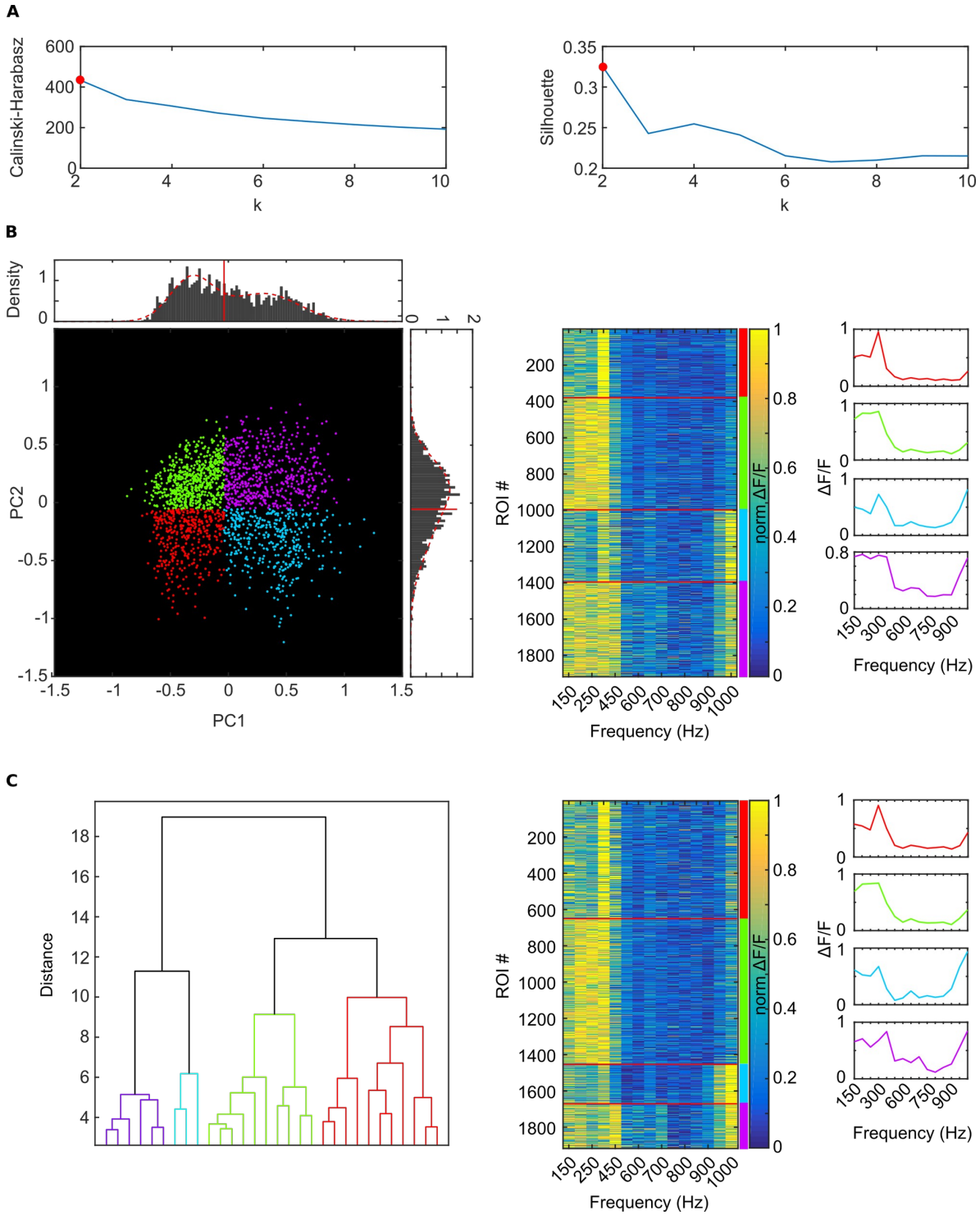

Figure S5. Validation of tuning curves clustering. Related to Figure 2.
(A) Calinski-Harabasz and Silhouette indexes for clustering solution with 2 to 10 clusters (k). Red dot: optimal value.
(B) Left: Tuning curves projected in principal component (PC) space. A two-component Gaussian mixture model was fit to the distribution of scores of PC1 and PC2 (red dotted line), and a threshold was selected as the best separation between the two components for each PC (red bar). Tuning curves were color coded according to their position respective to these two thresholds. Right: ROIs tuning curves organized according to the thresholds set on PC1 and PC2.

(C) Hierarchical clustering using euclidean distance and Ward's variance criterion. Left: simplified dendrogram of the hierarchical clustering solution, Right: ROIs tuning curves organized according to the hierarchical clustering solution. Note the similarity with those obtained using k-means (Figure 2B).

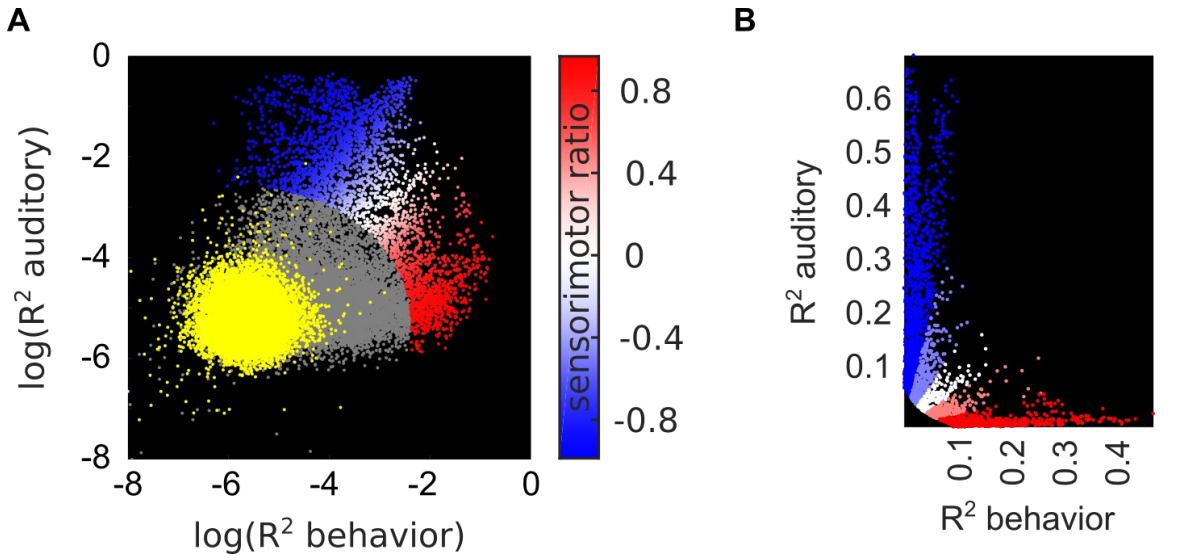

Figure S6. Distribution of the percentage of variance explained by the linear models. Related to Figure 6.

(A) A null model was obtained by shifting all the fluorescence time series by the same amount, which preserves the temporal structure of the data but destroys the association with stimulus and behavior. Distribution of R^2 for the null model are shown in yellow. A two-dimensional Gaussian, was fit to the null model, ROIs were deemed responsive either to the stimulus or behavior if they had a Mahalanobis distance of 7 with respect to the mean of the Gaussian fit to the null model. Those responsive ROIs are color-coded based on the value of their sensorimotor ratio (STAR Methods).

(B) Sensorimotor ratio bins used in Figure 6A.

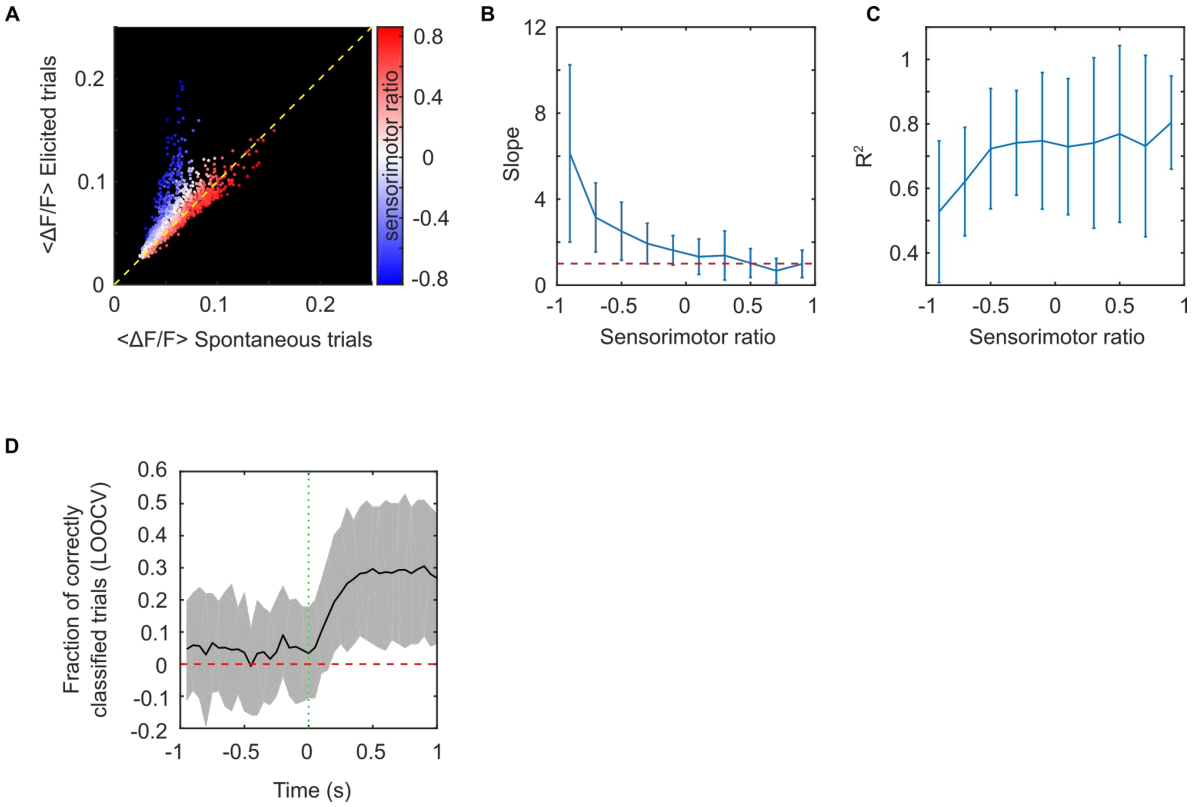

Figure S7. Motor networks display similar activity during self-generated and auditory elicited behavior and spontaneous activity preceding the auditory stimulus fails to predict behavior. Related to Figure 7.

(A) Example of ΔF/F averaged over elicited trials versus ΔF/F averaged over spontaneous trials for one larva. ROIs are color coded according to their sensorimotor ratio. Yellow doted line represents the time where activity was the same for spontaneous and elicited trials.

(B) A linear regression was fit for 10 bins of the sensorimotor ratio between ΔF/F averaged over elicited trials and ΔF/F averaged over spontaneous trials (27 larvae). The average slope and standard deviation of the linear fit are plotted against the centers of the sensorimotor ratio bins. Red dotted line: slope = 1.

(C) Average percentage of variance explained by the linear models and standard deviation versus sensorimotor ratio.

(D) Fraction of trials correctly classified (tail movement vs no tail movement) using linear discriminant analysis on the neural activity around the onset of auditory stimulation (estimated using leave one out cross-validation). Chance level was estimated by disrupting the association between neural activity and behavior (100 permutations of the class labels) and subtracted from the fraction of trials correctly classified to obtain the fraction of trial correctly classified above chance level. Red dashed line : chance level. Green dotted line: onset of auditory stimulus. Gray area: 5^{th} to 95^{th} percentile of the distributions obtained by shuffling the labels.

3

Neuronal basis of spontaneous behavior

3.1 Introduction

Early theories of behavior strongly focused on stimulus-response associations, and perceived animal as primarily driven by external sensory stimuli. It is estimated that the adult human brain, which represents approximately 2% of the body mass, accounts for nearly 20% of the body's overall energy expenditure. As little as 1% of this energy could be devoted to interacting with the environment [Raichle and Mintun, 2006], which stands largely at odds with a purely reflexive view of brain function, a discrepancy termed the 'Brain's Dark Energy' by the neuroscientist Marcus Raichle [Raichle, 2006]. The rich intrinsic dynamics of the brain does not reflect purely random fluctuations, but is highly structured in space and time [Ringach, 2009], and to some extent correlated with spontaneous behavior [Stringer et al., 2019]. This rich dynamics is matched at the behavioral level: well-fed animals in laboratory conditions still exhibit complex behaviors with intricate spatial and temporal dynamics to explore their environment even in the absence of salient sensory cues [Jung et al., 2014, Dunn et al., 2016b].

As we have discussed earlier, spontaneous actions in mammals are preceded by a gradual buildup of activity called the readiness potential [Kornhuber and Deecke, 1964]. The readiness potential is only one aspect of preparatory activity which may be related with the timing of the release of behavior via a ramp-to-threshold mechanism, but other

cognitive tasks may as well be ongoing before the onset of behavior, such as selecting what action to perform, or predicting the rewards and costs associated to possible actions. These tasks, as well as the timing of the action, could also be specified by the concerted dynamics of non-ramping populations of neurons [Shenoy et al., 2013, Murakami and Mainen, 2015].

The vertebrate motor systems is organized hierarchically, from higher brain centers, such as the motor cortices in mammmals, down to the spinal cord central pattern generators. At what level of the hierarchy could spontaneous action be generated? It seems plausible that coordinated spontaneous action do not emerge at the level of the spinal cord, but higher in the hierarchy. Depending on the complexity of the movements produced, it could occur as early as in neurons of the descending pathways. Spontaneous behavior could also be generated through the influence of non-motor areas such as sensory regions: Romano *et al.* observed that 11% of spontaneous tail bouts were preceded by the activation of assemblies in the optic tectum [Romano et al., 2015]. In primates, there seems to be a dedicated circuit for the generation of spontaneous movements in the pre-supplementary motor area and rostral cingulate zone [Brass and Haggard, 2008, Haggard, 2008], but there may also exist a substantial overlap with the circuits used to generate behavior in response to sensory stimuli.

Classically, studies on the generation of spontaneous behavior have relied on rigid experimental designs to study the timing of self-generated actions or action selection: the experiment is split in trials where the animal is free to choose the timing of an imposed action, or select between a set of pre-determined actions. Zebrafish larvae have a rich behavioral repertoire, but rely on chaining together basic categories of tail bouts to produce these behaviors: in a recent study, Marques *et al.* found 13 such categories of tail bouts [Marques et al., 2018]. Therefore, it is possible to record behaving zebrafish larvae displaying the full diversity of their locomotor repertoire to study the natural action selection process without imposing behavioral constraints on the animal. Using zebrafish larvae will also allow us the monitor simultaneously motor as well as sensory brain regions to disentangle their respective contribution to the generation of spontaneous behavior.

For this project we are interested in several questions:

- What are the circuits involved in the timing of spontaneous actions (*when*)?
- What are the circuits involved in action selection (*what*)?
- Are those two circuits independent?
- Are there several or unique pathways to generate the same type of spontaneous behavior?

- What is the contribution of spontaneous activity in sensory regions to the generation of spontaneous actions?
- How long before the onset of a movement can we predict the timing and selected action based on neuronal activity?
- What is the role of inhibition and neuromodulation in the generation of spontaneous behavior.

Here, I will only show preliminary results on the *when* pathway using single plane and whole brain recordings of the neural activity of behaving zebrafish larvae with a light-sheet microscope.

3.2 Materials and Methods

3.2.1 Zebrafish Larvae

Experiments were performed on transgenic zebrafish larvae between 6 and 8 days post-fertilization (dpf), expressing pan-neuronally the genetically encoded calcium indicators GCaMP5 and GCaMP6f, in the Tg(HuC:GcaMP5)^{ens102Tg} [Boulanger-Weill et al., 2017] and Tg(HuC:H2B-GCaMP6f) nacre lines. The embryos were collected and raised at 28 °C in 0.5X E3 embryo medium. Larvae were kept under 14/10 hours on/off light cycles and fed after 5 dpf with *paramecia*. All experiments were approved by the *comité d'éthique pour l'expérimentation animale Charles Darwin* (03839.03).

3.2.2 Recording setup

Light-sheet microscope

The exact setup used was described in [Ponce-Alvarez et al., 2018]. In summary, we used selective-plane illumination microscopy (SPIM) to record the neuronal activity at near cellular resolution across the brain of 6 to 8 dpf *Huc:GCaMP5G* and *HuC:H2B-GCaMP6f* zebrafish larvae, embedded in agarose. The volumetric brain recordings were obtained by sequentially recording the fluorescence in 40 coronal sections spaced by 5 mm. For this purpose, the light sheet was scanned vertically in the dorso-ventral direction with galvo mirrors, in synchrony with the objective of the emission path, that was translated in the z-axis with a piezo. The camera was triggered to acquire an image every 10 ms. Once the 40 coronal sections were recorded, the position of the light sheet and the objective of the emission path was reset to their initial dorsal position, with a flyback time of 70 ms.

The acquisition time for a whole volume was therefore 0.47 s, corresponding to a rate of 2.1 Hz. Due to the serial nature of the recording technique, each plane was recorded at a slightly different time. We also imaged single planes in the brain at 20 Hz, in order to monitor more finely the temporal dynamics of the neuronal activity.

Recording protocol

For this study we used three different datasets.

1. 3D recordings with *HuC:H2B-GCaMP6f* larvae. 8 larvae were recorded in the dark during 1h, with no salient sensory cues, except for the light-sheet itself which may provide unilateral visual stimulation.
2. 3D recordings with *HuC:GCaMP5*. 6 larvae expressing GCaMP5 were recorded during sessions lasting between 1 h and 7 h at a frame rate of 2.1 Hz. The experiment was composed of consecutive segments of 20 min of spontaneous activity and 4 min of visual stimulation. Each visual stimulation period contained 8 sub-episodes separated by 20 s, during which a moving grating was presented below the larva for 10 s at different angles (0°,60°,180°,-60°,0°, 60°,180°,-60°).
3. For the 2D recordings, 23 *HuC:GCaMP5* larvae were recorded at different depth in the brain at a frame rate of 20 Hz. Recordings lasted 2h20. The same visual stimulation protocol was used as in dataset 2.

For the study of spontaneous behavior, we removed all episodes of visual stimulation (datasets 2 and 3), with a margin of 30 s before and after each block of stimulation to avoid contamination by long lasting effects of the visual stimulation (fig 3.1).

Behavioral recordings

We removed the agarose around the eyes and tail of head-embedded larvae in the light-sheet recording chamber. The larva were illuminated with an infrared LED (NG50L 810 nm, BDlaser), and we recorded the locomotor behavior of the larva (tail and eye movements), using a small microscope (DZ 1/L.75-5, The Imaging Source) connected to a fast infrared camera (HXG20NIR, Baumer), at 300 Hz for dataset for datasets 2 and 3, and 5 Hz for dataset 1. From the binarized image of the larva, we extracted the tail curvature using the method described in Jouary *et al.* [Jouary and Sumbre, 2016].

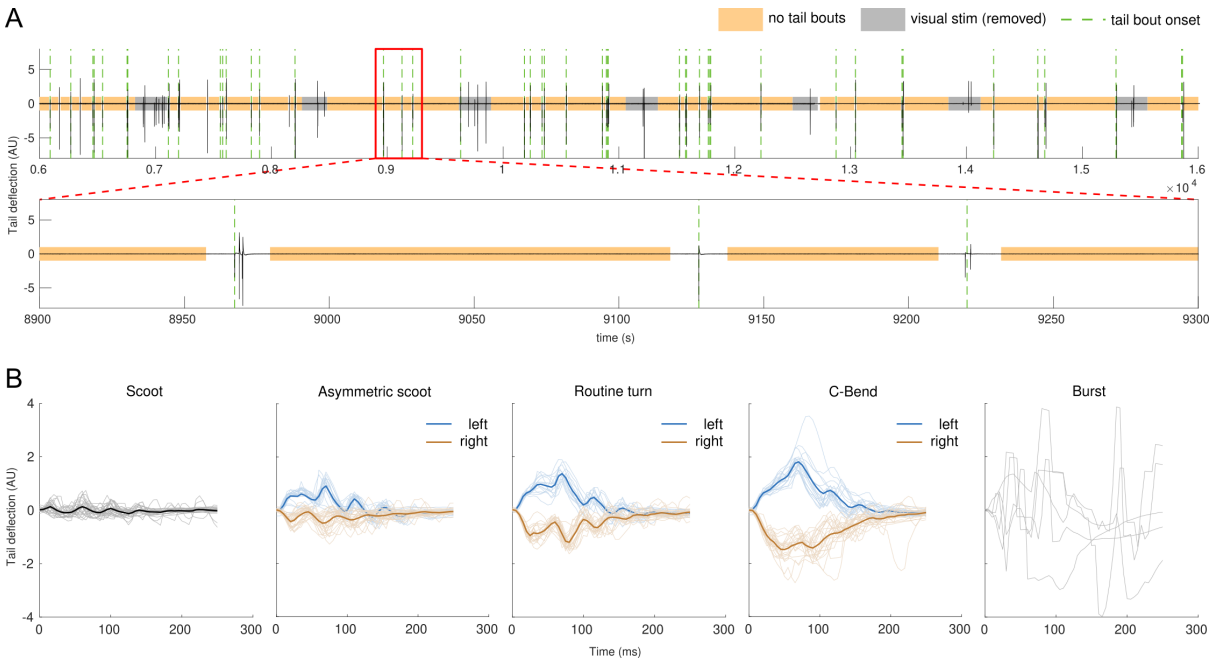

Figure 3.1: **Recording protocol and extraction of isolated spontaneous tail bouts**. **A**. Top: Tail deflection across 10000 s from the recording of one representative larva. Bottom: zoom on a 400 s interval (red box) showing isolated tail bouts, an intervals were the larva did not move its tail (yellow boxes). When tail bouts were chained together and spaced by less than 6 s, only the first tail bout was conserved in our analysis. The onsets of isolated spontaneous movements kept in our analysis are marked by green dotted vertical lines. Visual stimulations (gray boxes) elicited motor behavior, and were removed from our analysis. **B**. Bottom: Classification of tail movements for one larva into five categories: scoot, asymmetric scoot, routine turn, C-bend and burst. Movements to the left are represented in blue, and movements to the right in dark orange.

3.2.3 Data preprocessing

Image registration

The first step consisted in compensating for possible drifts in the horizontal plane. For this purpose, each frame was registered according to the maximal cross-correlation with a reference frame. The reference frame was the average of 10 s of activity were the larva did not move. The registered stacks were then manually inspected to evaluate the drift in the ventro-dorsal plane, a drift that could not be compensated. Experiments with such drifts were discarded. Movement artifacts were detected according to large deviations in the maximum of the cross-correlation between successive frames. All frames with large deviations were discarded, they mostly occurred during large tail movements.

Image segmentation

For dataset 1, the expression of GCaMP6f in the nucleus allowed the segmentation of individual neurons using a procedure consisting in a binary thresholding based on absolute pixel intensity and local image contrast followed by an iterative normalization and smoothing procedure [Kawashima et al., 2016]. For dataset 2 and 3, in order to include GCaMP5 signal in neuropil regions, individual regions of interest (ROIs) were defined, in each plane, as hexagons of side lengths equal to 6.3 μm, corresponding to an area roughly equal to a neuron's soma of the zebrafish larva. The advantage of using a hexagonal grid was to maximize the area of the brain covered by the ROIs. The neuropil and neuronal somata were not dissociated in the analysis. Hereafter we will refer to those segmented regions as regions of interest (ROIs).

Spatial normalization

In order to compare activity of neurons in 3D from multiple brain regions, we aligned the 3D recordings with a reference *Huc:GCaMP5* larva brain imaged with a confocal microscope (Leica SP5) at a resolution of 1.21 $\times$ 1.21 $\times$ 2.98 μm. We manually aligned the brain from the SPIM recordings with our reference brain by selecting landmarks in 3D with a custom made GUI interface written in MATLAB, and performed an affine registration (12 degrees of freedom) to register all our datasets in this common space (fig 3.2). Our reference brain can be further aligned to online brain atlases such as the ZBrain atlas [Randlett et al., 2015].

2D planes were also aligned to the same reference brain using manually selected landmarks followed by a manual fine tuning of the affine registration.

Extraction of the fluorescence signal

In each ROI, the fluorescence time signal was extracted by evaluating the average intensity across the pixels in each hexagon for each registered image. A smooth estimate of the fluorescence baseline $B(t)$ was calculated for each ROI by computing the 30 s-long running average of the 8^{th} percentile of the raw data of the fluorescence signal $F(t)$ [Dombeck et al., 2007]. Importantly, the smooth baseline was estimated at each time point using activity before that time point. This causal estimation of the baseline ensures that premotor activity cannot be contaminated by the signal occurring during movements. We then computed the relative variation in fluorescence intensity for each ROI:

$$\frac{\Delta F}{F} = \frac{F(t) - B(t)}{B(t)}$$

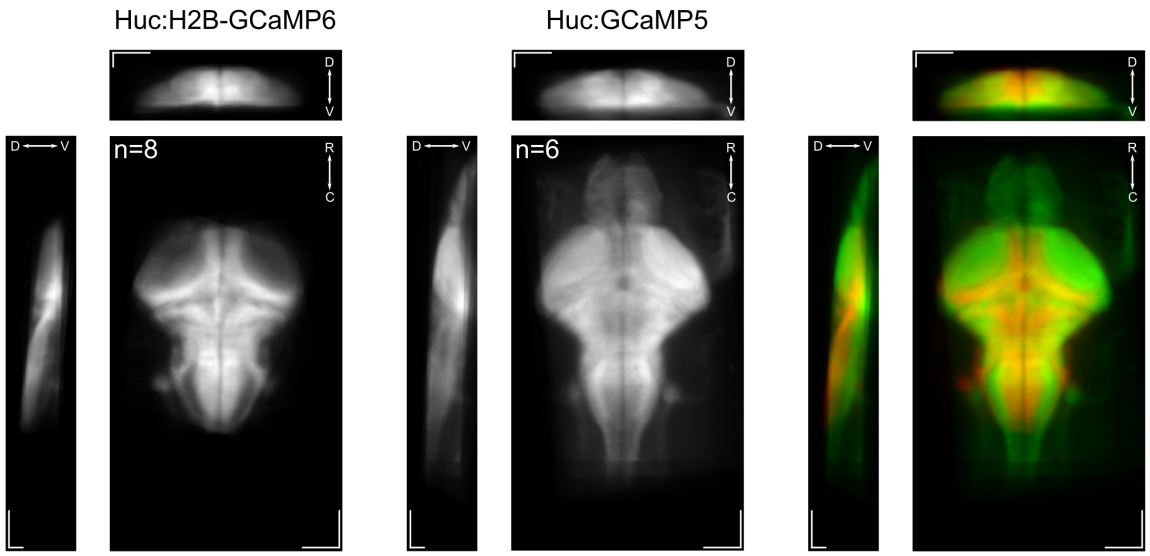

Figure 3.2: **3D registration to a common reference brain**. The 3D recordings from 8 HuC:H2B-GCaMP6 larvae (left) and 6 HuC:GCaMP5 larvae (middle) were aligned manually to a common reference brain using an affine registration procedure. The 14 larvae are overlaid on top of each other (right) for comparison (red HuC:H2B-GCaMP6, green HuC:GCaMP5). Scale bar 100 μm.

where F is the raw fluorescence, and B is the smooth baseline estimate.

Detection of significant calcium events

For a given ROI, the distribution of the relative variation in fluorescence is the result of two sources: noise in the recording and signal due to neural activity. Since neural activity results only in an increase of fluorescence, the distribution of $\Delta F/F$ is skewed to the right in active ROIs (fig 3.3). In contrast, the leftmost part of the distribution corresponds to random fluctuations in the fluorescence when the ROI is inactive, and can be used to infer the level of noise σ, and compute a threshold to detect significant calcium events. To infer the timing of significant calcium events, we fitted the negative part of the distribution with a normal distribution. We then binarized the activity of each of the cells by thresholding the fluctuations of fluorescence intensity $\Delta F/F$ with a threshold equal to 3σ [Romano et al., 2017]. ROIs with noise poorly fitted by a Gaussian ($R^2 < 0.9$), or with large-noise level ($\sigma > 0.015$) were discarded. Above this threshold the activity was set to 1, otherwise it was set to 0.

Classification of tail movements

Tail bouts were classified into 5 different categories: scoots, asymmetric scoots, routine turns, C-bends and bursts. We used dynamic time warping to measure similarity between

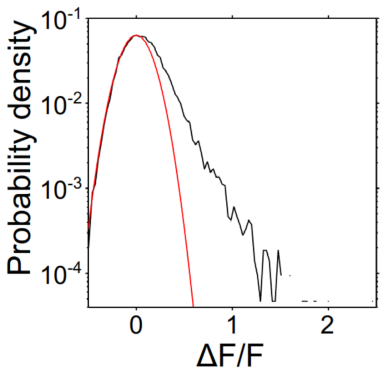

Figure 3.3: **Significant calcium events**. Probability density of relative change in fluorescence ($\Delta F/F$) of a typical neuron (black) and the corresponding Gaussian fit to its negative $\Delta F/F$ values (red), used to estimate the standard deviation (σ) of the baseline. From [Romano et al., 2015].

bouts and a fuzzy k-nearest neighbors algorithm to classify bouts into these 5 categories. The directionality (left/right) of asymmetric tail bouts (asymmetric scoots, routine turns, C-bends) was also recovered using the integral of the cube of the curvature time series (this gives more weight to large curvature values while preserving the sign). An example of this classification is shown in fig 3.1. The details of the method are described in [Jouary and Sumbre, 2016]. For the analysis of spontaneous tail bouts, only tail bouts that were isolated by at least 6 s from previous motor activity were kept to ensure that pre-motor neural activity truly reflects spontaneous motor preparation.

3.2.4 Data processing

Null model

In order to get a reference for the levels of activity and variability for each ROI, we extracted stretches of activity away from any visual stimulation (at least 30 s) or motor activity (at least 6 s) to compute a null model. We will call those stretches of activity null trials as opposed to trials defined by the occurrence of tail bouts.

We estimated the average level of activity and variability across null trials by selecting 1000 different random subsets of K null trials without replacement, where K is the total number of tail bout trials, and computing the distribution of the average activity and standard deviation across null trials, averaged across time points for significant calcium events, and for the relative change of fluorescence $\Delta F/F$.

We used this null model to implement a mass-univariate non-parametric testing strategy, but it should be noted that we did not implement a procedure to control the false discovery rate.

Percentage of active ROI, probability of activity, Z-score

The probability of activity of each ROI before the onset of isolated spontaneous movement was computed by averaging significant calcium transient over trials at each time point before the onset of movement. Let $R(t, n, k)$ denote the occurrence of a significant calcium event at time t, for neuron n and trial k, where the values taken by R are either 0 (no significant calcium transient) or 1 (presence of a significant calcium transient). The probability of activity before trial P is:

$$P(t, n) = \frac{1}{K} \sum_{k=1}^{K} R(t, n, k)$$

where K is the total number of spontaneous tail bouts. Based on the null model, we then define significant probability of activity P_{signif} as:

$$P_{signif}(t, n) = \begin{cases} P(t, n), & \text{if } P(t, n) > p_{99}(n). \\ 0, & \text{otherwise.} \end{cases}$$

where $p_{99}(n)$ is the 99^{th} percentile of the probability of activity across null trials, averaged across the 1000 random subsamples (see null model).

We also compute the percentage of active ROIs A for each trial as:

$$A(t, k) = \frac{1}{N} \sum_{n=1}^{N} R(t, n, k)$$

where N is the total number of ROIs.

From those two variables we compute the trial averaged percentage of active ROIs $\langle A \rangle_{trial}$ as:

$$\langle A(t) \rangle_{trial} = \frac{1}{K} \sum_{k=1}^{K} A(t, k)$$

and the population average of the probability of activity as:

$$\langle P(t) \rangle_{ROI} = \frac{1}{N} \sum_{n=1}^{N} P_{signif}(t, n)$$

Finally, in addition to the binarized activity, we also used the null model to compute the normalized activity $Z(t, n, k)$ computed as:

$$Z(t, n, k) = \frac{\Delta F/F(t, n, k) - \mu(n)}{\sigma(n)}$$

where $\mu(n)$ and $\sigma(n)$ represents respectively the average $\Delta F/F$ and average standard deviation of the $\Delta F/F$ across trials for ROI n during null trials, averaged over time and random subsamples.

Reconstruction of 3D activity from 2D planes

For each larva in the dataset 3, regions of interest in a 2D plane were registered to a reference 3D volume (see Spatial normalization). The probability of activity P_{signif} was averaged between larvae for ROIs in the same 3D location for each time window, and the results were smoothed using a 3D gaussian filter with a standard deviation of 3.63 $\mu m \times 3.63$ $\mu m \times 8.94$ μm.

3D density maps

3D density maps were computed from the position of groups of neurons selected according to some criterion. We used multivariate kernel density estimation on a downsized grid (half the size of our reference volume in XY) with a fixed bandwidth of 6.05 $\mu m \times$ 6.05 $\mu m \times 14.9$ μm,followed by a cubic interpolation to upsample the data back to its original size.

3.3 Contribution statement

Dataset 1 was recorded and pre-processed by Emiliano Marachlian. Datasets 2 and 3 were recorded by Adrien Jouary and pre-processed by Adrien Jouary and Ruggero Bettinardi. Ruggero Bettinardi analyzed dataset 3 and created the figures 3.4 and 3.5. I realized the 3D spatial normalization to a common reference brain for 3D recordings, analyzed datasets 1 and 2 and created the figures 3.1, 3.2, 3.6, 3.7, and 3.8.

3.4 Results

3.4.1 Extracting isolated spontaneous movements

In order to study the neuronal mechanisms underlying the generation of spontaneous movements, we recorded the neuronal activity of zebrafish larvae expressing the calcium indicators GCaMP5 and GCaMP6f with a light-sheet microscope. The larvae were restrained in a drop of low melting agarose but the tail was left free to move. To correlate neuronal activity with behavior, we recorded movements of the larva's tail with a high

speed infrared camera. The recordings lasted at least 1 h in order to record enough spontaneous tail movements of the larva (see Methods).

To study both the fine temporal dynamics of pre-movement activity and large scale network activity throughout the whole brain of the larva, we recorded series of horizontal sections at 20 Hz at different depth in the brain (23 larvae), as well as whole-brain activity at 2.1 Hz (14 larvae).

The larvae were recorded in the dark and were free to move their tail spontaneously. Some of the recordings were interspersed with episodes of visual stimulation (see Methods) consisting in moving gratings projected below the larva at different angles, a stimulus known to elicit a visuomotor behavior called the optomotor response [Orger et al., 2008]. The experimental design will allow us to compare the mechanisms underlying the generation of spontaneous tail movements with those driving visuomotor behavior. Hereafter, I will only focus on spontaneous activity, and visual stimulation episodes were removed from our analysis (fig 3.1).

Zebrafish larvae move their tail in discrete bouts of activity, and often tend to chain together bouts during short interval of times [Johnson et al., 2020, Jouary, 2015]. To disentangle neuronal activity related to the generation of spontaneous tail movements from ongoing motor activity, we focused our analysis on spontaneous movements that were isolated from other movements by at least 6 s (fig 3.1).

3.4.2 Probabilistic activation of hindbrain circuits before spontaneous movements

Our first attempt to describe the neuronal activity preceding spontaneous tail movement was to try to find ROIs with ramping activity before movements at the single trial level. We used different analysis techniques such as linear regression, or using the Spearman correlation coefficient between the activity of each neuron and the time to the onset of movements to account for non-linear but monotonic increase in activity. We found some ROIs with a ramping profile but we failed to find robust populations of ramping neurons across larvae (data not shown). While it is possible that there is a sparse network of neurons with ramping activity instead of well-defined ramping regions, we did not pursue this analysis further as we did not find a statistically sound way to ensure that the ramping activity we saw was not a fluke in a rather large neuronal population.

However, we realized that some ROIs were more likely to be active during a time window of a few seconds before the onset of movements in some trials, so we looked at the probability of activity for each ROI before the onset of movement, as well as the percentage of active ROIs across the whole optical section recorded (fig 3.4) in 23 larvae

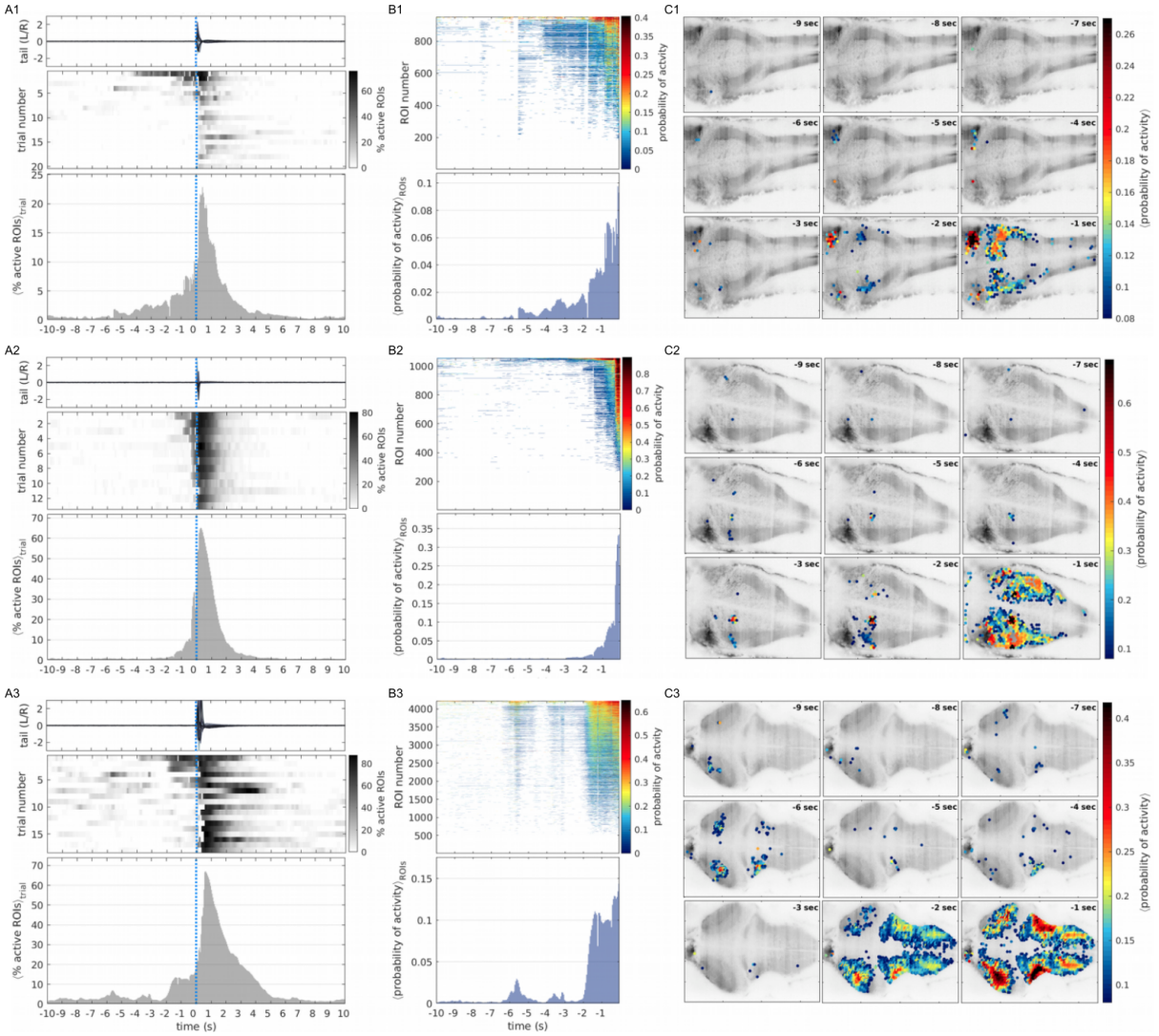

Figure 3.4: **Probabilistic activation of hindbrain and tectal networks before spontaneous tail movements**. The results for 3 different larvae recorded at different depths are presented. **A1-A3**. Top: Tail isolated tail movements aligned at their onset. Middle: temporal dynamics of the percentage of active ROIs for each spontaneous tail bout (trial). Bottom: temporal dyanamics of the average percentage of active ROIs across trials. **B1-B3**. Top: temporal dynamics of the probability of activity for each ROI above a threshold defined by a null-model. Bottom: temporal dynamics of the network average of the probability of activity before spontaneous tail bouts. **C1-C3**. Topography of the above-threshold probability of activity averaged over 1 s time windows before the onset of spontaneous tail bouts. Courtesy of Ruggero Bettinardi.

recorded at 20 Hz, at different depths in the brain. To ensure that the probability of activity reflected a significant increase before the onset of movements, we built a null model based on neuronal activity during periods of motor inactivity (see Methods). The probability of activity across trial was set to zero for each ROI if it did not exceed the 99^{th} percentile of the probability of activity for that ROI in the null model. We found a gradual increase in the fraction of cell active before the onset of movements across trials (fig 3.4.A1-A3), associated with an increase in the probability of activity in the whole

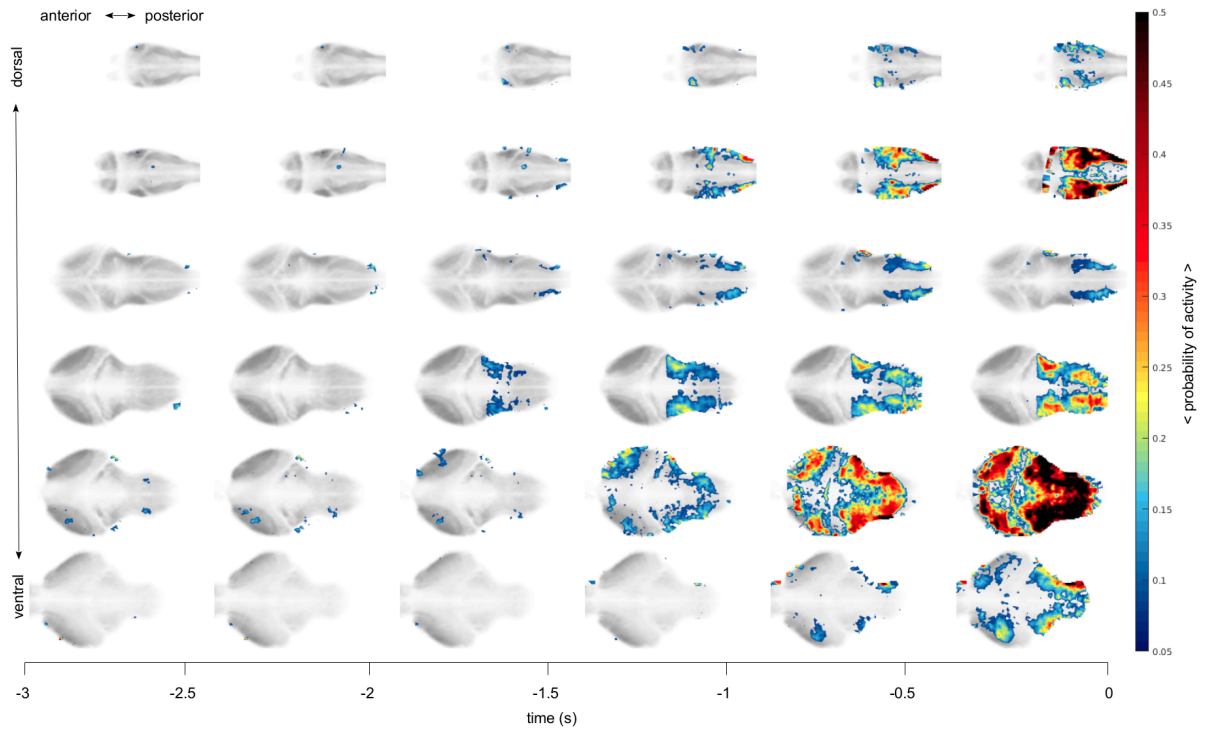

Figure 3.5: **3D reconstruction of the temporal dynamics of the probability of activity before spontaneous tail bouts**. The topography of the probability of activity before the onset of spontaneous tail bouts was pooled over 23 2D recordings in different larvae at different depths, aligned to a reference 3D brain, averaged over 500 ms time windows and spatially smoothed with a 3D gaussian filter. Courtesy of Ruggero Bettinardi.

network (fig 3.4.B1-B3).

This increase in the probability of activity close to the onset of spontaneous movements was observed in the hindbrain, especially in the neuropil regions of the vagal lobe and a group of cells lying medially to the vagal lobe neuropil, and in the lateral neuropil of the rostral hindbrain (octaval nuclei), as well as in the optic tectum (fig 3.4.C1-C3), up to 2 s before the onset of movement at least. This was further confirmed by pooling all 23 larvae together after aligning them to a common 3D reference brain (fig 3.5).

While those 23 larvae covered a large portion of the hindbrain, parts of the ventral hindbrain, tegmentum and forebrain were absent from the recordings. It was also impossible to study the flow of information between regions at different depths in the 2D recordings so we decided to record whole-brain neuronal activity to remedy those issues, at the expense of a lower temporal resolution.

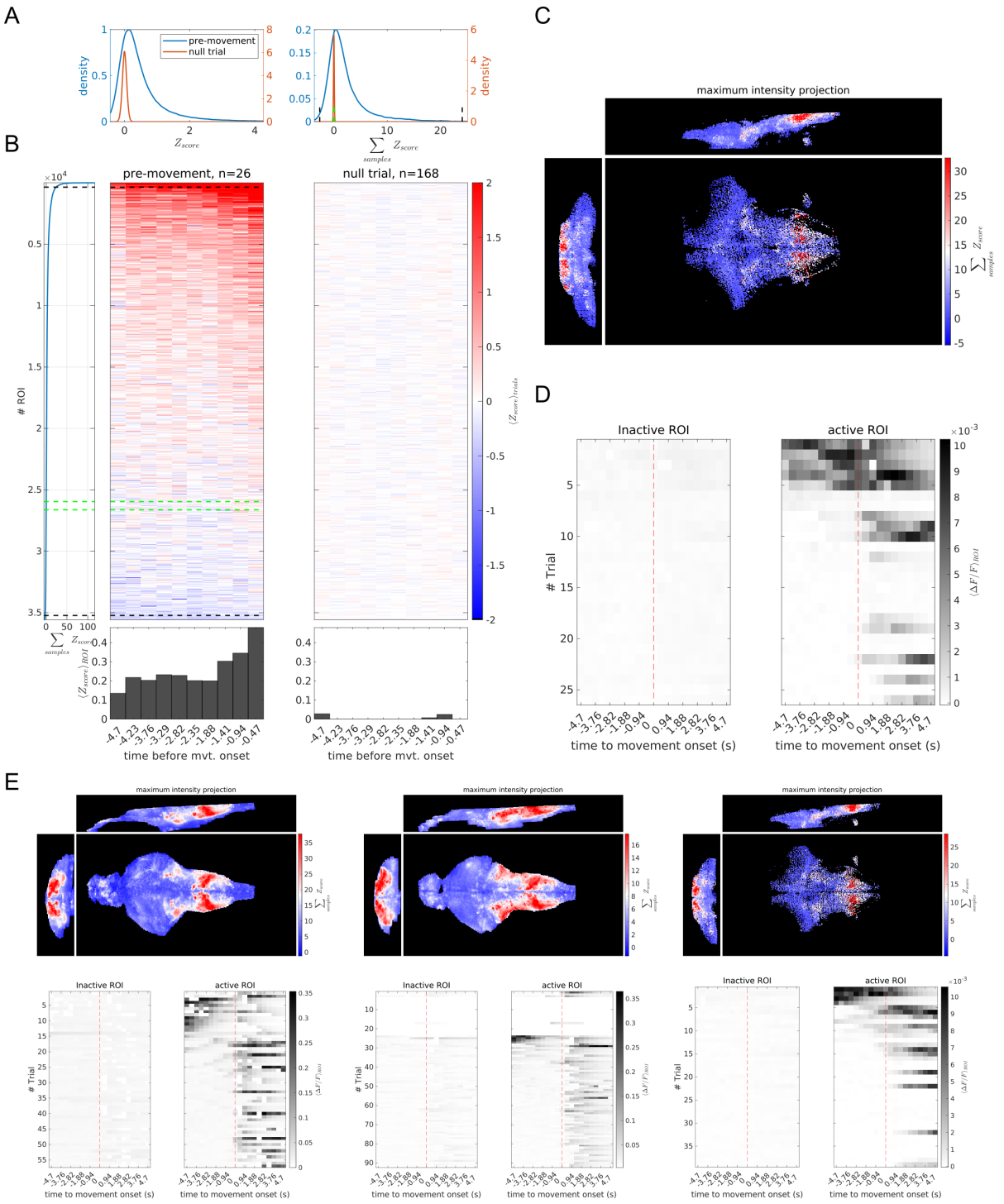

Figure 3.6: **Whole-brain pre-movement activity before spontaneous tail bouts**. **A**. Left: distribution of Z-scores before spontaneous tail movements (pre-movement, blue) and during intervals of corresponding length with no tail activity (null trials, orange) for one larva. Right: distribution of the sum of Z-scores across the 4.7 s time window before the onset of spontaneous tail bouts (blue), and null trials (orange) for the same larva. (legend continued next page)

3.4.3 Comprehensive 3D mapping of spontaneous pre-movement activity

To identify ROIs that were active before the onset of spontaneous movements, I normalized the relative change of fluorescence $\Delta F/F$ by using an estimate of the levels of activity and variance for each neurons in the null model to obtain Z-scores. The procedure is similar to the one used to compute the probability of activity, but using the full range of values of $\Delta F/F$ instead of the binary values of the significant calcium events. In theory this approach could enable us to find neurons which are inhibited during the pre-movement period, but in practice we did not find any coherent population of ROIs with decreased activity with respect to the null model during that period.

The distribution of Z-scores was right skewed for the period of preparatory activity before the onset of spontaneous movements, in comparison to the distribution of Z-scores during null trials (fig 3.6.A), indicating an excess of activity with respect to the null model. To identify ROIs that were the most active during that preparatory period, I summed all the Z-scores across a time window of 4.70 s preceding the onset of movements. We classified the top 5% of ROIs with the largest sum of Z-scores as active ROIs, and the ROIs lying between the 25^{th} and 75^{th} percentiles of the null distribution of Z-scores as inactive ROIs (green dotted lines, fig 3.6.A,B).

As for the 2D recordings, we observed a widespread average increase in activity before the onset of spontaneous movements with respect to the null model (fig 3.6.B). In agreement with the results in the 2D recordings, we found that the active ROIs were located in the vagal lobe, as well as in the rostrolateral hindbrain neuropil (octaval nuclei), and

Figure 3.6 (continued): The top 5% of ROIs with the largest sum of Z-scores (dotted black line on the right, see also B) were categorized as active ROIs (see D,E), while the ROIs with a sum of Z-scores lying between the 25^{th} and 75^{th} percentile of the null distribution of the sum of Z-scores (green dotted lines, see also B) were categorized as inactive ROIs (see D,E). **B**. Top: Temporal dynamics of the Z-scored neuronal activity before spontaneous tail movements (middle) and during null trials (right) averaged over trials for one larva. ROIs were sorted according to the sum of Z-scores across the 4.7 s time window before spontaneous tail movements (left). Black dotted lines correspond to the 5^{th} and 95^{th} percentile of the distribution of the sum of Z-scores before the onset of spontaenous tail bouts, geen dotted lines correspond to the 25^{th} and 75^{th} percentile of the null distribution of the sum of Z-scores (see A). Bottom: temporal dynamics of the network average of Z-scores before spontaneous tail bouts (left), and null trials (right). **C**. Topographic map of the sum of Z-scores during a 4.7 s time window before the onset of spontaneous tail bouts. **D**. Temporal dynamics of the population average of normalized activity around the onset of spontaneous tail bouts for the inactive and active groups of ROIs (see A,B) for each trial. **E**. Same as C and D for 3 other example larvae.

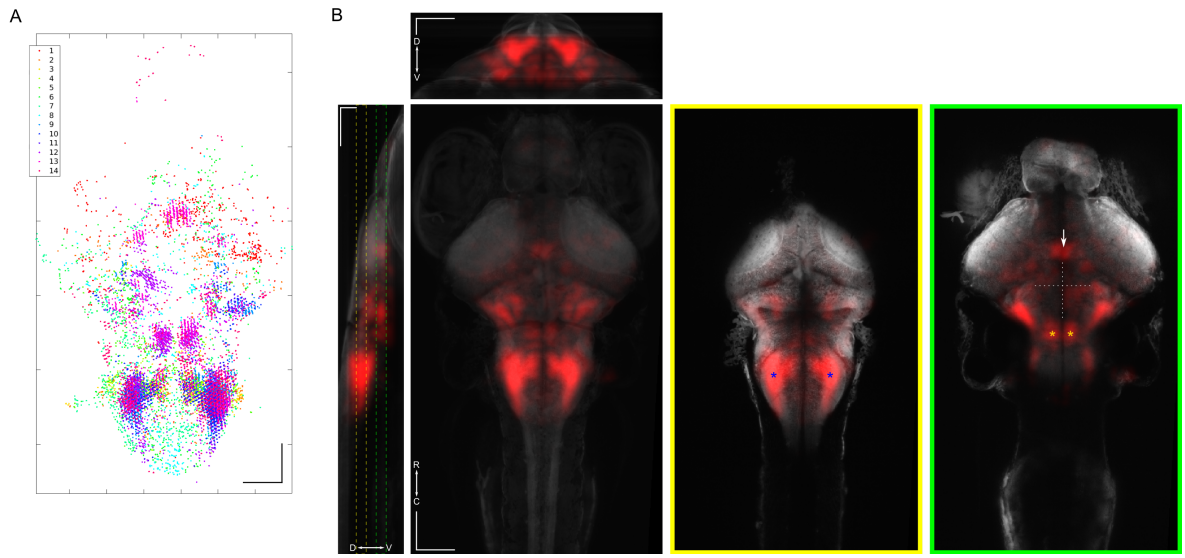

Figure 3.7: **Topography of active ROIs before spontaneous tail bouts**. **A**. Position of the ROIs active before the onset of spontaneous tail movement from 14 larvae, projected along the Z axis. **B**. 3D density of the ROIs in A estimated with a multivariate kernel density estimation procedure. The Z projection of the green and yellow dotted sections on the lateral projection (left) are shown in the green and yellow boxes on the right. Blue asterisks: vagal lobe. Yellow asterisks: paired ventral structure that may belong to the reticular formation. White arrow, isthmal or tegmental area lying close to the nucleus of the medial longitudinal fascicle. White dotted line, separation between rhombomeres 1 and 2 (horizontal) and midline (vertical). Scale bar 100 μm.

more diffusely in the isthmus and tegmentum areas (fig 3.6.C,E). However, we did not find many active ROIs in the optic tectum in the 3D recordings. It could be due to the fact that we normalized the activity by the variance for the 3D activity, while we just put a threshold on the probability of activity for the 2D recordings. The optic tectum is a region that displays a large variance. Using a multivariate kernel density estimation procedure, we estimate the density of active ROIs in the whole brain by pooling the positions of the active ROIs across all 14 larvae (fig 3.7): we identified the vagal lobe (blue asterisks, fig 3.7.B), a paired ventral structure that may belong to the reticular formation (yellow asterisks, fig 3.7.B) as well as an area in the rostral tegmentum (white arrow, fig 3.7.B) which lies close to the posterior tuberculum, pretectum, nucMLF, occulomotor nucleus (nIII) and caudal thalamus/preglomerular complex.

Finally we also confirmed that the active ROIs did not necessarily display a ramping dynamics (fig 3.6.D,E), and were not recruited for all trials (fig 3.6.D,E).

3.4.4 Mapping the flow of information during spontaneous premotor activity

Spontaneous motor activity could be generated by entirely dedicated circuits, or through the activation of neural circuits used for sensorimotor behaviors. In order to better understand the flow of information before the onset of spontaneous movements, we computed the cross-correlation of active ROIs with the rest of the brain for all 14 larvae. We selected the top 5% of the most correlated cells for negative (fig 3.8.A,left) and positive lags (fig 3.8.A,right), and computed the average Z-score around the onset of spontaneous movement across larvae to estimate the average lag between those populations of cells (approximately 1 s at the peak, fig 3.8.B).

Interestingly, in addition to different groups of ROIs in the hindbrain, we found that the telencephalon may be active before the group of most active ROIs that we identified earlier, and functionally connected to that group of ROIs (fig 3.8.A). We also found activity in the left habenula after the activity of the group of active ROIs that we identified earlier (fig 3.8.A). It should be noted that these results are very preliminary and exploratory, and they warrant further experiments to determine the exact role of the telencephalon and habenula, which were not sampled in the 2D recordings, in the generation of spontaneous tail bouts.

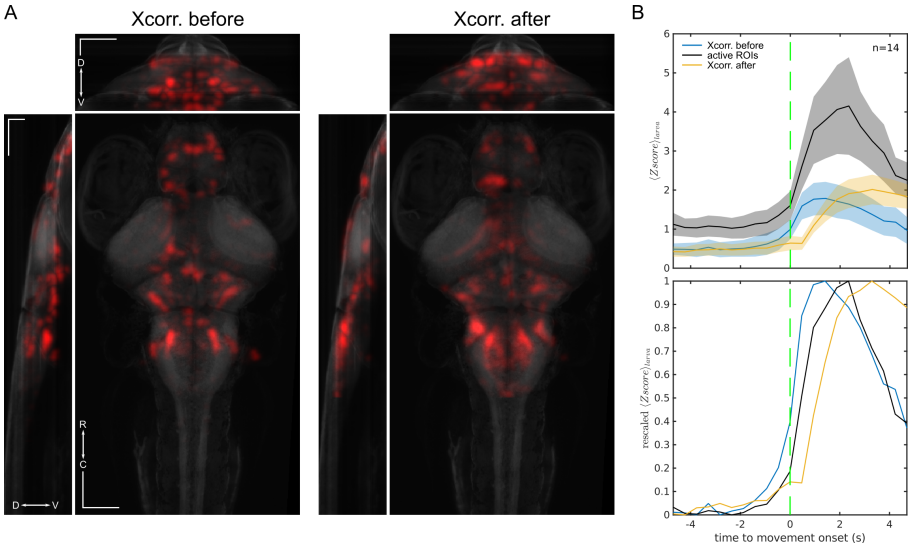

Figure 3.8: **Information flow between regions active before spontaneous tail bouts**. **A**. Topography of the 5% ROIs most cross-correlated to the active ROIs for negative lags (left, up to -10 s) and positive lags (right, up to +10 s) across the whole recording for the 14 larvae. **B**. Average activity across the 14 larvae of the active ROIs as the ROIs identified via cross-correlation (see A) around the onset of spontaneous tail bouts. Top: average and standard error of the mean across larvae. Bottom: rescaled normalized activity. Scale bar 100 μm.

4

Conclusions and perspectives

4.1 Sensorimotor integration in the auditory system

The first part of my PhD was dedicated to the study of the sensorimotor integration of auditory stimuli by the zebrafish larva to generate long latency tail movements (LLTMs), a previously undescribed behavior. In this section, I will summarize and discuss the results found in our article "Sensorimotor Transformations in the Zebrafish Auditory System".

4.1.1 A low dimensional representation of frequency, conserved throughout early development

Two frequency channels with spatially segregated representations In order to understand the mechanisms underlying sensorimotor integration in the zebrafish larva auditory system, I first set out to map sound representations of frequency. I designed and 3D-printed a recording chamber with an array of waterproof speakers to record the neural activity of head-embedded larvae, expressing the cytosolic GCaMP5 sensor, with a two-photon microscope. Neural activity was recorded while monitoring motor behavior of the tail and delivering pure tone stimuli.

I found sensory-evoked activity in the octaval nuclei and torus semicircularis, as well

as in the lateral part of the cerebellum (eminentia granularis) and a small group of ROIs close to the lateral lemniscus which could be the paralemniscal nucleus. These locations are consistent with previously observerd sound responses in larval zebrafish [Olive, 2015, Vanwalleghem et al., 2017, Poulsen et al., 2020, Favre-Bulle et al., 2020, Constantin et al., 2020] as well as other teleost species [McCormick, 1999]. I did not observe responses in the pallium, thalamus, or the deep optic tectum as in studies from the group of Ethan Scott [Thompson et al., 2016, Vanwalleghem et al., 2017], but those areas were unfortunately poorly sampled in my data. To characterize the diversity of the auditory response profile in my data, I performed a clustering analysis using the k-means algorithm at different developmental stages. Different clustering methods yielded similar results, and indicated a low number of response profiles. To represent the variability in the data, I selected 4 clusters, which suggest a low-dimensional representation of frequency information, with two main frequency bands (150–400 Hz and 950–1000 Hz). While the separation between the 4 clusters is a bit arbitrary, this separation between low frequency and low+high frequency seemed robust, as it goes along the direction that explains the largest amount of variance in the data (supported by the first principal component of the matrix of normalized tuning curves, see Fig S5.B). A crude analysis using PCA to reveal network trajectories during stimulations also revealed that it should be possible to discriminate between low and high frequencies at the population level (data not shown). The spatial distribution of these two channels suggested that high frequency representation was predominant in the midbrain, while low frequency information was more distributed between the midbrain and hindbrain, suggesting a potentially different ethological relevance for those two frequency bands.

Mid-range frequency gap (450–900 Hz) Interestingly, frequencies in the mid-range were not represented at all in the brain for the 155 dB *re.* $1\mu Pa$ stimulus. However, some fish responded in that frequency range at higher sound intensities (Fig S3). There are several potential explanations for this. One could be that the two channels I observed reflect different sensitivities at the auditory periphery, for instance between groups of hair cells, as suggested by Furukawa *et al.* in the goldfish saccule [Furukawa and Ishii, 1967], or between sensory epithelia of the saccule and utricule. Scott and colleagues have built an optical trap system that allows to stimulate independently the saccular and utricular otoliths, which may help to clarify this issue [Favre-Bulle et al., 2020]. The issue could also be resolved by performing the mapping of auditory response in mutant lacking an otolith such as *rock solo* [Mo et al., 2010], or by surgical removal of the otoliths. A second possibility could be that these two bands correspond to a switch in auditory sensitivity between particle velocity and pressure levels, the two components of underwater sound sensed by fish [Higgs, 2020]. The swim bladder of some fish can increase sensitivity to higher frequencies by contacting the inner ear *via* the Weberian ossicles, a small chain

of bones. 7 days old larvae have not yet developed the weberian ossicles necessary for the transduction of sound from the swim bladder (supposed to be sensitive to pressure level changes at high frequency) to the inner ear [Higgs et al., 2003, Zeddies and Fay, 2005], which makes that second hypothesis unlikely, unless young larva have other means to sense pressure level changes. A third explanation could be that the actual stimulus delivered to the ear of the fish was weaker in the mid-range frequencies. The stimulus chamber was calibrated with an underwater hydrophone and an accelerometer to equalize all presented frequencies (Fig S1), but the agarose gel around the head could differentially filter the frequencies. I did some pilot experiments where I removed the agarose around the ears, which didn't drastically increase responses in the mid-range (data not shown). Another way would be to embed some markers in the gel and measure the small vibrations of the marker during auditory stimulation with a fast camera, or find a way to directly measure the vibrations of the otoliths, which is probably not trivial. Finally, the fact that I averaged the fluorescence changes over hexagonal ROIs, mainly in neuropil region may obscure a bit the diversity of auditory responses. It is possible that frequency representations are a bit richer if we look only at cell bodies. Projections in the neuropil on the other hand could be well separated (labelled-lines) or completely intermingled. I tried to vary the size of the hexagons that I used during my analysis, and this didn't change the profile responses that I saw (data not shown), which could indicate that averaging over ROIs may not affect the results. A 2017 article suggested that auditory responses were scarce above 400 Hz [Vanwalleghem et al., 2017]. This finding could be consistent with the audiograms I recorded, since this is the range where larvae are the most sensitive (Fig S3). A more recent study suggests that zebrafish larvae could hear up to 4 kHz [Poulsen et al., 2020], and did find responses in the 400–900 Hz range. They do not however provide in-water measurement of sound pressure level and particle acceleration, which makes it hard to compare to my results.

Comparison with vestibular and lateral line processing The regions involved in the processing of auditory information seem extremely similar to the regions recruited during vestibular [Bianco et al., 2012, Migault et al., 2018, Favre-Bulle et al., 2018] and lateral line stimulations [Vanwalleghem et al., 2020]. However, these regions may not be recruited similarly: excitation of the left and right otoliths may be crucially different during vestibular stimulation, while both otoliths should move in a similar manner during auditory stimulation. The temporal dynamics of the neural activity may also be different when driven by vestibular (less than 10 Hz) versus auditory inputs. Lateral-line activity seems to be particularly tuned to head-to-tail water flow, which may enable the larvae to escape from the attack of predators using suction feeding from behind them, but also to allow a fine control of swimming and navigation [Vanwalleghem et al., 2020].

4.1.2 Long latency tail movements (LLTMs)

During my thesis, I have found a new type of auditory induced behavior, that I named long latency tail movements (LLTMs). These movements are generated by low amplitude, low frequency stimuli (150–450 Hz). This behavior is not mediated by the Mauthner-cells, and is characterized by a larger variability in terms of movement kinematics (data not shown), onset latency (Fig 5), and probability of response, in comparison to previously described escape behaviors [Burgess and Granato, 2007b]. However, this result should be strengthened by a more comprehensive characterization of the kinematics of LLTMs, as well as a proper demonstration that they are not mediated by the Mauthner cells, *e.g.* by ablating the Mauthner cells. The variability in latency and probabilistic nature of the release of behavior is interesting since it suggests a more complex processing of auditory information in the brain (with respect to the escape response), potentially some form of evidence accumulation, and decision-making mechanisms that lead to the generation of movements in some but not all instances. The dependence of the variability of LLTMs (kinematics, latency, probability) on the intensity of the stimulation should also be investigated further: is there a gradual transformation of LLTMs into C-bends (escape response), or a more abrupt change corresponding to the threshold of activation of the Mauthner cells? Our description of LLTMs is strikingly similar to results reported by Bhattacharyya and colleagues in the visual system of the zebrafish larva [Bhattacharyya et al., 2017]. They show that fast looming stimuli evoke either freezing, or short-latency escapes mediated mostly by the Mauthner cells, while slow looming stimuli produce long-latency, kinematically variable movements mediated by alternative reticulospinal circuits. They propose that this organization could reflect the assessment of threat, to produce a graded and proportionate behavioral response. Whether similar mechanisms and purpose are shared by auditory LLTMs and the long-latency visual escape behaviors remains to be investigated. Finally, a population of prepontine hindbrain neurons lying medially to the octaval nuclei neuropil has been identified for its role in the generation of non-mauthner mediated escapes [Marquart et al., 2019]. This population projects to the eminentia granularis, and may correspond to the population of motor-related neurons in the octaval nuclei identified in my study.

4.1.3 Circuits involved in the sensorimotor transformation

Motor circuits engaged in spontaneous and sensory-evoked behavior Low-amplitude auditory stimuli were able to trigger behavioral responses with a probability below 40% for the different type of stimuli used. This property is ideal for studying the neural circuits involved in the sensorimotor integration. To do so, I constructed a new set of regressors in my linear regression approach to capture the variability in neuronal

activity correlated to tail movements. All movements (both spontaneous and evoked by auditory stimuli) were considered when fitting the model. I tried fitting models with separate components for spontaneous and motor behavior, which yielded very similar results (data not shown), suggesting that the same motor circuits, at least at the level of the hindbrain, are involved in the production of self-generated and stimulus-evoked locomotor behavior (see also Fig S7.A-C). We found motor responses in the cerebellum, the rostro-lateral octaval nuclei the reticular formation, and the nucleus of the medial longitudinal fascicle (nMLF).

Sensorimotor processing at the cerebello-octaval boundary and in the nMLF To understand the mechanisms underlying the sensorimotor transformation, I took advantage of the fact that LLTMs are not generated for every stimulus. If every stimulus generated a movement, then only temporal aspects of the response could help us to discriminate between sensory-related and motor activity. Instead, in my dataset, ROIs could be differentially tuned to sensory or motor activity. I therefore classified the ROIs according to the percentage of variance in the fluorescence traces explained by sensory and motor signals (Fig 6A). I projected these values along a 1-dimensional axis, which allowed describing ROIs from purely motor to purely sensory responses (sensorimotor index). Sensorimotor ROIs (with mid-range sensorimotor indices) were observed diffusely in the octaval nuclei, at the boundary between the cerebellum and the octaval nuclei, as well as in the nMLF (Fig 6A). Sensorimotor ROIs were characterized by a larger activation during sensory evoked movements with respect to sensory activity that did not lead to locomotor behavior, and the onset of their activity followed the activation of purely sensory ROIs, and preceded the activation of purely motor ROIs.

4.1.4 Future perspectives

Temporal features of auditory stimuli Frequency is only one feature of auditory stimuli, but other features may be ethologically relevant for the larva. Our study does not take into account how the nervous system processes temporal modulations of sound frequency or amplitude. While calcium imaging is not the most suited technique to study fast temporal dynamics, special sound stimuli can be implemented such as presenting many stimuli with slightly different temporal features, like ramps in amplitude or frequency sweeps. Voltage dies, with a much higher temporal resolution, could also be used to study the temporal representation of frequency or amplitude modulation in the central nervous system, as well as enable the reconstruction of spectro-temporal receptive fields, which are believed to carry more information about what is processed by a neuron, especially in higher areas along the auditory hierarchy [Aertsen and Johannesma, 1980].

Refined circuit model for the generation of auditory induced LLTMs One of the main shortcomings of my article is the lack of a functional model to explain the sensorimotor integration process. I will review some of the brain structures we identified and speculate about their potential role in the sensorimotor integration process. Finally, I will propose a path to build a comprehensive circuit model that can account for both function and anatomy in the processing of auditory information.

The cerebellum could be involved in sensorimotor integration in two ways: most of the efferent projections from the cerebellum come from the eurydendroid cells, but there are also vestibulocerebellar projections that emerge directly from Purkinje cells [Bae et al., 2009] and innervate the octaval nuclei. Octaval inputs also project to the granule cells of the eminentia granularis in the lateral cerebellum [McCormick, 1999]. Purkinje cells are gabaergic, and could provide inhibition to the octaval nuclei and form the basis for a corollary discharge. This however does not seem completely coherent with our observation of increased duration of activity throughout the sensorimotor network during auditory-evoked behavior (Fig 7E). It would be useful to look at the activity of Purkinje cells and granule cells separately during acousticomotor behavior. This is possible using specific gal4 driver lines and enhancers that target those sub-populations [Knogler et al., 2017, Knogler et al., 2019]. We could for instance activate the Purkinje cells with channelrhodopsin and check if GABA is released in the octaval nuclei in a HuC:iGABASnFR larva [Marvin et al., 2019].

The nMLF is involved in the control of swimming speed and could steer the direction of swimming [Severi et al., 2014, Thiele et al., 2014]. It may be the final relay in the transformation of auditory inputs to motor signals sent to the spinal cord. Other reticulospinal neurons, particularly the vestibulospinal neurons, may be involved in the generation of movements. To properly identify which spinal projection neurons are involved in the generation of LLTMs, we could backfill those neurons with calcium dyes such as dextran-conjugated calcium green, and record their activity with a two-photon microscope [Orger et al., 2008].

Additionally, we could try to reconstruct the morphology of sensory, motor, and sensorimotor cells to study the connectivity between the octaval nuclei, torus semicircularis, cerebellum and reticulospinal system. We could try to do this by registering our data to a cellular resolution atlas [Helmbrecht et al., 2018, Kunst et al., 2019].

Since sensorimotor ROIs were found predominantly in regions of dense neuropil, we cannot exclude that the results we found do not emerge from averaging together purely sensory and purely motor activity. I believe that reconstructing the circuit piece by piece as I have proposed above should help to solve that ambiguity.

Finally, sensorimotor circuits were identified using a correlational approach, but we

don't know if sensorimotor ROIs play a causal role in the integration of auditory stimuli. We could try to test if sensorimotor ROIs are necessary and sufficient to generate LLTMs by activating them selectively by using channelrhodopsin expression in the whole brain coupled with patterned illumination with a DMD, or ablating them with a laser, while monitoring behavior. With all those elements in hand, we could propose a brain-wide model of acousticomotor integration in the zebrafish larva.

Basal ganglia and anterior hindbrain In many visuomotor behaviors, the anterior hindbrain in rhombomeres 1 and 2 (aHB[1-2]) was identified as a zone of sensorimotor convergence to drive downstream motor circuits [Chen et al., 2018]. I did not find activity in a similar region involved in acousticomotor integration. I can imagine two explanations: either acousticomotor behaviors use different circuits to mediate behavior, or alternatively the low level of expression of GCaMP5 in that brain area may have reduced the signal-to-noise ratio of the calcium signal preventing the detection of activity in aHB[1-2].

The basal ganglia are thought to play an important role in the generation of behavior in mammals. At the beginning of the last decade, there was an accumulation of evidence that both lampreys and teleost possess circuits homologous to the mammalian basal ganglia [Grillner and Robertson, 2016]. Yet, despite many articles describing whole-brain dynamics during various kind of behaviors in the zebrafish larva, none have emphasized an important role of a zebrafish basal ganglia homologue for the generation of behavior, to the best of my knowledge. This could be due to the position of the zebrafish striatum and posterior tuberculum, between the eyes of the larvae, that make them less optically accessible. My article makes no exception to this rule; while I may have imaged regions close to the posterior tuberculum, the striatum was not imaged in my recordings.

Temporal processing, evidence accumulation and decision-making In the last part of the article, I asked whether several features of the neuronal activity could help to explain what happens during the generation of auditory-evoked movements (Fig 7E). We found differences in the number of active cells, and the amplitude of the $\Delta F/F$ between stimulations capable of inducing movements and stimulations that failed to trigger a behavior, except for the sensory ROIs, which were not impacted by downstream motor outcomes. Nevertheless, we found that the duration of calcium events was increased in every part of the network, including the sensory ROIs. This increase in the duration of calcium events in the sensory ROIs could drive the sensorimotor integration as a result of a temporal integration of the sensory response (evidence accumulation). However, it is also possible that the increased duration of the sensory response is the consequence of a feedback from the motor system. I observed an increased latency in the onset of LLTMs with respect to the escape response, suggesting some additional neuronal processing, which

could favor the first hypothesis, but more proof is needed to reach a definitive conclusion. In order to do so, we will need to untangle the temporal dynamics of the response, unfortunately GCaMP5 is too slow for this. Genetically encoded voltage indicators could provide a solution to study the precise temporal dynamics of the accumulation of sensory evidence. It is however also possible that no decision-making based on evidence accumulation takes places, but rather that the observed probabilistic generation of behavior is just the result of a heightened sensitivity generated by the auditory stimulation on top of which noise in the neural dynamics could trigger behavior.

4.2 Spontaneous behavior

The second part of my PhD project was dedicated to the study of the neural mechanisms underlying the generation of spontaneous movements of the tail. One of the hallmarks of the generation of spontaneous movements in humans is the occurrence of a gradual buildup in activity called the readiness potential. We were not able to find such an increase in the neural activity at the single trial level, but we instead observed that some regions had a high probability of activity close to the onset of spontaneous tail bouts. Hereafter I will call these areas the pre-spontaneous tail bouts (PSTB) regions of interest.

One possible explanation could be that the generation of spontaneous movements is not governed by a single neuronal circuit, but that different categories of spontaneous movements are generated by different networks. This would suggest that there is some degree of overlap between the *when* (decision about the timing of movements) and *what* pathway (what action to perform). To shed some light into this issue, we recorded the kinematics of the tail with a good temporal resolution for 8 larvae, and we classified the recorded tail bouts into different categories and swimming direction (left/right). We plan to use this information to see if we find regions more robustly active before different categories of movements. Segregating the movements into left and right for instance may enable us to reveal the role of circuits known to play a role in biasing the direction of movements such as the anterior rhombencephalic turning region [Dunn et al., 2016a], whose activity may cancel out when averaging over both directions. A major challenge with such an endeavor is the relatively low number of tail bouts (especially when split across different categories) compared to the number of neurons, which makes any correlative analysis very prone to identify spurious associations. We will therefore need to develop stringent statistical tools to either implement some form of regularization (elastic net or other methods), dimensionality reduction (PCA-promax [Romano et al., 2015] or other), or to leverage the information we have about the location of neurons to identify neurons robustly active across fish in the same regions. One such approach has been proposed recently using a non-parametric technique called spatial P-values [Marques et al.,

2020], and could be applied to our data.

Another possibility is that the neural network that we identified are not directly causal for the generation of movements of the tail, but instead govern a process that is correlated with the generation of tail movements. I can think of two such possible mechanisms. (1) We know for instance that movements of the eyes and movement of the tail are correlated in the larva [Wolf et al., 2017], so it is possible that the regions that we observed are causing movements of the eyes, which in turn can induce tail movements. In 8 larvae we recorded the movements of the eyes at the same time as the tail and neuronal activity, so we will be able to check if the regions we identified are more correlated with eye movements or with tail movements. We did find a tegmental regions that could correspond to the occulomotor nucleus (nIII), but this remains to be confirmed. (2) The most active region before the onset of spontaneous tail bouts was in the vagal lobe. This region also contains motor neurons of the vagal nerve that innervate the viscera and the muscles of the pharyngeal arches which are used to move the pharynx, gills, and pharyngeal teeth [Barsh et al., 2017, Isabella et al., 2019]. Therefore the activity that we observed could be due to a correlation between movements of the pharyngeal muscles and tail movements, which may play some functional role in the fish for ventilation purposes [Burleson et al., 1992], or be due to the agarose embedding procedure as a response to hypoxia [Jonz and Nurse, 2005] or the mechanical constraint imposed by the gel. To test this hypothesis we could record the neural activity of zebrafish larvae in the vagal lobe while monitor both tail movements and the head of the larva with a better spatial resolution at the expense of a slower frame frame rate and try to track movements of the pharyngeal muscles. Additionally, we could also drive the expression of a red fluorescent protein under the control of the Islet1 promoter [Higashijima et al., 2000] in a GCaMP larva to identify cranial motorneurons.

Most of the PSTB regions were found in the hindbrain: in the vagal lobe, in a pair of ventral structures which could correspond to the Mauthner cells, and in the rostrolateral area corresponding to the octaval nuclei. We also found some active cells in the tegmentum, but they were found less robustly across larvae and may not have been sampled in all brains. To refine the identification of the regions active before spontaneous movements, we will need a better spatial normalization procedure with elastic deformation since some larvae are still slightly misaligned. We will then align the position of the ROIs active before spontaneous tail bouts to online atlases to try to identify their molecular identity, and compare them to hindbrain neurons known to be involved in the generation of behavior in the different stripes of the hindbrain [Kinkhabwala et al., 2011], in the hindbrain V2a population [Kimura et al., 2013], glycinergic poulation [Severi et al., 2018], the anterior rhombencephalic turning region [Dunn et al., 2016b], and prepontine neurons [Marquart et al., 2019].

Using a cross-correlation analysis we found ROIs whose activity precedes and follows the activity of the PSTB ROIs. Putative regions in the telencephalon could be active before the PSTB regions, while the left habenula seems to be active after the PSTB regions. The functional role of the telencephalon in the generation of behavior is not very well known in the zebrafish larva, but it contains regions homologous to the striatum which is active before spontaneous movements in primates [Schultz and Romo, 1992]. Other telencephalic regions could also be recruited for different cognitive processes involved in the generation of behavior as in mammals, although this is very speculative. The habenulae are a paired structure above the diencephalon that display a left-right asymmetry in the molecular identity, morphology and connectivity [Bianco and Wilson, 2009]. The habenulae regulate monoaminergic activity in the midbrain. This activity is important for the modulation of fear behavior, avoidance learning and attention [Agetsuma et al., 2010]. This analysis is still very prelimary, we still need to quantify the robustness of the association between the PSTB ROIs and the regions identified via the cross-correlation analysis. We are currently building a new light-sheet microscope with a second arm to illuminate the neurons between the eyes of the larva, which will enable us to have a better coverage of the telencephalon and habenula in future recordings.

During some of the recordings, we presented visual stimuli to the larva to elicit the optomotor response behavior. We will take advantage of these stimulation episodes to map the visuomotor circuits involved in the generation of the optomotor response in order to compare them with the circuits underlying the generation of spontaneous movements.

Finally, we will need to test the causal role of PSTB in the generation of tail bouts by activating or inhibiting the PSTB regions with optogenetics or laser ablations, while monitoring spontaneous movements of the tail.

4.3 Final conclusions

Spontaneous neuronal activity in the optic tectum closely matches behaviorally relevant features of sensory-induced activity in the zebrafish larva [Romano et al., 2015]. Whether spontaneous activity in sensory networks alone is sufficient to activate sensorimotor circuits normally recruited in response to a sensory stimulus is not known.

In my first project, I found similar patterns of activity in the circuits correlated with movements of the tail for auditory-induced behavior and spontaneous tail bouts (fig S7,A.B.C), which suggests that at least the most downstream portion of the motor hierarchy can be used by different neuronal circuits to generate behavior. Interestingly, in the second project, we also found activity before spontaneous tail bouts in the octaval nuclei and a tegmental area that could correspond to the nucleus of the medial longitudinal

fascicle.

Zebrafish larvae are unstable and need to maintain stability by adopting corrective actions. When left free to swim, zebrafish larvae will rotate nose-down during periods of inactivity, but will actively swim to maintain a nose-up posture: a large fraction of the tail bouts they generate occur when their position strays too much from an equilibrium [Ehrlich and Schoppik, 2017]. Therefore the octaval nuclei, which receive vestibular [Migault et al., 2018, Favre-Bulle et al., 2018], lateral line [Vanwalleghem et al., 2020], and auditory inputs, may play a crucial role for the initiation of those self-righting movements, and more generally for the generation of tail bouts.

To conclude, I have tried to convey the idea that the zebrafish larva is a good model to study the neural basis of locomotor behavior. In the introduction, I have outlined that the functional role of many putative homologs of motor structures in mammals is still unclear in the zebrafish larva. Further work in functional comparative anatomy, and the establishment of mesoscale and microscale connectomes [Hildebrand et al., 2017] coupled with detailed brain atlases of molecular identity, will be important to understand the role and diversity of spinal projection neurons, and to indentify potential regions that could fulfill the role of the midbrain locomotor region. If other regions higher in the motor hierarchy such as the basal ganglia are conserved in teleosts, as is suggested by recent findings in lampreys, the zebrafish larva could become an instrumental model for the study of locomotor disorders such as Parkinson's disease. In the lab, we will use our findings on the neuronal basis of sensory-evoked and spontaneous behavior to shed lights on pathological mechanisms at play in an mecp2-null model of Rett syndrome, which displays altered motor behaviors [Pietri et al., 2013].

Bibliography

[Aertsen and Johannesma, 1980] Aertsen, A. M. and Johannesma, P. I. (1980). Spectro-temporal receptive fields of auditory neurons in the grassfrog - I. Characterization of tonal and natural stimuli. *Biological Cybernetics*, 38(4):223–234.

[Agetsuma et al., 2010] Agetsuma, M., Aizawa, H., Aoki, T., Nakayama, R., Takahoko, M., Goto, M., Sassa, T., Amo, R., Shiraki, T., Kawakami, K., Hosoya, T., Higashijima, S. I., and Okamoto, H. (2010). The habenula is crucial for experience-dependent modification of fear responses in zebrafish. *Nature Neuroscience*, 13(11):1354–1356.

[Ahissar and Assa, 2016] Ahissar, E. and Assa, E. (2016). Perception as a closed-loop convergence process. *eLife*, 5.

[Ahrens et al., 2013a] Ahrens, M. B., Huang, K. H., Narayan, S., Mensh, B. D., and Engert, F. (2013a). Two-photon calcium imaging during fictive navigation in virtual environments. *Front Neural Circuits*, 7(June):104.

[Ahrens et al., 2012] Ahrens, M. B., Li, J. M., Orger, M. B., Robson, D. N., Schier, A. F., Engert, F., and Portugues, R. (2012). Brain-wide neuronal dynamics during motor adaptation in zebrafish. *Nature*, 485(7399):471–477.

[Ahrens et al., 2013b] Ahrens, M. B., Orger, M. B., Robson, D. N., Li, J. M., and Keller, P. J. (2013b). Whole-brain functional imaging at cellular resolution using light-sheet microscopy. *Nat Methods*, 10(5):413–420.

[Allen et al., 2019] Allen, W. E., Chen, M. Z., Pichamoorthy, N., Tien, R. H., Pachitariu, M., Luo, L., and Deisseroth, K. (2019). Thirst regulates motivated behavior through modulation of brainwide neural population dynamics. *Science*, 364(6437).

[Aoki et al., 2019] Aoki, S., Smith, J. B., Li, H., Yan, X., Igarashi, M., Coulon, P., Wickens, J. R., Ruigrok, T. J., and Jin, X. (2019). An open cortico-basal ganglia loop allows limbic control over motor output via the nigrothalamic pathway. *eLife*, 8.

[Armstrong et al., 2018] Armstrong, S., Sale, M. V., and Cunnington, R. (2018). Neural Oscillations and the Initiation of Voluntary Movement. *Frontiers in Psychology*, 9(DEC):2509.

[Avitan et al., 2016] Avitan, L., Pujic, Z., Hughes, N. J., Scott, E. K., and Goodhill, G. J. (2016). Limitations of Neural Map Topography for Decoding Spatial Information. *Journal of Neuroscience*, 36(19).

[Bae et al., 2009] Bae, Y. K., Kani, S., Shimizu, T., Tanabe, K., Nojima, H., Kimura, Y., ichi Higashijima, S., and Hibi, M. (2009). Anatomy of zebrafish cerebellum and screen for mutations affecting its development. *Developmental Biology*, 330(2):406–426.

[Bahl and Engert, 2020] Bahl, A. and Engert, F. (2020). Neural circuits for evidence accumulation and decision making in larval zebrafish. *Nature Neuroscience*, 23(1):94–102.

[Baker et al., 1971] Baker, P. F., Hodgkin, A. L., and Ridgway, E. B. (1971). Depolarization and calcium entry in squid giant axons. *The Journal of Physiology*, 218(3):709–755.

[Bargmann, 2006] Bargmann, C. (2006). Chemosensation in C. elegans. *WormBook*, pages 1–29.

[Bargmann et al., 1993] Bargmann, C. I., Hartwieg, E., and Horvitz, H. R. (1993). Odorant-selective genes and neurons mediate olfaction in C. elegans. *Cell*, 74(3):515–527.

[Barker and Baier, 2015] Barker, A. J. and Baier, H. (2015). Sensorimotor Decision Making in the Zebrafish Tectum. *Current Biology*, 25(21):2804–2814.

[Barsh et al., 2017] Barsh, G. R., Isabella, A. J., and Moens, C. B. (2017). Vagus Motor Neuron Topographic Map Determined by Parallel Mechanisms of hox5 Expression and Time of Axon Initiation. *Current Biology*, 27(24):3812–3825.e3.

[Barthas and Kwan, 2017] Barthas, F. and Kwan, A. C. (2017). Secondary Motor Cortex: Where 'Sensory' Meets 'Motor' in the Rodent Frontal Cortex. *Trends in Neurosciences*, 40(3):181–193.

[Basso and May, 2017] Basso, M. A. and May, P. J. (2017). Circuits for Action and Cognition: A View from the Superior Colliculus. *Annual Review of Vision Science*, 3(1):197–226.

[Baum, 2013] Baum, W. M. (2013). What counts as behavior? The molar multiscale view. In *Behavior Analyst*, volume 36, pages 283–293. Springer International Publishing.

[Berg et al., 2018] Berg, E. M., Björnfors, E. R., Pallucchi, I., Picton, L. D., and El Manira, A. (2018). Principles Governing Locomotion in Vertebrates: Lessons From Zebrafish. *Frontiers in Neural Circuits*, 12:73.

[Berman et al., 2016] Berman, G. J., Bialek, W., and Shaevitz, J. W. (2016). Predictability and hierarchy in Drosophila behavior. *Proceedings of the National Academy of Sciences of the United States of America*, 113(42):11943–11948.

[Bernhardt et al., 1990] Bernhardt, R. R., Chitnis, A. B., Lindamer, L., and Kuwada, J. Y. (1990). Identification of spinal neurons in the embryonic and larval zebrafish. *Journal of Comparative Neurology*, 302(3):603–616.

[Bernstein, 1967] Bernstein, N. (1967). *The co-ordination and regulation of movements.* Pergamon Press., New York.

[Bhattacharyya et al., 2017] Bhattacharyya, K., McLean, D. L., and MacIver, M. A. (2017). Visual Threat Assessment and Reticulospinal Encoding of Calibrated Responses in Larval Zebrafish. *Current Biology*, 27(18):2751–2762.e6.

[Bianco and Engert, 2015] Bianco, I. H. and Engert, F. (2015). Visuomotor transformations underlying hunting behavior in zebrafish. *Current biology : CB*, 25(7):831–46.

[Bianco et al., 2012] Bianco, I. H., Ma, L.-H., Schoppik, D., Robson, D. N., Orger, M. B., Beck, J. C., Li, J. M., Schier, A. F., Engert, F., and Baker, R. (2012). The Tangential Nucleus Controls a Gravito-inertial Vestibulo-ocular Reflex. *Current Biology*, 22(14):1285–1295.

[Bianco and Wilson, 2009] Bianco, I. H. and Wilson, S. W. (2009). The habenular nuclei: a conserved asymmetric relay station in the vertebrate brain. *Philosophical Transactions of the Royal Society B: Biological Sciences*, 364(1519):1005–1020.

[Bloch et al., 2020] Bloch, S., Hagio, H., Thomas, M., Heuzé, A., Hermel, J. M., Lasserre, E., Colin, I., Saka, K., Affaticati, P., Jenett, A., Kawakami, K., Yamamoto, N., and Yamamoto, K. (2020). Non-thalamic origin of zebrafish sensory nuclei implies convergent evolution of visual pathways in amniotes and teleosts. *eLife*, 9.

[Bouchard et al., 2015] Bouchard, M. B., Voleti, V., Mendes, C. S., Lacefield, C., Grueber, W. B., Mann, R. S., Bruno, R. M., and Hillman, E. M. (2015). Swept confocally-aligned planar excitation (SCAPE) microscopy for high-speed volumetric imaging of behaving organisms. *Nature Photonics*, 9(2):113–119.

[Boulanger-Weill et al., 2017] Boulanger-Weill, J., Candat, V., Jouary, A., Romano, S. A., Pérez-Schuster, V., and Sumbre, G. (2017). Functional Interactions between

Newborn and Mature Neurons Leading to Integration into Established Neuronal Circuits. *Current Biology*, 27(12):1707–1720.e5.

[Brass and Haggard, 2008] Brass, M. and Haggard, P. (2008). The what, when, whether model of intentional action. *Neuroscientist*, 14(4):319–325.

[Brette, 2019] Brette, R. (2019). Is coding a relevant metaphor for the brain? *Behavioral and Brain Sciences*, 42:e215.

[Briggman et al., 2005] Briggman, K. L., Abarbanel, H. D., and Kristan, W. B. (2005). Optical imaging of neuronal populations during decision-making. *Science*, 307(5711):896–901.

[Brinkman and Porter, 1979] Brinkman, C. and Porter, R. (1979). Supplementary motor area in the monkey: Activity of neurons during performance of a learned motor task. *Journal of Neurophysiology*, 42(3):681–709.

[Brown and de Bivort, 2018] Brown, A. E. X. and de Bivort, B. (2018). Ethology as a physical science. *Nature Physics*, 14(7):653–657.

[Brustein et al., 2003] Brustein, E., Chong, M., Holmqvist, B., and Drapeau, P. (2003). Serotonin Patterns Locomotor Network Activity in the Developing Zebrafish by Modulating Quiescent Periods. *Journal of Neurobiology*, 57(3):303–322.

[Budick and O'Malley, 2000] Budick, S. and O'Malley, D. (2000). Locomotor repertoire of the larval zebrafish: swimming, turning and prey capture. *Journal of Experimental Biology*, 203(17).

[Buonomano and Maass, 2009] Buonomano, D. V. and Maass, W. (2009). State-dependent computations: spatiotemporal processing in cortical networks. *Nature Reviews Neuroscience*, 10(2):113–125.

[Burgess and Granato, 2007a] Burgess, H. A. and Granato, M. (2007a). Modulation of locomotor activity in larval zebrafish during light adaptation. *Journal of Experimental Biology*, 210(14):2526–2539.

[Burgess and Granato, 2007b] Burgess, H. A. and Granato, M. (2007b). Sensorimotor Gating in Larval Zebrafish. *Journal of Neuroscience*, 27(18).

[Burgess et al., 2010] Burgess, H. A., Schoch, H., and Granato, M. (2010). Distinct Retinal Pathways Drive Spatial Orientation Behaviors in Zebrafish Navigation. *Current Biology*, 20(4):381–386.

[Burleson et al., 1992] Burleson, M. L., Smatresk, N. J., and Milsom, W. K. (1992). Afferent inputs associated with cardioventilatory control in fish. *Fish Physiology*, 12(PB):389–426.

[Buss and Drapeau, 2001] Buss, R. R. and Drapeau, P. (2001). Synaptic Drive to Motoneurons During Fictive Swimming in the Developing Zebrafish. *Journal of Neurophysiology*, 86(1):197–210.

[Cardinal et al., 2002] Cardinal, R. N., Parkinson, J. A., Hall, J., and Everitt, B. J. (2002). Emotion and motivation: the role of the amygdala, ventral striatum, and prefrontal cortex. *Neuroscience & Biobehavioral Reviews*, 26(3):321–352.

[Chalasani et al., 2007] Chalasani, S. H., Chronis, N., Tsunozaki, M., Gray, J. M., Ramot, D., Goodman, M. B., and Bargmann, C. I. (2007). Dissecting a circuit for olfactory behaviour in Caenorhabditis elegans. *Nature*, 450(7166):63–70.

[Chen and Engert, 2014] Chen, X. and Engert, F. (2014). Navigational strategies underlying phototaxis in larval zebrafish. *Frontiers in Systems Neuroscience*, 8.

[Chen et al., 2018] Chen, X., Mu, Y., Hu, Y., Kuan, A. T., Nikitchenko, M., Randlett, O., Chen, A. B., Gavornik, J. P., Sompolinsky, H., Engert, F., and Ahrens, M. B. (2018). Brain-wide Organization of Neuronal Activity and Convergent Sensorimotor Transformations in Larval Zebrafish. *Neuron*, 100(4):876—-890.e5.

[Churchland and Kiani, 2016] Churchland, A. K. and Kiani, R. (2016). Three challenges for connecting model to mechanism in decision-making. *Current Opinion in Behavioral Sciences*, 11:74–80.

[Churchland et al., 2012] Churchland, M. M., Cunningham, J. P., Kaufman, M. T., Foster, J. D., Nuyujukian, P., Ryu, S. I., Shenoy, K. V., and Shenoy, K. V. (2012). Neural population dynamics during reaching. *Nature*, 487(7405):51–56.

[Churchland et al., 2006] Churchland, M. M., Yu, B. M., Ryu, S. I., Santhanam, G., and Shenoy, K. V. (2006). Neural variability in premotor cortex provides a signature of motor preparation. *Journal of Neuroscience*, 26(14):3697–3712.

[Cisek, 2007] Cisek, P. (2007). Cortical mechanisms of action selection: The affordance competition hypothesis. *Philosophical Transactions of the Royal Society B: Biological Sciences*, 362(1485):1585–1599.

[Cong et al., 2017] Cong, L., Wang, Z., Chai, Y., Hang, W., Shang, C., Yang, W., Bai, L., Du, J., Wang, K., and Wen, Q. (2017). Rapid whole brain imaging of neural activity in freely behaving larval zebrafish (Danio rerio). *eLife*, 6.

[Constantin et al., 2020] Constantin, L., Poulsen, R. E., Scholz, L. A., Favre-Bulle, I. A., Taylor, M. A., Sun, B., Goodhill, G. J., Vanwalleghem, G. C., and Scott, E. K. (2020). Altered brain-wide auditory networks in a zebrafish model of fragile X syndrome. *BMC Biology*, 18(1):1–17.

[Crapse and Sommer, 2008] Crapse, T. B. and Sommer, M. A. (2008). Corollary discharge across the animal kingdom. *Nature Reviews Neuroscience*, 9(8):587–600.

[Croll, 1975] Croll, N. A. (1975). Components and patterns in the behaviour of the nematode Caenorhabditis elegans. *Journal of Zoology*, 176(2):159–176.

[Cunnington, 2002] Cunnington, R. (2002). The preparation and execution of self-initiated and externally-triggered movement: a study of event-related fMRI. *Neuroimage*, 15:373–385.

[Da Silva et al., 2018] Da Silva, J. A., Tecuapetla, F., Paixão, V., and Costa, R. M. (2018). Dopamine neuron activity before action initiation gates and invigorates future movements. *Nature*, 554(7691):244–248.

[dal Maschio et al., 2017] dal Maschio, M., Donovan, J. C., Helmbrecht, T. O., and Baier, H. (2017). Linking Neurons to Network Function and Behavior by Two-Photon Holographic Optogenetics and Volumetric Imaging. *Neuron*, 94(4).

[D'Avella et al., 2003] D'Avella, A., Saltiel, P., and Bizzi, E. (2003). Combinations of muscle synergies in the construction of a natural motor behavior. *Nature Neuroscience*, 6(3):300–308.

[Dayan, 2012] Dayan, P. (2012). How to set the switches on this thing. *Current Opinion in Neurobiology*, 22(6):1068–1074.

[Deecke and Kornhuber, 1978] Deecke, L. and Kornhuber, H. H. (1978). An electrical sign of participation of the mesial 'supplementary' motor cortex in human voluntary finger movement. *Brain Research*, 159(2):473–476.

[Denk et al., 1990] Denk, W., Strickler, J. H., and Webb, W. W. (1990). Two-photon laser scanning fluorescence microscopy. *Science*, 248(4951):73–76.

[Dohaku et al., 2019] Dohaku, R., Yamaguchi, M., Yamamoto, N., Shimizu, T., Osakada, F., and Hibi, M. (2019). Tracing of afferent connections in the zebrafish cerebellum using recombinant rabies virus. *Frontiers in Neural Circuits*, 13:30.

[Dombeck et al., 2007] Dombeck, D. A., Khabbaz, A. N., Collman, F., Adelman, T. L., and Tank, D. W. (2007). Imaging Large-Scale Neural Activity with Cellular Resolution in Awake, Mobile Mice. *Neuron*, 56(1):43–57.

[Dragomir et al., 2020] Dragomir, E. I., Štih, V., and Portugues, R. (2020). Evidence accumulation during a sensorimotor decision task revealed by whole-brain imaging. *Nature Neuroscience*, 23(1):85–93.

[Dubuc et al., 2008] Dubuc, R., Brocard, F., Antri, M., Fénelon, K., Gariépy, J.-F., Smetana, R., Ménard, A., Le Ray, D., Viana Di Prisco, G., Pearlstein, É., Sirota, M. G., Derjean, D., St-Pierre, M., Zielinski, B., Auclair, F., and Veilleux, D. (2008). Initiation of locomotion in lampreys. *Brain Research Reviews*, 57(1):172–182.

[Dunn et al., 2016a] Dunn, T., Gebhardt, C., Naumann, E., Riegler, C., Ahrens, M., Engert, F., and Del Bene, F. (2016a). Neural Circuits Underlying Visually Evoked Escapes in Larval Zebrafish. *Neuron*, 89(3):613–628.

[Dunn et al., 2016b] Dunn, T. W., Mu, Y., Narayan, S., Randlett, O., Naumann, E. A., Yang, C.-T., Schier, A. F., Freeman, J., Engert, F., and Ahrens, M. B. (2016b). Brain-wide mapping of neural activity controlling zebrafish exploratory locomotion. *eLife*, 5.

[Eaton et al., 1977] Eaton, R. C., Bombardieri, R. A., and Meyer, D. L. (1977). The Mauthner-initiated startle response in teleost fish. *Journal of Experimental Biology*, 66(1).

[Ebbesen et al., 2018] Ebbesen, C. L., Insanally, M. N., Kopec, C. D., Murakami, M., Saiki, A., and Erlich, J. C. (2018). More than just a "motor": Recent surprises from the frontal cortex. *Journal of Neuroscience*, 38(44):9402–9413.

[Eccles, 1982] Eccles, J. C. (1982). The initiation of voluntary movements by the supplementary motor area. *Archiv für Psychiatrie und Nervenkrankheiten*, 231(5):423–441.

[Ehrlich and Schoppik, 2017] Ehrlich, D. E. and Schoppik, D. (2017). Control of Movement Initiation Underlies the Development of Balance. *Current Biology*, 27(3):334–344.

[Eklöf Ljunggren et al., 2014] Eklöf Ljunggren, E., Haupt, S., Ausborn, J., Ampatzis, K., and El Manira, A. (2014). Optogenetic activation of excitatory premotor interneurons is sufficient to generate coordinated locomotor activity in larval zebrafish. *Journal of Neuroscience*, 34(1):134–139.

[Eklöf-Ljunggren et al., 2012] Eklöf-Ljunggren, E., Haupt, S., Ausborn, J., Dehnisch, I., Uhleń, P., Higashijima, S. I., and El Manira, A. (2012). Origin of excitation underlying locomotion in the spinal circuit of zebrafish. *Proceedings of the National Academy of Sciences of the United States of America*, 109(14):5511–5516.

[El Manira et al., 1997] El Manira, A., Pombal, M. A., and Grillner, S. (1997). Diencephalic projection to reticulospinal neurons involved in the initiation of locomotion in

adult lampreys Lampetra fluviatilis. *Journal of Comparative Neurology*, 389(4):603–616.

[Elliott and Leys, 2010] Elliott, G. R. and Leys, S. P. (2010). Evidence for glutamate, GABA and NO in coordinating behaviour in the sponge, Ephydatia muelleri (Demospongiae, Spongillidae). *Journal of Experimental Biology*, 213(13):2310–2321.

[Elsayed et al., 2016] Elsayed, G. F., Lara, A. H., Kaufman, M. T., Churchland, M. M., and Cunningham, J. P. (2016). Reorganization between preparatory and movement population responses in motor cortex. *Nature Communications*, 7(1):1–15.

[Engert, 2013] Engert, F. (2013). Fish in the matrix: motor learning in a virtual world. *Frontiers in Neural Circuits*, 6.

[Engeszer et al., 2007] Engeszer, R. E., Patterson, L. B., Rao, A. A., and Parichy, D. M. (2007). Zebrafish in The Wild: A Review of Natural History And New Notes from The Field. *Zebrafish*, 4(1):21–40.

[Fairhall, 2014] Fairhall, A. (2014). The receptive field is dead. Long live the receptive field? *Current Opinion in Neurobiology*, 25:9–12.

[Favre-Bulle et al., 2020] Favre-Bulle, I. A., Taylor, M. A., Marquez-Legorreta, E., Vanwalleghem, G., Poulsen, R. E., Rubinsztein-Dunlop, H., and Scott, E. K. (2020). Sound generation in zebrafish with Bio-Opto-Acoustics. *Nature Communications*, 11(1):6120.

[Favre-Bulle et al., 2018] Favre-Bulle, I. A., Vanwalleghem, G., Taylor, M. A., Rubinsztein-Dunlop, H., and Scott, E. K. (2018). Cellular-Resolution Imaging of Vestibular Processing across the Larval Zebrafish Brain. *Current Biology*, 28(23):3711–3722.e3.

[Fetcho and O'Malley, 1995] Fetcho, J. R. and O'Malley, D. M. (1995). Visualization of active neural circuitry in the spinal cord of intact zebrafish. *Journal of Neurophysiology*, 73(1):399–406.

[Filippi et al., 2014] Filippi, A., Mueller, T., and Driever, W. (2014). vglut2 and gad expression reveal distinct patterns of dual GABAergic versus glutamatergic cotransmitter phenotypes of dopaminergic and noradrenergic neurons in the zebrafish brain. *Journal of Comparative Neurology*, 522(9):2019–2037.

[Fine et al., 1988] Fine, A., Amos, W. B., Durbin, R. M., and McNaughton, P. A. (1988). Confocal microscopy: applications in neurobiology. *Trends in Neurosciences*, 11(8):346–351.

[Flash and Hochner, 2005] Flash, T. and Hochner, B. (2005). Motor primitives in vertebrates and invertebrates. *Current Opinion in Neurobiology*, 15(6):660–666.

[Fried et al., 2011] Fried, I., Mukamel, R., and Kreiman, G. (2011). Internally Generated Preactivation of Single Neurons in Human Medial Frontal Cortex Predicts Volition. *Neuron*, 69(3):548–562.

[Fukushima, 1987] Fukushima, K. (1987). The interstitial nucleus of Cajal and its role in the control of movements of head and eyes. *Progress in Neurobiology*, 29(2):107–192.

[Furukawa and Ishii, 1967] Furukawa, T. and Ishii, Y. (1967). Neurophysiological studies on hearing in goldfish. *Journal of Neurophysiology*, 30(6):1377–403.

[Gahtan et al., 2005] Gahtan, E., Tanger, P., and Baier, H. (2005). Visual prey capture in larval zebrafish is controlled by identified reticulospinal neurons downstream of the tectum. *The Journal of neuroscience : the official journal of the Society for Neuroscience*, 25(40):9294–303.

[Gallivan et al., 2018] Gallivan, J. P., Chapman, C. S., Wolpert, D. M., and Flanagan, J. R. (2018). Decision-making in sensorimotor control. *Nature Reviews Neuroscience*, 19(9):519–534.

[Garst-Orozco et al., 2014] Garst-Orozco, J., Babadi, B., and Ölveczky, B. P. (2014). A neural circuit mechanism for regulating vocal variability during song learning in zebra finches. *eLife*, 3:e03697.

[Gold and Shadlen, 2007] Gold, J. I. and Shadlen, M. N. (2007). The Neural Basis of Decision Making. *Annual Review of Neuroscience*, 30(1):535–574.

[Gottlieb and Oudeyer, 2018] Gottlieb, J. and Oudeyer, P.-Y. (2018). Towards a neuroscience of active sampling and curiosity. *Nature Reviews Neuroscience*, 19(12):758–770.

[Gottlieb et al., 2013] Gottlieb, J., Oudeyer, P.-Y., Lopes, M., and Baranes, A. (2013). Information-seeking, curiosity, and attention: computational and neural mechanisms. *Trends in Cognitive Sciences*, 17(11):585–593.

[Goulding, 2009] Goulding, M. (2009). Circuits controlling vertebrate locomotion: moving in a new direction. *Nature Reviews Neuroscience*, 10(7):507–518.

[Gray et al., 2005] Gray, J. M., Hill, J. J., and Bargmann, C. I. (2005). A circuit for navigation in Caenorhabditis elegans. *Proceedings of the National Academy of Sciences of the United States of America*, 102(9):3184–3191.

[Graziano, 2006] Graziano, M. (2006). The organization of behavioral repertoire in motor cortex. *Annual Review of Neuroscience*, 29(1):105–134.

[Graziano et al., 2005] Graziano, M. S., Aflalo, T. N., and Cooke, D. F. (2005). Arm movements evoked by electrical stimulation in the motor cortex of monkeys. *Journal of Neurophysiology*, 94(6):4209–4223.

[Grewe et al., 2010] Grewe, B. F., Langer, D., Kasper, H., Kampa, B. M., and Helmchen, F. (2010). High-speed in vivo calcium imaging reveals neuronal network activity with near-millisecond precision. *Nature methods*, 7(5):399–405.

[Grienberger and Konnerth, 2012] Grienberger, C. and Konnerth, A. (2012). Imaging Calcium in Neurons.

[Grillner, 2006] Grillner, S. (2006). Biological Pattern Generation: The Cellular and Computational Logic of Networks in Motion. *Neuron*, 52(5):751–766.

[Grillner and El Manira, 2020] Grillner, S. and El Manira, A. (2020). Current principles of motor control, with special reference to vertebrate locomotion. *Physiological Reviews*, 100(1):271–320.

[Grillner and Robertson, 2016] Grillner, S. and Robertson, B. (2016). The Basal Ganglia Over 500 Million Years. *Current Biology*, 26(20):R1088–R1100.

[Groschner et al., 2018] Groschner, L. N., Chan Wah Hak, L., Bogacz, R., DasGupta, S., and Miesenböck, G. (2018). Dendritic Integration of Sensory Evidence in Perceptual Decision-Making. *Cell*, 173(4):894–905.e13.

[Gründemann et al., 2019] Gründemann, J., Bitterman, Y., Lu, T., Krabbe, S., Grewe, B. F., Schnitzer, M. J., and Lüthi, A. (2019). Amygdala ensembles encode behavioral states. *Science*, 364(6437).

[Grynkiewicz et al., 1985] Grynkiewicz, G., Poenie, M., and Tsien, R. Y. (1985). A new generation of Ca2+ indicators with greatly improved fluorescence properties. *Journal of Biological Chemistry*, 260(6):3440–3450.

[Guillermin et al., 2017] Guillermin, M. L., Carrillo, M. A., and Hallem, E. A. (2017). A Single Set of Interneurons Drives Opposite Behaviors in C. elegans. *Current Biology*, 27(17):2630–2639.e6.

[Haggard, 2008] Haggard, P. (2008). Human volition: towards a neuroscience of will. *Nature Reviews Neuroscience*, 9(12):934–946.

[Hale et al., 2001] Hale, M. E., Ritter, D. A., and Fetcho, J. R. (2001). A confocal study of spinal interneurons in living larval zebrafish. *Journal of Comparative Neurology*, 437(1):1–16.

[Hallett and Carbone, 1972] Hallett, M. and Carbone, E. (1972). Studies of calcium influx into squid giant axons with aequorin. *Journal of Cellular Physiology*, 80(2):219–226.

[Hamilos et al., 2020] Hamilos, A. E., Spedicato, G., Hong, Y., Sun, F., and Li, Y. (2020). Dynamic dopaminergic activity controls the timing of self-timed movement. *bioRxiv*, page 2020.05.13.094904.

[Hanks et al., 2015] Hanks, T. D., Kopec, C. D., Brunton, B. W., Duan, C. A., Erlich, J. C., and Brody, C. D. (2015). Distinct relationships of parietal and prefrontal cortices to evidence accumulation. *Nature*, 520(7546):220–223.

[Hart and Giszter, 2010] Hart, C. B. and Giszter, S. F. (2010). A neural basis for motor primitives in the spinal cord. *Journal of Neuroscience*, 30(4):1322–1326.

[Hatsopoulos et al., 2003] Hatsopoulos, N. G., Paninski, L., and Donoghue, J. P. (2003). Sequential movement representations based on correlated neuronal activity. *Experimental Brain Research*, 149(4):478–486.

[Helmbrecht et al., 2018] Helmbrecht, T. O., Dal Maschio, M., Donovan, J. C., Koutsouli, S., and Baier, H. (2018). Topography of a Visuomotor Transformation. *Neuron*, 100(6):1429–1445.e4.

[Hendricks, 2012] Hendricks, M. (2012). Compartmentalized calcium dynamics in a C. elegans interneuron encode head movement. *Nature*, 487(7405):99–103.

[Higashijima et al., 2000] Higashijima, S. I., Hotta, Y., and Okamoto, H. (2000). Visualization of cranial motor neurons in live transgenic zebrafish expressing green fluorescent protein under the control of the Islet-1 promoter/enhancer. *Journal of Neuroscience*, 20(1):206–218.

[Higashijima et al., 2004a] Higashijima, S. I., Mandel, G., and Fetcho, J. R. (2004a). Distribution of prospective glutamatergic, glycinergic, and gabaergic neurons in embryonic and larval zebrafish. *Journal of Comparative Neurology*, 480(1):1–18.

[Higashijima et al., 2003] Higashijima, S. I., Masino, M. A., Mandel, G., and Fetcho, J. R. (2003). Imaging Neuronal Activity during Zebrafish Behavior with a Genetically Encoded Calcium Indicator. *Journal of Neurophysiology*, 90(6):3986–3997.

[Higashijima et al., 2004b] Higashijima, S. I., Masino, M. A., Mandel, G., and Fetcho, J. R. (2004b). Engrailed-1 expression marks a primitive class of inhibitory spinal interneuron. *Journal of Neuroscience*, 24(25):5827–5839.

[Higashijima et al., 2004c] Higashijima, S.-I., Schaefer, M., and Fetcho, J. R. (2004c). Neurotransmitter properties of spinal interneurons in embryonic and larval zebrafish. *The Journal of Comparative Neurology*, 480(1):19–37.

[Higgs, 2020] Higgs, D. M. (2020). Functional review of hearing in zebrafish. *Behavioral and Neural Genetics of Zebrafish*, pages 73–91.

[Higgs et al., 2003] Higgs, D. M., Rollo, A. K., Souza, M. J., and Popper, A. N. (2003). Development of form and function in peripheral auditory structures of the zebrafish (Danio rerio). *The Journal of the Acoustical Society of America*, 113(2):1145–1154.

[Hildebrand et al., 2017] Hildebrand, D. G. C., Cicconet, M., Torres, R. M., Choi, W., Quan, T. M., Moon, J., Wetzel, A. W., Scott Champion, A., Graham, B. J., Randlett, O., Plummer, G. S., Portugues, R., Bianco, I. H., Saalfeld, S., Baden, A. D., Lillaney, K., Burns, R., Vogelstein, J. T., Schier, A. F., Lee, W.-C. A., Jeong, W.-K., Lichtman, J. W., and Engert, F. (2017). Whole-brain serial-section electron microscopy in larval zebrafish. *Nature*, 545(7654):345–349.

[Hoffstaedter et al., 2013] Hoffstaedter, F., Grefkes, C., Zilles, K., and Eickhoff, S. B. (2013). The "what" and "when" of self-initiated movements. *Cerebral Cortex*, 23(3):520–530.

[Holekamp et al., 2008] Holekamp, T. F., Turaga, D., and Holy, T. E. (2008). Fast Three-Dimensional Fluorescence Imaging of Activity in Neural Populations by Objective-Coupled Planar Illumination Microscopy. *Neuron*, 57(5):661–672.

[Horstick et al., 2016] Horstick, E. J., Mueller, T., and Burgess, H. A. (2016). Motivated state control in larval zebrafish: behavioral paradigms and anatomical substrates. *Journal of Neurogenetics*, 30(2):122–132.

[Howe et al., 2013] Howe, K., Clark, M. D., Torroja, C. F., Torrance, J., Berthelot, C., Muffato, M., Collins, J. E., Humphray, S., McLaren, K., Matthews, L., McLaren, S., Sealy, I., Caccamo, M., Churcher, C., Scott, C., Barrett, J. C., Koch, R., Rauch, G. J., White, S., Chow, W., Kilian, B., Quintais, L. T., Guerra-Assunção, J. A., Zhou, Y., Gu, Y., Yen, J., Vogel, J. H., Eyre, T., Redmond, S., Banerjee, R., Chi, J., Fu, B., Langley, E., Maguire, S. F., Laird, G. K., Lloyd, D., Kenyon, E., Donaldson, S., Sehra, H., Almeida-King, J., Loveland, J., Trevanion, S., Jones, M., Quail, M., Willey, D., Hunt, A., Burton, J., Sims, S., McLay, K., Plumb, B., Davis, J., Clee, C., Oliver, K., Clark, R., Riddle, C., Eliott, D., Threadgold, G., Harden, G., Ware, D., Mortimer, B., Kerry, G., Heath, P., Phillimore, B., Tracey, A., Corby, N., Dunn, M., Johnson, C., Wood, J., Clark, S., Pelan, S., Griffiths, G., Smith, M., Glithero, R., Howden, P., Barker, N., Stevens, C., Harley, J., Holt, K., Panagiotidis, G., Lovell, J.,

Beasley, H., Henderson, C., Gordon, D., Auger, K., Wright, D., Collins, J., Raisen, C., Dyer, L., Leung, K., Robertson, L., Ambridge, K., Leongamornlert, D., McGuire, S., Gilderthorp, R., Griffiths, C., Manthravadi, D., Nichol, S., Barker, G., Whitehead, S., Kay, M., Brown, J., Murnane, C., Gray, E., Humphries, M., Sycamore, N., Barker, D., Saunders, D., Wallis, J., Babbage, A., Hammond, S., Mashreghi-Mohammadi, M., Barr, L., Martin, S., Wray, P., Ellington, A., Matthews, N., Ellwood, M., Woodmansey, R., Clark, G., Cooper, J., Tromans, A., Grafham, D., Skuce, C., Pandian, R., Andrews, R., Harrison, E., Kimberley, A., Garnett, J., Fosker, N., Hall, R., Garner, P., Kelly, D., Bird, C., Palmer, S., Gehring, I., Berger, A., Dooley, C. M., Ersan-Ürün, Z., Eser, C., Geiger, H., Geisler, M., Karotki, L., Kirn, A., Konantz, J., Konantz, M., Oberländer, M., Rudolph-Geiger, S., Teucke, M., Osoegawa, K., Zhu, B., Rapp, A., Widaa, S., Langford, C., Yang, F., Carter, N. P., Harrow, J., Ning, Z., Herrero, J., Searle, S. M., Enright, A., Geisler, R., Plasterk, R. H., Lee, C., Westerfield, M., De Jong, P. J., Zon, L. I., Postlethwait, J. H., Nüsslein-Volhard, C., Hubbard, T. J., Crollius, H. R., Rogers, J., and Stemple, D. L. (2013). The zebrafish reference genome sequence and its relationship to the human genome. *Nature*, 496(7446):498–503.

[Huang et al., 2013] Huang, K. H., Ahrens, M. B., Dunn, T. W., and Engert, F. (2013). Spinal projection neurons control turning behaviors in zebrafish. *Current Biology*, 23(16).

[Hughes, 2013] Hughes, V. (2013). Mapping brain networks: Fish-bowl neuroscience. *Nature*, 493(7433):466–468.

[Huisken et al., 2004] Huisken, J., Swoger, J., Del Bene, F., Wittbrodt, J., and Stelzer, E. H. K. (2004). Optical Sectioning Deep Inside Live Embryos by Selective Plane Illumination Microscopy. *Science*, 305(5686):1007–1009.

[Hums et al., 2016] Hums, I., Riedl, J., Mende, F., Kato, S., Kaplan, H. S., Latham, R., Sonntag, M., Traunmüller, L., and Zimmer, M. (2016). Regulation of two motor patterns enables the gradual adjustment of locomotion strategy in caenorhabditis elegans. *eLife*, 5(MAY2016).

[Iino and Yoshida, 2009] Iino, Y. and Yoshida, K. (2009). Parallel use of two behavioral mechanisms for chemotaxis in Caenorhabditis elegans. *Journal of Neuroscience*, 29(17):5370–5380.

[Ikemoto et al., 2015] Ikemoto, S., Yang, C., and Tan, A. (2015). Basal ganglia circuit loops, dopamine and motivation: A review and enquiry. *Behavioural Brain Research*, 290:17–31.

[Inagaki et al., 2019] Inagaki, H. K., Fontolan, L., Romani, S., and Svoboda, K. (2019). Discrete attractor dynamics underlies persistent activity in the frontal cortex. *Nature*, 566(7743):212–217.

[Irons et al., 2013] Irons, T. D., Kelly, P. E., Hunter, D. L., MacPhail, R. C., and Padilla, S. (2013). Acute administration of dopaminergic drugs has differential effects on locomotion in larval zebrafish. *Pharmacology Biochemistry and Behavior*, 103(4):792–813.

[Isabella et al., 2019] Isabella, A. J., Barsh, G. R., Stonick, J. A., and Moens, C. B. (2019). Retinoic acid organizes the vagus motor topographic map via spatiotemporal regulation of Hgf/Met signaling.

[Itskovits et al., 2018] Itskovits, E., Ruach, R., and Zaslaver, A. (2018). Concerted pulsatile and graded neural dynamics enables efficient chemotaxis in C. elegans. *Nature Communications*, 9(1).

[Izhikevich, 2007] Izhikevich, E. M. (2007). *Dynamical Systems in Neuroscience*. Massachusetts: The MIT Press.

[Jahanshahi, 1995] Jahanshahi, M. (1995). Self-initiated versus externally triggered movements. I. An investigation using measurement of regional cerebral blood flow with PET and movement-related potentials in normal and Parkinson's disease subjects. *Brain*, 118:913–933.

[Jay et al., 2015] Jay, M., De Faveri, F., and McDearmid, J. R. (2015). Firing dynamics and modulatory actions of supraspinal dopaminergic neurons during zebrafish locomotor behavior. *Current Biology*, 25(4):435–444.

[Johnson et al., 2020] Johnson, R. E., Linderman, S., Panier, T., Wee, C. L., Song, E., Herrera, K. J., Miller, A., and Engert, F. (2020). Probabilistic Models of Larval Zebrafish Behavior Reveal Structure on Many Scales. *Current Biology*, 30(1):70–82.e4.

[Jonz and Nurse, 2005] Jonz, M. G. and Nurse, C. A. (2005). Development of oxygen sensing in the gills of zebrafish. *Journal of Experimental Biology*, 208(8):1537–1549.

[Jorgensen, 2014] Jorgensen, E. M. (2014). Animal Evolution: Looking for the First Nervous System. *Current Biology*, 24(14):R655–R658.

[Jouary, 2015] Jouary, A. (2015). *Comportement moteur induit visuellement et spontané chez la larve du poisson zèbre*. PhD thesis.

[Jouary and Sumbre, 2016] Jouary, A. and Sumbre, G. (2016). Automatic classification of behavior in zebrafish larvae. *bioRxiv*, page 052324.

[Jung et al., 2014] Jung, K., Jang, H., Kralik, J. D., and Jeong, J. (2014). Bursts and Heavy Tails in Temporal and Sequential Dynamics of Foraging Decisions. *PLoS Computational Biology*, 10(8):1003759.

[Kagaya and Takahata, 2011] Kagaya, K. and Takahata, M. (2011). Sequential Synaptic Excitation and Inhibition Shape Readiness Discharge for Voluntary Behavior. *Science*, 332(6027):365–368.

[Kaplan and Zimmer, 2018] Kaplan, H. S. and Zimmer, M. (2018). Sensorimotor Integration for Decision Making: How the Worm Steers. *Neuron*, 97(2):258–260.

[Karpenko et al., 2020] Karpenko, S., Wolf, S., Lafaye, J., Le Goc, G., Panier, T., Bormuth, V., Candelier, R., and Debrégeas, G. (2020). From behavior to circuit modeling of light-seeking navigation in zebrafish larvae. *eLife*, 9.

[Kaufman et al., 2014] Kaufman, M. T., Churchland, M. M., Ryu, S. I., and Shenoy, K. V. (2014). Cortical activity in the null space: Permitting preparation without movement. *Nature Neuroscience*, 17(3):440–448.

[Kawashima et al., 2016] Kawashima, T., Zwart, M. F., Yang, C. T., Mensh, B. D., and Ahrens, M. B. (2016). The Serotonergic System Tracks the Outcomes of Actions to Mediate Short-Term Motor Learning. *Cell*, 167(4):933–946.e20.

[Keller et al., 2014] Keller, P. J., Ahrens, M. B., and Freeman, J. (2014). Light-sheet imaging for systems neuroscience. *Nature Methods*, 12(1):27–29.

[Khalighinejad et al., 2020] Khalighinejad, N., Priestley, L., Jbabdi, S., and Rushworth, M. F. (2020). Human decisions about when to act originate within a basal forebrain-nigral circuit. *Proceedings of the National Academy of Sciences of the United States of America*, 117(21):11799–11810.

[Kim et al., 2011] Kim, D., Park, S., Mahadevan, L., and Shin, J. H. (2011). The shallow turn of a worm. *Journal of Experimental Biology*, 214(9):1554–1559.

[Kim et al., 2017] Kim, D. H., Kim, J., Marques, J. C., Grama, A., Hildebrand, D. G. C., Gu, W., Li, J. M., and Robson, D. N. (2017). Pan-neuronal calcium imaging with cellular resolution in freely swimming zebrafish. *Nature Methods*, 14(11):1107–1114.

[Kimmel et al., 1974] Kimmel, C. B., Patterson, J., and Kimmel, R. O. (1974). The development and behavioral characteristics of the startle response in the zebra fish. *Developmental Psychobiology*, 7(1):47–60.

[Kimmel et al., 1982] Kimmel, C. B., Powell, S. L., and Metcalfe, W. K. (1982). Brain neurons which project to the spinal cord in young larvae of the zebrafish. *Journal of Comparative Neurology*, 205(2):112–127.

[Kimura et al., 2006] Kimura, Y., Okamura, Y., and Higashijima, S. I. (2006). alx, a zebrafish homolog of Chx10, marks ipsilateral descending excitatory interneurons that participate in the regulation of spinal locomotor circuits. *Journal of Neuroscience*, 26(21):5684–5697.

[Kimura et al., 2013] Kimura, Y., Satou, C., Fujioka, S., Shoji, W., Umeda, K., Ishizuka, T., Yawo, H., and Higashijima, S. I. (2013). Hindbrain V2a neurons in the excitation of spinal locomotor circuits during zebrafish swimming. *Current Biology*, 23(10):843–849.

[Kinkhabwala et al., 2011] Kinkhabwala, A., Riley, M., Koyama, M., Monen, J., Satou, C., Kimura, Y., Higashijima, S.-i., and Fetcho, J. (2011). A structural and functional ground plan for neurons in the hindbrain of zebrafish. *Proceedings of the National Academy of Sciences*, 108(3):1164–1169.

[Klaus et al., 2019] Klaus, A., Alves da Silva, J., and Costa, R. M. (2019). What, If, and When to Move: Basal Ganglia Circuits and Self-Paced Action Initiation. *Annual Review of Neuroscience*, 42(1):459–483.

[Knafo and Wyart, 2018] Knafo, S. and Wyart, C. (2018). Active mechanosensory feedback during locomotion in the zebrafish spinal cord. *Current Opinion in Neurobiology*, 52:48–53.

[Knogler et al., 2019] Knogler, L. D., Kist, A. M., and Portugues, R. (2019). Motor context dominates output from purkinje cell functional regions during reflexive visuomotor behaviours. *eLife*, 8.

[Knogler et al., 2017] Knogler, L. D., Markov, D. A., Dragomir, E. I., Štih, V., and Portugues, R. (2017). Sensorimotor Representations in Cerebellar Granule Cells in Larval Zebrafish Are Dense, Spatially Organized, and Non-temporally Patterned. *Current Biology*, 27(9):1288–1302.

[Kocabas et al., 2012] Kocabas, A., Shen, C. H., Guo, Z. V., and Ramanathan, S. (2012). Controlling interneuron activity in Caenorhabditis elegans to evoke chemotactic behaviour. *Nature*, 490(7419):273–277.

[Kohashi and Oda, 2008] Kohashi, T. and Oda, Y. (2008). Initiation of Mauthner-or Non-Mauthner-Mediated Fast Escape Evoked by Different Modes of Sensory Input. *The Journal of Neuroscience*, 28(42):10641–10653.

[Korn and Faber, 2005] Korn, H. and Faber, D. S. (2005). The Mauthner Cell Half a Century Later: A Neurobiological Model for Decision-Making? *Neuron*, 47(1):13–28.

[Kornhuber and Deecke, 1964] Kornhuber, H. H. and Deecke, L. (1964). Hirnpotentialanderungen beim Menschen vor und nach Willkurbewegungen dargestellt mit Magnetbandspeicherung und Ruckwartsanalyse. *Pflugers Archiv-European Journal of Physiology*, 281(1):52.

[Kornhuber and Deecke, 2016] Kornhuber, H. H. and Deecke, L. (2016). Brain potential changes in voluntary and passive movements in humans: readiness potential and reafferent potentials. *Pflugers Archiv European Journal of Physiology*, 468(7):1115–1124.

[Kouneiher et al., 2009] Kouneiher, F., Charron, S., and Koechlin, E. (2009). Motivation and cognitive control in the human prefrontal cortex. *Nature Neuroscience*, 12(7):939–945.

[Koyama et al., 2011] Koyama, M., Kinkhabwala, A., Satou, C., Higashijima, S. I., and Fetcho, J. (2011). Mapping a sensory-motor network onto a structural and functional ground plan in the hindbrain. *Proceedings of the National Academy of Sciences of the United States of America*, 108(3):1170–1175.

[Krieghoff, 2009] Krieghoff, V. (2009). Dissociating what and when of intentional actions. *Frontiers in Human Neuroscience*, 3:3.

[Krieghoff et al., 2011] Krieghoff, V., Waszak, F., Prinz, W., and Brass, M. (2011). Neural and behavioral correlates of intentional actions. *Neuropsychologia*, 49(5):767–776.

[Kunimatsu et al., 2018] Kunimatsu, J., Suzuki, T. W., Ohmae, S., and Tanaka, M. (2018). Different contributions of preparatory activity in the basal ganglia and cerebellum for self-timing. *eLife*, 7.

[Kunst et al., 2019] Kunst, M., Laurell, E., Mokayes, N., Kramer, A., Kubo, F., Fernandes, A. M., Förster, D., Dal Maschio, M., and Baier, H. (2019). A Cellular-Resolution Atlas of the Larval Zebrafish Brain. *Neuron*, 103(1):21–38.e5.

[Laje and Buonomano, 2013] Laje, R. and Buonomano, D. V. (2013). Robust timing and motor patterns by taming chaos in recurrent neural networks. *Nature Neuroscience*, 16(7):925–933.

[Larsch et al., 2015] Larsch, J., Flavell, S. W., Liu, Q., Gordus, A., Albrecht, D. R., and Bargmann, C. I. (2015). A Circuit for Gradient Climbing in C. elegans Chemotaxis. *Cell Reports*, 12(11):1748–1760.

[Larsch et al., 2013] Larsch, J., Ventimiglia, D., Bargmann, C. I., and Albrecht, D. R. (2013). High-throughput imaging of neuronal activity in Caenorhabditis elegans. *Proceedings of the National Academy of Sciences of the United States of America*, 110(45):E4266–E4273.

[Latimer et al., 2015] Latimer, K. W., Yates, J. L., Meister, M. L., Huk, A. C., and Pillow, J. W. (2015). Single-trial spike trains in parietal cortex reveal discrete steps during decision-making. *Science*, 349(6244):184–187.

[Lau et al., 2004] Lau, H. C., Rogers, R. D., Haggard, P., and Passingham, R. E. (2004). Attention to Intention. *Science*, 303(5661):1208–1210.

[Lemon, 2008] Lemon, R. N. (2008). Descending Pathways in Motor Control. *Annual Review of Neuroscience*, 31(1):195–218.

[Levitis et al., 2009] Levitis, D. A., Lidicker, W. Z., and Freund, G. (2009). Behavioural biologists do not agree on what constitutes behaviour. *Animal Behaviour*, 78:103–110 Contents.

[Leys et al., 2019] Leys, S. P., Mah, J. L., McGill, P. R., Hamonic, L., De Leo, F. C., and Kahn, A. S. (2019). Sponge Behavior and the Chemical Basis of Responses: A Post-Genomic View. In *Integrative and Comparative Biology*, volume 59, pages 751–764. Oxford University Press.

[Libet et al., 1983] Libet, B., Gleason, C. A., Wright, E. W., and Pearl, D. K. (1983). Time of conscious intention to act in relation to onset of cerebral activity (readiness-potential). The unconscious initiation of a freely voluntary act. *Brain*, 106:623–642.

[Lin et al., 2020] Lin, Q., Manley, J., Helmreich, M., Schlumm, F., Li, J. M., Robson, D. N., Engert, F., Schier, A., Nöbauer, T., and Vaziri, A. (2020). Cerebellar Neurodynamics Predict Decision Timing and Outcome on the Single-Trial Level. *Cell*, 180(3):536–551.e17.

[Liu et al., 2018a] Liu, H., Yang, W., Wu, T., Duan, F., Soucy, E., Jin, X., and Zhang, Y. (2018a). Cholinergic Sensorimotor Integration Regulates Olfactory Steering. *Neuron*, 97(2):390–405.e3.

[Liu and Fetcho, 1999] Liu, K. S. and Fetcho, J. R. (1999). Laser ablations reveal functional relationships of segmental hindbrain neurons in zebrafish. *Neuron*, 23(2):325–335.

[Liu et al., 2018b] Liu, Q., Kidd, P. B., Dobosiewicz, M., and Bargmann, C. I. (2018b). C. elegans AWA Olfactory Neurons Fire Calcium-Mediated All-or-None Action Potentials. *Cell*, 175(1):57–70.e17.

[Llinás et al., 1972] Llinás, R., Blinks, J. R., and Nicholson, C. (1972). Calcium transient in presynaptic terminal of squid giant synapse: detection with aequorin. *Science*, 176(39):1127–1129.

[Lovett-Barron et al., 2017] Lovett-Barron, M., Andalman, A. S., Allen, W. E., Vesuna, S., Kauvar, I., Burns, V. M., and Deisseroth, K. (2017). Ancestral Circuits for the Coordinated Modulation of Brain State. *Cell*, 171(6):1411–1423.e17.

[Lu and Ashe, 2005] Lu, X. and Ashe, J. (2005). Anticipatory activity in primary motor cortex codes memorized movement sequences. *Neuron*, 45(6):967–973.

[Mante et al., 2013] Mante, V., Sussillo, D., Shenoy, K. V., and Newsome, W. T. (2013). Context-dependent computation by recurrent dynamics in prefrontal cortex. *Nature*, 503(7474):78–84.

[Maoz et al., 2019] Maoz, U., Yaffe, G., Koch, C., and Mudrik, L. (2019). Neural precursors of decisions that matter—an ERP study of deliberate and arbitrary choice. *eLife*, 8.

[Marquart et al., 2019] Marquart, G. D., Tabor, K. M., Bergeron, S. A., Briggman, K. L., and Burgess, H. A. (2019). Prepontine non-giant neurons drive flexible escape behavior in zebrafish. *PLOS Biology*, 17(10):e3000480.

[Marques et al., 2018] Marques, J. C., Lackner, S., Félix, R., and Orger, M. B. (2018). Structure of the Zebrafish Locomotor Repertoire Revealed with Unsupervised Behavioral Clustering. *Current Biology*, 28(2):181–195.e5.

[Marques et al., 2020] Marques, J. C., Li, M., Schaak, D., Robson, D. N., and Li, J. M. (2020). Internal state dynamics shape brainwide activity and foraging behaviour. *Nature*, 577(7789):239–243.

[Marvin et al., 2019] Marvin, J. S., Shimoda, Y., Magloire, V., Leite, M., Kawashima, T., Jensen, T. P., Kolb, I., Knott, E. L., Novak, O., Podgorski, K., Leidenheimer, N. J., Rusakov, D. A., Ahrens, M. B., Kullmann, D. M., and Looger, L. L. (2019). A genetically encoded fluorescent sensor for in vivo imaging of GABA. *Nature Methods*, 16(8):763–770.

[Matsui, 2017] Matsui, H. (2017). Dopamine system, cerebellum, and nucleus ruber in fish and mammals. *Development, Growth & Differentiation*, 59(4):219–227.

[Matsui et al., 2014a] Matsui, H., Namikawa, K., Babaryka, A., and Köster, R. W. (2014a). Functional regionalization of the teleost cerebellum analyzed in vivo. *Proceedings of the National Academy of Sciences of the United States of America*, 111(32):11846–11851.

[Matsui et al., 2014b] Matsui, H., Namikawa, K., and Köster, R. W. (2014b). Identification of the zebrafish red nucleus using wheat germ agglutinin transneuronal tracing. *Communicative and Integrative Biology*, 7(6).

[Mauk and Buonomano, 2004] Mauk, M. D. and Buonomano, D. V. (2004). The neural basis of temporal processing. *Annual Review of Neuroscience*, 27(1):307–340.

[McCormick, 1999] McCormick, C. A. (1999). Anatomy of the central auditory pathways of fish and amphibians. In *Comparative hearing: Fish and Amphibians*, volume 11, pages 155–217.

[McKenna et al., 1994] McKenna, T. M., McMullen, T. A., and Shlesinger, M. F. (1994). The brain as a dynamic physical system. *Neuroscience*, 60(3):587–605.

[McLean et al., 2007] McLean, D. L., Fan, J., Higashijima, S. I., Hale, M. E., and Fetcho, J. R. (2007). A topographic map of recruitment in spinal cord. *Nature*, 446(7131):71–75.

[McLean and Fetcho, 2004a] McLean, D. L. and Fetcho, J. R. (2004a). Ontogeny and innervation patterns of dopaminergic, noradrenergic, and serotonergic neurons in larval zebrafish. *Journal of Comparative Neurology*, 480(1):38–56.

[McLean and Fetcho, 2004b] McLean, D. L. and Fetcho, J. R. (2004b). Relationship of tyrosine hydroxylase and serotonin immunoreactivity to sensorimotor circuitry in larval zebrafish. *Journal of Comparative Neurology*, 480(1):57–71.

[McLean et al., 2008] McLean, D. L., Masino, M. A., Koh, I. Y., Lindquist, W. B., and Fetcho, J. R. (2008). Continuous shifts in the active set of spinal interneurons during changes in locomotor speed. *Nature Neuroscience*, 11(12):1419–1429.

[McPherson et al., 2016] McPherson, A. D., Barrios, J. P., Luks-Morgan, S. J., Manfredi, J. P., Bonkowsky, J. L., Douglass, A. D., and Dorsky, R. I. (2016). Motor Behavior Mediated by Continuously Generated Dopaminergic Neurons in the Zebrafish Hypothalamus Recovers after Cell Ablation. *Current Biology*, 26(2):263–269.

[Mearns et al., 2020] Mearns, D. S., Donovan, J. C., Fernandes, A. M., Semmelhack, J. L., and Baier, H. (2020). Deconstructing Hunting Behavior Reveals a Tightly Coupled Stimulus-Response Loop. *Current Biology*, 30(1):54–69.e9.

[Mellem et al., 2008] Mellem, J. E., Brockie, P. J., Madsen, D. M., and Maricq, A. V. (2008). Action potentials contribute to neuronal signaling in C. elegans. *Nature Neuroscience*, 11(8):865–867.

[Metcalfe et al., 1986] Metcalfe, W. K., Mendelson, B., and Kimmel, C. B. (1986). Segmental homologies among reticulospinal neurons in the hindbrain of the zebrafish larva. *The Journal of Comparative Neurology*, 251(2):147–159.

[Migault et al., 2018] Migault, G., van der Plas, T. L., Trentesaux, H., Panier, T., Candelier, R., Proville, R., Englitz, B., Debrégeas, G., and Bormuth, V. (2018). Whole-Brain Calcium Imaging during Physiological Vestibular Stimulation in Larval Zebrafish. *Current biology : CB*, 28(23):3723—-3735.e6.

[Miller, 2003] Miller, G. A. (2003). The cognitive revolution: a historical perspective. *Trends in Cognitive Sciences*, 7(3):141–144.

[Miyawaki et al., 1997] Miyawaki, A., Llopis, J., Heim, R., Michael McCaffery, J., Adams, J. A., Ikura, M., and Tsien, R. Y. (1997). Fluorescent indicators for Ca2+ based on green fluorescent proteins and calmodulin. *Nature*, 388(6645):882–887.

[Mo et al., 2010] Mo, W., Chen, F., Nechiporuk, A., and Nicolson, T. (2010). Quantification of vestibular-induced eye movements in zebrafish larvae. *BMC neuroscience*, 11(1):110.

[Montgomery et al., 2018] Montgomery, J. E., Wahlstrom-Helgren, S., Wiggin, T. D., Corwin, B. M., Lillesaar, C., and Masino, M. A. (2018). Intraspinal serotonergic signaling suppresses locomotor activity in larval zebrafish. *Developmental Neurobiology*, 78(8):807–827.

[Moreaux, 2007] Moreaux, L. (2007). Estimating firing rates from calcium signals in locust projection neurons in vivo. *Frontiers in Neural Circuits*, 1:2.

[Mori and Ohshima, 1995] Mori, I. and Ohshima, Y. (1995). Neural regulation of thermotaxis in Caenorhabditis elegans. *Nature*, 376(6538):344–348.

[Mueller, 2012] Mueller, T. (2012). What is the Thalamus in Zebrafish? *Frontiers in Neuroscience*, 6(MAY):64.

[Mueller et al., 2011] Mueller, T., Dong, Z., Berberoglu, M. A., and Guo, S. (2011). The dorsal pallium in zebrafish, Danio rerio (Cyprinidae, Teleostei). *Brain Research*, 1381(49):95–105.

[Mueller et al., 2008] Mueller, T., Wullimann, M. F., and Guo, S. (2008). Early teleostean basal ganglia development visualized by zebrafish Dlx2a, Lhx6, Lhx7, Tbr2 (eomesa), and GAD67 gene expression. *Journal of Comparative Neurology*, 507(2):1245–1257.

[Mueller et al., 2007] Mueller, V. A., Brass, M., Waszak, F., and Prinz, W. (2007). The role of the preSMA and the rostral cingulate zone in internally selected actions. *NeuroImage*, 37(4):1354–1361.

[Murakami and Mainen, 2015] Murakami, M. and Mainen, Z. F. (2015). Preparing and selecting actions with neural populations: toward cortical circuit mechanisms. *Current Opinion in Neurobiology*, 33:40–46.

[Murakami et al., 2014] Murakami, M., Vicente, M. I., Costa, G. M., and Mainen, Z. F. (2014). Neural antecedents of self-initiated actions in secondary motor cortex. *Nature Neuroscience*, 17(11):1574–1582.

[Murphy et al., 2016] Murphy, P. R., Boonstra, E., and Nieuwenhuis, S. (2016). Global gain modulation generates time-dependent urgency during perceptual choice in humans. *Nature Communications*, 7(1):1–15.

[Muto et al., 2017] Muto, A., Lal, P., Ailani, D., Abe, G., Itoh, M., and Kawakami, K. (2017). Activation of the hypothalamic feeding centre upon visual prey detection. *Nature Communications*, 8(1):15029.

[Myers, 1985] Myers, P. Z. (1985). Spinal motoneurons of the larval zebrafish. *Journal of Comparative Neurology*, 236(4):555–561.

[Nachev and Husain, 2010] Nachev, P. and Husain, M. (2010). Action and the fallacy of the 'internal': Comment on Passingham et al. *Trends in Cognitive Sciences*, 14(5):192–193.

[Nachev et al., 2008] Nachev, P., Kennard, C., and Husain, M. (2008). Functional role of the supplementary and pre-supplementary motor areas. *Nature Reviews Neuroscience*, 9(11):856–869.

[Nakai et al., 2001] Nakai, J., Ohkura, M., and Imoto, K. (2001). A high signal-to-noise ca2+ probe composed of a single green fluorescent protein. *Nature Biotechnology*, 19(2):137–141.

[Nann et al., 2019] Nann, M., Cohen, L. G., Deecke, L., and Soekadar, S. R. (2019). To jump or not to jump - The Bereitschaftspotential required to jump into 192-meter abyss. *Scientific Reports*, 9(1):1–9.

[Naumann et al., 2016] Naumann, E. A., Fitzgerald, J. E., Dunn, T. W., Rihel, J., Sompolinsky, H., and Engert, F. (2016). From Whole-Brain Data to Functional Circuit Models: The Zebrafish Optomotor Response. *Cell*, 167(4):947–960.e20.

[Noë, 2004] Noë, A. (2004). *Action in perception*. MIT Press.

[Olive, 2015] Olive, R. (2015). *Perception des écoulements et des vibrations chez la larve de poisson-zèbre : étude comportementale et imagerie*. PhD thesis.

[Olive et al., 2016] Olive, R., Wolf, S., Dubreuil, A., Bormuth, V., Debrégeas, G., and Candelier, R. (2016). Rheotaxis of Larval Zebrafish: Behavioral Study of a Multi-Sensory Process. *Frontiers in Systems Neuroscience*, 10:14.

[Oliveira and Yonehara, 2018] Oliveira, A. F. and Yonehara, K. (2018). The Mouse Superior Colliculus as a Model System for Investigating Cell Type-Based Mechanisms of Visual Motor Transformation. *Frontiers in Neural Circuits*, 12:59.

[Olshausen and Field, 2004] Olshausen, B. and Field, D. (2004). Sparse coding of sensory inputs. *Current Opinion in Neurobiology*, 14(4):481–487.

[O'Malley et al., 1996] O'Malley, D. M., Kao, Y. H., and Fetcho, J. R. (1996). Imaging the functional organization of zebrafish hindbrain segments during escape behaviors. *Neuron*, 17(6):1145–1155.

[O'Regan and Noë, 2001] O'Regan, J. K. and Noë, A. (2001). A sensorimotor account of vision and visual consciousness. *Behavioral and Brain Sciences*, 24(5):939–973.

[Orger et al., 2008] Orger, M. B., Kampff, A. R., Severi, K. E., Bollmann, J. H., and Engert, F. (2008). Control of visually guided behavior by distinct populations of spinal projection neurons. *Nature Neuroscience*, 11(3):327–333.

[Orger et al., 2000] Orger, M. B., Smear, M. C., Anstis, S. M., and Baier, H. (2000). Perception of Fourier and non-Fourier motion by larval zebrafish. *Nature Neuroscience*, 3(11):1128–1133.

[Panier et al., 2013] Panier, T., Romano, S. A., Olive, R., Pietri, T., Sumbre, G., Candelier, R., and Debrégeas, G. (2013). Fast functional imaging of multiple brain regions in intact zebrafish larvae using selective plane illumination microscopy. *Frontiers in Neural Circuits*, 7(65):65.

[Parichy, 2015] Parichy, D. M. (2015). Advancing biology through a deeper understanding of zebrafish ecology and evolution. *eLife*, 4.

[Park et al., 2020] Park, J., Coddington, L. T., and Dudman, J. T. (2020). Basal Ganglia Circuits for Action Specification. *Annual Review of Neuroscience*, 43(1).

[Passingham et al., 2010a] Passingham, R. E., Bengtsson, S. L., and Lau, H. C. (2010a). Is it fallacious to talk of self-generated action?: Response to Nachev and Husain. *Trends in Cognitive Sciences*, 14(5):193–194.

[Passingham et al., 2010b] Passingham, R. E., Bengtsson, S. L., and Lau, H. C. (2010b). Medial frontal cortex: from self-generated action to reflection on one's own performance. *Trends in Cognitive Sciences*, 14(1):16–21.

[Patel et al., 2014] Patel, G. H., Kaplan, D. M., and Snyder, L. H. (2014). Topographic organization in the brain: searching for general principles. *Trends in Cognitive Sciences*, 18(7):351–363.

[Penfield and Boldrey, 1937] Penfield, W. and Boldrey, E. (1937). Somatic motor and sensory representation in the cerebral cortex of man as studied by electrical stimulation. *Brain*, 60(4):389–443.

[Pierce-Shimomura et al., 1999] Pierce-Shimomura, J. T., Morse, T. M., and Lockery, S. R. (1999). The fundamental role of pirouettes in Caenorhabditis elegans chemotaxis. *Journal of Neuroscience*, 19(21):9557–9569.

[Pietri et al., 2013] Pietri, T., Roman, A.-C., Guyon, N., Romano, S. A., Washbourne, P., Moens, C. B., de Polavieja, G. G., and Sumbre, G. (2013). The first mecp2-null zebrafish model shows altered motor behaviors. *Frontiers in neural circuits*, 7:118.

[Pnevmatikakis et al., 2016] Pnevmatikakis, E. A., Soudry, D., Gao, Y., Machado, T. A., Merel, J., Pfau, D., Reardon, T., Mu, Y., Lacefield, C., Yang, W., Ahrens, M., Bruno, R., Jessell, T. M., Peterka, D. S., Yuste, R., and Paninski, L. (2016). Simultaneous Denoising, Deconvolution, and Demixing of Calcium Imaging Data. *Neuron*, 89(2):299.

[Ponce-Alvarez et al., 2018] Ponce-Alvarez, A., Jouary, A., Privat, M., Deco, G., and Sumbre, G. (2018). Whole-Brain Neuronal Activity Displays Crackling Noise Dynamics. *Neuron*, 100(6):1446–1459.e6.

[Portugues and Engert, 2011] Portugues, R. and Engert, F. (2011). Adaptive Locomotor Behavior in Larval Zebrafish. *Frontiers in Systems Neuroscience*, 5:72.

[Poulsen et al., 2020] Poulsen, R. E., Sholz, L. A., Constantin, L., Favre-Bulle, I., Vanwalleghem, G. C., and Scott, E. K. (2020). Broad frequency sensitivity and complex neural coding in the larval zebrafish auditory system. *bioRxiv*, page 2020.09.17.301242.

[Prescott, 2007] Prescott, T. J. (2007). Forced Moves or Good Tricks in Design Space? Landmarks in the Evolution of Neural Mechanisms for Action Selection. *Adaptive Behavior*, 15(1):9–31.

[Proville et al., 2014] Proville, R. D., Spolidoro, M., Guyon, N., Dugué, G. P., Selimi, F., Isope, P., Popa, D., and Léna, C. (2014). Cerebellum involvement in cortical sensorimotor circuits for the control of voluntary movements. *Nature Neuroscience*, 17(9):1233–1239.

[Raichle, 2006] Raichle, M. E. (2006). The Brain's Dark Energy. *Science*, 314(5803).

[Raichle and Mintun, 2006] Raichle, M. E. and Mintun, M. A. (2006). BRAIN WORK AND BRAIN IMAGING. *Annual Review of Neuroscience*, 29(1):449–476.

[Ramirez and Aksay, 2020] Ramirez, A. and Aksay, E. (2020). Ramp-to-Threshold Dynamics in a Hindbrain Population Controls the Timing of Spontaneous Saccades. *bioRxiv*, page 430645.

[Randlett et al., 2015] Randlett, O., Wee, C. L., Naumann, E. a., Nnaemeka, O., Schoppik, D., Fitzgerald, J. E., Portugues, R., Lacoste, A. M. B., Riegler, C., Engert, F., and Schier, A. F. (2015). Whole-brain activity mapping onto a zebrafish brain atlas. *Nature Methods*, 12(September).

[Ratcliff et al., 2016] Ratcliff, R., Smith, P. L., Brown, S. D., and McKoon, G. (2016). Diffusion Decision Model: Current Issues and History. *Trends in Cognitive Sciences*, 20(4):260–281.

[Redgrave et al., 1999] Redgrave, P., Prescott, T., and Gurney, K. (1999). The basal ganglia: a vertebrate solution to the selection problem? *Neuroscience*, 89(4):1009–1023.

[Reinig et al., 2017] Reinig, S., Driever, W., and Arrenberg, A. B. (2017). The Descending Diencephalic Dopamine System Is Tuned to Sensory Stimuli. *Current Biology*, 27(3):318–333.

[Reiser, 2009] Reiser, M. (2009). The ethomics era? *Nature Methods*, 6(6):413–414.

[Rimmer, 2019] Rimmer, N. (2019). *The physiological and functional characterisation of the subpallial dopaminergic neurons in larval zebrafish*. PhD thesis.

[Ringach, 2009] Ringach, D. L. (2009). Spontaneous and driven cortical activity: implications for computation. *Current Opinion in Neurobiology*, 19(4):439–444.

[Rink and Wullimann, 2001] Rink, E. and Wullimann, M. F. (2001). The teleostean (zebrafish) dopaminergic system ascending to the subpallium (striatum) is located in the basal diencephalon (posterior tuberculum). *Brain Research*, 889(1-2):316–330.

[Rinner et al., 2005] Rinner, O., Rick, J. M., and Neuhauss, S. C. (2005). Contrast sensitivity, spatial and temporal tuning of the larval zebrafish optokinetic response. *Investigative Ophthalmology and Visual Science*, 46(1):137–142.

[Rochefort et al., 2009] Rochefort, N. L., Garaschuk, O., Milos, R. I., Narushima, M., Marandi, N., Pichler, B., Kovalchuk, Y., and Konnerth, A. (2009). Sparsification of neuronal activity in the visual cortex at eye-opening. *Proceedings of the National Academy of Sciences of the United States of America*, 106(35):15049–15054.

[Romano et al., 2017] Romano, S. A., Pérez-Schuster, V., Jouary, A., Boulanger-Weill, J., Candeo, A., Pietri, T., and Sumbre, G. (2017). An integrated calcium imaging processing toolbox for the analysis of neuronal population dynamics. *PLOS Computational Biology*, 13(6):e1005526.

[Romano et al., 2015] Romano, S. A., Pietri, T., Pérez-Schuster, V., Jouary, A., Haudrechy, M., and Sumbre, G. (2015). Spontaneous Neuronal Network Dynamics Reveal Circuit's Functional Adaptations for Behavior. *Neuron*, 85(5):1070–1085.

[Romo and Schultz, 1987] Romo, R. and Schultz, W. (1987). Neuronal activity preceding self-initiated or externally timed arm movements in area 6 of monkey cortex. *Experimental Brain Research*, 67(3):656–662.

[Saigusa et al., 2008] Saigusa, T., Tero, A., Nakagaki, T., and Kuramoto, Y. (2008). Amoebae anticipate periodic events. *Physical Review Letters*, 100(1):018101.

[Sanes and Donoghue, 1993] Sanes, J. N. and Donoghue, J. P. (1993). Oscillations in local field potentials of the primate motor cortex during voluntary movement. *Proceedings of the National Academy of Sciences of the United States of America*, 90(10):4470–4474.

[Sanes and Schieber, 2001] Sanes, J. N. and Schieber, M. H. (2001). Orderly Somatotopy in Primary Motor Cortex: Does It Exist? *NeuroImage*, 13(6):968–974.

[Satou et al., 2012] Satou, C., Kimura, Y., and ichi Higashijima, S. (2012). Generation of multiple classes of V0 neurons in Zebrafish spinal cord: Progenitor heterogeneity and temporal control of neuronal diversity. *Journal of Neuroscience*, 32(5):1771–1783.

[Schmidt et al., 2016] Schmidt, S., Jo, H.-G., Wittmann, M., and Hinterberger, T. (2016). 'Catching the waves' – slow cortical potentials as moderator of voluntary action. *Neuroscience & Biobehavioral Reviews*, 68:639–650.

[Scholes, 2008] Scholes, E. (2008). Evolution of the courtship phenotype in the bird of paradise genus Parotia (Aves: Paradisaeidae): homology, phylogeny, and modularity. *Biological Journal of the Linnean Society*, 94(3):491–504.

[Schultz and Romo, 1992] Schultz, W. and Romo, R. (1992). Role of primate basal ganglia and frontal cortex in the internal generation of movements - I. Preparatory activity in the anterior striatum. *Experimental Brain Research*, 91(3):363–384.

[Schurger et al., 2012] Schurger, A., Sitt, J. D., and Dehaene, S. (2012). An accumulator model for spontaneous neural activity prior to self-initiated movement. *Proceedings of the National Academy of Sciences of the United States of America*, 109(42).

[Scott, 2009] Scott, E. K. (2009). The cellular architecture of the larval zebrafish tectum, as revealed by Gal4 enhancer trap lines. *Frontiers in Neural Circuits*, 3(OCT):13.

[Scott et al., 2007] Scott, E. K., Mason, L., Arrenberg, A. B., Ziv, L., Gosse, N. J., Xiao, T., Chi, N. C., Asakawa, K., Kawakami, K., and Baier, H. (2007). Targeting neural circuitry in zebrafish using GAL4 enhancer trapping. *Nature Methods*, 4(4):323–326.

[Scott, 2012] Scott, S. H. (2012). The computational and neural basis of voluntary motor control and planning. *Trends in Cognitive Sciences*, 16(11):541–549.

[Semmelhack et al., 2014] Semmelhack, J. L., Donovan, J. C., Thiele, T. R., Kuehn, E., Laurell, E., and Baier, H. (2014). A dedicated visual pathway for prey detection in larval zebrafish. *eLife*, 3.

[Severi et al., 2018] Severi, K. E., Böhm, U. L., and Wyart, C. (2018). Investigation of hindbrain activity during active locomotion reveals inhibitory neurons involved in sensorimotor processing. *Scientific Reports*, 8(1):13615.

[Severi et al., 2014] Severi, K. E., Portugues, R., Marques, J. C., O'Malley, D. M., Orger, M. B., and Engert, F. (2014). Neural Control and Modulation of Swimming Speed in the Larval Zebrafish. *Neuron*, 83(3).

[Shadlen et al., 2016] Shadlen, M. N., Kiani, R., Newsome, W. T., Gold, J. I., Wolpert, D. M., Zylberberg, A., Ditterich, J., de Lafuente, V., Yang, T., and Roitman, J. (2016). Comment on "Single-trial spike trains in parietal cortex reveal discrete steps during decision-making". *Science*, 351(6280):1406–1406.

[Shadlen and Newsome, 2001] Shadlen, M. N. and Newsome, W. T. (2001). Neural basis of a perceptual decision in the parietal cortex (area LIP) of the rhesus monkey. *Journal of Neurophysiology*, 86(4):1916–1936.

[Shenoy et al., 2013] Shenoy, K. V., Sahani, M., and Churchland, M. M. (2013). Cortical Control of Arm Movements: A Dynamical Systems Perspective. *Annual Review of Neuroscience*, 36(1):337–359.

[Shimomura et al., 1962] Shimomura, O., Johnson, F. H., and Saiga, Y. (1962). Extraction, purification and properties of aequorin, a bioluminescent. *Journal of cellular and comparative physiology*, 59(3):223–239.

[Sirota et al., 2000] Sirota, M. G., Di Prisco, G. V., and Dubuc, R. (2000). Stimulation of the mesencephalic locomotor region elicits controlled swimming in semi-intact lampreys. *European Journal of Neuroscience*, 12(11):4081–4092.

[Skinner, 1974] Skinner, B. F. (1974). *About behaviorism*. New York, knopf edition.

[Smeets and Timerick, 1981] Smeets, W. J. A. J. and Timerick, S. J. B. (1981). Cells of origin of pathways descending to the spinal cord in two chondrichthyans, the sharkScyliorhinus canicula and the rayRaja clavata. *The Journal of Comparative Neurology*, 202(4):473–491.

[Sompolinsky, 2014] Sompolinsky, H. (2014). Computational neuroscience: Beyond the local circuit. *Current Opinion in Neurobiology*, 25:13–18.

[Souza et al., 2011] Souza, B. R., Romano-Silva, M. A., and Tropepe, V. (2011). Dopamine D2 receptor activity modulates Akt signaling and alters GABaergic neuron development and motor behavior in Zebrafish larvae. *Journal of Neuroscience*, 31(14):5512–5525.

[Sprague and Meikle, 1965] Sprague, J. M. and Meikle, T. H. (1965). The role of the superior colliculus in visually guided behavior. *Experimental Neurology*, 11(1):115–146.

[Stephenson-Jones et al., 2011] Stephenson-Jones, M., Samuelsson, E., Ericsson, J., Robertson, B., and Grillner, S. (2011). Evolutionary conservation of the basal ganglia as a common vertebrate mechanism for action selection. *Current Biology*, 21(13):1081–1091.

[Stinnakre and Tauc, 1973] Stinnakre, J. and Tauc, L. (1973). Calcium influx in active aplysia neurones detected by injected aequorin. *Nature New Biology*, 242(117):113–115.

[Stringer et al., 2019] Stringer, C., Pachitariu, M., Steinmetz, N., Reddy, C. B., Carandini, M., and Harris, K. D. (2019). Spontaneous behaviors drive multidimensional, brainwide activity. *Science*, 364(6437).

[Sumbre et al., 2001] Sumbre, G., Gutfreund, Y., Fiorito, G., Flash, T., and Hochner, B. (2001). Control of octopus arm extension by a peripheral motor program. *Science*, 293(5536):1845–1848.

[Suzuki et al., 2019] Suzuki, D. G., Pérez-Fernández, J., Wibble, T., Kardamakis, A. A., and Grillner, S. (2019). The role of the optic tectum for visually evoked orienting and evasive movements. *Proceedings of the National Academy of Sciences of the United States of America*, 116(30):15272–15281.

[Svoboda et al., 1997] Svoboda, K., Denk, W., Kleinfeld, D., and Tank, D. W. (1997). In vivo dendritic calcium dynamics in neocortical pyramidal neurons. *Nature*, 385(6612):161–165.

[Tay et al., 2011] Tay, T. L., Ronneberger, O., Ryu, S., Nitschke, R., and Driever, W. (2011). Comprehensive catecholaminergic projectome analysis reveals single-neuron

integration of zebrafish ascending and descending dopaminergic systems. *Nature Communications*, 2(1):171.

[Temizer et al., 2015] Temizer, I., Donovan, J. C., Baier, H., and Semmelhack, J. L. (2015). A Visual Pathway for Looming-Evoked Escape in Larval Zebrafish. *Current Biology*, 25(14).

[Thiele et al., 2014] Thiele, T. R., Donovan, J. C., and Baier, H. (2014). Descending Control of Swim Posture by a Midbrain Nucleus in Zebrafish. *Neuron*, 83(3).

[Thompson et al., 2016] Thompson, A., Vanwalleghem, G., Heap, L., and Scott, E. (2016). Functional Profiles of Visual-, Auditory-, and Water Flow-Responsive Neurons in the Zebrafish Tectum. *Current Biology*, 26(6):743–754.

[Tinbergen, 1951] Tinbergen, N. (1951). *The study of instinct.* Clarendon Press/Oxford University Press, New York.

[Tinbergen, 1963] Tinbergen, N. (1963). On aims and methods of Ethology. *Zeitschrift für Tierpsychologie*, 20(4):410–433.

[Tosches, 2017] Tosches, M. A. (2017). Developmental and genetic mechanisms of neural circuit evolution. *Developmental Biology*, 431(1):16–25.

[Travers et al., 2020] Travers, E., Friedemann, M., and Haggard, P. (2020). The Readiness Potential reflects expectation, not uncertainty, in the timing of action. *bioRxiv*, page 2020.04.16.045344.

[Troemel et al., 1997] Troemel, E. R., Kimmel, B. E., and Bargmann, C. I. (1997). Reprogramming chemotaxis responses: Sensory neurons define olfactory preferences in C. elegans. *Cell*, 91(2):161–169.

[Tsien, 1980] Tsien, R. Y. (1980). New calcium indicators and buffers with high selectivity against magnesium and protons: design, synthesis, and properties of prototype structures. *Biochemistry*, 19(11):2396–2404.

[Vanwalleghem et al., 2017] Vanwalleghem, G., Heap, L. A., and Scott, E. K. (2017). A profile of auditory-responsive neurons in the larval zebrafish brain. *Journal of Comparative Neurology*, 525(14):3031–3043.

[Vanwalleghem et al., 2020] Vanwalleghem, G., Schuster, K., Taylor, M. A., Favre-Bulle, I. A., and Scott, E. K. (2020). Brain-Wide Mapping of Water Flow Perception in Zebrafish. *The Journal of Neuroscience*, 40(21):4130–4144.

[Varela et al., 1991] Varela, F. J., Thompson, E., and Rosch, E. (1991). *The embodied mind: Cognitive science and human experience.* The MIT Press, Cambridge, MA, US.

[Varoqueaux et al., 2018] Varoqueaux, F., Williams, E. A., Grandemange, S., Truscello, L., Kamm, K., Schierwater, B., Jékely, G., and Fasshauer, D. (2018). High Cell Diversity and Complex Peptidergic Signaling Underlie Placozoan Behavior. *Current Biology*, 28(21):3495–3501.e2.

[Voleti et al., 2019] Voleti, V., Patel, K. B., Li, W., Perez Campos, C., Bharadwaj, S., Yu, H., Ford, C., Casper, M. J., Yan, R. W., Liang, W., Wen, C., Kimura, K. D., Targoff, K. L., and Hillman, E. M. (2019). Real-time volumetric microscopy of in vivo dynamics and large-scale samples with SCAPE 2.0. *Nature Methods*, 16(10):1054–1062.

[von Trotha et al., 2014] von Trotha, J. W., Vernier, P., and Bally-Cuif, L. (2014). Emotions and motivated behavior converge on an amygdala-like structure in the zebrafish. *European Journal of Neuroscience*, 40(9):3302–3315.

[Vyas et al., 2020] Vyas, S., Golub, M. D., Sussillo, D., and Shenoy, K. V. (2020). Computation through Neural Population Dynamics. *Annual Review of Neuroscience*, 43:249–275.

[Wakabayashi et al., 2004] Wakabayashi, T., Kitagawa, I., and Shingai, R. (2004). Neurons regulating the duration of forward locomotion in Caenorhabditis elegans. *Neuroscience Research*, 50(1):103–111.

[Walton et al., 2004] Walton, M. E., Devlin, J. T., and Rushworth, M. F. (2004). Interactions between decision making and performance monitoring within prefrontal cortex. *Nature Neuroscience*, 7(11):1259–1265.

[Wang et al., 2014] Wang, K., Milkie, D. E., Saxena, A., Engerer, P., Misgeld, T., Bronner, M. E., Mumm, J., and Betzig, E. (2014). Rapid adaptive optical recovery of optimal resolution over large volumes. *Nature Methods*, 11(6):625–628.

[White et al., 1986] White, J., Southgate, E., Thomson, J., and Brenner, S. (1986). The structure of the nervous system of the nematode Caenorhabditis elegans. *Philosophical Transactions of the Royal Society of London. B, Biological Sciences*, 314(1165):1–340.

[Wolf et al., 2017] Wolf, S., Dubreuil, A. M., Bertoni, T., Böhm, U. L., Bormuth, V., Candelier, R., Karpenko, S., Hildebrand, D. G. C., Bianco, I. H., Monasson, R., and Debrégeas, G. (2017). Sensorimotor computation underlying phototaxis in zebrafish. *Nature Communications*, 8(1):651.

[Wolpert and Ghahramani, 2000] Wolpert, D. M. and Ghahramani, Z. (2000). Computational principles of movement neuroscience. *Nature Neuroscience*, 3(11s):1212–1217.

[Wolpert et al., 1998] Wolpert, D. M., Miall, R., and Kawato, M. (1998). Internal models in the cerebellum. *Trends in Cognitive Sciences*, 2(9):338–347.

[Woods et al., 2014] Woods, I. G., Schoppik, D., Shi, V. J., Zimmerman, S., Coleman, H. A., Greenwood, J., Soucy, E. R., and Schier, A. F. (2014). Neuropeptidergic signaling partitions arousal behaviors in zebrafish. *Journal of Neuroscience*, 34(9):3142–3160.

[Wullimann, 2011] Wullimann, M. F. (2011). Basal Ganglia: Insights into Origins from Lamprey Brains. *Current Biology*, 21(13):R497–R500.

[Wullimann, 2014] Wullimann, M. F. (2014). Ancestry of basal ganglia circuits: New evidence in teleosts. *Journal of Comparative Neurology*, 522(9):2013–2018.

[Wullimann and Mueller, 2004] Wullimann, M. F. and Mueller, T. (2004). Teleostean and mammalian forebrains contrasted: Evidence from genes to behavior. *The Journal of Comparative Neurology*, 475(2):143–162.

[Wullimann et al., 1996] Wullimann, M. F., Rupp, B., and Reichert, H. (1996). *Neuroanatomy of the Zebrafish Brain*. Birkhäuser Basel.

[Yaksi and Friedrich, 2006] Yaksi, E. and Friedrich, R. W. (2006). Reconstruction of firing rate changes across neuronal populations by temporally deconvolved Ca2+ imaging. *Nature methods*, 3(5):377–383.

[Yamamoto and Ito, 2008] Yamamoto, N. and Ito, H. (2008). Visual, lateral line, and auditory ascending pathways to the dorsal telencephalic area through the rostrolateral region of the lateral preglomerular nucleus in cyprinids. *The Journal of Comparative Neurology*, 508(4):615–647.

[Yamamoto et al., 2017] Yamamoto, N., Nakayama, T., and Hagio, H. (2017). Descending pathways to the spinal cord in teleosts in comparison with mammals, with special attention to rubrospinal pathways. *Development, Growth & Differentiation*, 59(4):188–193.

[Yoshida et al., 2012] Yoshida, K., Hirotsu, T., Tagawa, T., Oda, S., Wakabayashi, T., Iino, Y., and Ishihara, T. (2012). Odour concentration-dependent olfactory preference change in C. elegans. *Nature Communications*, 3(1):1–11.

[Yuste and Denk, 1995] Yuste, R. and Denk, W. (1995). Dendritic spines as basic functional units of neuronal integration. *Nature*, 375(6533):682–684.

[Zeddies and Fay, 2005] Zeddies, D. G. and Fay, R. R. (2005). Development of the acoustically evoked behavioral response in zebrafish to pure tones. *The Journal of experimental biology*, 208(Pt 7):1363–1372.

5

Annexes

5.1 Naturalistic Behavior: The Zebrafish Larva Strikes Back

Current Biology
Dispatches

Naturalistic Behavior: The Zebrafish Larva Strikes Back

Martin Privat and Germán Sumbre*
Institut de Biologie de l'ENS (IBENS), Département de Biologie, École Normale Supérieure, CNRS, INSERM, Université; PSL, 75005 Paris, France
*Correspondence: sumbre@biologie.ens.fr
https://doi.org/10.1016/j.cub.2019.11.014

Two recent studies show that zebrafish larvae alternate between two behavioral modes: exploration and hunting. Both behaviors are structured on multiple time scales, and require the integration of internal and external cues to generate sequences of stereotyped swimming movements.

The term behavior is in common use and has a very general meaning: it refers to what an organism does, its physical response to its internal and/or external environments or to its own internal decisions. The motor movements that constitute this response lead to dynamic interactions with the environment through sensorimotor feedback loops where the senses play an active role in gathering information — what has been termed 'enactive perception' [1,2]. To some extent, animal behavior is a heritable phenotypic trait, and it is therefore subject to natural selection [3], and consequently is strongly dependent on an organism's environment. In order to ensure they are studying the full behavioral repertoire of an organism, therefore, ethologists should study animal behavior in environments as similar as possible to the natural ones. In this issue of *Current Biology*, two papers [4,5] report studies of the naturalistic behavior of young zebrafish larvae resulting in descriptions at an unprecedented level of kinematic detail.

Zebrafish has been an important model for developmental biology and genetics, and in more recent years, it has become a powerful vertebrate model for systems neuroscience and behavior. Even at the larval stage, zebrafish has a large variety of complex behaviors, yet these can be decomposed into a few stereotyped discrete movements, known as tail bouts, making the larva an advantageous model for large-scale and precise behavioral quantification. Moreover, the small size of the zebrafish larva enables monitoring behavior in a relatively large naturalistic arena.

Early studies on zebrafish behavior focused on stereotyped, sensory-induced startle behaviors, which were analysed according to their onset, speed and body shape [6]. Later, McElligot *et al.* [7] described the prey-capture behavior of the zebrafish larva, a complex behavior that can be decomposed into a series of orienting sub-movements later called J-turns, small forward swims called approaches or pursuits, and a final strike (Figure 1); in most cases, the larva also makes convergent eye movements. Two decades of detailed kinematics studies have shifted the field from hand-crafted descriptions of behavior to unsupervised machine learning approaches applied to high-dimensional large datasets, pushing the study of behavior into the era of 'ethomics' [8]. More recently, using state-of-the-art experimental and computational approaches, Marques *et al.* [9] demonstrated that the entire behavioral repertoire of the zebrafish larva is based on the combination of just a few basic swim types, organized into sequences of actions.

Despite these important advances, it has been unclear precisely how the larva selects the different sequences of movements according to the sensory information in the environment, its previous experience and its internal state. The two new studies from Johnson *et al.* [4] and Mearns *et al.* [5] address these open questions. The authors used high-speed cameras to record behavior of freely swimming zebrafish larvae in minute detail with high spatial and temporal resolution, enabling them to dissect animal behavior while resolving fine anatomical structures of the behaving larvae.

Mearns *et al.* [5] tracked the curvature of the tail, the orientation of the eyes, and the elevation of the cranium and the jaws of behaving larvae to analyse their coordination during behavior. They recorded several thousands of swim bouts, which gave a comprehensive and high-dimensional representation of the larva's behavioral repertoire. To classify the different tail bouts, both Johnson *et al.* [4] and Mearns *et al.* [5] used state-of-the-art non-linear dimensionality reduction techniques (tSNE and isomap). These methods place each bout type on a low-dimensional space, in which bouts with similar characteristics are close by.

With this approach, Mearns *et al.* [5] were able to show that, during prey capture, zebrafish larvae coordinate capture strikes with the protrusion of their jaw and elevation of the cranium to catch paramecia (Figure 1). Remarkably, they also found that zebrafish larvae use only a subset of their behavioral repertoire in the absence of prey. These results highlight the importance of using naturalistic environments to understand the diversity and complexity of animal behavior.

Subsequently, Mearns *et al.* [5] studied the statistical properties of sequences of bouts. To do so, they took into account the history of bout types produced by the larvae and the inter-bout interval duration. The authors used the singular value

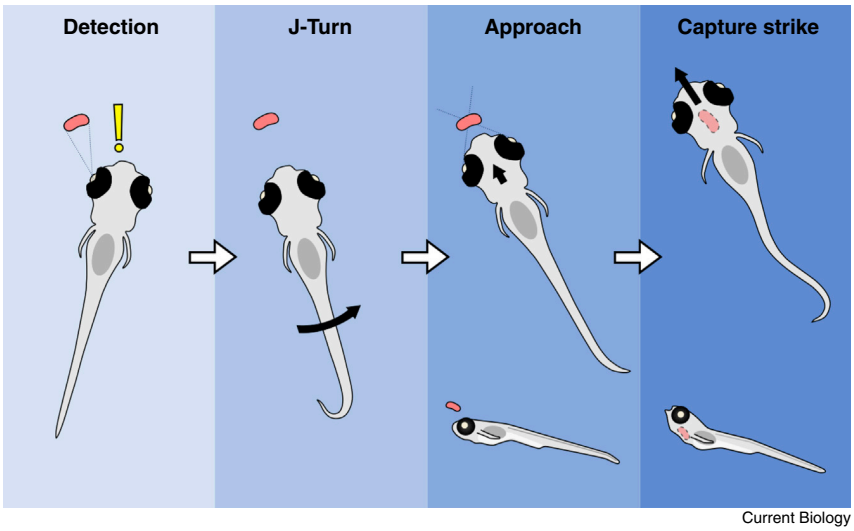

Figure 1. Prey-capture sequence.
Prey-capture sequence ending in a successful capture strike. Bottom: lateral view. Note the position of the paramecia (red shape) in the anterior dorsal visual field before the capture strike is released, as well as the protrusion of the jaw and the elevation of the cranium during the capture strike. Black arrows: change in position of the larva after the movement is completed.

decomposition of the bout transition matrix to understand the structure of transitions between bout types. This method makes it possible to identify the most relevant transition patterns in the dataset. Johnson *et al.* [4] modeled bout history on multiple time scales using generalized linear models and marked renewal processes. The latter are probabilistic models that allowed the authors to predict future actions based on the behavioral history and the visual experience of the larva. The parameters of these probabilistic models are learned from the data using generalized linear models, flexible generalizations of linear regression that take into account non-Gaussian errors.

Both studies [4,5] reveal the importance of short-term history on action selection. Using Markov models — probabilistic models that take into account a fixed number of recent states of a system to predict its next state — Mearns *et al.* [5] show that the selection of the type of swimming bout, for both prey capture and exploration, is strongly influenced by the type of the preceding bout. Similarly, Johnson *et al.* [4] argue that the bout type and the inter-bout interval duration can be predicted by the preceding ones, and that bouts are chained together preferentially through ipsilateral transitions, meaning that larvae will often turn in the same direction during successive bouts. Those observations could be linked to either intrinsic or external factors, for example brain state or sensory experience.

Zebrafish prey-capture behavior is vision dependent [7]. Johnson *et al.* [4] show that taking into account the location of objects in the field of view improves researchers' ability to predict the type of the larva's future bouts, especially in the case of hunting bouts. Moreover, prediction performance is further improved by taking into account complex interactions between visual features, in particular the positions, sizes and velocities of objects. This finding corroborates previous descriptions of tectal neurons with mixed selectivity to different features in the visual scene [10]. Along similar lines, Mearns *et al.* [5] propose that prey-capture sequences are maintained through sensorimotor loops. They show that J-turns and approaches bring prey to the center of the dorsal visual field and within a stereotyped distance from the mouth, from where a capture strike can be released (Figure 1). This sequence is impaired in blind zebrafish mutants (*lakritz*), mutants with vision defects (*blumenkohl*), and in larvae that are blind following genetic ablation of the retinas. Interestingly, the authors show that removing a virtual prey as soon as the eyes of the larva converge induces the termination of the larva's whole hunting sequence, indicating that prey-capture behavior requires continuous visual feedback. This finding suggests that hunting is dependent on sensorimotor feedback loops rather than representing a fixed-action pattern (a stereotypical feed-forward sequence of movements that run to completion once engaged).

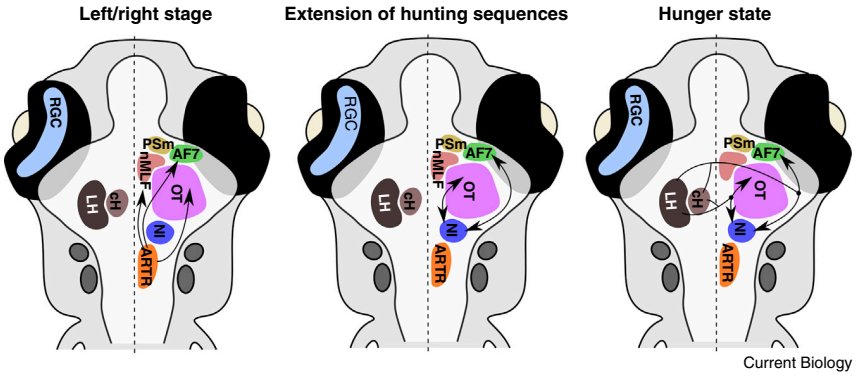

Figure 2. Putative neural circuits underlying behavior.
Brain regions involved in prey capture and exploratory behavior: PSm, magnocellular superficial pretectal nucleus; AF7, arborization field 7; RGC, retinal ganglion cells; nMLF, nucleus of the medial longitudinal fascicle; OT, optic tectum; NI, nucleus isthmi; ARTR, anterior rhombencephalic turning region; cH, caudal hypothalamus; LH, lateral hypothalamus. The arrows indicate the interactions between the different brain regions.

Johnson *et al.* [4] also show that internal factors can influence behavior at different time scales [11]: on the intermediate time scale of several bouts, they found that transitions between swim bouts are affected by the time spent exploring or hunting; over a longer run, lasting tens of minutes, they observed an effect of hunger on behavior [12]. They further found that starved larvae converge their eyes more often than fed larvae, even during non-hunting behaviors, and tend to have shorter inter-bout intervals during exploratory behavior. Taken together, their results suggest that starvation promotes food seeking through an up-regulation of hunting behaviors, while satiety promotes safety seeking, lower energy expenditure, and low-risk exploration.

While they found that the previous bout type and inter-bout interval are the best single predictors of future behaviors, Johnson *et al.* [4] also show that there is a high order, non-Markovian, memory-dependent structure in the transitions between swim bouts, most likely associated with the change in internal states of the animals. This feature has also been found in *Drosophila* [13] and *C. elegans* [14], supporting the idea that behavior is modular and hierarchically organized [13,14]. These hypotheses are sparking a renewed interest in the study of internal states and their role in animal behavior [15].

These two new studies [4,5] raise questions about the neural mechanisms underlying the integration of internal states and external cues in order to produce relevant, context-dependent behavior across different time scales. In zebrafish, prey capture is dependent on the optic tectum [10]. In addition, the arborization of the pretectal field 7 (AF7) seems to mediate prey-capture initiation [16,17] , while a second pretectal nucleus called PSm is involved in prey detection [17]. Activity in the nucleus isthmi (NI) seems to be required for sustained prey capture sequences [16]. Finally, downstream motor activity is driven by a pair of spinal projection neurons in the nucleus of the medial longitudinal fascicle [18] (Figure 2). Dunn *et al.* [19] have found a region in the hindbrain, the anterior rhombencephalic turning region (ARTR), activity of which is linked to swim direction. This region could be involved in the generation of ipsilateral transitions between bouts observed by Johnson *et al.* [4]. How the ARTR could bias the generation of movements is still unknown and warrants further studies.

Furthermore, recent studies suggest that the hypothalamus is involved in the representation of hunger [12,17] and could influence prey-capture behavior. Johnson *et al.* [4] propose testable hypotheses for the connections between ARTR, hypothalamus, and the regions involved in prey capture, as well as pre-motor targets, that could create a large neuronal circuit distributed across several brain regions capable of driving behavior at different time scales (Figure 2). Despite these advances on the neuronal basis of behavior, it is still not known how these prey-capture related areas interconnect and interact to drive action selection. Future progress in this area may come from new technological innovations allowing the measurement of neural activity and behavior in freely swimming larvae feeding on paramecia [20].

Taken together, these new studies from Mearns *et al.* [5] and Johnson *et al.* [4] shed light on the structure of the behavioral repertoire of the zebrafish larva in naturalistic conditions, and may pave the way to the understanding of their underlying neural network mechanisms and the neural basis of enactive perception.

REFERENCES

1. Noë, A. (2004). Action in Perception (MIT Press).
2. Ahissar, E., and Assa, E. (2016). Perception as a closed-loop convergence process. eLife *5*. e12830. https://doi.org/10.7554/eLife.12830.
3. Tinbergen, N. (1951). The Study of Instinct (New York, NY, US: Clarendon Press/Oxford University Press).
4. Johnson, R.E., Linderman, S., Panier, T., Wee, C.L., Song, E., Herrera, K.J., Miller, A., and Engert, F. (2020). Probabilistic models of larval zebrafish behavior reveal structure on many scales. Curr. Biol. *30*, 70–82.
5. Mearns, D.S., Donovan, J.C., Fernandes, A.M., Semmelhack, J.L., and Baier, H. (2020). Deconstructing hunting behavior reveals a tightly coupled stimulus-response loop. Curr. Biol. *30*, 54–69.
6. Kimmel, C.B., Patterson, J., and Kimmel, R.O. (1974). The development and behavioral characteristics of the startle response in the zebra fish. Dev. Psychobiol. *7*, 47–60.
7. McElligott, M.B., and O'Malley, D.M. (2005). Prey tracking by larval zebrafish: Axial kinematics and visual control. Brain. Behav. Evol. *66*, 177–196.
8. Reiser, M. (2009). The ethomics era? Nat. Meth. *6*, 413–414.
9. Marques, J.C., Lackner, S., Félix, R., and Orger, M.B. (2018). Structure of the zebrafish locomotor repertoire revealed with unsupervised behavioral clustering. Curr. Biol. *28*, 181–195.
10. Bianco, I., and Engert, F. (2014). Visuomotor transformations underlying hunting behavior in zebrafish. Curr. Biol. *25*, 831–846.
11. Berman, G.J. (2018). Measuring behavior across scales. BMC Biol. *16*, 23.
12. Filosa, A., Barker, A.J., Dal Maschio, M., and Baier, H. (2016). Feeding state modulates behavioral choice and processing of prey stimuli in the zebrafish tectum. Neuron *90*, 596–608.
13. Berman, G.J., Bialek, W., and Shaevitz, J.W. (2016). Predictability and hierarchy in Drosophila behavior. Proc. Natl. Acad. Sci. USA *113*, 11943–11948.
14. Gupta, S., and Gomez-Marin, A. (2019). A context-free grammar for Caenorhabditis elegans behavior. bioRxiv, 708891.
15. Calhoun, A.J., Pillow, J.W., and Murthy, M. (2019). Unsupervised identification of the internal states that shape natural behavior. Nat. Neurosci. *22*, 2040–2049.
16. Henriques, P.M., Rahman, N., Jackson, S.E., and Bianco, I.H. (2019). Nucleus isthmi is required to sustain target pursuit during visually guided prey-catching. Curr. Biol. *29*, 1771–1786.
17. Muto, A., Lal, P., Ailani, D., Abe, G., Itoh, M., and Kawakami, K. (2017). Activation of the hypothalamic feeding centre upon visual prey detection. Nat. Commun. *8*, 15029.
18. Gahtan, E. (2005). Visual prey capture in larval zebrafish is controlled by identified reticulospinal neurons downstream of the tectum. J. Neurosci. *25*, 9294–9303.
19. Dunn, T.W., Mu, Y., Narayan, S., Randlett, O., Naumann, E.A., Yang, C.-T., Schier, A.F., Freeman, J., Engert, F., and Ahrens, M.B. (2016). Brain-wide mapping of neural activity controlling zebrafish exploratory locomotion. eLife *5*, e12741.
20. Kim, D.H., Kim, J., Marques, J.C., Grama, A., Hildebrand, D.G.C., Gu, W., Li, J.M., and Robson, D.N. (2017). Pan-neuronal calcium imaging with cellular resolution in freely swimming zebrafish. Nat. Methods *14*, 1107–1114.

5.2 Whole-Brain Neuronal Activity Displays Crackling Noise Dynamics

Article

Neuron

Whole-Brain Neuronal Activity Displays Crackling Noise Dynamics

Highlights

- Zebrafish whole-brain activity displays scale-invariant neuronal avalanches
- These scale-invariant avalanches are suggestive of critical phenomena
- Sensory inputs and self-generated behaviors deviate the dynamics from criticality
- Blocking gap junctions disrupts criticality and deteriorates sensory processing

Authors

Adrián Ponce-Alvarez, Adrien Jouary, Martin Privat, Gustavo Deco, Germán Sumbre

Correspondence

adrian.ponce@upf.edu (A.P.-A.), sumbre@biologie.ens.fr (G.S.)

In Brief

Ponce-Alvarez et al. show that zebrafish larvae generate spontaneous neuronal avalanches across the entire brain. These collective cascading events exhibit scale invariance, typical of critical phenomena (e.g., earthquakes, paper crumpling). The brain's critical dynamics are modulated during interactions with the environment.

Ponce-Alvarez et al., 2018, Neuron *100*, 1446–1459
December 19, 2018
https://doi.org/10.1016/j.neuron.2018.10.045

CellPress

CellPress

Neuron
Article

Whole-Brain Neuronal Activity Displays Crackling Noise Dynamics

Adrián Ponce-Alvarez,[1,7,*] Adrien Jouary,[2,3,7] Martin Privat,[2] Gustavo Deco,[1,4,5,6,8] and Germán Sumbre[2,8,9,*]
[1]Center for Brain and Cognition, Computational Neuroscience Group, Department of Information and Communication Technologies, Universitat Pompeu Fabra, Barcelona 08005, Spain
[2]Institut de biologie de l'Ecole normale supérieure (IBENS), Ecole normale supérieure, CNRS, INSERM, PSL Université Paris, Paris 75005, France
[3]Champalimaud Research, Champalimaud Centre for the Unknown, Lisbon 1400-038, Portugal
[4]Institució Catalana de la Recerca i Estudis Avançats (ICREA), Barcelona 08010, Spain
[5]Department of Neuropsychology, Max Planck Institute for Human Cognitive and Brain Sciences, Leipzig 04103, Germany
[6]School of Psychological Sciences, Monash University, Melbourne, Clayton VIC 3800, Australia
[7]These authors contributed equally
[8]These authors contributed equally
[9]Lead Contact
*Correspondence: adrian.ponce@upf.edu (A.P.-A.), sumbre@biologie.ens.fr (G.S.)
https://doi.org/10.1016/j.neuron.2018.10.045

SUMMARY

Previous studies suggest that the brain operates at a critical point in which phases of order and disorder coexist, producing emergent patterned dynamics at all scales and optimizing several brain functions. Here, we combined light-sheet microscopy with GCaMP zebrafish larvae to study whole-brain dynamics *in vivo* at near single-cell resolution. We show that spontaneous activity propagates in the brain's three-dimensional space, generating scale-invariant neuronal avalanches with time courses and recurrence times that exhibit statistical self-similarity at different magnitude, temporal, and frequency scales. This suggests that the nervous system operates close to a non-equilibrium phase transition, where a large repertoire of spatial, temporal, and interactive modes can be supported. Finally, we show that gap junctions contribute to the maintenance of criticality and that, during interactions with the environment (sensory inputs and self-generated behaviors), the system is transiently displaced to a more ordered regime, conceivably to limit the potential sensory representations and motor outcomes.

INTRODUCTION

Recent studies have shown that neuronal populations display collective activity patterns that are characterized by sequences of activations called "neuronal avalanches" (Beggs and Plenz, 2003; Mazzoni et al., 2007; Pasquale et al., 2008; Friedman et al., 2012; Hahn et al., 2010, 2017; Shriki et al., 2013; Tagliazucchi et al., 2012; Priesemann et al., 2014). It has been proposed that the statistics of neuronal avalanches are signatures of criticality, a particular operating regime between phases of order and disorder in which several brain functions could be optimized, such as input sensitivity and dynamic range (Shew and Plenz, 2013). Indeed, previous reports show that the sizes and durations of neuronal avalanches are scale invariant (i.e., they follow power-law statistics with power exponents that depend on each other, which are typical features of systems at criticality). Another signature of criticality is the presence of scaling relations. For instance, Friedman et al. (2012) have shown that the dynamics of long-duration avalanches are similar to those of short-duration avalanches when they are properly rescaled. These previous studies suggest signs of criticality in spiking activity and local field potentials (LFPs) of neural cultures *in vitro* (Beggs and Plenz, 2003; Mazzoni et al., 2007; Pasquale et al., 2008; Friedman et al., 2012), LFP signals *in vivo* (Hahn et al., 2010), field potentials and fMRI blood-oxygen-level-dependent (BOLD) signals *in vivo* (Shriki et al., 2013; Tagliazucchi et al., 2012), voltage imaging *in vivo* (Scott et al., 2014), and 10–100 single-unit or multi-unit spiking and calcium-imaging activity *in vivo* (Priesemann et al., 2014; Bellay et al., 2015; Hahn et al., 2017; Seshadri et al., 2018). Despite these advances, criticality in the brain remains an open question, since mesoscopic measurements (from LFPs to BOLD signals) might distort the dynamics, and spiking data from a limited number of neurons are prone to subsampling effects (Priesemann et al., 2014) that are known to strongly bias the characterization of collective behavior, even in the case of scale-free networks (Levina and Priesemann, 2017; Stumpf et al., 2005). Therefore, to study criticality in the nervous system, it is necessary to monitor whole-brain dynamics with single-cell resolution. Moreover, how criticality is affected when the organism interacts with the environment remains elusive, and the functional connectivity mechanisms that promote a critical state are unknown.

Here, we addressed these open questions by studying the statistics of the zebrafish whole-brain dynamics and by interpreting them within the framework of criticality. Specifically, we used transgenic zebrafish larvae expressing genetically encoded

calcium indicators (GCaMP5 or GCaMP6f) in combination with selective-plane illumination microscopy (SPIM) to monitor whole-brain dynamics with near single-neuron resolution in an intact, behaving vertebrate (Ahrens et al., 2013; Panier et al., 2013; Romano et al., 2017). Using this approach, we were able to study the collective dynamics of neuronal activity and its propagation across the whole brain, in three-dimensional space and time, in the form of neuronal avalanches, and at a wide range of scales. Analyzing the spatiotemporal activity patterns in 3D space is important because scale-invariant behaviors observed at criticality do not depend on the microscopic details of the system. Instead, they often depend on the dimension of the system and the type of phase transition. Thus, a system at criticality has universal properties that can be explained by simple mathematical models (Sethna et al., 2001). We were particularly interested in comparing the statistics of neuronal avalanches with those of critical three-dimensional systems that operate close to a non-equilibrium disorder-induced phase transition, for which the associated dynamics produce avalanches at all scales, or "crackling noise" (Sethna et al., 2001). Crackling noise arises in heterogeneous systems under external drive when the heterogeneity of the system's elements (quenched disorder) is strong enough to compete with the interactions between them.

Here, we detected neuronal avalanches propagating in the brain during periods of both spontaneous and visually induced activity. We analyzed the spatial statistics of the activity patterns (their number, sizes, scaling properties, and correlation functions) and the spatiotemporal dynamics of the neuronal avalanches (sizes, durations, scaling properties, and spectral content) and compared these statistics during spontaneous activity, during the presentation of visual stimuli, during self-generated motor behaviors, and in pharmacologically perturbed conditions. Our results suggest that whole-brain dynamics fluctuate close to the critical point of a non-equilibrium disorder-induced phase transition, from which it can be displaced by interactions with the environment (sensory inputs and behavioral outputs). In addition, we found that gap junctions might be involved in maintaining a critical regime in the vertebrate nervous system.

RESULTS

To study the spatiotemporal activity patterns emerging from whole-brain dynamics, we analyzed the neuronal activity from six zebrafish larvae (6–8 days post-fertilization [dpf]) recorded using SPIM (see STAR Methods and Figures S1A–S1C). In our study, morphological images were segmented into regions of interest (ROIs) corresponding to putative single neurons and neuropil regions, from which fluorescence fluctuations were extracted. Larvae were head restricted to simultaneously monitor neuronal activity and spontaneous tail movements. The six datasets were composed of N = 41,115–89,349 selected ROIs recorded during long recordings of 1–2 hr composed of Q segments that each included a period of spontaneous activity (20 min) and a shorter period (4 min) of visual stimulation (Q ranges between 3 and 9, see Table S1 and Figure S1D). Visual stimulation was composed of gratings moving in different directions. Whole-brain activity was characterized by the activation of groups of ROIs that could span large parts of the brain (see Video S1). We aimed to describe the statistics of these events. For this, the activity of each putative neuron was binarized by imposing an activity threshold. Then, we identified clusters of co-active and spatially contiguous ROIs and quantified their number, size, and evolution over time (see STAR Methods).

Percolation Transition of the Spatial Clusters of Co-active and Contiguous ROIs

First, we characterized the spatial patterns of collective neuronal activity by calculating the number of clusters and their sizes (number of activations; see STAR Methods). We studied the cluster statistics within the framework of percolation theory. Percolation describes the behavior of clusters in a graph and how the cluster sizes change with the number of active units, going from small clusters to the emergence of a large cluster beyond a critical level of activity. Throughout this study, we analyzed the spontaneous and the visually evoked activity together, unless specified otherwise. For each time t, we computed the proportion of active ROIs (ρ), the number of clusters (m), and the size of the i-th cluster ($C_s(i)$, $1 \leq i \leq m$). First, we calculated the relation between ρ and m and found that the number of clusters peaked when $\sim$ 15% of the ROIs were active, a value that we denoted as ρ_c (Figures 1A, S2A, and S2B; Table S1). Interestingly, the variability of m was also maximized at this level of activation. Thus, there exists a fraction of active ROIs, ρ_c, for which the largest diversity of clusters was observed. Second, we calculated the relationship between ρ and the normalized size of the largest cluster (i.e., $C_{max} = \max(C_s)/C_{all}$, where C_{all} is the size of the largest cluster obtained when all recorded ROIs are hypothetically active, i.e., above the activity threshold), which ranges between 91.40% and 99.74% of the ROIs for the different datasets. We found that C_{max} grows with ρ and spans a broad range of scales, from few ROIs to almost the entire brain, as it can be essentially as large as $\sim$ 1 (Figures 1B and S2C). Third, we found that the level of network activation was different during the spontaneous and stimulus-evoked activity: the distribution of ρ, denoted as $P(\rho)$, showed that most often, the level of spontaneous activation was below ρ_c, and 10.52%–44.93% of the time, ρ was larger than ρ_c (Figures 1C and S2F). The activation level during the stimulus-evoked activity exceeded the value ρ_c significantly more often than in the spontaneous activity in 5 of the 6 datasets (17.82%–60.29% of the time, $p < 0.01$, paired t test comparing $P(\rho > \rho_c)$ during spontaneous and visual stimulation periods; see Figure 1G).

The above behaviors are signatures of the existence of a percolation critical point (ρ_c). Percolation theory shows that, close to the critical probability, the distribution of cluster sizes follows a power law with an exponent that depends only on the dimensions of the system (it does not depend on the details of the physical system). To test this, we computed the distribution of cluster sizes C_s, noted $P(C_s)$, and approximated it by a power law, which appears as a straight line in a log-log plot, such that $P(C_s) \sim C_s^{-\sigma}$ (Figures 1D–1F). We used a maximum likelihood estimation (MLE) method to assess the power law that best fitted the size distribution of the set of clusters that appeared with ρ comprised within small intervals $(\rho - \Delta; \rho + \Delta)$, with $\Delta = 0.02$. In the interval between $\rho_c - \Delta$ and $\rho_c + \Delta$, $P(C_s)$ was well

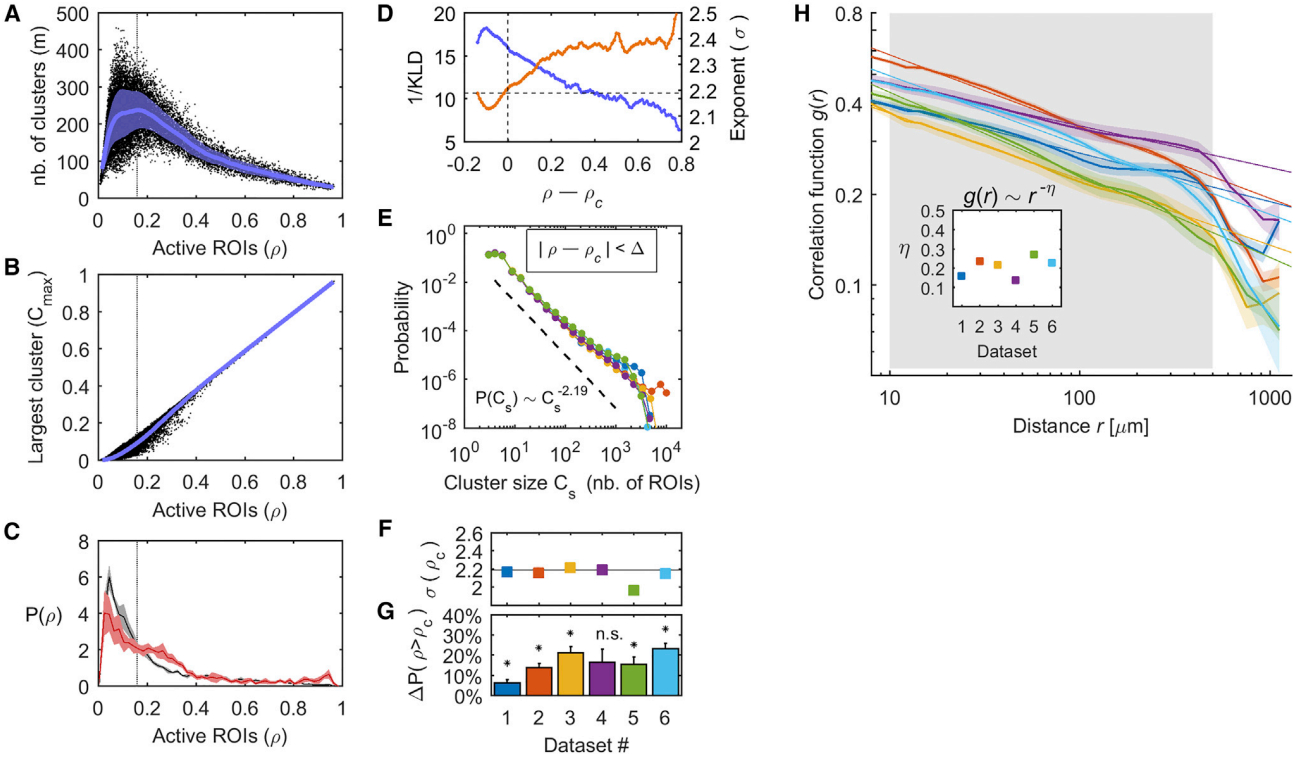

Figure 1. Statistics of the Clusters of Co-active and Contiguous ROIs

(A) Number of clusters (m) as a function of the proportion of active ROIs (ρ). Blue line, mean of m; blue area, its standard deviation.

(B) Normalized size of the largest cluster (C_{max}) as a function of ρ (blue trace: average C_{max}).

(C) Distribution of ρ (black, spontaneous activity; red, stimulus-evoked activity) calculated for each of the Q spontaneous and evoked segments (solid line, mean distribution; shaded area, SEM). Note that the stimulus-evoked distribution is skewed to the right.

(D) We calculated the cluster size distribution for the set of clusters that appeared with ρ comprised within small intervals ($\rho - \Delta$; $\rho + \Delta$). Using the Kullback-Leibler divergence (KLD), we calculated the goodness of fit of the power law (blue) and, using MLE, we estimated the power exponent (orange) as a function of ρ. (A)–(D) show results for dataset 1. Note that, for $\rho = \rho_c$, the goodness of fit is close to its maximum and the corresponding power exponent is equal to one predicted in the case of 3D percolation, equal to 2.19 (dashed horizontal line).

(E) Size distribution P(C_s) of clusters that appeared with ρ between $\rho_c - \Delta$ and $\rho_c + \Delta$. Each color represents a dataset. Error bars are smaller than the symbols' size. Black line, power-law distribution predicted in 3D percolation.

(F) Power exponents $\sigma(\rho_c)$ estimated using MLE.

(G) Difference between the proportion of time that $\rho > \rho_c$ during the stimulus-evoked activity and the proportion of time that $\rho > \rho_c$ during the spontaneous activity (*p < 0.01, paired t test). Error bars, SEM across the Q spontaneous-evoked segments. See also Figure S2.

(H) Correlation function $g(r)$: average correlation between pairs of cells as a function of the Euclidean distance r, for each dataset (calculated for each of the Q segments and then averaged; colored areas, SEM). The straight lines represent power-law fits using least squares for r falling between 50 μm and 500 μm (gray area). Note that for distances longer than 500 μm, r approximates the size of the larva in one of its 3 dimensions.

Inset: estimated power-law exponent (estimation errors are smaller than the symbols' size).

approximated by a power law (Kolmogorov-Smirnov [KS] test, ks < 0.05) with log-likelihood ratio (LLR) tests supporting the power law when compared to an alternative heavy-tailed distribution such as the lognormal (see STAR Methods and Table S1). Moreover, the power law goodness of fit (calculated using the inverse of the Kullback-Leibler divergence) was close to its maximum for all datasets in the interval between $\rho_c - \Delta$ and $\rho_c + \Delta$ (Figures 1D and S2D). The corresponding power law exponent $\sigma(\rho_c)$ was between 1.97 and 2.22 for the different datasets, with an average of 2.15 ± 0.04 (Figures 1E, 1F, and S2E; Table S1). The values of $\sigma(\rho_c)$ were close to the theoretical exponent of a 3D percolation process close to the critical point, equal to 2.19 (Jan and Stauffer, 1998).

The Correlation between ROIs Decays as a Power Law of the Distance

The previous results (Figures 1B and 1E) show that ROIs can form activity clusters of practically all sizes. This suggests the presence of long-range functional correlations between ROIs. We tested this hypothesis by studying the correlations between pairs of cells as a function of the Euclidean distance r between them (i.e., the correlation function $g(r)$). Specifically, for each dataset, we calculated Pearson's pairwise correlations and the Euclidean distance between all possible pairs among 40,000 randomly selected ROIs. We found that $g(r)$ decays approximately as a power law (i.e., $g(r) \sim r^{-\eta}$ with a least-squares exponent η equal to 0.22 ± 0.02 on average) for r between 50 μm and

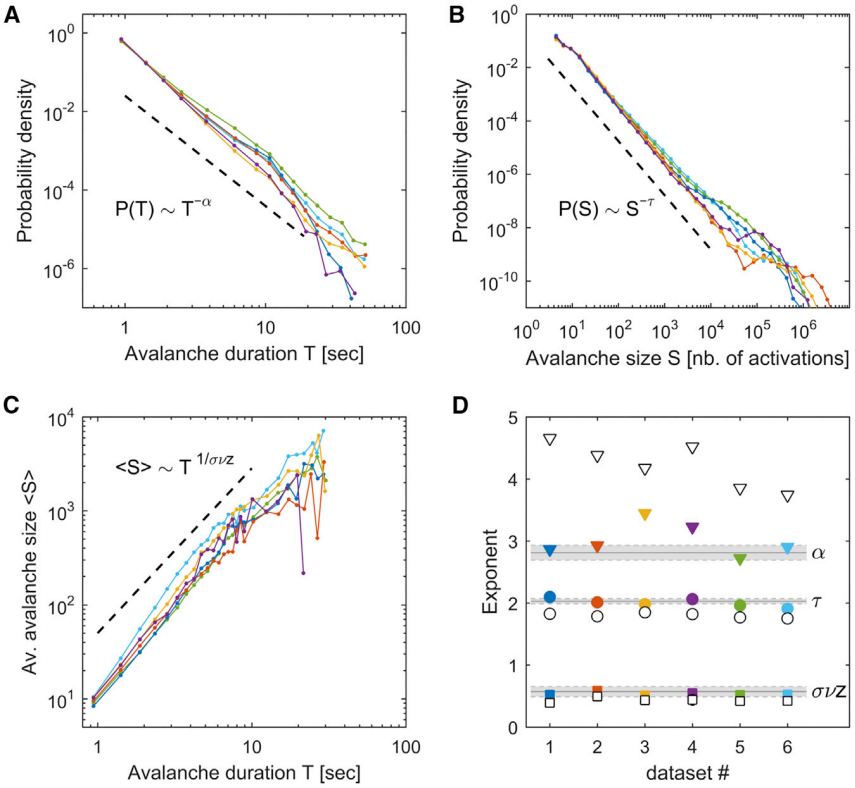

Figure 2. Neuronal Avalanches Show Critical Statistics

(A) Distribution of avalanche durations T (in s).

(B) Distribution of avalanche sizes S (i.e., cumulative sum of the number of activated ROIs).

(C) Relation between S and T, for each dataset. In (A), (B), and (C), each color corresponds to a dataset and the black dashed line indicates the power law expected in the case of critical behavior. The validity of the power-law fitting was evaluated using Kolmogorov-Smirnov statistics and log-likelihood ratio tests; see Table S2 for more details.

(D) Measured exponents for each dataset (colored filled symbols) and the corresponding time-shuffled data (open symbols). Triangles, α exponent; circles, τ exponent; squares, $\sigma\nu z$ exponent. Error bars (estimation errors) are smaller than the size of the symbols. The gray horizontal lines and the gray shaded areas indicate the expected critical exponents and their uncertainty, respectively, in 3D random field Ising models.

See Table S2 for more details. See also Figures S3 and S4.

500 μm (Figure 1H). These power-law exponents were preserved during spontaneous and stimulus-evoked activity ($p = 0.18$, paired t test; correlation coefficient = 0.65). Long-range power-law correlations are a hallmark of complex systems at criticality, which are characterized by non-trivial emergent collective spatiotemporal dynamics (Expert et al., 2011). Consequently, we next characterized how patterned activity propagates when including the time dimension.

The Temporal Dynamics of the Clusters Show Neuronal Avalanches Suggestive of Critical Behavior

We observed that, once a cluster was initiated, it could grow, collide with other clusters, or terminate. We tracked the clusters across time using the following procedure, which is a usual definition of avalanches in sand-pile models, Ising models, and analyses of fMRI recordings (Tagliazucchi et al., 2012): a new avalanche was initiated at time t_0 if a cluster i was composed of ROIs that were not active at time $t_0 - 1$; if at time $t_0 + 1$, at least one of the ROIs of the cluster i pertained to a cluster, then the avalanche was continued until this condition no longer held (see STAR Methods and Figure S3).

The total number of detected avalanches, n_{av}, ranged between 2.39×10^5 and 7.94×10^5 for the different datasets. An avalanche was described by its duration T (the time it lasted) and its size S (the number of neuronal activations during the avalanche). Using KS statistics and LLR tests to compare candidate heavy-tailed distributions, we found that avalanche durations and sizes were both well approximated by truncated power-law distributions (i.e., $P(T) \sim T^{-\alpha}$ and $P(S) \sim S^{-\tau}$) for all datasets (Figures 2A and 2B, and Table S2 for details). Thus, avalanches spanned a broad range of scales. The averaged MLE power-law exponents, α and τ, were equal to 3.01 ± 0.11 and 2.01 ± 0.03, respectively. In contrast, shuffled data that preserved the spatial correlations but randomized the temporal structure (time-shuffled data, see STAR Methods) led to significantly different exponents ($\alpha = 4.22 \pm 0.15$ and $\tau = 1.80 \pm 0.02$; $p < 0.001$, two-sample t test; Figure 2D). Notably, the power laws observed in the data (but not in the shuffled data) are typical of critical systems that operate close to a non-equilibrium disorder-induced phase transition, producing avalanches at all scales, a phenomenon known as crackling noise (Sethna et al., 2001). The universal critical exponents for the avalanche durations and sizes of such systems are known to be equal to 2.81 ± 0.11 and 2.03 ± 0.03, respectively, as obtained by numerical simulations of the random field Ising model (RFIM) in three dimensions, which is the paradigmatic theoretical model of disorder-induced critical dynamics (Perković et al., 1995; Sethna et al., 2001; see also STAR Methods). Thus, the observed scaling exponents of the neuronal avalanches are suggestive of non-equilibrium critical behavior.

Criticality theory also predicts that the average size $\langle S \rangle(T)$ of avalanches of duration T is given by the scaling relation $\langle S \rangle(T) \sim T^{1/\sigma\nu z}$ (Perković et al., 1995; Sethna et al., 2001; Friedman et al., 2012). This relation was confirmed in the data for durations shorter than the power-law cutoffs (Figures 2C; see also Table S2). Moreover, using least squares to estimate the exponent, we found that for all datasets, the value of the exponent $\sigma\nu z$ was consistent with that expected for criticality in three dimensions, equal to 0.57 ± 0.09 (Perković et al., 1995) (Figure 2D; see also Table S2), while time-shuffled datasets displayed significantly different exponents: on average, $\sigma\nu z = 0.54 \pm 0.01$ for the

original data and $\sigma\nu z$ = 0.43 ± 0.02 for the shuffled data ($p < 0.001$, two-sample t test). Furthermore, the critical exponents α, τ, and $\sigma\nu z$ must obey $(\tau-1)/(\alpha-1)=\sigma\nu z$ (Perković et al., 1995; Sethna et al., 2001; Friedman et al., 2012). This relation is consistent with the exponents we measured. Indeed, the obtained values of $q=(\tau-1)/[\sigma\nu z(\alpha-1)]$ fluctuate around ~1 (q ranges between 0.79 and 1.13 and $q=$ 0.94 ± 0.05 on average), and when the analyses were performed using the avalanche durations and sizes of all datasets, we found exponent values that were strongly consistent with the theory (α = 2.90 ± 0.01, τ = 1.99 ± 0.01, and $\sigma\nu z$ = 0.54 ± 0.02, see Figures S4A–S4C). In contrast, time-shuffled data largely deviated from this relationship (q ranges between 0.47 and 0.65, $q=$ 0.58 ± 0.03 on average). Finally, we tested whether the exponents depend on the size of the clusters composing the neuronal avalanches and on the temporal resolution of the data (dt = 0.47 s). For this, active ROIs were assigned to the same cluster when their distance, in 3D space, was shorter than a given value (Figures S4D–S4F). We found that avalanche exponents were close to the theoretically predicted ones, for all larvae, for clusters defined within spheres of a radius up to ~30 μm; longer radii led to different and inconsistent exponents. The size of the clustering neighborhood used in the present study lies below this threshold. We also note that the exponents were consistent for time bins shorter or equal to 1.41 s (Figures S4G–S4I).

Universal Scaling Functions as Signs of Criticality

Besides scale invariance and power exponent relations, a further signature of criticality is the existence of universal scaling functions that capture the systems' dynamics at different scales. We studied two aspects of the avalanche dynamics: the temporal profile of the avalanches and the time intervals between avalanches. Let $S(t,T)$ be the number of activations at time t in an avalanche of duration T. Close to criticality, the average avalanche profile, $\langle S(t,T)\rangle$, is expected to be similar across temporal scales (Perković et al., 1995; Sethna et al., 2001; Friedman et al., 2012). Specifically, the relation between the normalized time t/T and the scaled avalanche profile $\langle S(t,T)\rangle T^{-a}$ follows a single form that does not depend on the temporal scale, $\langle S(t,T)\rangle T^{-a}=F(t/T)$. This invariance across scales is known as "shape collapse." To estimate the scaling parameter a, we used the method of Marshall et al. (2016), which produces the best possible collapse of the data (see STAR Methods). Note that close to criticality, the scaling parameter a and the exponent $\sigma\nu z$ are related: $a=\sigma\nu z^{-1}-1$. This is the consequence of the relationship $\langle S\rangle(T)\sim T^{1/\sigma\nu z}$ and $\langle S\rangle(T)$ being equal to the integral of $\langle S(t,T)\rangle=T^{a}F(t/T)$ between $t=0$ and $t=T$. Thus, data collapse is a different, more precise method both to assess criticality and to estimate the exponent $\sigma\nu z$. The empirical avalanche profiles showed that avalanches built up and terminated in a stereotypical way for a wide range of durations (Figure 3A) such that the average time-course of short avalanches resembled that of longer avalanches. We found that empirical avalanche profiles could indeed be collapsed (scaling reduces the variance by an amount of $\Delta\sigma_F^2$ = 3.78 – 12.52), with a scaling parameter $\sigma\nu z$ ranging between 0.47 and 0.58 for the different datasets with an average of 0.55 ± 0.02 (Figures 3B and 3C; see also Table S2). Note that the exponent values were consistent with the values of $\sigma\nu z$ estimated through the relationship between $\langle S\rangle$ and T (Figure 3D). In contrast, in time-shuffled datasets, the temporal profiles of avalanches did not collapse (Figures 3E–3H).

Criticality theory predicts that the frequency content of the dynamics within the avalanches scales as $\Phi_S(f)\sim f^{-1/\sigma\nu z}$, with the same critical exponent as in the scaling relation $\langle S\rangle(T)\sim T^{1/\sigma\nu z}$ and as in the shape collapse of avalanche profiles (Kuntz and Sethna, 2000; Travesset et al., 2002). Therefore, we next investigated the time courses of neuronal avalanches in the frequency domain (see STAR Methods). We found that the power spectral density (PSD) of the time courses of the avalanches, $\Phi_S(f)$, decayed with the frequency f approximately as a power law (Figures 4A and 4B). Using least squares, we estimated the power-law decay exponent of $\Phi_S(f)$ and found that, indeed, the values of $\sigma\nu z$ were close to those obtained through the relation $\langle S\rangle(T)$ and the shape collapse analysis, and they were consistent with the theoretical values ($\sigma\nu z$ ranges between 0.50 and 0.69 for the different datasets and $\sigma\nu z$ = 0.57 ± 0.04 on average). For time-shuffled datasets, the PSD became more uniform across frequencies and largely deviated from the predicted power law ($\sigma\nu z$ ranges between 3.30 and 4.45 for the different shuffled datasets and $\sigma\nu z$ = 3.76 ± 0.23 on average). Hence, the exponent $\sigma\nu z$ was consistently close to its theoretically predicted critical value using different approaches (scaling relation between avalanche size and duration, avalanche shape collapse, and PSD of avalanche profiles), constituting consistent evidence suggesting that neuronal avalanche dynamics were critical.

Avalanche dynamics can also be characterized by the time between the avalanches, called the recurrence time interval. We studied the conditional distributions $P(\Delta t, S>s)$ of time intervals Δt between consecutive avalanches of size larger than a given threshold s. As expected, large avalanches were separated by longer intervals (Figures 5A and 5C), so that the mean interval $\langle\Delta t\rangle$ increased with threshold s. For each minimum size s, it is possible to express the time in units of the mean interval, such that Δt becomes $\Delta t/\langle\Delta t\rangle$, which implies that the conditional distribution is changed to $P(\Delta t, S>s)\langle\Delta t\rangle$. Notably, in these re-scaled axes, the distributions collapsed onto a single curve, or scaling function, independent of the threshold s (Figures 5B and 5D). This suggests that the occurrence of avalanches can be described by a self-similar process (i.e., a process showing the same statistical properties at different scales or magnitudes). As in previous studies, the scaling function can be approximated by a single gamma distribution with one single shape parameter γ ranging between 0.20 and 0.51 (Corral, 2007) (see STAR Methods; see also Table S2). In the gamma distribution assumption, the scaling function decays approximately as a power law with exponent $1-\gamma$ for $\Delta t<\langle\Delta t\rangle$; for $\Delta t>\langle\Delta t\rangle$ the decay is exponential. A gamma point process with $\gamma=1$ is equivalent to a Poisson process, while if $\gamma<1$, as in the present data, the process is more irregular and more burst-like than a Poisson process. Consistent with previous findings, these scaling features are similar to those reported for the recurrence time distributions of critical phenomena such as earthquakes and rock fractures (Corral, 2007; Davidsen et al., 2007). In contrast, shuffled

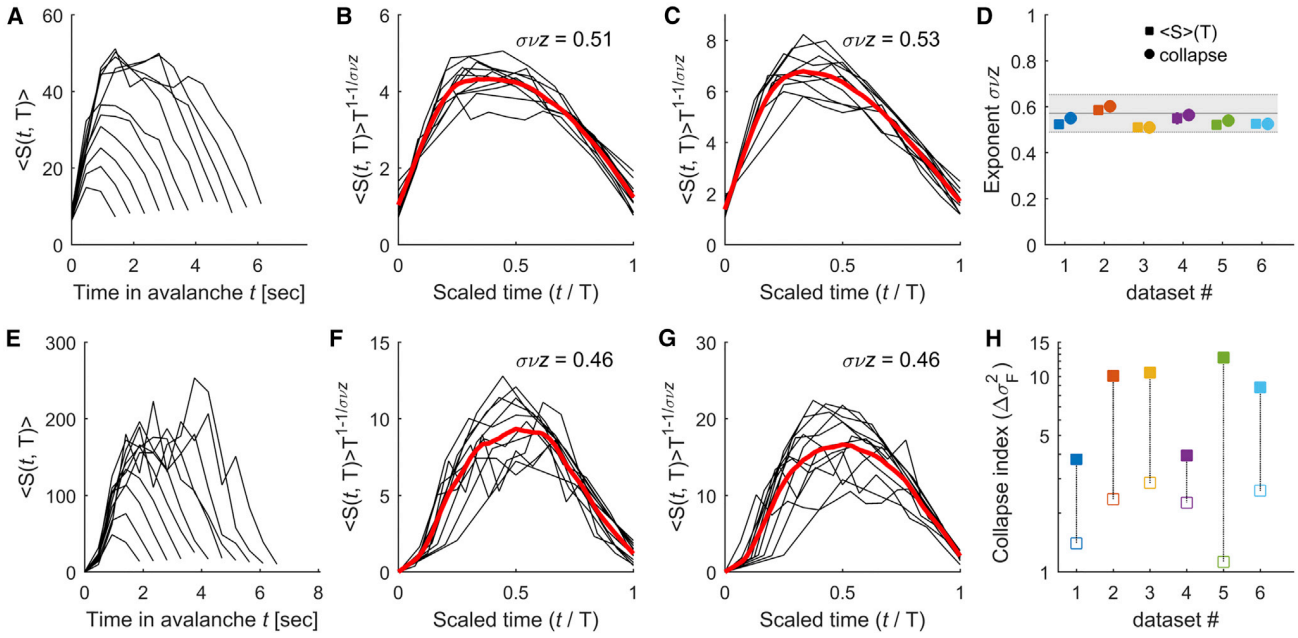

Figure 3. Universal Scaling Functions: Avalanche Profiles

(A) Averaged temporal profile, $\langle S(t,T)\rangle$, of avalanches of durations T, where T = 2.82 – 7.99 s (data from dataset 3).

(B) Scaled avalanche profiles as a function of the scaled time t/T. Red line, averaged scaled avalanche profile; $\sigma\nu z$, best scaling parameter (data from dataset 3).

(C) Same as (B) but for dataset 6.

(D) Estimated $\sigma\nu z$ exponents using scaling collapse (circles) and the relation $\langle S\rangle(T)$ (squares). Each color represents a different dataset. Estimation errors are smaller than the size of the symbols. Note the similarity between the exponents calculated with the two different methods. The gray area indicates the theoretically expected critical exponent and its uncertainty. See Table S2 for more details.

(E–G) Same as (A)–(C), respectively, but for the corresponding time-shuffled datasets, for which collapse was substantially reduced.

(H) Amount of collapse $(\Delta\sigma_F^2)$ for the original datasets (filled symbols) and the shuffled datasets (open symbols).

datasets in which we randomly permuted the avalanche sizes, while keeping the sequence of avalanches onsets, did not collapse (Figures 5E–5H). Hence, correlations between avalanche times and sizes are necessary for the process to be self-similar.

Propagation of Neuronal Avalanches in the Brain

Our data allowed us to analyze the spatial and temporal statistics of neuronal avalanches and to provide insights into which mechanisms contribute to their initiation. For this, we examined how avalanches propagated throughout the brain. We tracked the averaged location of an avalanche by calculating its center of mass (CM) and followed its temporal evolution by computing the averaged velocity of the CM, noted $\overrightarrow{V}$ (see STAR Methods). We next examined the distribution of $\overrightarrow{V_{xy}}$ (i.e., the projection of $\overrightarrow{V}$ into the coronal section [x-y plane] of the brain) (Figures 6A and 6B). We found that the direction of propagation (θ) of avalanches was constrained by the brain's anatomy: avalanches preferentially traveled parallel to the caudo-rostral axis, as shown by the anisotropy of the direction of propagation (Figure 6C). When pooling all datasets, the average propagation velocity of the CMs in 3D space (i.e., $\langle \| \overrightarrow{V} \| \rangle$, was 389 ± 23 μm/s) and the average distance traveled by the avalanches' CMs was $\langle D \rangle$ = 261 ± 23 μm (Figures 6D and 6E).

Interestingly, propagating avalanches during periods of visual stimulation were significantly faster than those during the spontaneous activity period ($p < 0.001$, two-sided Wilcoxon rank-sum test) for all datasets, with differences in median velocity ΔV ranging between 3 and 19 μm/s (Figure 6D, right). In contrast, the median distances traveled by the avalanches were not significantly different between spontaneous and visually induced activity ($p > 0.05$, two-sided Wilcoxon rank-sum test, Figure 6E, right).

Furthermore, our analysis allowed us to study the correlation between neuronal avalanches that occurred quite evenly in different locations of the brain (Figure 6F). We were interested in the interaction between parallel avalanches that occurred simultaneously at different spatial locations. Indeed, the distribution of the number of concomitant avalanches N_s largely deviated from a Poisson distribution (i.e., the expected distribution if simultaneous avalanches occurred by chance), indicating the presence of correlations (Figure 6G). We calculated the probability distribution of observing two avalanches that initiated simultaneously with CMs separated by a distance d and compared it to the expected distribution when the times of avalanche initiation were randomized (see STAR Methods). Overall, pairs of avalanches with CMs less than 150 μm apart tended to occur in the same time frame with a probability that was ~8% greater than expected by chance (Figure 6H). These results suggest that neuronal avalanches are initiated through a local mechanism with weak short-range spatial correlations due to local connectivity.

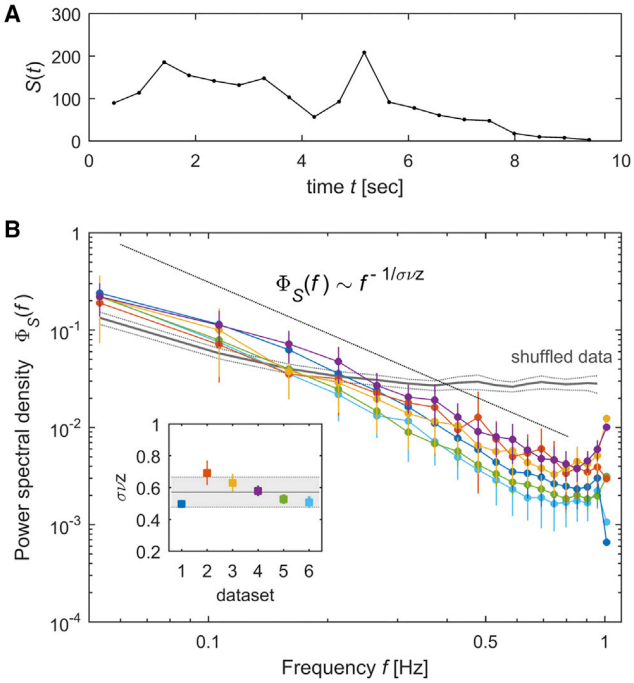

Figure 4. Universal Scaling Functions: Power Spectrum of Avalanche Time Courses

(A) Temporal profile $S(t)$ of an example avalanche of duration 9.4 s.

(B) We calculated the power spectral density (PSD) of the time courses of neuronal avalanches. Each color represents a different dataset. Error bars indicate SEM. The PSD of avalanche time courses, $\Phi_S(f)$, decays approximately as a power law of the frequency f with an exponent equal to $1/\sigma\nu z$ (black line). In contrast, the PSD of time-shuffled data was uniform across frequencies and largely deviated from the predicted power law (the gray solid line is the mean PSD across shuffled datasets, and the thin gray lines depict SEM).

Inset: exponent $\sigma\nu z$ estimated using least-squares for each dataset. Error bars indicate the exponent estimation error. The values of $\sigma\nu z$ estimated using this analysis are close to the expected critical exponent (0.57) indicated by the solid black line; the gray shaded area indicates the uncertainty of the critical exponent.

Our results suggest that criticality is an emergent phenomenon of whole-brain dynamics. To examine whether criticality also emerges at the level of local networks, we analyzed neuronal avalanches in two distinct anatomical brain regions with different functions (the optic tectum involved in sensory processing and integration and the rhombomere 7 region containing the reticulospinal circuit implicated in the generation of motor patterns; see Figure S5). Both regions displayed avalanches with durations and sizes distributions showing power-law statistics with power exponents close to the corresponding critical values. Nevertheless, while durations and average sizes of the avalanches in the optic tectum showed the expected scaling relation ($\langle S\rangle(T) \sim T^{1/\sigma\nu z}$, with $\sigma\nu z \approx 0.57$), reticulospinal avalanches deviated from it. This means that for a given duration T, the average size of the avalanches was larger than that predicted by criticality theory. Thus, in contrast to the optic tectum, avalanches in the reticulospinal circuit were faster than expected in a critical system.

Sensory Stimulation and Self-Generated Behaviors Deviate Brain Dynamics to an Ordered Regime

Our previous results (Figures 1G and 6D) show that sensory drive affects the propagation of neuronal activity in the larva's brain. To further test whether sensory stimulation affects criticality in the brain, we studied how visual stimuli affect the statistics of the neuronal avalanches. For this, we compared several avalanche properties during periods of spontaneous activity with those during periods in which visual stimulation was presented to the larvae. Using sliding windows of 120.32 s, shifted in steps of 60.16 s, we calculated the rate of avalanche initiation, the average avalanche size and duration, and the exponents α and τ. Notably, during periods of spontaneous activity, the statistical properties of neuronal avalanches remained constant (p values ranged between 0.33 and 0.85; one-way repeated-measures [RM] ANOVA tests comparing the values of each statistical property in the different time windows during periods of spontaneous activity), with size and duration exponents close to those predicted by theory in critical systems (Figures 7A–7D). However, during the visual stimulation periods, the avalanche characteristics significantly changed ($p < 0.05$, two-sided Wilcoxon rank-sum tests) and we observed: a decrease in the avalanche initiation rate (64.77 ± 0.72 versus 55.78 ± 1.16 avalanches per second, Figure 7A), an increase in the average size of the avalanches ($\langle S/N\rangle$ = 0.307% ± 0.007% versus $\langle S/N\rangle$ = 0.454% ± 0.016%, Figure 7B), an increase in the average duration of the avalanches ($\langle T\rangle$ = 1.37 ± 0.005 s versus $\langle T\rangle$ = 1.445 ± 0.012 s), and a decrease in the duration and size power exponents (τ = 2.02 ± 0.01 versus τ = 2.00 ± 0.01, α = 2.94 ± 0.02 versus α = 2.71 ± 0.03, Figures 7C and 7D). Recently, it has been proposed that stimulus-induced changes in neuronal avalanches can be fully explained by changes in the rate of activity events (Yu et al., 2017). Here, we showed that the differences between spontaneous and stimulus-induced activity patterns cannot be explained by differences in the rate of calcium events alone but rather by changes in their correlation structure (Figures S6A–S6E). Together, our results suggest that, at rest, the nervous system of the larva constantly functions in a critical regime rather than fluctuating between phases of order and disorder. In contrast, visual stimulation affects the characteristics of the avalanches, slightly shifting the dynamics of the nervous system away from criticality, toward a regime where neuronal avalanches are more ordered (i.e., faster, larger, and longer).

These results show that sensory inputs affect the dynamical regime of neuronal avalanches. We further asked how the statistics of spontaneous avalanches are influenced by the generation of spontaneous (self-generated) behavioral outputs. The head-restrained configuration of our recordings allowed us to monitor both spontaneous neuronal activity and self-generated tail movements (see STAR Methods). During spontaneous activity, larvae produced isolated and sporadic tail movements, called swimming bouts (with occurrence frequency equal to 0.051 ± 0.033 Hz), which occurred irregularly in time (coefficient of variation equal to 1.72 ± 0.26) and had short-term serial correlations in terms of movement laterality (consecutive bouts within less than 10 s had a significantly higher probability to be toward similar directions than for longer intervals; 0.74 ± 0.09 versus

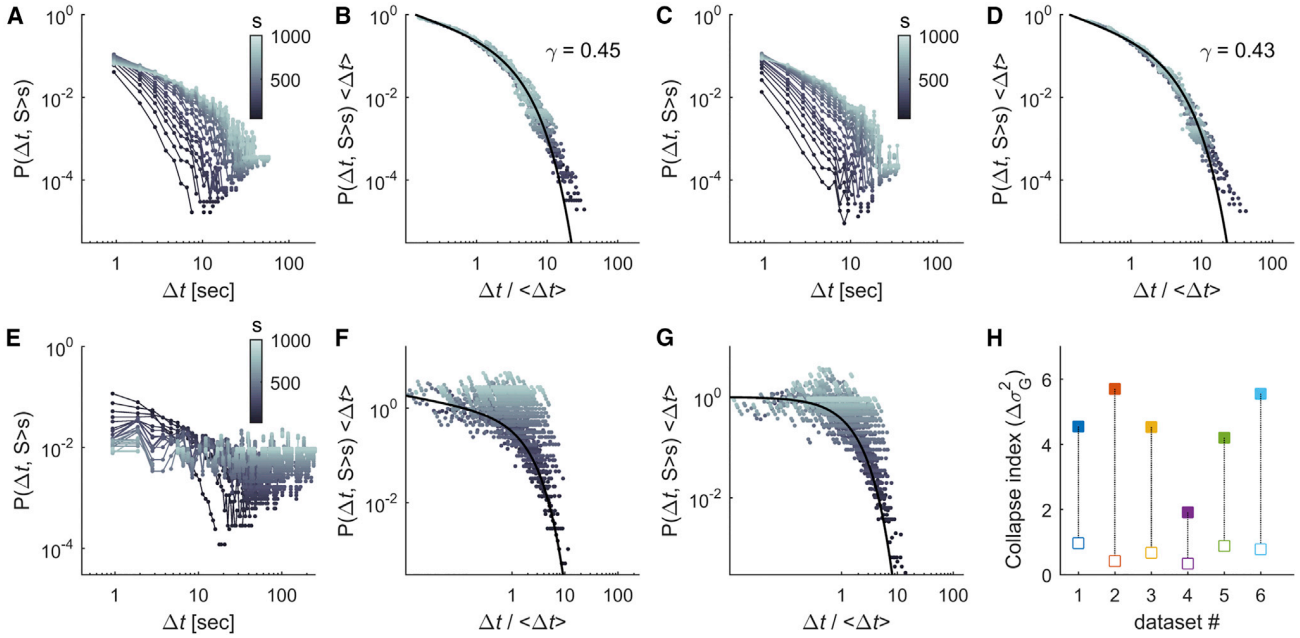

Figure 5. Universal Scaling Functions: Recurrence Time Intervals

(A) Recurrence time distributions $P(\Delta t, S > s)$. The distributions of time intervals Δt between consecutive avalanches of sizes larger than a given threshold s were calculated for different values of s (gray color code; data from dataset 2).

(B) Rescaled recurrence time distributions as a function of the rescaled time $\Delta t/\langle\Delta t\rangle$. The black curve indicates the gamma distribution onto which the scaled recurrence time distributions collapsed (γ: shape parameter of the gamma distribution; data from dataset 2).

(C and D) Same as (A) and (B), respectively, but for dataset 3. See Table S2 for more details.

(E–G) Same as (A), (B), and (D), respectively, but for the corresponding shuffled datasets. Note the absence of collapse for the shuffled data.

(H) Amount of collapse ($\Delta\sigma^2_G$) for the original datasets (filled symbols) and the shuffled datasets (open symbols).

0.61 ± 0.13, $p < 0.001$, Mann-Whitney test). We observed that, with respect to periods of spontaneous activity, neuronal avalanches during tail movements had larger sizes, and their distribution across different brain regions was biased toward hindbrain motor areas (Figure S7). We calculated the avalanche statistics around the onsets of detected tail movement events, t_{on}, and compared them to those in the absence of movements (Figures 7E and 7F). Specifically, we collected the durations and sizes of neuronal avalanches initiated at each time frame within t_{on} ± 100 s. We observed a significant ($p < 0.001$, two-sample t test) decrease in the exponent values describing the distribution of the sizes and the durations of avalanches around t_{on}, with respect to the values in the absence of movements (from –100 to –10 s and from +10 to +100 s, with respect to movement onsets). The decreases in exponent values were accompanied by deviations from power-law statistics (Figures 7G and 7H). These differences were not fully explained by differences in the rate of calcium events but rather by changes in their correlation structure (Figures S6F–S6J). Hence, these results suggest that, during the emergence of self-generated behaviors, brain dynamics transiently deviate from criticality.

Disrupting Electrical Coupling Deviates the Brain Activity from Criticality

To get insights into the physiological mechanisms contributing to stabilization of the brain's activity on the critical regime, we characterized the statistical properties of neuronal avalanches when zebrafish larvae were exposed to a low concentration of heptanol, a gap junction blocker (see STAR Methods) (Saint-Amant and Drapeau, 2000; Muto and Kawakami, 2011; Warp et al., 2012). We first quantified the freely swimming behavior of a cohort of larvae with and without exposure to 90 μM heptanol. At this concentration of heptanol, the locomotor activity of the larvae could not be distinguished from that of the controls (see STAR Methods and Figures S8A–S8D). However, when analyzing the spontaneous avalanches, we found that larvae exposed to heptanol displayed substantially fewer avalanches than the original datasets (~1 versus ~30 avalanches per frame), with (α, τ, $\sigma\nu z$) exponents that significantly deviated from the critical values observed in normal conditions (Figure 8A; Table S2). Moreover, larvae exposed to heptanol displayed neuronal avalanches for which neither the temporal profiles nor the recurrence-time distributions collapsed, showing no evidence of self-similarity (Figures 8B and 8C).

Furthermore, to investigate the role of the brain critical dynamics in the processing of sensory information, we performed experiments in which visual stimuli were projected on a screen at different locations in the field of view of the larva (see STAR Methods). The visual stimuli consisted of single light spot randomly presented at four possible closely spaced azimuth locations in the visual field (75°, 85°, 90°, 110°, with 0° defined as the head-tail longitudinal axis of the larva, facing the larva's

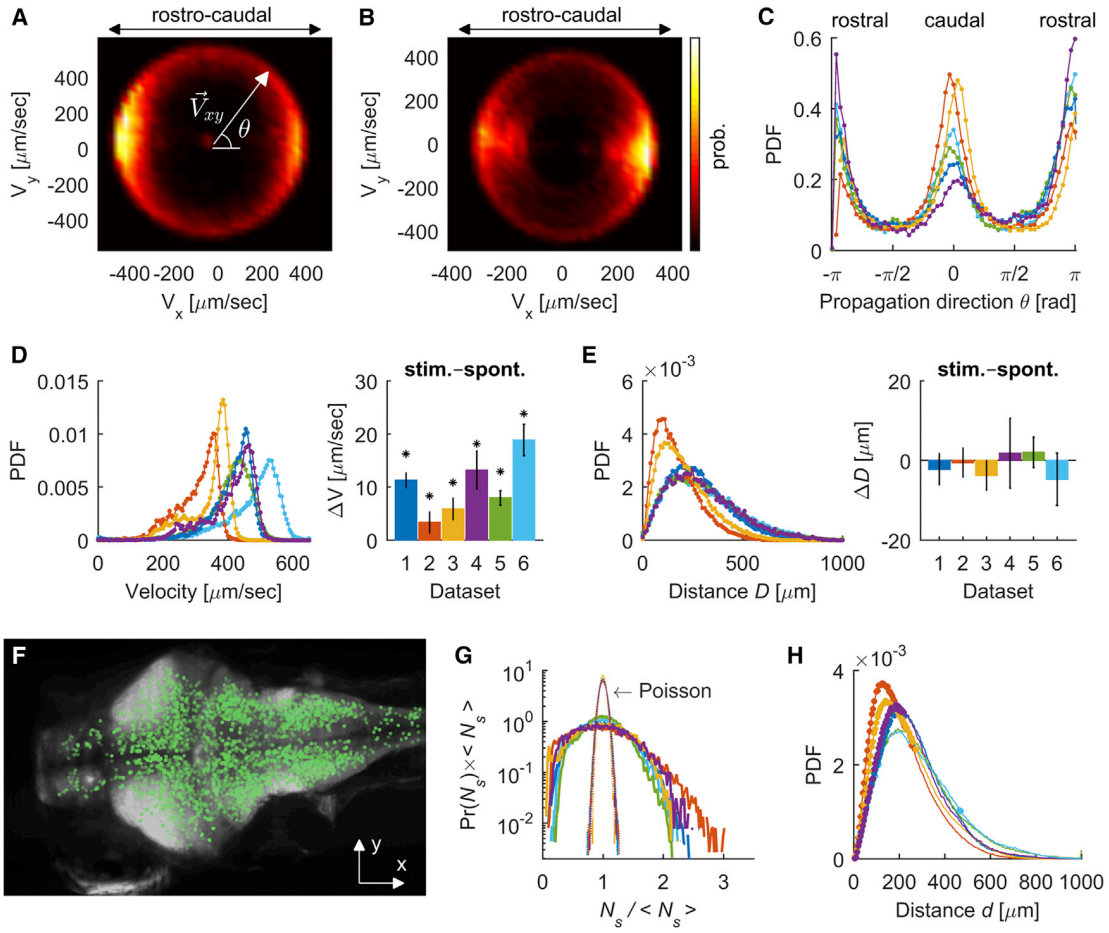

Figure 6. Propagation of Neuronal Avalanches

(A and B) Probability distribution of the projection of the velocity vector into the coronal (x-y) plane of the brain, $\vec{V}_{xy}$, for two representative datasets (A, dataset 1; B, dataset 2). The probability density is shown in color scale.

(C) Probability distribution of the direction of propagation in the coronal (x-y) plane, θ, for each dataset.

(D) Left: distribution of velocity magnitude. Right: differences in median velocities ΔV of the avalanches during periods of spontaneous and the stimulus-driven activity. *p < 0.001, two-sided Wilcoxon rank-sum test.

(E) Left: probability distribution of the distance traveled by the neuronal avalanches. Right: differences in median distances ΔD of the avalanches during periods of spontaneous and the stimulus-driven activity ($p > 0.05$, two-sided Wilcoxon rank-sum test).

(F) Locations of the initial centers of mass (i.e., $\overrightarrow{CM}(t = 1)$), of neuronal avalanches projected on the coronal (x-y) plane of the brain (for dataset 1). Each green dot corresponds to an avalanche. Note that the vast majority of the initiation sites occurred in the neuronal somata rather than in the neuropil (dense white regions).

(G) Probability distribution of the number of simultaneous avalanches, N_s, normalized by its mean $\langle N_s \rangle$, for each dataset (solid lines). The narrow distributions are the expected Poisson distributions given $\langle N_s \rangle$.

(H) Probability distribution of detecting two simultaneous avalanches with CMs separated by a distance d, for each dataset. Points indicate distance bins for which the probability of simultaneous avalanches is significantly ($p < 0.01$) higher than chance (i.e., randomized data; see STAR Methods).

See also Figure S5.

head). The visually induced calcium responses, recorded at one optical plane of the optic tectum, were used to classify the spatial location of the stimuli, by means of a maximum likelihood decoder (MLD; see STAR Methods and Figures S8E–S8G). We found that exposure to heptanol led to a significant decrease in the decoder's average classification performance with respect to larvae in normal conditions (for a population of 1,000 ROIs, the average classification performance was: 54.3% ± 4.5% versus 44.7% ± 2.8%, $p < 0.001$, two-sample t test; the chance level was 25%; see Figures 8D and 8E). Altogether, these results suggest that pharmacological perturbation of electrical synapses deviates the brain's dynamical state from criticality, stressing the role of gap junctions in maintaining the dynamics of the brain at criticality, and that criticality may enhance sensory processing.

DISCUSSION

Criticality is a regime at the border between phases of order and disorder, producing the maximal diversity of possible

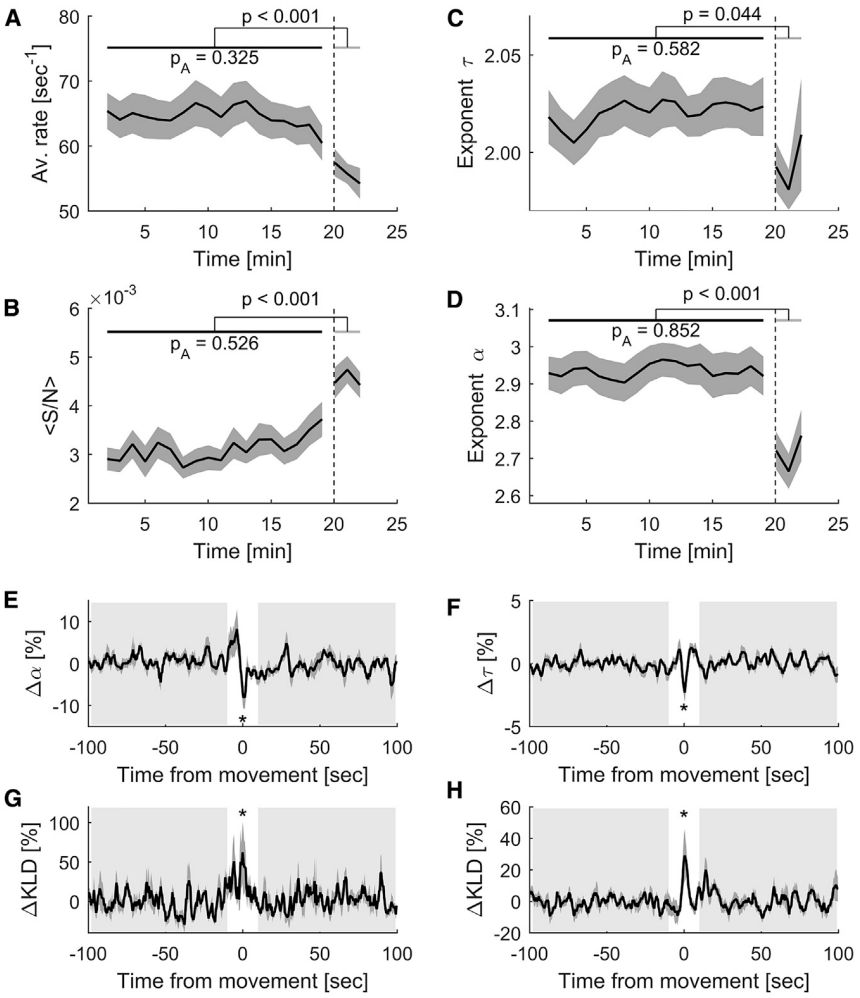

Figure 7. Sensory Stimulation and Self-Generated Behavior Transiently Deviate the Brain's Dynamical State from Criticality

(A–D) The average rate of avalanche initiation (A), the average avalanche size (B), and the average power exponents of the distribution of avalanche sizes (C) and durations (D) were calculated for avalanches included within sliding time windows, for all spontaneous and evoked segments and all datasets. Shaded areas indicate SEM. We compared the values during periods of spontaneous activity (black horizontal line) and during periods of visual stimulation (gray horizontal line) using a two-sided Wilcoxon rank-sum test (p, p value). We also compared the values measured in all windows during spontaneous activity using a RM-ANOVA; p_A indicates the resulting p value (high p values suggest that avalanche properties were constant during periods of spontaneous activity).

(E and F) Averaged exponents describing the distributions of durations (E) and sizes (F) of spontaneous neuronal avalanches around self-generated tail movement onsets. Exponents were normalized by the corresponding averaged values during the reference periods (from –100 to –10 s and from +10 to +100 s, shaded areas; with respect to movement onsets, white areas).

(G and H) Averaged changes of the Kullback-Leibler divergence (KLD) between the distributions of durations (G) and sizes (H) of spontaneous avalanches and theoretical power laws (relative to reference periods).

In (E)–(H), *p < 0.001, two-sample t test comparing values at movement onset and values in the absence of movements.

See also Figures S6 and S7.

emergent patterned dynamics. It has been suggested that neuronal circuits and many other biological networks, such as gene regulatory networks, operate at criticality to optimize information processing and to accomplish tradeoffs between stability and responsiveness and between robustness and evolvability (Torres-Sosa et al., 2012). Here, we monitored whole-brain dynamics with near single-neuron resolution in the intact, behaving zebrafish larvae and interpreted the observed collective statistics in the framework of criticality. Our results are consistent with critical phenomena associated with phase transitions. As in models of disorder-induced phase transitions in three dimensions (Seppälä et al., 2002), our results show that the spatial statistics of clusters of co-active contiguous ROIs, as measured by their size distribution, reached the theoretical values close to the percolation point ρ_c, at which maximal diversity of spatial patterns was observed. Spatial patterns were organized as emergent scale-invariant spatial correlations, producing a large repertoire of modes of interactions, allowing for short-range and long-range functional connectivity. Moreover, the temporal evolution of the spatial clusters (neuronal avalanches) presented scale-invariant distributions, with power-law exponent values and exponent relations predicted in critical phenomena that exhibit crackling dynamics, as observed in earthquakes, Barkhausen noise in ferromagnets, paper crumpling, rock fractures, and many others (Perković et al., 1995; Sethna et al., 2001). Furthermore, neuronal avalanche evolution and recurrence in time can be described by single universal scaling functions across many size and timescales, as predicted in critical phenomena (Perković et al., 1995; Sethna et al., 2001; Corral, 2007), and as observed in cortical cultures (Friedman et al., 2012; Lombardi et al., 2014). Here, we also found that power spectra of avalanche time courses decayed with a $1/f^{1/\sigma\nu z}$ power law with an exponent close to the scaling exponent relating the avalanche size to its duration, as expected in crackling dynamics (Kuntz and Sethna, 2000; Travesset et al., 2002). These findings are all signatures of self-similarity and scale invariance of brain activity, with functional consequences in terms of an enhanced repertoire of spatial, temporal, and interactive modes, which are essential to adapt, process, and represent complex environments (Chialvo, 2010; Hidalgo et al., 2015). In other words, a critical nervous system could encode complex and ever-changing environmental conditions into a large diversity of distinct collective neuronal patterns that span multiple

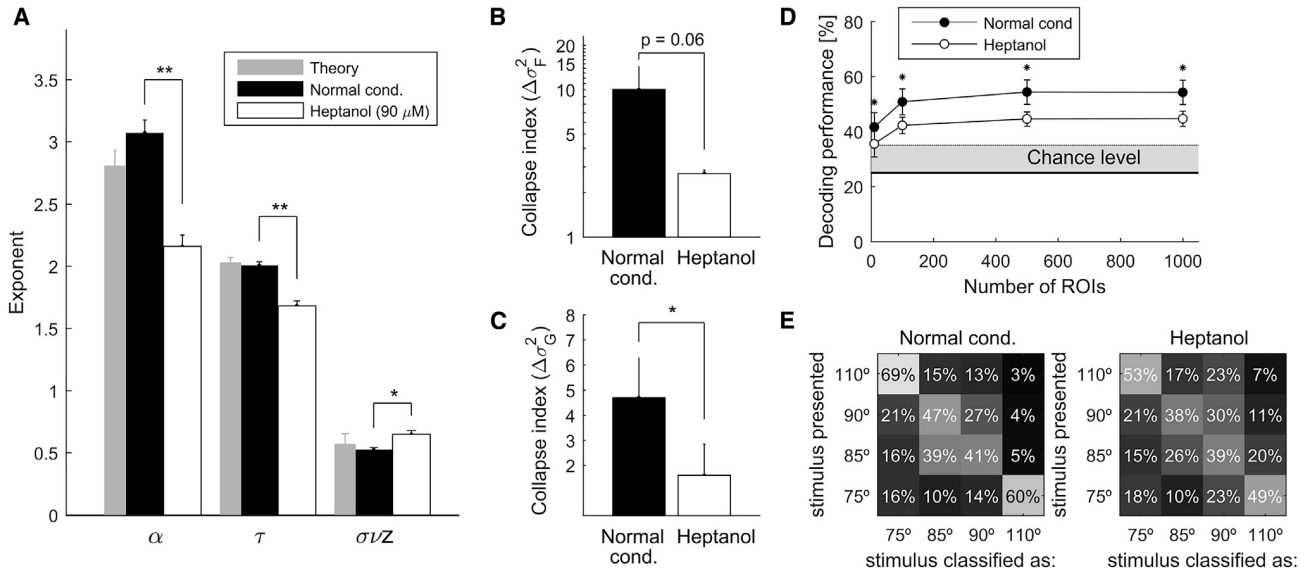

Figure 8. Gap Junctions Play a Role in Maintaining Criticality in the Nervous System

(A) Average distribution exponents (α, τ, $\sigma\nu z$) of spontaneous neuronal avalanches displayed by larvae in normal experimental conditions (datasets 1–6; black bars) and by larvae exposed to heptanol (90 μM) (datasets 7 and 8; white bars). For comparison, the gray bars indicate the critical exponents of 3D random field Ising theoretical models.

(B and C) Profile (B) and recurrence-time (C) collapse indices of neuronal avalanches calculated in normal conditions (black bars) and under heptanol exposure (white bars). In (A)–(C), p indicates the p value of two-sample t tests; *p < 0.05, **p < 0.01. Error bars, SEM.

(D) Decoding of visual stimuli at one optical plane of the optic tectum (n = 14 larvae, 8 in normal conditions and 6 after expsure to heptanol at 90 μM). Stimuli consisted of single light spots randomly presented at 4 possible closely spaced azimuth locations in the visual field (75°, 85°, 90°, and 110°). A maximum likelihood decoder was used to classify the stimuli location based on the activity of *n* ROIs. For $n > 100$, the classification performance was significantly higher than chance (i.e., 25%) for larvae in normal conditions. However, the decoding efficiency was significantly lower for larvae exposed to heptanol. *p < 0.001, two-sample t test.

(E) Decoding confusion matrices averaged across larvae in normal conditions (left) and across larvae exposed to heptanol (right), for $n = 1{,}000$. The off-diagonal matrix elements represent the probability of erroneously classifying one stimulus as a different one. The diagonal corresponds to correct classifications. Notice that, as expected, the decoder confused nearby stimuli.

See also Figure S8.

temporal and spatial scales, both locally (segregation) and across specialized brain regions (integration) (Sporns, 2013).

Close to phase transitions, complex systems show properties that are independent of the system's details and can thus be captured by simple models. The RFIM is the archetypal model of interconnected binary units presenting a non-equilibrium disorder-induced phase transition and producing avalanche dynamics at all scales (Perković et al., 1995; Sethna et al., 2001, 2005). When this system interacts with the environment through an external force *H*, avalanches arise as a competition between an ordering force, due to interactions, and a disordering force, due to heterogeneity. In models of neural networks, heterogeneity and interactions can be described by the variance of excitabilities of the neurons (Δ) and synaptic couplings of strength *J*, respectively (Hernández-Navarro et al., 2017). When $\Delta \sim J$, the balance between order and disorder is achieved and avalanches of all scales are observed. In this case, if *H* is fixed and equal to a critical value H_c, avalanche distributions have exponents equal to $(\alpha, \tau, \sigma\nu z) \approx$ (3/2, 2, 1/2). However, if $H(t)$ varies over time, the predicted exponents become $(\alpha, \tau, \sigma\nu z) \approx$ (2.03, 2.81, 0.57), as observed in our study. The avalanche statistics observed here can thus be interpreted as produced by a critical system exposed to time-varying inputs, as expected for the nervous system of an intact, non-anesthetized, non-paralyzed organism.

Systems at criticality are assumed to reach optimal computation capabilities (under specific definitions of optimality), in terms of stimulus discriminability, information transmission, and state repertoire (Shew and Plenz, 2013). Moreover, it is suggested that brain diseases shift the nervous system away from criticality—as during epileptic seizures (Meisel et al., 2012; Hobbs et al., 2010). For these reasons, it has been argued that healthy neural systems are poised at a critical point, especially during rest (Massobrio et al., 2015). It is believed that this dynamical regime stabilizes without fine-tuning through self-organization, implemented by synaptic plasticity and by excitation/inhibition (E/I) balance (Levina et al., 2007; Magnasco et al., 2009; Bellay et al., 2015), and evolutionarily selected to adapt to complex environments (Hidalgo et al., 2015). Consistent with these views, we found that larvae exposed to a low concentration of heptanol, a gap junction blocker (Saint-Amant and Drapeau, 2000; Muto and Kawakami, 2011; Warp et al., 2012), displayed neuronal avalanches with altered exponents and showed no evidence of self-similarity, presumably deviating the brain from a critical point. This suggests the involvement of gap junctions in maintaining criticality in the zebrafish brain, either due to

gap-junction-specific synaptic properties or by affecting neuronal excitability and the E/I balance (Lewis and Rinzel, 2000; Traub et al., 2001; Memelli et al., 2012). Most probably, gap junctions are only a part of a functioning system that could settle at criticality due to a combination of multiple factors (synaptic plasticity, homeostasis, etc.) that tend to balance the amount of order and disorder in the system. Moreover, when decoding the tectal responses to visual stimuli, we found that the neuronal activity of larvae exposed to heptanol led to a decrease in classification performance. This suggests that deviation from critical dynamics is accompanied by a degradation of information processing, thus suggesting a functional and computational relevant role of criticality in the nervous system.

Furthermore, our results suggest that sensory stimulation and self-generated behaviors transiently change the critical dynamics, which are otherwise constantly observed during periods of spontaneous activity. Collective activity during stimulus-elicited activity was more ordered, with faster, larger, and longer avalanches. This is consistent with recent findings using LFPs in an *ex vivo* preparation (Shew et al., 2015) and previous functional imaging studies in humans (He, 2011), and it has functional relevance in terms of enhanced stimulus detection (Clawson et al., 2017). Furthermore, we observed that spontaneous self-generated behaviors were accompanied by transient deflections of the avalanche exponents, slightly displacing the system away from the critical behavior. Overall, our study suggests that crackling noise dynamics might be the default mode of the healthy nervous system, a suitable regime for internal representations and exploration of the spontaneous state repertoire, which can be seen as the prior expectations of potential sensory inputs and behavioral outputs (Berkes et al., 2011). However, when the animal interacts with the environment, the nervous system transiently imbalances the amounts of order and disorder to limit the potential sensory responses to comply with the expectations about the detected stimulus and to restrict motor outcomes to select coherent behaviors (e.g., efficient foraging strategies). The latter is supported by the observation that consecutive movements are more likely to have a similar laterality if they were chained within less than 10 s than for longer inter-bout intervals.

Our analysis allowed the study of the spatiotemporal distribution of simultaneous neuronal avalanches at different locations of the brain. We showed that the locations at which avalanches began, or "epicenters," were evenly distributed across the neuronal somata regions of the brain. We found that pairs of avalanches were slightly correlated for short and moderate distances (~150 μm), suggesting that avalanche initiation is a locally driven process with moderate correlations due to local connectivity. Ignition of avalanches might occur due to a local imbalance of the E/I ratio, where activity nucleates and spreads (Orlandi et al., 2013). Furthermore, by studying the statistics of neuronal avalanches in different brain regions, we found that, while criticality was observed at the whole-brain level, the dynamics of single anatomical brain regions can be suggestive of critical behavior (e.g., optic tectum) or slightly deviate from it (e.g., reticulospinal circuit). Interestingly, the avalanches in the reticulospinal circuit were faster than those predicted by crackling noise dynamics and those observed in the optic tectum. We speculate that this difference may reflect the discrepancy in the connectivity architectures of the local circuits adapted for their functional role, with a recurrent network in the optic tectum to serve integration and processing of the sensory information, and a feedforward architecture in the reticulospinal network producing large volleys of activity to rapidly trigger motor movements.

In conclusion, whole-brain spontaneous neuronal activity displays cascading events, exhibiting scale-invariant and order-disorder balance properties that can be interpreted within the framework of criticality. These events initiate locally and spread to large portions of the brain, as needed for integrated communication among segregated specialized brain regions. Moreover, our results support the view that the vertebrate nervous system can rebalance the amounts of order and disorder depending on the interactions with the environment (e.g., strong oncoming sensory inputs and emergent spontaneous behavioral outputs) to rapidly return to a preferred state where levels of order and disorder are balanced enabling the largest possible dynamical repertoire.

STAR★METHODS

Detailed methods are provided in the online version of this paper and include the following:

- KEY RESOURCES TABLE
- CONTACT FOR REAGENT AND RESOURCE SHARING
- EXPERIMENTAL MODEL AND SUBJECT DETAILS
- METHOD DETAILS
  - Selective-plane illumination microscopy
  - Random Field Ising Model
- QUANTIFICATION AND STATISTICAL ANALYSIS
  - Image segmentation and GCaMP signal extraction
- DATA AND SOFTWARE AVAILABILITY

SUPPLEMENTAL INFORMATION

Supplemental Information includes eight figures, two tables, and one video and can be found with this article online at https://doi.org/10.1016/j.neuron.2018.10.045.

ACKNOWLEDGMENTS

A.P.-A. was supported by a Juan de la Cierva fellowship (IJCI-2014-21066) from the Spanish Ministry of Economy and Competitiveness. A.J. was supported by the Fondation pour la Recherche Medicale (FRM: FDT20140930915) and the ENS Cachan. M.P. was supported by the ENS Lyon. G.D. was funded by the European Research Council (ERC) Advanced Grant DYSTRUCTURE (No. 295129), by the Spanish Research Project PSI2016-75688-P (AEI/FEDER), and by the European Union's Horizon 2020 research and innovation program under grant agreement No. 720270 (HBP SGA1). G.S. was supported by ERC StG 243106, ERC CoG 726280, ANR-10-LABX-54 MEMO LIFE, and ANR-11-IDEX-0001-02 PSL Research University. We thank J. Boulanger-Weill for technical assistance and discussions, Patricia Gongal for editorial assistance, and David Hildebrand for providing GCaMP6f line.

AUTHOR CONTRIBUTIONS

G.S., A.J., and M.P. designed and conducted the experiments. A.P.-A., A.J., and M.P. analyzed the data. A.P.-A., A.J., G.D., and G.S. designed the research and wrote the manuscript.

DECLARATION OF INTERESTS

The authors declare no competing interests.

Received: January 9, 2018
Revised: July 5, 2018
Accepted: October 24, 2018
Published: November 15, 2018

REFERENCES

Ahrens, M.B., Orger, M.B., Robson, D.N., Li, J.M., and Keller, P.J. (2013). Whole-brain functional imaging at cellular resolution using light-sheet microscopy. Nat. Methods *10*, 413–420.

Alstott, J., Bullmore, E., and Plenz, D. (2014). Powerlaw: a Python package for analysis of heavy-tailed distributions. PLoS ONE *9*, e85777.

Avitan, L., Pujic, Z., Hughes, N.J., Scott, E.K., and Goodhill, G.J. (2016). Limitations of neural map topography for decoding spatial information. J. Neurosci. *36*, 5385–5396.

Beggs, J.M., and Plenz, D. (2003). Neuronal avalanches in neocortical circuits. J. Neurosci. *23*, 11167–11177.

Bellay, T., Klaus, A., Seshadri, S., and Plenz, D. (2015). Irregular spiking of pyramidal neurons organizes as scale-invariant neuronal avalanches in the awake state. eLife *4*, e07224.

Berkes, P., Orbán, G., Lengyel, M., and Fiser, J. (2011). Spontaneous cortical activity reveals hallmarks of an optimal internal model of the environment. Science *331*, 83–87.

Boulanger-Weill, J., Candat, V., Jouary, A., Romano, S.A., Pérez-Schuster, V., and Sumbre, G. (2017). Functional interactions between newborn and mature neurons leading to integration into established neuronal circuits. Curr. Biol. *27*, 1707–1720.e5.

Brainard, D.H. (1997). The psychophysics toolbox. Spat. Vis. *10*, 433–436.

Chialvo, D. (2010). Emergent complex neural dynamics: the brain at the edge. Nat. Phys. *6*, 744–750.

Clauset, A., Shalizi, C.R., and Newman, M.E.J. (2009). Power-law distributions in empirical data. SIAM Rev. *51*, 661–703.

Clawson, W.P., Wright, N.C., Wessel, R., and Shew, W.L. (2017). Adaptation towards scale-free dynamics improves cortical stimulus discrimination at the cost of reduced detection. PLoS Comput. Biol. *13*, e1005574.

Corral, A. (2007). Statistical features of earthquake temporal occurrence, Volume 705, Lecture notes in physics (Springer), pp. 191–221.

Davidsen, J., Stanchits, S., and Dresen, G. (2007). Scaling and universality in rock fracture. Phys. Rev. Lett. *98*, 125502.

Expert, P., Lambiotte, R., Chialvo, D.R., Christensen, K., Jensen, H.J., Sharp, D.J., and Turkheimer, F. (2011). Self-similar correlation function in brain resting-state functional magnetic resonance imaging. J. R. Soc. Interface *8*, 472–479.

Friedman, N., Ito, S., Brinkman, B.A., Shimono, M., DeVille, R.E., Dahmen, K.A., Beggs, J.M., and Butler, T.C. (2012). Universal critical dynamics in high resolution neuronal avalanche data. Phys. Rev. Lett. *108*, 208102.

Hahn, G., Petermann, T., Havenith, M.N., Yu, S., Singer, W., Plenz, D., and Nikolic, D. (2010). Neuronal avalanches in spontaneous activity in vivo. J. Neurophysiol. *104*, 3312–3322.

Hahn, G., Ponce-Alvarez, A., Monier, C., Benvenuti, G., Kumar, A., Chavane, F., Deco, G., and Frégnac, Y. (2017). Spontaneous cortical activity is transiently poised close to criticality. PLoS Comput. Biol. *13*, e1005543.

He, B. (2011). Scale-free properties of the fMRI signal during rest and task. J. Neurosci. *31*, 13786–13795.

Hernández-Navarro, L., Orlandi, J.G., Cerruti, B., Vives, E., and Soriano, J. (2017). Dominance of metric correlations in two-dimensional neuronal cultures described through a random field ising model. Phys. Rev. Lett. *118*, 208101.

Hidalgo, J., Grilli, J., Suweis, S., Muñoz, M.A., Banavar, J.R., and Maritan, A. (2015). Information-based fitness and the emergence of criticality in living systems. Proc. Natl. Acad. Sci. USA *111*, 10095–10100.

Hildebrand, D.G.C., Cicconet, M., Torres, R.M., Choi, W., Quan, T.M., Moon, J., Wetzel, A.W., Scott Champion, A., Graham, B.J., Randlett, O., et al. (2017). Whole-brain serial-section electron microscopy in larval zebrafish. Nature *545*, 345–349.

Hobbs, J.P., Smith, J.L., and Beggs, J.M. (2010). Aberrant neuronal avalanches in cortical tissue removed from juvenile epilepsy patients. J. Clin. Neurophysiol. *27*, 380–386.

Jan, N., and Stauffer, D. (1998). Random site percolation in three dimensions. Int. J. Mod. Phys. C *9*, 341–347.

Jouary, A., and Sumbre, G. (2016). Automatic classification of behavior in zebrafish larvae. bioRxiv. https://doi.org/10.1101/052324.

Klaus, A., Yu, S., and Plenz, D. (2011). Statistical analyses support power law distributions found in neuronal avalanches. PLoS ONE *6*, e19779.

Kuntz, M.C., and Sethna, J.P. (2000). Noise in disordered systems: the power spectrum and dynamic exponents in avalanche models. Phys. Rev. B *62*, 11699.

Levina, A., and Priesemann, V. (2017). Subsampling scaling. Nat. Commun. *8*, 15140.

Levina, A., Herrmann, J., and Geisel, T. (2007). Dynamical synapses causing self-organized criticality in neural networks. Nat. Phys. *3*, 857–860.

Lewis, T.J., and Rinzel, J. (2000). Self-organized synchronous oscillations in a network of excitable cells coupled by gap junctions. Network *11*, 299–320.

Lombardi, F., Herrmann, H.J., Plenz, D., and De Arcangelis, L. (2014). On the temporal organization of neuronal avalanches. Front. Syst. Neurosci. *8*, 204.

Magnasco, M.O., Piro, O., and Cecchi, G.A. (2009). Self-tuned critical anti-Hebbian networks. Phys. Rev. Lett. *102*, 258102.

Marshall, N., Timme, N.M., Bennett, N., Ripp, M., Lautzenhiser, E., and Beggs, J.M. (2016). Analysis of power laws, shape collapses, and neural complexity: new techniques and MATLAB support via the NCC Toolbox. Front. Physiol. *7*, 250.

Massobrio, P., de Arcangelis, L., Pasquale, V., Jensen, H.J., and Plenz, D. (2015). Criticality as a signature of healthy neural systems. Front. Syst. Neurosci. *9*, 22.

Mazzoni, A., Broccard, F.D., Garcia-Perez, E., Bonifazi, P., Ruaro, M.E., and Torre, V. (2007). On the dynamics of the spontaneous activity in neuronal networks. PLoS ONE *2*, e439.

Meisel, C., Storch, A., Hallmeyer-Elgner, S., Bullmore, E., and Gross, T. (2012). Failure of adaptive self-organized criticality during epileptic seizure attacks. PLoS Comput. Biol. *8*, e1002312.

Memelli, H., Horn, K.G., Wittie, L.D., and Solomon, I.C. (2012). Analyzing the effects of gap junction blockade on neural synchrony via a motoneuron network computational model. Comput. Intell. Neurosci. *2012*, 575129.

Muto, A., and Kawakami, K. (2011). Imaging functional neural circuits in zebrafish with a new GCaMP and the Gal4FF-UAS system. Commun. Integr. Biol. *4*, 566–568.

Orlandi, J.G., Soriano, J., Álvarez-Lacalle, E., Teller, S., and Casademunt, J. (2013). Noise focusing and the emergence of coherent activity in neuronal cultures. Nat. Phys. *9*, 582–590.

Panier, T., Romano, S.A., Olive, R., Pietri, T., Sumbre, G., Candelier, R., and Debrégeas, G. (2013). Fast functional imaging of multiple brain regions in intact zebrafish larvae using selective plane illumination microscopy. Front. Neural Circuits *7*, 65.

Pasquale, V., Massobrio, P., Bologna, L.L., Chiappalone, M., and Martinoia, S. (2008). Self-organization and neuronal avalanches in networks of dissociated cortical neurons. Neuroscience *153*, 1354–1369.

Pelli, D.G. (1997). The VideoToolbox software for visual psychophysics: transforming numbers into movies. Spat. Vis. *10*, 437–442.

Perković, O., Dahmen, K., and Sethna, J.P. (1995). Avalanches, Barkhausen noise, and plain old criticality. Phys. Rev. Lett. *75*, 4528–4531.

Priesemann, V., Wibral, M., Valderrama, M., Pröpper, R., Le Van Quyen, M., Geisel, T., Triesch, J., Nikolić, D., and Munk, M.H. (2014). Spike avalanches in vivo suggest a driven, slightly subcritical brain state. Front. Syst. Neurosci. *8*, 108.

Romano, S.A., Pietri, T., Pérez-Schuster, V., Jouary, A., Haudrechy, M., and Sumbre, G. (2015). Spontaneous neuronal network dynamics reveal circuit's functional adaptations for behavior. Neuron *85*, 1070–1085.

Romano, S.A., Pérez-Schuster, V., Jouary, A., Boulanger-Weill, J., Candeo, A., Pietri, T., and Sumbre, G. (2017). An integrated calcium imaging processing toolbox for the analysis of neuronal population dynamics. PLoS Comput. Biol. *13*, e1005526.

Saint-Amant, L., and Drapeau, P. (2000). Motoneuron activity patterns related to the earliest behavior of the zebrafish embryo. J. Neurosci. *20*, 3964–3972.

Scott, G., Fagerholm, E.D., Mutoh, H., Leech, R., Sharp, D.J., Shew, W.L., and Knöpfel, T. (2014). Voltage imaging of waking mouse cortex reveals emergence of critical neuronal dynamics. J. Neurosci. *34*, 16611–16620.

Seppälä, E.T., Pulkkinen, A.M., and Alava, M.J. (2002). Percolation in three-dimensional random field Ising magnets. Phys. Rev. B *66*, 144403.

Seshadri, S., Klaus, A., Winkowski, D.E., Kanold, P.O., and Plenz, D. (2018). Altered avalanche dynamics in a developmental NMDAR hypofunction model of cognitive impairment. Transl. Psychiatry *8*, 3.

Sethna, J.P., Dahmen, K.A., and Myers, C.R. (2001). Crackling noise. Nature *410*, 242–250.

Sethna, J.P., Dahmen, K.A., and Perković, O. (2005). Random-field Ising models of hysteresis. In The Science of Hysteresis, *Volume II*, G. Bertotti and I. Mayergoyz, eds. (Elsevier), pp. 107–179.

Shew, W.L., and Plenz, D. (2013). The functional benefits of criticality in the cortex. Neuroscientist *19*, 88–100.

Shew, W.L., Clawson, W.P., Pobst, J., Karimipanah, Y., and Wessel, R. (2015). Adaptation to sensory input tunes visual cortex to criticality. Nat. Phys. *11*, 659–663.

Shriki, O., Alstott, J., Carver, F., Holroyd, T., Henson, R.N., Smith, M.L., Coppola, R., Bullmore, E., and Plenz, D. (2013). Neuronal avalanches in the resting MEG of the human brain. J. Neurosci. *33*, 7079–7090.

Sporns, O. (2013). Network attributes for segregation and integration in the human brain. Curr. Opin. Neurobiol. *23*, 162–171.

Stumpf, M.P.H., Wiuf, C., and May, R.M. (2005). Subnets of scale-free networks are not scale-free: sampling properties of networks. Proc. Natl. Acad. Sci. USA *102*, 4221–4224.

Tagliazucchi, E., Balenzuela, P., Fraiman, D., and Chialvo, D.R. (2012). Criticality in large-scale brain FMRI dynamics unveiled by a novel point process analysis. Front. Physiol. *3*, 15.

Torres-Sosa, C., Huang, S., and Aldana, M. (2012). Criticality is an emergent property of genetic networks that exhibit evolvability. PLoS Comput. Biol. *8*, e1002669.

Traub, R.D., Kopell, N., Bibbig, A., Buhl, E.H., LeBeau, F.E., and Whittington, M.A. (2001). Gap junctions between interneuron dendrites can enhance synchrony of gamma oscillations in distributed networks. J. Neurosci. *21*, 9478–9486.

Travesset, A., White, R.A., and Dahmen, K.A. (2002). Crackling noise, power spectra, and disorder-induced critical scaling. Phys. Rev. B *66*, 024430.

Uchida, D., Yamashita, M., Kitano, T., and Iguchi, T. (2002). Oocyte apoptosis during the transition from ovary-like tissue to testes during sex differentiation of juvenile zebrafish. J. Exp. Biol. *205*, 711–718.

Warp, E., Agarwal, G., Wyart, C., Friedmann, D., Oldfield, C.S., Conner, A., Del Bene, F., Arrenberg, A.B., Baier, H., and Isacoff, E.Y. (2012). Emergence of patterned activity in the developing zebrafish spinal cord. Curr. Biol. *22*, 93–102.

Wolf, S., Dubreuil, A.M., Bertoni, T., Böhm, U.L., Bormuth, V., Candelier, R., Karpenko, S., Hildebrand, D.G.C., Bianco, I.H., Monasson, R., and Debrégeas, G. (2017). Sensorimotor computation underlying phototaxis in zebrafish. Nat. Commun. *8*, 651.

Yu, S., Ribeiro, T.L., Meisel, C., Chou, S., Mitz, A., Saunders, R., and Plenz, D. (2017). Maintained avalanche dynamics during task-induced changes of neuronal activity in nonhuman primates. eLife *6*, e27119.

STAR★METHODS

KEY RESOURCES TABLE

REAGENT or RESOURCE	SOURCE	IDENTIFIER
Experimental Models: Organisms/Strains		
Tg(elavl3:GCaMP5G)	Boulanger-Weill et al., 2017	RRID: ZFIN_DB-ALT-161209-7
Tg(elavl3:GCaMP6f)	Wolf et al., 2017	RRID: ZFIN_ZDB-ALT-180201-1
Software and Algorithms		
HCImageLive 4.3 (Image acquisition)	This paper	https://hcimage.com/hcimage-overview/hcimage-live/
MATLAB scripts (Data Analysis, stimulus control, scanner and piezo control)	This paper	https://www.mathworks.com/products/matlab.html
NCC MATLAB Toolbox	Marshall et al., 2016	http://www.nicholastimme.com/software.html
Python package Powerlaw	Alstott et al., 2014	https://github.com/jeffalstott/powerlaw

CONTACT FOR REAGENT AND RESOURCE SHARING

Further information and requests for resources and reagents should be directed to and will be fulfilled by the Lead Contact, Germán Sumbre (sumbre@biologie.ens.fr)

EXPERIMENTAL MODEL AND SUBJECT DETAILS

Zebrafish larvae were raised in 0.5x E3 embryo medium and kept under a 14/10 hr on/off light cycle. After 5 days-post-fertilization (dpf), larvae were fed with paramecia. Calcium imaging experiments were performed using 6-8 dpf Tg(huC:GCaMP5)^{ens102Tg} (Boulanger-Weill et al., 2017) or Tg(huC:GCaMP6f) zebrafish larvae (datasets 1–6, see Table S1). Tg(huC:GCaMP6f)^{a12200Tg} was provided by DGC. Hildebrand (Harvard, USA) (Wolf et al., 2017). Both transgenic lines are in Nacre background (mitfa−/−). Note that zebrafish sex differentiation begins only between 21 and 23 dpf (Uchida et al., 2002). For imaging purposes, the larvae were placed dorsal-side up on a coverslip platform (5mm high, 5 mm wide) and head-fixed in 2% low-melting agarose (Invitrogen, USA) in E3 embryo medium. Once jellified, the agarose around the tail was removed, letting it free to move. No paralyzer agents or anesthetics were used. All protocols used in this study were approved by *Le Comité d'Éthique pour l'Expérimentation Animale Charles Darwin* (038393.03).

METHOD DETAILS

Selective-plane illumination microscopy

We used selective-plane illumination microscopy (SPIM) to record the neuronal activity at near cellular resolution across the brain (Figure S1). Optical sectioning was achieved by the generation of a micrometer-thick light sheet to excite GCaMP from the side of the larva. The GCaMP emission was collected by a camera whose optical axis was orthogonal to the excitation plane (a 488 nm laser, Phoxx 480-200, Omicron). The laser beam was first filtered by a 488 cleanup filter (XX.F488 Omicron) and coupled to a single-mode fiber optic. The beam was expanded using a telescope (f = 50 mm, LA1131-A, and f = 150 mm, LA1433-A, Thorlabs) and projected onto two orthogonal galvanometric mirrors (HP 6215H Cambridge technology) to scan the laser beam, whose angular displacement were converted into position displacement by a scan lens (f = 75 mm AC508-075-A-ML, Thorlabs). The laser beam was then refocused by a tube lens (f = 180 mm, U-TLUIR, Olympus) and focused on the pupil of a low-NA (0.16) 5x objective lens (UPlan SAPO 4x, NA = 0.16, Olympus) facing the specimen chamber. The arrangement yielded a 1mm-wide illumination sheet and a beam waist of 3.2 μm (1/e2). The emitted fluorescence light was collected by a high-NA water-dipping objective (N16XLWD-PF, 16x, NA = 0.8, Nikon) mounted vertically on a piezo translation stage (PI PZ222E). A tube lens (f = 180mm U-TR30IR, Olympus), a notch filter (NF03-488, to filter the laser's excitation light), a band-pass filter (FF01 525/50 Semrock) and a low-pass filter (FF01 680 SP25 Semrock, to filter the IR light) were used to create an image of the GCaMP emitted fluorescence on a sCMOS sensor (Orca Flash 4.0, Hamamatsu). The volumetric brain recordings were obtained by sequentially recording the fluorescence in 40 coronal sections spaced by 5 μm. For this purpose, the light sheet was scanned vertically in the dorso-ventral direction in synchrony with the objective of the emission path. The camera was triggered to acquire an image every $T_{exposure}$ = 10 ms. Once the 40 coronal sections were recorded, the position of the light sheet and the objective of the emission path was reset to their initial dorsal position (T_{reset} = 70 ms). This resulted in a volumetric acquisition time of 0.47 s (i.e., 40 × $T_{exposure}$ + T_{reset}) or a rate of 2.1 Hz.

Spontaneous and visual stimulation periods

The experiment was composed of Q consecutive segments of 20 min of spontaneous activity and 4 min of visual stimulation (Figure S1D). Q was different for different datasets and ranges between 3–9 (see Table S1). Each visual stimulation period contained 8 sub-episodes during which a moving grating was presented below the larva for 10 s. The inter-stimulus interval was equal to 20 s. The stimuli were projected on a screen (#216 White Diffusion, Rosco Cinegel) placed 5 mm below the larva and covering a field of view of 35 × 25 mm (148°, 136°), using a pico-projector (PK320, Optoma). To avoid interference with the GCaMP5 and GCaMP6f emission signal (peaking at 547 nm and filtered using a band-pass filter, FF01-520/70 Semrock), only the projector's red (620 nm) LED was used, and a band-pass filter (629/56, FF01629/56, Semrock) was placed in the projector's lens. To focus the stimulus on the screen we used a Plano-Convex lens (f = 125 mm, LA1986-B Thorlabs). Gratings had a spatial period of 10 mm, with maximal contrast, and they moved orthogonally to the stripes with velocity equal to 1 cm/s. During each visual stimulation period, the orientations of the 8 consecutive gratings were equal to 0°,60°,180°, −60°,0°,60°,180°, and −60°, respectively, relative to the larva. In the cases in which larvae were exposed to heptanol, the experiment did not include visual stimulation periods and was composed of 70.5 min of spontaneous activity.

Monitoring motor behavior

A small hole in the stimulus projecting screen allowed imaging of the locomotor behavior of the larva (e.g., tail movements), using a small microscope (DZ 1/L.75-5, The Imaging Source) connected to a fast infrared camera (Hxg20nir, Baumer). The larva was illuminated using an IR LED (NG50L 810nm, BDlaser). To separate between the IR light and the projected visual stimuli, we used a dichroic mirror (FM201, Thorlabs). From the binarized image of the larva, we extracted the tail curvature using the method described in (Jouary and Sumbre, 2016).

In order to compute the similarity between successive tail movements, we additionally recorded the behavior of 25 head-restrained Nacre larvae during 3 h while a homogeneous non-patterned illumination was projected below the larvae. The directionality of a tail movement was computed as the sign of the average of the cubed value of the tail curvature for movement classified as Asymmetrical Scoots, Routine Turn or C Bends (Jouary and Sumbre, 2016).

Heptanol experiments

To study the role of gap junctions on spontaneous activity patterns, the neuronal activity from two 7-dpf zebrafish GCaMP5 larvae were exposed to 90 μM heptanol. The heptanol was added to the bath for a duration of 3 hours and washed out just before the experiments (datasets 7 and 8). The concentration of heptanol used here was ∼ 10 times lower than previously used in zebrafish to block gap junctions (Saint-Amant and Drapeau, 2000; Muto and Kawakami, 2011; Warp et al., 2012), and did not significantly affected the larva's behavior under free-swimming conditions. This was tested by comparing the trajectory of 15 freely swimming GCaMP5 larvae at 7 dpf with 15 other larvae exposed to 90 μM of heptanol for 3 hours prior to the recordings. The larvae were placed in a custom-made Plexiglas 30 well plate (15 mm diameter x 5 mm height) filled with embryo medium at room temperature and let habituate for 10 min before the experiment. Homogeneous illumination from below was provided by an electroluminescent panel (MiniNeon, France). Spontaneous behavior was monitored with an Imaging Source DMK 21BF04 camera at 30 Hz for 20 min. We located the position of each larva as the centroid of the background-subtracted images (custom-made code, MATLAB). Figure S8A displays the swimming trajectories and averaged speeds of the control and the heptanol groups.

We additionally tested whether heptanol affects the information processing of sensory stimuli, we ran experiments using 14 larvae at 6 dpf, among them 6 larvae were exposed to 90 μM of heptanol for 3 hours prior to the recordings. The heptanol was then washed out and the larva was introduced in the SPIM recording chamber filled with embryo medium. The chamber was 3D-printed using resin (FormLabs FLGPBK04), and measures 45 mm (l) x 35 mm (w) x 35 mm (h). The larva was restrained in low-melting agarose and placed dorsal-side up at 8 mm from the side of the excitation objective. For experiments in which the tail movement was monitored, we removed the agarose around the tail. Stimuli consisted of single light spot of 4 deg. displayed at four possible closely spaced locations in the visual field (75°, 85°, 90°, 110°, with 0° defined as the longitudinal head-tail axis of the larva, facing the larva's head), which were randomly presented for a duration of 1 s each, at an inter-stimulus interval of 10 s, on a screen (#216 White Diffusion, Rosco Cinegel) placed on the side of the camber opposite to the excitation objective. The stimuli were generated using MATLAB and Psychtoolbox (Pelli, 1997; Brainard, 1997), and projected using a pico-projector (PK320, Optoma). To avoid interference with the GCaMP emission signal, only the projector's red (620 nm) LED was used, and a BLP01-561 Semrock long-pass filter was placed in the front of the projector.

Random Field Ising Model

We interpreted our data in the framework of crackling noise dynamics. The Random Field Ising Model (RFIM) is a canonical model to study non-equilibrium disorder-induced phase transitions that produce crackling dynamics (Perković et al., 1995; Sethna et al., 2001, 2005). The RFIM was introduced to describe a simplified three-dimensional ferromagnetic system. The model is defined on a cubic lattice of magnetic spins s_i with $s_i = \pm 1$ (pointing up or down). Neighboring spins interact through ferromagnetic couplings J. Quenched disorder (representing impurity, defects, inhomogeneities, etc.) is modeled by imposing a random field h_i at each spin, taken from a normal distribution with standard deviation Δ, i.e.,

$$P(h) = \frac{1}{\Delta\sqrt{2\pi}} e^{-\frac{h^2}{2\Delta^2}}$$

The parameter Δ controls the amount of (quenched) disorder of the system. An external driving magnetic field $H(t)$ is applied to the system. The Hamiltonian of the system is given by:

$$\mathcal{H} = -\sum_{i,j} J_{ij} s_i s_j - \sum_i (H + h_i) s_i.$$

The force $F_i = \left(H + s_i + \sum_j J_{ij} s_j\right)$ exerted on the spin i makes the spin flip either because of the external field (initiation of a new avalanche), or due to the influence of the neighboring spins (propagating an existing avalanche).

Here, we briefly review the scaling properties of the RFIM. If the disorder Δ is large (i.e., $\Delta \gg J$) then the spins flip independently, producing small avalanches. If the disorder is small (i.e., $\Delta \ll J$) large avalanches are observed that can span the entire system. When $\Delta \sim J$ the balance between order and disorder is achieved and avalanches of all scales are observed. This last case represents a disorder-induced phase transition, achieved at a critical value Δ_c of the disorder.

At the critical point the expected behavior of the system would yield the following scaling relations. The distribution of avalanche sizes measured at a field H, or in a small range of fields centered around H at the critical quenched disorder Δ_c scales as:

$$P(S, H) \sim S^{-\tau},$$

with $\tau = 3/2$ for $H = H_c$ (in mean-field; for simulations one gets: $\tau \approx 1.6$). However, the avalanche-size distribution *integrated* over the field H, scales as:

$$P(S) \sim S^{-(\tau + \sigma\beta\delta)},$$

with $\tau + \sigma\beta\delta \approx 2.03$ at the critical quenched disorder Δ_c. Note that when analyzing empirical data, it is not possible to know a priori if the distribution is integrated or not. Thus, the *observed* exponent τ can be "τ" or " $\tau + \sigma\beta\delta$ ". Therefore, we simply write $P(S) \sim S^{-\tau}$.

Similarly, the distribution of avalanche durations T at the critical quenched disorder Δ_c scales as:

$$P(T) \sim T^{-\alpha},$$

with $\alpha = 2$ for $H = H_c$ and $\alpha \approx 2.81$ for the avalanche-duration distribution *integrated* over the field H. The avalanche duration scales with average avalanche size as: $\langle S \rangle(T) \sim T^{1/\sigma\nu z}$. The exponent $\sigma\nu z$ satisfies the following relation: $\sigma\nu z = (\tau - 1)/(\alpha - 1)$. Thus, in the integrated case, we obtain $\sigma\nu z \approx 0.57$.

QUANTIFICATION AND STATISTICAL ANALYSIS

Image segmentation and GCaMP signal extraction

The first step consisted in compensating for possible drifts in the horizontal plane. For this purpose, each frame was registered according to the maximal cross-correlation with a reference frame. The reference frame was the average of a 10 s. The registered stacks were then manually inspected to evaluate the drift in the ventro-dorsal plane, a drift that could not be compensated. Experiments with such drifts were discarded. Movement artifacts were detected according to large deviations in the maximum of the cross-correlation between successive frames. All frames with large deviations were discarded, they mostly occurred during large tail movements. Individual regions of interest (ROIs) were defined, in each plane, as hexagons of side lengths equal to 6.3 μm, corresponding to an area roughly equal to a neuron's soma of the zebrafish larva. The advantage of using a hexagonal grid was to maximize the area of the brain covered by the ROIs. The neuropil and neuronal somata were not dissociated in the analysis. We selected the hexagonal ROIs that showed coherent activity among the pixels composing them. For this, we calculated the average correlation (c_{pix}) between the fluctuations of fluorescence intensity $\Delta F/F$ of the pixels composing a ROI and the average fluorescence of the ROI. We selected ROIs with $c_{pix} > 0.25$, for datasets 1–5, and $c_{pix} > 0.20$, for datasets 6–8. To avoid taking into account ROIs with baselines difficult to estimate, we excluded ROIs with extreme fluorescence intensity variance (> 90th percentile of the distribution of signal variances). The hexagonal ROIs that passed these selection criteria were associated to putative single neurons. The number of selected ROIs for further analyses ranged between N = 41,115–89,349 (see Table S1).

Activity clusters and neuronal avalanches

We were interested on the clusters of co-active and contiguous ROIs. For this, we first binarized the activity of each of the cells by thresholding the fluctuations of fluorescence intensity $\Delta F/F$ with a threshold equal to $3\sigma_{noise}$, where σ_{noise} is the standard deviation of the baseline fluctuations of the cell (Romano et al., 2017). Above this threshold the activity was set to 1, otherwise it was set to 0. Next, at each time step t, we detected the connected components, i.e., clusters formed by contiguous co-activated ROIs, on the three-dimensional spatial distribution of the active cells. This was done using the MATLAB function *bwconncomp*. The algorithm finds the connected components in a co-activated nearest neighbors graph: two ROIs i and j of the 3D matrix are connected if they are both active and j is in the neighborhood of i. The neighborhood of a ROI i is composed of the 20 ROIs that surround it (6 within the same plane and 7 in each of the two planes above and below it). A cluster is composed of at least 3 co-active, contiguous ROIs. At each time frame t, we obtained m clusters that we noted $C_{i,t}$, where $i \in \{1, \ldots, m\}$, with associated sizes (number of ROIs) noted $C_s(i)$.

Neuronal avalanches describe the spatiotemporal evolution of the activity clusters. A new avalanche was initiated at time t_0 by the activation of a cluster (C_{i,t_0}) of ROIs that were not active at the preceding time frame, i.e., $C_{i,t_0} \cap C_{j,t_0-1} = \varnothing$. If at least one ROI of the

cluster C_{i,t_0} continued to be part of a cluster at time $t_0 + 1$, i.e., $C_{i,t_0} \cap C_{j,t_0+1} \neq \emptyset$, then the avalanche was continued, and so on, until this condition no longer held (Figure S3). The size of the avalanche was given by the number of activations during the avalanche.

The definition of avalanches used here is that used in studies of sand-pile, Ising models, and in a recent fMRI study (Tagliazucchi et al., 2012), but it is different from that used in most of previous studies on neuronal avalanches (Beggs and Plenz, 2003; Mazzoni et al., 2007; Pasquale et al., 2008; Friedman et al., 2012; Hahn et al., 2010, 2017; Shriki et al., 2013; Priesemann et al., 2014). In those studies, avalanches were defined as consecutive time bins with at least one active site (among tens to hundreds of signals). In the present study, this standard definition is not practical since at each time frame the probability that at least one among the N recorded ROIs ($N >$ 40,000) is active is extremely high, leading to one single avalanche that never terminates. Thus, a spatial constraint needs to be included. Ideally, one would like to concentrate on cascade patterns produced by synaptically coupled neurons, but unfortunately, we do not have this connectivity information. Thus, we focused on nearby ROIs which we assumed are putative neurons that are likely to be connected. The size of the clusters used to analyze the avalanches was chosen within a range in which the statistics of the neuronal avalanches were consistent. We observed that for clusters of a radius below ~30 μm, the avalanches showed consistent exponents for the power-law distributions for the size, the duration and their relationship, that matched those from theory. Above 30 μm, the exponents were inconsistent and deviated from the theoretical ones (Figures S4D–S4F). The definition of the size of the clustering neighborhood used in the present study lies below this threshold. We also note that the exponents were consistent for time bins shorter or equal to 1.41 s (Figures S4G–S4I). Notice that since nearby neurons share common tuning properties, spatially compact avalanches are likely to transmit functionally relevant information (Romano et al., 2015), making the avalanche definition biologically meaningful. Zebrafish larvae connectome will allow us in the future, to exactly define avalanches and test dynamic models that produce the observed statistics (Hildebrand et al., 2017).

Power-law fitting

We used maximum likelihood estimation (MLE) to fit truncated power laws to the data as described in Marshall et al. (2016). The cutoffs used to truncate the data are indicated in Tables S1 and S2. This method estimates the power-law exponent. The estimation error of the exponent was calculated using bootstrap re-sampling (1,000 re-samplings). To evaluate the fit between the empirical data and the MLE fit we used Kolmogorov-Smirnov (KS) statistics.

Clauset et al. (2009) proposed to evaluate the significance of power-law fits using synthetic power-law surrogates to derive a distribution of KS values. These are then compared to the KS statistic of the empirical distribution: the p value of rejecting the power-law fit is given by the proportion of sample distributions with KS-statistics larger than the KS statistic between the original distribution and the model distribution. In our data, we found that this method systematically rejects the power-law hypothesis ($p < 0.05$). However, it is known that, due to its dependence on sample size, this method is not informative in the large sample size regime (Clauset et al., 2009; Klaus et al., 2011; Alstott et al., 2014; Marshall et al., 2016), as in our case where the number of observed avalanches per experiment is > 100,000. Indeed, because any empirical data rarely follows an idealized mathematical relationship in the large sample regime, even small deviations from a perfect power law (due to noise) would lead to the rejection of the power-law hypothesis. For this reason, we tested the power-law hypothesis by asking whether the power law is the best descriptor of the data compared to an alternative heavy-tailed distribution, i.e., the lognormal distribution. For this, we calculated the log-likelihood ratio (LLR) between the two candidate distributions, as follows:

The lognormal distribution follows the density function: $P(x) = 1/(x\sigma\sqrt{2\pi})\exp[-1/2(\log(x-\mu)/\sigma)^2]$, with dispersion parameter $\sigma >$ 0 and location parameter $\mu >$ 0. For a given data $x = (x_1, \ldots, x_n)$, the LLR between the power-law and the lognormal was given by $LLR(x) = LL_{PL}(x) - LL_{LN}(x)$, where LL_{PL} and LL_{LN} are the log-likelihoods of the power law and the lognormal, respectively. LLR is positive if the likelihood of the power law model for a given empirical dataset is larger than the likelihood of the exponential model, and it is negative otherwise. To test whether the LLR is significantly different from zero, the p value for the LLR test is given by: $p = erfc\left(\left|LLR/\sqrt{2n\kappa^2}\right|\right)$, where $erfc$ is the complementary error function, $\kappa^2 = 1/n\sum_{i=1}^{n}[(LL_{PL}(x_i) - LL_{PL}(x)/n) - (LL_{LN}(x_i) - LL_{LN}(x)/n)]^2$, and $|LLR|/\sqrt{2n\kappa^2}$ is the normalized log-likelihood ratio (Klaus et al., 2011; Alstott et al., 2014). See Tables S1 and S2.

Scaling shape collapse

We evaluated the similarity of average avalanche profiles, $\langle S(t,T)\rangle$, across different temporal scales. For this, we used the method of Marshall et al. (2016) to automatically find the scaling parameter a that produces the best possible collapse given by: $\langle S(t,T)\rangle T^{-a} = F(t/T)$. The method estimates the scaling parameter a that minimizes the variance σ_F^2 across the avalanche profiles in the normalized time (t/T). The amount of collapse, $\Delta\sigma_F^2$, was quantified by comparing the variance across avalanche profiles in the normalized time with and without scaling, i.e., $\Delta\sigma_F^2 = \sigma_F^2(0)/\sigma_F^2(a)$, where a is the estimated scaling parameter.

We estimated the curve onto which the scaled inter-avalanche time intervals conditional distributions $P(\Delta t, S > s)\langle\Delta t\rangle$ collapse using a gamma distribution, as in previous studies on earthquake temporal occurrence (Corral, 2007). The gamma distribution is given by:

$$G_\gamma(\theta) = \frac{\gamma}{\Gamma(\gamma)}(\gamma\theta)^{\gamma-1}e^{-\gamma\theta},$$

where γ is the shape parameter, θ represents the normalized time interval $(\theta = \Delta t/\langle\Delta t\rangle)$, and Γ is the Euler gamma function. The shape parameter was estimated using least-squares. As for avalanche profiles, we quantified the amount of collapse $\Delta\sigma_G^2$ by

comparing the variance across recurrence time log-distributions in the normalized time with and without scaling ($\Delta\sigma_G^2$ is equal to the variance of $log[P(\Delta t/\langle\Delta t\rangle, S>s)]$ divided by the variance of $log[P(\Delta t/\langle\Delta t\rangle, S>s)\langle\Delta t\rangle]$) (see Table S2).

Kullback-Leibler divergence

We quantified how well a given empirical distribution can be described by a power law, $PL(x) = Kx^a$, where the constant K is chosen so that the integral of PL equals 1, and where the power-law exponent a was estimated from the empirical distribution using MLE. We calculated the Kullback-Leibler divergence (KLD) between the empirical distribution and PL. The KLD is a measure of dissimilarity between the empirical distribution and the theoretical power law; thus, the inverse of KLD can be used as a measure of goodness-of-fit of the power-law model. Let $P_{emp}(x)$ be the empirical distribution constructed using a histogram of B bins that partition the data into $\{x_1, x_2, \ldots, x_B\}$. The KLD between $P_{emp}(x)$ and $PL(x)$ is given by:

$$KLD = \sum_{k=1}^{B} P_{emp}(x_k) \log \frac{P_{emp}(x_k)}{PL(x_k)}.$$

Power spectrum of avalanche time courses

We calculated the power spectral density (PSD) of the neuronal avalanche time-course $S(t)$ using the fast Fourier transform. The PSD of an avalanche of duration T is given as $2\left|\tilde{S}(f)\right|^2/T$, where $\tilde{S}(f)$ is the Fourier transform of $S(t)$ and f is the frequency. We restricted the analysis to avalanches of duration T comprised between 3.76 s (8 time points) and 18.8 s (40 time points). The choice of the upper limit of T is determined by the upper cutoff used in the other avalanche analyses, and the lower limit of T was chosen to get enough time points. To estimate the PSD from avalanche time courses of different durations, we interpolated the PSD to the same spectral resolution. Specifically, we calculated the average PSD across all avalanches of duration T, denoted by $\Phi_S(f, T)$. We then linearly interpolated it to a fixed spectral resolution given by $f \in [1/T_{max}, 2/T_{max}, \ldots, 1/(2dt) - 1/T_{max}]$, where $T_{max} =$ 18.8 s and dt is the temporal resolution of the data ($dt =$ 0.47 s). Finally, we averaged the interpolated PSDs across all durations.

Surrogate datasets

For each dataset, the data could be represented as an $N \times L$ binary matrix, where N is the number of cells and L is the number of time frames. Our neuronal avalanche analysis describes the spatiotemporal statistics of the data. We compared these statistics to several types of surrogate/shuffled data. The first type of surrogate, called *time-shuffled data*, was designed to probe the sensitivity to the temporal organization of the ensemble activity. It was obtained by randomizing the time indices of the N-dimensional activity vectors, thus destroying the temporal organization of the data while preserving the spatial correlations. This control is important since Ca^{2+} transients last significantly longer than the voltage fluctuations that produced them, thus, fundamentally limiting the temporal resolution of neural activity as measured through Ca^{2+} signals. The second type of re-sampling was specifically designed to assess whether the collapse of the conditional recurrence time interval distributions $P(\Delta t, S>s)$ artifactually arises due to thresholding. Specifically, this surrogate dataset randomizes the neuronal avalanche sizes while keeping the sequence of starting/ending times fixed, thus destroying the correlation between avalanche sizes and recurrence times. Due to the large amount of data and the computational cost of our analyses, the data was re-sampled once for the two first types of surrogates. A third surrogate was used to compare the distribution of observing two avalanches that initiated simultaneously with centers of mass separated by a distance d to the expected distribution when the times of avalanche initiation were randomized. In this case, randomization was repeated 20 times for each of the Q data segments composing each dataset.

Center of mass of a neuronal avalanche

The center of mass (CM) of a given neuronal avalanche of duration T was given by the average location of the distribution of active ROIs composing the avalanche at each time t. Let n be the number of ROIs participating in the avalanche at time t and $\vec{x}_i$ the 3D spatial coordinates of the i-th ROI. The CM is given as: $\overrightarrow{CM}(t) = 1/n\sum_{i=1}^{n}\vec{x}_i$, for $1 \le t \le T$. We followed the temporal evolution of the avalanche by calculating its averaged velocity of the CM, $\vec{V}$, given by the averaged time derivative of the CM: $\vec{V} = \sum_{t=1}^{T-1}\left[\overrightarrow{CM}(t+1) - \overrightarrow{CM}(t)\right]/(T-1)$. To get reliable estimates of $\vec{V}$, only avalanches of duration $T \ge$ 2.35 s were used. It is important to note that the velocity of the center of mass should not be confounded with transmission velocity, nor with front propagation (V = 0 for an avalanche that grows in a perfect isotropic way). We instead used it here to describe global tendencies of propagation and to compare spontaneous versus stimulus-driven activity (see Figure 6).

Maximum likelihood decoder

We used a maximum likelihood decoder (MLD, see Figures S8E–S8G) to classify the location of visual stimuli presented to larvae from the fluorescence signals $\Delta F/F$ in the optic tectum (Avitan et al., 2016). For this purpose, we compared the decoding efficiency between larvae in normal conditions (n = 8) with respect to larvae exposed to 90 μM heptanol (n = 6, see STAR Methods). Specifically, we presented to the larvae a set of four light spots projected at different spatial locations (75°, 85°, 90°, 110°). Each stimulus lasted 1 s and was presented for n_{stim} = 40 repetitions. The inter-stimulus interval was equal to 10 s. As a measure of neuronal response, we used the mean fluorescence signal during the stimulus presentation for each ROI. The number of ROIs ranged between 1766–2490 for the different larvae. The MLD chooses the stimulus that is statistically most likely to have elicited an observed response of n signals, i.e., $\vec{r} = [r_1, r_2, \ldots, r_n]$. It uses a leave-one and cross-validation procedure. For this, the probability distribution of the response of each ROI to each stimulus type j was computed, i.e., $P(r_i|j)$, using $n_{stim} - 1$ observations of the stimulus. The remaining observation,

$r_{i,test}$, was used for testing. To obtain continuous conditional probability estimates, the histograms $P(r_i|j)$ were smoothed using a normal kernel function. With the simplifying assumption that the responses of the ROIs were statistically independent from each other, the learned conditional probability of the population response is given by the product over all individual conditional probabilities:

$$P(\vec{r}|j) = \prod_{i=1}^{n} P(r_i|j).$$

Decoding the population response consisted of searching for the stimulus (s_{ML}) which maximized the probability of the testing response: $s_{ML} = \underset{j \in \{1,\,2,\,3,4\}}{\operatorname{argmax}} P(\vec{r}_{test}|j)$. This procedure was repeated, each time leaving one response vector out and using the remaining population response vectors to learn the conditional probabilities. The performance was defined as the proportion of population response vectors that were correctly classified. To assess statistical significance of the classification performance we calculated the probability of getting correct classifications by chance, which is given by the binomial distribution: $P(k) = \binom{m}{k} p^k (1-p)^{m-k}$, where p is the probability of getting a correct classification by chance (p = 1/4) and m is the number of tests. Significant decoding was reached when the decoding performance exceeded the 95th percentile of $P(k)$. The classification performance was computed using the fluorescence signals of 10 randomly chosen ensembles of n ROIs and then averaged over ensembles and larvae.

Statistical tests and software

The significance of power-law fits was evaluated using Kolmogorov-Smirnov (KS) statistics between the empirical data and the MLE fit and by log-likelihood ratio (LLR) tests between the power-law distribution and the log-normal distribution. When using one-way repeated-measures (rm) ANOVA, where the ANOVA's sphericity assumption was not met (using the Mauchly test), p values were corrected using the Huynh-Feldt estimates of sphericity. No statistical methods were used to determine sample sizes in advance, but sample sizes are similar to those reported in other studies in the field.

Data was analyzed with custom routines written in MATLAB. Power-law and scaling shape collapse analyses were performed using the NCC MATLAB Toolbox described in Marshall et al. (2016) and available at: www.nicholastimme.com/software.html. LLR tests were performed using the Python package Powerlaw, described in Alstott et al. (2014), and available at: https://github.com/jeffalstott/powerlaw. The Orca Flash 4.0 sCMOS camera (Hamamatsu) was controlled using HCImageLive 4.3 (Hamamatsu). The scanner and the piezo were controlled using custom-made routines in MATLAB.

DATA AND SOFTWARE AVAILABILITY

Custom written MATLAB code will be made available by the authors upon request.

Neuron, Volume *100*

Supplemental Information

Whole-Brain Neuronal Activity Displays Crackling Noise Dynamics

Adrián Ponce-Alvarez, Adrien Jouary, Martin Privat, Gustavo Deco, and Germán Sumbre

Supplemental Information

Inventory

- **Table S1.** Summary of the statistics of the spatial clusters for each dataset. Related to Figure 1.
- **Table S2.** Summary of the statistics of the neuronal avalanches for each dataset. Related to Figure 2; Figure 3; Figure 5.
- **Supplemental figure S1.** Selective-plane illumination microscopy (SPIM). Related to Methods: Selective-plane illumination microscopy.
- **Supplemental figure S2.** Statistics of spatial clusters. Related to Figure 1.
- **Supplemental figure S3.** Illustration of avalanche definition. Related to Figure 2.
- **Supplemental figure S4.** Avalanches at the population level and the effect of coarse graining on avalanche exponents. Related to Figure 2.
- **Supplemental figure S5.** Single anatomical brain regions also show critical dynamics. Related to Figure 6.
- **Supplemental figure S6.** Activity during sensory stimulation and self-generated behavior presents changes not only in the rate of calcium events but also in their correlation structure. Related to Figure 7.
- **Supplemental figure S7.** Neuronal avalanches during self-generated behavior had larger sizes and their distribution across different brain regions was biased towards hind-brain motor areas. Related to Figure 7.
- **Supplemental figure S8.** Effect of heptanol on free-swimming behavior and visual stimulus decoding scheme. Related to Figure 8.
- **Supplemental video S1.** Whole-brain neuronal activity. Related to Figure 1; Figure 2.

Supplementary tables, figures, and videos

Supplementary tables

Dataset #	Ca^{2+} indicator	Nb. of ROIs	Q	ρ_c	$P(C_s) \sim C_s^{-\sigma}$				$g(r) \sim r^{-\eta}$	
					KS stat.	$\sigma(\rho_c)$	cutoffs	LLR (norm.)	η	cutoffs
1	GCAMP5	41,115	9	0.24	0.036	2.17 ± 0.01	[6, 10^3]	+55.2*	0.16 ± 0.01	[10, 500]
2	GCAMP6f	84,177	6	0.16	0.031	2.16 ± 0.01	[6, 10^3]	+72.1*	0.24 ± 0.01	[10, 500]
3	GCAMP6f	86,110	6	0.11	0.021	2.22 ± 0.01	[6, 10^3]	+113.5*	0.22 ± 0.01	[10, 500]
4	GCAMP6f	89,349	3	0.08	0.041	2.20 ± 0.01	[6, 10^3]	+75.88*	0.14 ± 0.01	[10, 500]
5	GCAMP5	51,466	8	0.15	0.043	1.97 ± 0.01	[6, 10^3]	+112.6*	0.27 ± 0.01	[10, 500]
6	GCAMP5	50,731	5	0.14	0.046	2.15 ± 0.01	[6, 10^3]	+70.5*	0.23 ± 0.01	[10, 500]

Table S1. Summary of the statistics of the spatial clusters for each dataset. Related to Figure 1. Q: number of spontaneous and stimulus segments (20 min of spontaneous activity and 4 min of visual stimulation). ρ_c: fraction of activated ROIs that maximizes the average number of connected components ($\langle m \rangle$). The probability of cluster sizes C_s was evaluated for the set of clusters with ρ comprised between $\rho_c - \Delta$ and $\rho_c + \Delta$, where Δ=0.02, and for $C_{s,\min} \leq C_s \leq C_{s,\max}$ (cutoffs). The probability density was fitted to a truncated power law using MLE (Marshall et al., 2016). In the table, we reported the MLE power exponent $\sigma(\rho_c)$ (± the estimation error), the KS-statistics between the data distribution and the fitted MLE power law, and the cutoffs $[C_{s,\min}, C_{s,\max}]$. We also reported the normalized log-likelihood ratio (LLR) for the comparison between the power-law and the log-normal distributions. Significantly positive values of LLR indicate that the power-law distribution was a better predictor of the data than the log-normal distribution; asterisks indicate that LLR were statistically different from zero ($p < 0.001$). Finally, we calculated the correlation function $g(r)$, i.e., the average correlation between pairs of ROIs as a function of the Euclidean distance between them (r). We fitted the relation $g(r) \sim r^{-\eta}$ using least squares for $r_{\min} \leq r \leq r_{\max}$ (cutoffs, in μm) and obtained the exponent η and its estimation error.

Data-set	$P(T)\sim T^{-\alpha}$				$P(S)\sim S^{-\tau}$				$\langle S\rangle(T)\sim T^{1/\sigma\nu z}$	Profile collapse		Recurrence-time collapse	
	KS stat.	α	cutoffs	LLR	KS stat.	τ	cutoffs	LLR	$\sigma\nu z$	$\sigma\nu z$	$\Delta\sigma_F^2$	γ	$\Delta\sigma_G^2$
1	0.015	2.86 ± 0.01	[1.88, 18.8]	+192.3*	0.022	2.10 ± 0.01	[6; 10^4]	+99.9*	0.52 ± 0.02	0.55	3.8	0.17	4.6
2	0.007	2.92 ± 0.02	[2.35, 18.8]	+23.1*	0.035	2.01 ± 0.01	[6; 2×10^4]	+35.5*	0.59 ± 0.02	0.60	10.1	0.45	5.7
3	0.008	3.44 ± 0.01	[0.94, 18.8]	+172.5*	0.046	1.98 ± 0.01	[6; 2×10^4]	+27.2*	0.51 ± 0.02	0.51	10.5	0.43	4.5
4	0.013	3.22 ± 0.03	[2.82, 18.8]	+5.9*	0.039	2.06 ± 0.01	[6; 2×10^4]	+41.8*	0.55 ± 0.03	0.56	3.9	0.37	1.9
5	0.018	2.72 ± 0.01	[1.41, 18.8]	+69.0*	0.024	1.96 ± 0.01	[6; 10^4]	+30.7*	0.52 ± 0.01	0.54	12.5	0.23	4.2
6	0.013	2.90 ± 0.02	[2.35, 18.8]	+46.4*	0.026	1.91 ± 0.01	[6; 10^4]	+77.83*	0.53 ± 0.02	0.53	8.8	0.33	5.6
7	0.017	2.25 ± 0.02	[1.41, 18.8]	+36.9*	0.018	1.64 ± 0.01	[6; 10^4]	+32.6*	0.57 ± 0.03	0.65	2.8	0.30	2.6
8	0.028	2.07 ± 0.02	[1.41, 18.8]	+5.2*	0.041	1.73 ± 0.002	[6; 10^4]	-1.5$^{n.s.}$	0.68 ± 0.02	0.67	2.6	0.86	0.7

Table S2. Summary of the statistics of the neuronal avalanches for each dataset. Related to Figure 2; Figure 3; Figure 5. We evaluated the probability distribution of avalanche durations T and sizes S. For each distribution, we fitted truncated power laws using MLE ($P(T)\sim T^{-\alpha}$ and $P(S)\sim S^{-\tau}$) and further evaluated the fitting using KS-statistics. The estimation error of the MLE power exponent was calculated using bootstrap re-sampling. The cutoffs ($T \in [T_{\min}, T_{\max}]$ and $S \in [S_{\min}, S_{\max}]$) of the truncated power laws are also indicated. We also reported the normalized log-likelihood ratio (LLR) for the comparison between the power-law and the log-normal distributions. Significantly positive values of LLR indicate that the power-law distribution was a better predictor of the data than the log-normal distribution; asterisks indicate that LLR were statistically different from zero ($p < 0.001$). We also calculated the average size $\langle S\rangle(T)$ of avalanches of duration T and fit the relation $\langle S\rangle(T)\sim T^{-1/\sigma\nu z}$ using least squares (within the corresponding duration and size cutoffs) to obtain the exponent $\sigma\nu z$ and its estimation error. We estimated the best possible collapse of the avalanche profiles given by: $\langle S(t,T)\rangle T^{1-1/\sigma\nu z} = F(t/T)$. The exponent $\sigma\nu z$ was estimated using the method of Marshall et al. (2016). $\Delta\sigma_F^2$: amount of collapse. The curve onto which the scaled recurrence time distributions collapse was approximated by a gamma distribution with the shape parameter given by γ. The amount of collapse was evaluated by $\Delta\sigma_G^2$. Datasets 7 and 8 correspond to larvae exposed to heptanol before the experiments.

Supplementary figures

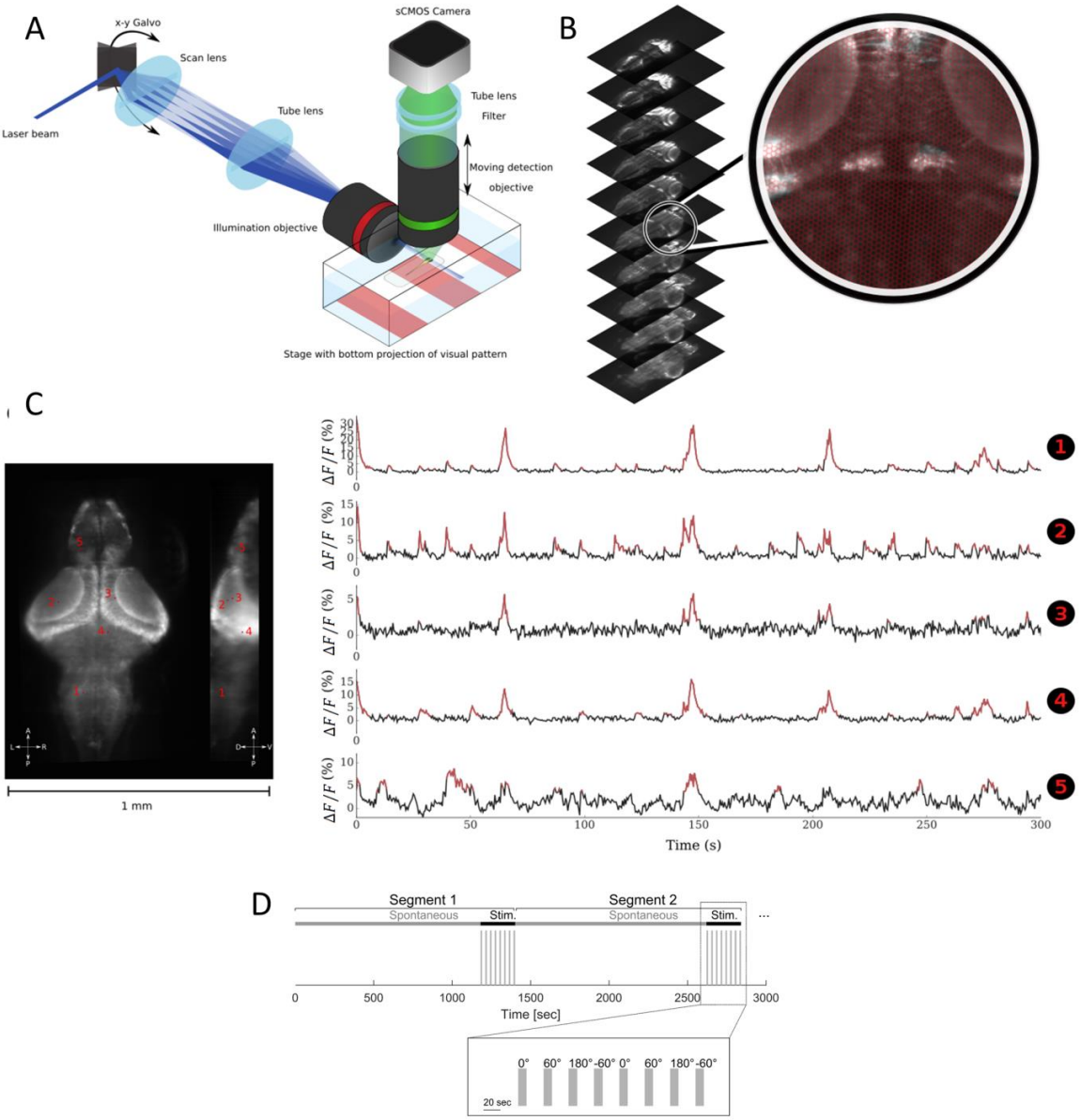

Supplemental figure S1. Selective-plane illumination microscopy (SPIM). Related to Methods: *Selective-plane illumination microscopy*. **A**: Scheme of the optical path of the light-sheet microscope. **B**: Subset of coronal sections obtained with the SPIM. The full stack corresponds to 40 coronal sections recorded every 5 µm. In each coronal section, a hexagonal grid was applied to obtain the ROIs from which the average fluorescence signal was extracted. **C.** The relative increase in fluorescence intensity ($\Delta F/F$) of five example ROIs. *Left*: location of the ROIs. *Right*: fluorescence intensity for the example ROIs; Ca^{+2} transients that exceed the binarization threshold are shown in red. **D:** Experimental paradigm. The experiment was composed of *Q* consecutive segments of 20 min of spontaneous activity and 4 min of visual stimulation. *Q* was different for different datasets and ranges between 3–9 (see **Table S1**). *Inset*: Each visual stimulation period contained 8 sub-episodes during which a moving grating was presented below the larva for 10 sec (represented in gray). The motion directions of the 8 gratings were equal to 0°, 60°, 180°, -60°, 0°, 60°, 180°, and -60°, respectively, relative to the larva's caudo-rostral axis. The inter-stimulus interval was equal to 20 sec.

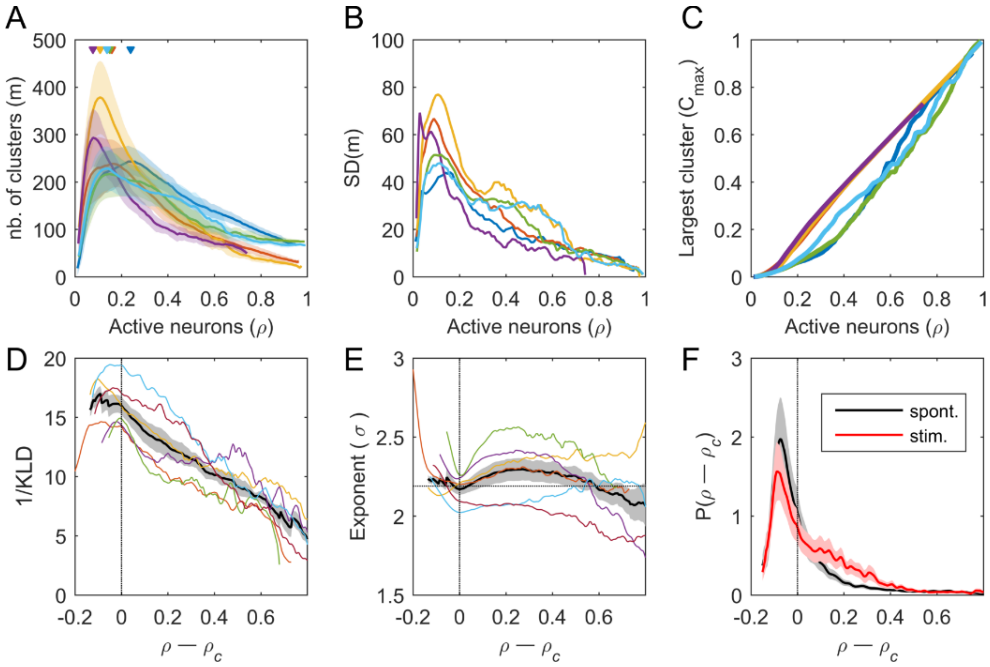

Supplemental figure S2. Spatial clusters. Related to Figure 1. A-B: Number of activity clusters (*m*) as a function of the proportion of active ROIs (ρ) for each dataset (color traces). In panel (A) the shaded areas represent standard deviation of *m*, which is represented in (B) as a function of ρ. **C:** Normalized size of the largest cluster (C_{max}) as a function of ρ. **D-E:** The cluster size distribution for the set of clusters that appeared with *p* comprised within small intervals $[\rho - \Delta; \rho + \Delta]$ with Δ=0.02 was fitted to a power law. The goodness-of-fit (1/KLD) of the power law (D) and the estimated power exponent (E) were calculated as a function of $\rho - \rho_c$, for each dataset (color traces). The black traces represent the average goodness-of-fit and the average power exponent. The gray areas represent SEM. **F:** Distribution of $\rho - \rho_c$ (*black*: spontaneous activity, *red*: for stimulus-evoked activity) averaged over all datasets (the mean and the SEM of the distributions are indicated by the solid line and the shaded area, respectively).

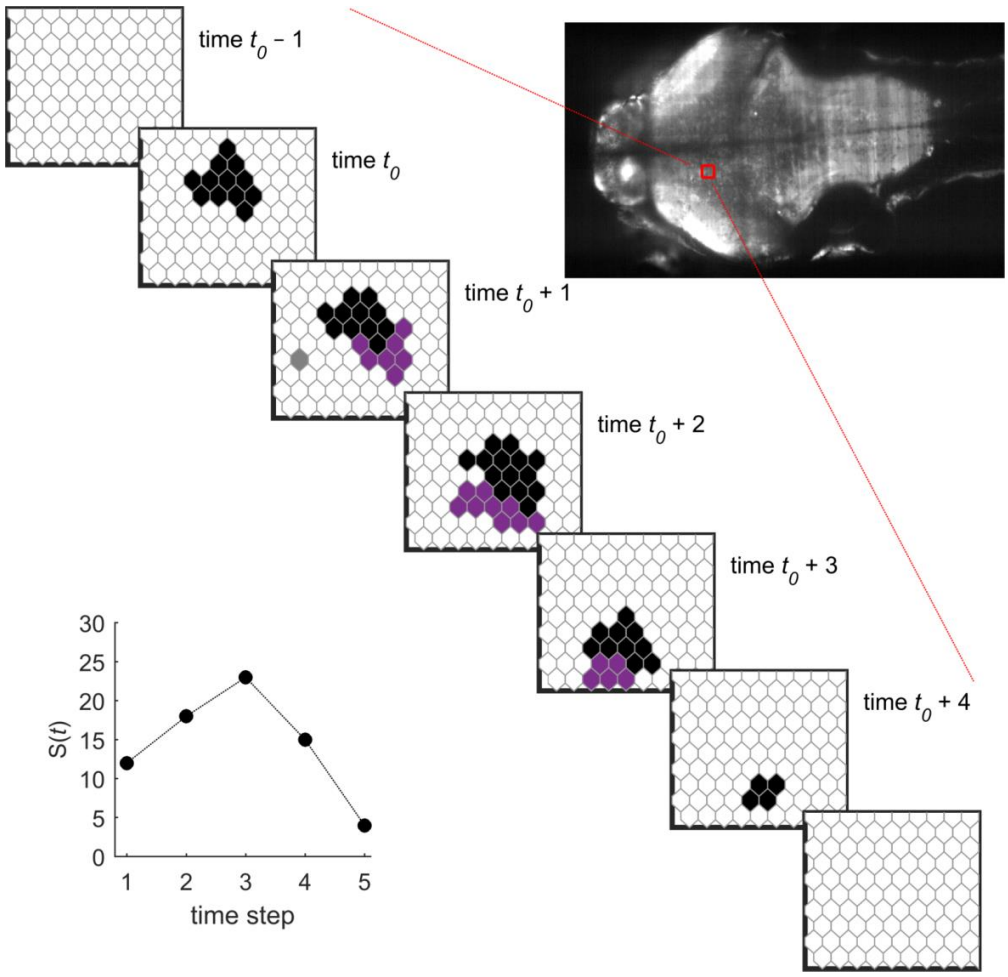

Supplemental figure S3. Avalanche definition. Related to Figure 2. The illustration of an avalanche is shown here in 2D for simplicity but note that the analysis was done in 3D. An avalanche was initiated with the detection of a cluster of active ROIs at time t_0, the avalanche continued at time t_0+1 with a cluster composed of ROIs that were active at the preceding time t_0 (represented in black) plus ROIs that activated at t_0+1 (represented in purple), and so on, until this condition no longer held. The avalanche terminated at time t_0+4. The ROI represented in gray that was activated at time t_0+1 did not participate in an avalanche, since it did not belong to any activity cluster. For this schematic example the size and duration of the avalanche were equal to S = 72 (the cumulative sum of the number of activated ROIs during the avalanche) and $T = 5 \times dt$ (number of frames multiply by the temporal resolution, dt, of the data), respectively. The time-course of the avalanche size, $S(t)$, is shown in the left bottom panel.

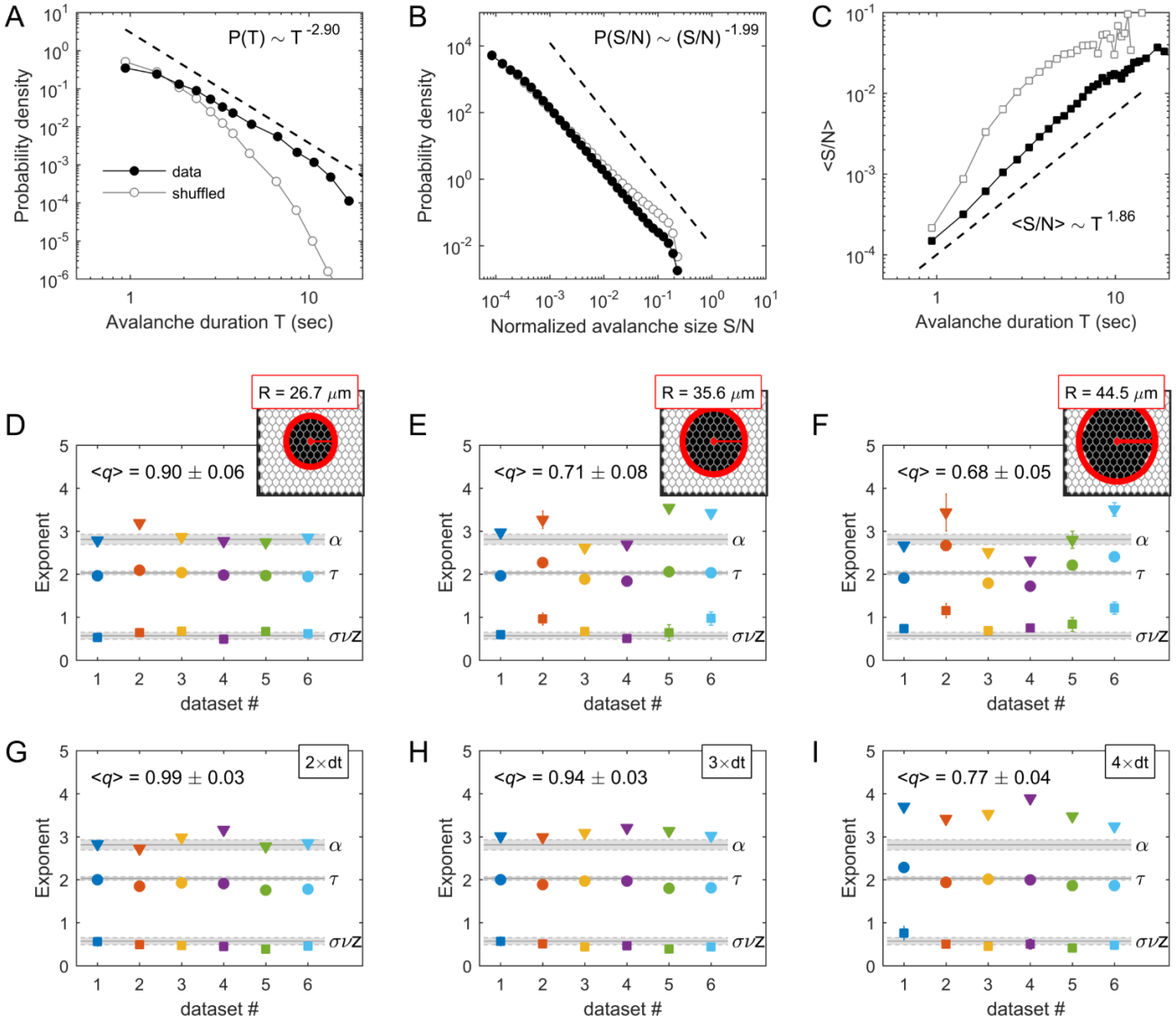

Supplemental figure S4. Avalanches at the population level and the effect of coarse graining on avalanche exponents. Related to Figure 2. A-C: We analyzed the neuronal avalanches' statistics after pooling the avalanche sizes and durations of all datasets. For each dataset, sizes were normalized by the total number of cells (*N*). **A:** Distribution of avalanche durations *T* (in sec). **B:** Distribution of avalanche normalized sizes *S/N*. **C:** Relation between <*S/N*> and *T*. In (A), (B), and (C) open symbols correspond to time-shuffled datasets and the black dashed lines indicate the expected power-law distributions in the case of a critical behavior. The measured exponents are indicated in each panel. **D-F:** Spatial coarse graining. Co-active ROIs were grouped to form 3D clusters if their Euclidean distance was shorter than a given value R, representing the level of coarse graining. For simplicity, only a 2D scheme is shown. The exponents of the neuronal avalanche obtained for different levels of coarse graining. Note that for clusters larger than a sphere of radius R~30 μm the values of the avalanche exponents deviate from the theoretical values and the exponent relation did not hold anymore (for R<30 μm the variable $q = (\tau - 1)/[\sigma\nu z(\alpha - 1)]$ is close to 1 on average but becomes ≤0.71 for larger radii). The size of the clustering neighborhood used in the present study lies below this threshold. **G-I:** Temporal coarse graining. Avalanche exponents were calculating after down-sampling the data, using time bins equal to 2×*dt* (E) 3×*dt* (G), and 4×*dt* (I), where *dt* is the original temporal resolution of the data (*dt* = 0.47 sec). The average variable q is also presented. For time bins longer than 4×*dt* the values of the avalanche exponents deviate from the theoretical values and the exponent relation did not hold anymore.

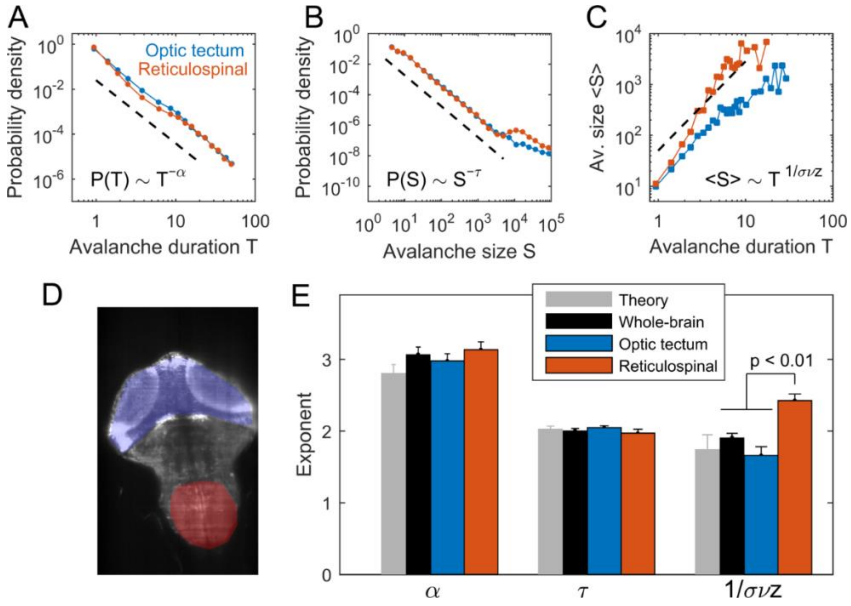

Supplemental figure S5. Single anatomical brain regions also show critical dynamics. Related to Figure 6. Neuronal avalanches observed within two brain regions with different functional roles, i.e, the optic tectum (sensory processing) and the rhombomere 7 (reticulospinal circuit for movement generation). **A-C:** Avalanche durations and sizes displayed power-law statistics with power exponents close to the corresponding critical values. Nevertheless, while durations and average sizes of neuronal avalanches in the optic tectum matched the expected scaling relation ($\langle S \rangle(T) \sim T^{1/\sigma\nu z}$, with $\sigma\nu z \approx 0.57$), reticulospinal avalanches deviated from it: for a given duration T, the average size of the avalanches were larger than predicted by criticality theory. **D:** Locations of the optic tectum (blue) and the rhombomere 7 containing the reticulospinal circuit (red) in one optical coronal plane. **E:** Average power-law exponents describing the distribution of durations (α), sizes (τ), and the relation between sizes and durations ($1/\sigma\nu z$) of spontaneous neuronal avalanches displayed in the optic tectum (blue) and the reticulospinal region (red). For comparison, the gray and the black bars indicate the critical exponents of 3D random field Ising theoretical models and the exponents observed in the whole-brain activity, respectively. Differences between whole-brain, optic tectum, and reticulospinal activities were evaluated using ANOVA followed by Tukey-Kramer multiple comparisons tests.

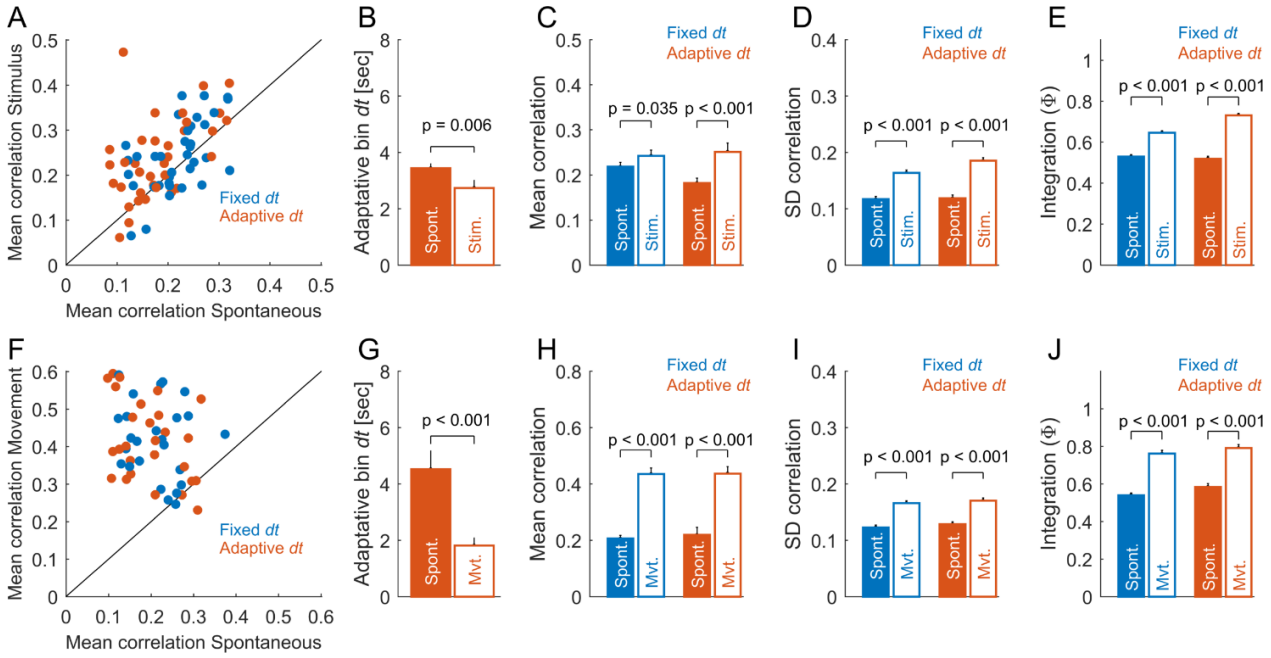

Supplemental figure S6. Activity during sensory stimulation and self-generated behavior presents changes not only in the rate of calcium events but also in their correlation structure. Related to Figure 7. We compared the rate and Pearson correlations of binary data during spontaneous activity, during sensory stimulation, and around spontaneous movements. We also analyzed the data using *adaptive binning*, i.e., by choosing a time bin dt according to the inverse of the average rate of the calcium point processes (Yu et al., 2017). Data with high rate led to a short dt, data with low rate led to a long dt. **A:** Average correlations during spontaneous activity and during sensory stimulation, for fixed dt (equal to a recording frame) and for an adaptive binning. Each dot represents the average correlation in one of the Q data segments, for a given larva. Correlations were calculated for all pairs among 40,000 ROIs. **B:** Adaptive binning for spontaneous and stimulus-induced activities. **C:** Average correlations during spontaneous and stimulus-induced activities, for both types of temporal binning. **D:** Standard deviation of the distribution of correlations during spontaneous and stimulus-induced activities, for both types of temporal binning. **E:** To characterize the topology of the correlation matrices during spontaneous and stimulus-induced activities, we calculated the integration measure, Φ, that quantifies the connectiveness of the matrix (Deco et al., 2015). Briefly, Φ is calculated by, first, thresholding the correlation matrix, making it a binary graph, using a threshold θ. Second, we calculated the largest connected component $LCC(\theta)$ of the binary graph. Finally, Φ is given by the integral of $LCC(\theta)/N$ over all tested thresholds θ, where N is the number of ROIs. p: p-value, two-sample t-test comparing values for spontaneous and stimulus-induced activities. **F-J:** same as panels (A-E) but for data around the onsets of detected tail movements, denoted ton, and compared them to those in the absence of movements. p: p-value, two-sample t-test comparing values around movement onsets and the values in the absence of movements. These results show that sensory stimulation and self-generated behavior change not only the rate of calcium vents but also their correlation level and topology, even in the case of adaptive binning. This shows that the stimulus/movement-induced changes in neuronal avalanche exponents that we observed (**Figure 7**) were not simply explained by a change in the rate of the point process.

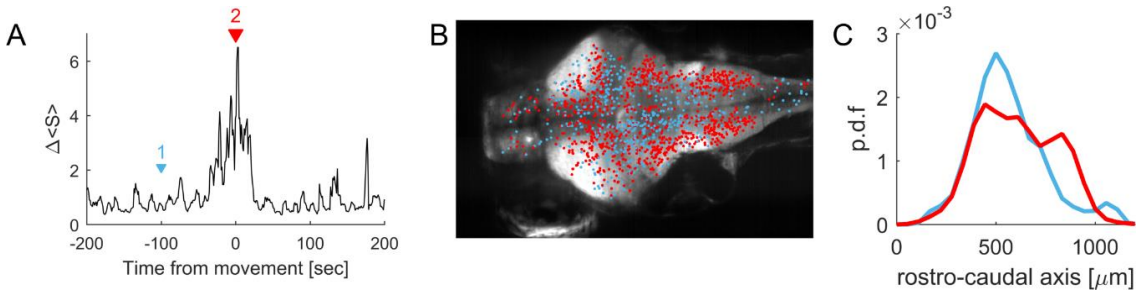

Supplemental figure S7. Neuronal avalanches during self-generated behavior had larger sizes and their distribution across different brain regions was biased towards hind-brain motor areas. Related to Figure 7. A: The average size of neuronal avalanches around self-generated tail movements (0 sec represents the onset of the movement). The values were normalized by the average across time, i.e., $\Delta S = \langle S(t) \rangle_{tails} T / \sum_{t=-200}^{t=+200} \langle S(t) \rangle_{tails}$, where $\langle . \rangle_{tails}$ represents the average over tail movements and T is the length of the observation window. **B:** Locations of the initial centers of mass of neuronal avalanches projected on the coronal (x–y) plane of the brain during periods of spontaneous activity (blue dots, corresponding to the blue epoch in panel A, 1) and during the onset of tail movements (red dots; corresponding to the red epoch in panel A, 2). Each dot represents a neuronal avalanche. **C:** Probability density function of avalanche origins along the rostro-caudal axis during periods of spontaneous activity (blue) and during the onset of tail movements (red). We observed that with respect to periods of spontaneous activity, during tail movements, the neuronal avalanches had larger sizes and their distribution across different brain regions was biased towards hind-brain motor areas (caudal).

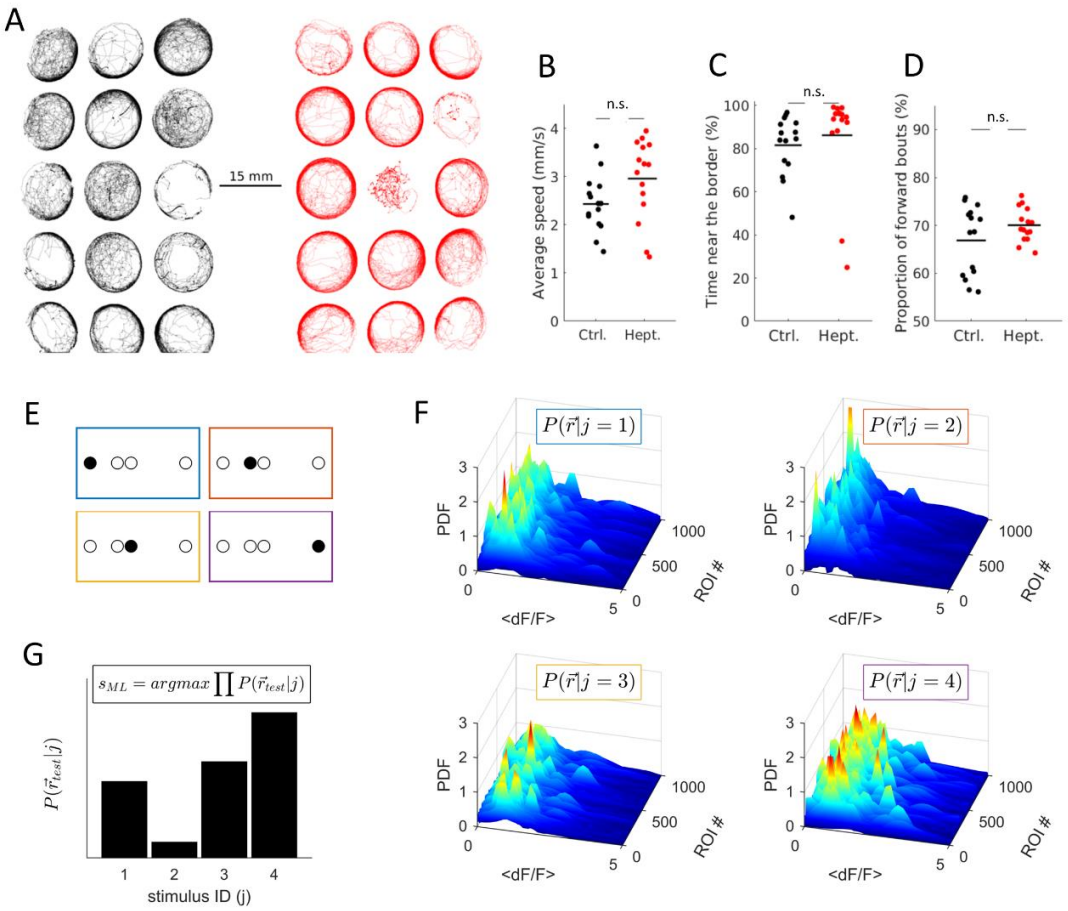

Supplemental figure S8. Effect of heptanol on free-swimming behavior and visual stimulus decoding scheme. Related to Figure 8. We compared the trajectory of 15 freely swimming GCaMP5 larvae at 7 dpf with 15 other GCaMP5 larvae exposed to 90 µM of heptanol for 3 h prior to the experiments. **A:** Paths of the image centroids of each of the 30 larvae in a multi-well plate during 30 min of spontaneous behavior. The paths are colored in black for the control larvae (*left*) and in red for the heptanol exposed larvae (*right*). Note that for visualization purposes only 5 min. of the larvae behavior are shown. **B:** Average speed of the larvae in the control and heptanol-treated conditions. Each dot represents one larva, a horizontal jitter was added for visualization. The horizontal lines represent the mean of the two distributions (Ctrl.: 2.43 ± 0.04 mm/sec vs. Hept.: 2.96 ± 0.06 mm/sec; p=0.054, two-sample t-test). **C:** The time the larvae spent near the border of the recording chamber (< 2mm from the border). The horizontal lines represent the mean of the two distributions (Ctrl.: 81.5 ± 13.6 % vs. Hept.: 86.08 ± 22.77 %; p=0.51, two-sample t-test). **D:** Distribution of the turning behavior quantified by the proportion of forward swimming bouts (a change in direction < 10 deg.). The horizontal lines represent the mean of the two distributions (Ctrl.: 66.85 ± 7.22 % vs. Hept.: 70.03 ± 3.5 %; p=0.14, two-sample t-test). **E-G:** A maximum likelihood decoder (MLD) was used to classify the location of visual stimuli presented to larvae from the fluorescence signals $\Delta F/F$ in the optic tectum. **E:** The stimulus set was composed of light spots of 4 deg. presented at four possible spatial locations (75º, 85º, 90º, 110º). **F:** The neuronal responses of n ROIs, $\vec{r} = [r_1, r_2, \dots, r_n]$, were used to learn the probability distributions of the response of each ROI to each stimulus of category *j*, i.e., $P(\vec{r}|j)$. **G:** The MLD chooses the stimulus that is statistically most likely to have elicited a newly observed response of the n signals, i.e., $\vec{r}_{test} = [r_1, r_2, \dots, r_n]$, given the learned probability distributions. With the simplifying assumption that the responses of the ROIs were assumed to be statistically independent from each other, the decoding of the population response consisted of searching for the stimulus (s_{ML}) which maximized the probability of the testing response: $s_{ML} = argmax \prod_{i=1}^{n} P(r_{i,test}|j)$. The performance was defined as the proportion of population response vectors that were correctly classified.

Supplementary Videos

Supplemental video S1. Whole-brain neuronal activity. Related to Figure 1; Figure 2. The first row displays the relative increase in fluorescence ($\Delta F/F$) in the hexagonal regions of interest (ROIs) in five different coronal sections. The second row shows the corresponding binarized activity used to compute the clusters. The last row depicts the time-course of the percentage of active ROIs in the entire volumetric recording.